

Structure-Reactivity Relationships in Metal Sulfide/C₃N₄ Based Semiconductor Catalysts Used for Photocatalytic H₂ Evolution

Dissertation

zur

Erlangung des akademischen Grades

doctor rerum naturalium (Dr. rer. nat.)

an der Mathematisch-Naturwissenschaftlichen Fakultät

der Universität Rostock

vorgelegt von

Ramesh Poonchi Sivasankaran, geboren am 19.06.1989 in Buchireddypalli, Tamil Nadu, aus Indien
Rostock, 26-07-2019

Referees

1. Prof. Dr. Angelika Brückner
Leibniz Institute for Catalysis, University of Rostock
2. Prof. Dr. Ralf Ludwig
Institute for Chemistry, University of Rostock

Date of thesis submission: 26-07-2019

Date of defense: 29-10-2019

Declaration

I declare that the research work presented in this thesis is my own and carried out entirely at the Leibniz Institute for Catalysis (LIKAT), Rostock, Germany under the supervision of Prof. Dr. Angelika Brückner (Head of the Department “Catalytic in situ-Studies”) and Dr. Nils Rockstroh.

Rostock, 26-07-2019

Poonchi Sivasankaran Ramesh

Contents

Acknowledgment	v
Abstract	vii
Zusammenfassung.....	viii
List of all abbreviations.....	x
1 Motivation, objective and state of the art	1
1.1 Motivation and objective.....	1
1.2 State of the art	6
1.2.1 Development of g-C ₃ N ₄ semiconductor for photocatalytic H ₂ production	10
1.2.2 Mesoporous and ordered mesoporous g-C ₃ N ₄	11
1.2.3 Morphology controlled g-C ₃ N ₄	13
1.2.4 Doped g-C ₃ N ₄	14
1.2.5 Role of co-catalysts in photocatalytic H ₂ and O ₂ evolution.....	17
1.2.6 Loading co-catalysts on g-C ₃ N ₄	19
1.2.7 Semiconductor/g-C ₃ N ₄ heterojunction.....	23
1.2.8 Role of sacrificial agents in photocatalytic H ₂ and O ₂ evolution.....	26
2 Experimental	28
2.1 Catalyst synthesis.....	28
2.1.1 Synthesis of mesoporous C ₃ N ₄ , AgIn ₅ S ₈ and AgIn ₅ S ₈ /C ₃ N ₄ composite	28
2.1.2 Synthesis of 2H and 1T phase MoS ₂ and MoS ₂ /C ₃ N ₄ composites.....	28
2.2 Catalytic testing	30
2.3 Catalyst characterization Techniques	32
2.3.1 X-ray diffraction (XRD).....	32
2.3.2 Ultraviolet-visible diffuse reflectance spectroscopy (UV-vis-DRS).....	33
2.3.3 Attenuated total reflectance-infrared (ATR-IR) spectroscopy.....	34
2.3.4 Scanning transmission electron microscopy (STEM).....	35
2.3.5 X-ray photoelectron spectroscopy (XPS)	37
2.3.6 Brunauer-Emmett-Teller (BET) surface area and pore size distribution analysis	38
2.3.7 Inductively coupled plasma-optical emission spectroscopy (ICP-OES).....	40
2.3.8 Carbon, hydrogen, nitrogen and sulfur (CHNS) elemental analysis	40
2.3.9 <i>In situ</i> electron paramagnetic resonance (EPR) spectroscopy	41
2.3.10 Photoluminescence (PL) spectroscopy	43
3 Relations between structure, activity and stability in AgIn₅S₈/C₃N₄ composite photocatalysts used for photocatalytic H₂ production.....	45
3.1 Catalytic activity.....	46
3.2 Catalyst characterization	48
3.2.1 Crystal structure, optical and structural properties.....	48
3.2.2 Surface area analysis: N ₂ adsorption-desorption isotherms	50

3.2.3	Morphology and microstructure analysis by STEM.....	51
3.2.4	Surface chemical analysis by XPS.....	54
3.2.5	CO adsorption study by FT-IR	55
3.3	Mechanism: charge separation and transfer.....	56
3.3.1	Visualization of charge separation and transfer by in situ-EPR	56
3.3.2	Photoluminescence spectroscopy study.....	58
3.4	Conclusions.....	59
4	Influence of MoS₂ on Activity and Stability of Carbon Nitride in Photocatalytic Hydrogen Production.....	61
4.1	Catalytic activity.....	61
4.2	Catalyst characterization.....	62
4.2.1	Crystal structure and optical properties.....	62
4.2.2	Surface area analysis: N ₂ adsorption-desorption isotherms	64
4.2.3	Morphology and microstructure analysis by STEM.....	65
4.2.4	Surface chemical analysis by XPS.....	66
4.3	Mechanism: charge separation and transfer.....	69
4.3.1	Monitoring charge separation and transfer by in situ-EPR	69
4.3.2	Photoluminescence spectroscopy study.....	70
4.4	Conclusions.....	71
5	Influence of different sacrificial agents on photocatalytic H₂ production over C₃N₄ photocatalysts..	72
5.1	Catalytic activity.....	72
5.2	Photocatalytic H ₂ production with basic sacrificial reagents	73
5.3	Photocatalytic H ₂ production with acidic sacrificial reagents.....	75
5.4	Conclusion.....	78
	References.....	79
	Appendix	I
	List of scientific publications and conferences	X

Acknowledgment

- First of all, I would like to express my sincere gratitude to my supervisor Prof. Angelika Brückner for giving me this great opportunity to work as a PhD student at LIKAT. Thank you so much for helpful guidance, support, discussions and useful suggestions throughout my research work.
- I would also like to extend my sincere thanks to Dr. Nils Rockstroh and Dr. Dirk Hollmann for helpful guidance, discussions, teaching photocatalytic experimental set-up and EPR spectroscopy. Further thanks go to Dr. Ursula Bentrup and Mrs. Christine Rautenberg for FT-IR measurements and discussions. And also, I would like to thank Dr. Jabor Rabeah for EPR discussions and strong encouragements.
- I would like to thank Dr. Henrik Junge for providing the photocatalytic experimental set-up in his laboratory and Mrs. Petra Bartels for the help and support with photocatalytic tests.
- I would like to thank Prof. Arne Thomas and Mr. Amitava Acharjya for providing mesoporous C_3N_4 materials.
- I would like to thank my colleagues Dr. Huyen Vuong Thanh, Reni Grauke, Sonja Keller, Dr. Sven Adomeit, Dr. Andrea Bellmann, Dr. Denise Heyl, Binh Ngoanh, Dr. Sudarsanam Putla, Dr. Aws Al-Abo, for their help in many aspects.
- I would like to give special thanks to all analytical staff at LIKAT, especially, Dr. Henrik Lund for XRD measurements, Dr. Giovanni Agostini and Dr. Stephan Bartling for XPS measurements, Dr. Carsten Robert Kreyenschulte for STEM measurements, Mrs. Anja Simmula for ICP-OES analysis, Mrs. Astrid Lehmann for CHNS analysis and Mr. Reinhard Eckelt for BET measurements.
- I would also like to extend my thanks to workshop, administration and purchasing department members of LIKAT for all assistance and the pleasant work atmosphere.
- I would like to express my grateful thanks to Leibniz foundation for providing the financial support.
- I would like to thank my friends in Rostock for the friendly events we shared together.
- I wish to express my heartfelt gratitude to my dear wife Sangeetha for her love, understanding and support during my PhD time.
- Finally, I express my deepest gratitude to my parents, father Sivasankaran and mother Jayalakshimi, brother Suresh, sister Durga, uncle Nagaraj for constant support and encouragement during the course of my doctoral studies.

Abstract

Hydrogen is an environmentally acceptable fuel due to its high gravimetric energy density and its clean combustion. Photocatalytic hydrogen production by using sunlight is an efficient method for direct conversion of solar energy into a usable or storable energy resource. With respect to a future practical application, the utilization of heterogeneous semiconductors is of advantage. One of the major problems in photocatalysis is the fast recombination of photogenerated electron-hole pairs, limiting the overall efficiency by releasing the absorbed energy in the form of heat or light. Typically, photogenerated electron-hole pairs have a recombination time in the order of 10^{-9} s, whereas the reaction time of electrons and holes with adsorbed species is quite longer (10^{-8} - 10^{-3} s). However, charge separation and recombination can be regarded as competitive processes if the recombination of charge carriers is efficiently decelerated. The sunlight-to-hydrogen conversion efficiency is directly determined by the absorption capability of the material that can be improved by loading of other elements or the formation of heterojunctions. In this context, developing nanocomposites of C_3N_4 (CN) with other semiconductors is a promising strategy that creates synergistic heterojunctions, eventually resulting in an improved absorption and charge separation and hence higher photocatalytic efficiency.

Subject of the present work is the synthesis of metal sulfide/CN composites and their application in photocatalytic hydrogen generation. However, the formation mechanism of photogenerated charge carriers as well as their separation and transfer during the photocatalytic reaction is still not clear, though its complete understanding is inevitable in order to tune the photocatalytic properties for achieving high photocatalytic H_2 production efficiency. For this reason, different strategies were employed to synthesize metal sulfide/CN heterojunction composites. Subsequently, these materials have been investigated in photocatalytic H_2 production and their crystal structure, optical properties, chemical composition and microstructure were analyzed by XRD, UV-vis-DRS, ATR-IR, XPS and HAADF-STEM. Moreover, photoluminescence (PL) and in situ electron paramagnetic resonance (in situ-EPR) spectroscopy were applied for monitoring charge separation and transfer.

First, investigation of pure CN in the presence of Pt (Pt/CN) and triethanolamine (TEOA) as sacrificial reagent showed a high initial H_2 formation rate that decreased during the course of the reaction due to inclusion of Pt NPs in the bulk matrix of CN as was confirmed by STEM, XPS and ICP-OES measurements. This behavior was not observed with oxalic acid (OA) as sacrificial reagent, since in this case Pt NPs were enriched on the outermost surface of CN. In the case of Pt/AIS-CN catalysts, Pt NPs were preferentially deposited on the surface of the AIS phase which prevents them from inclusion in the CN phase, keeping them accessible for proton reduction. In situ EPR data visualized that the EPR signal is much higher for pure CN under UV-vis light irradiation. When raising the AIS amount, the EPR signal is decreased, most likely due to transfer of electrons from CN to AIS. Similarly, the photoluminescence emission intensity of the composites decreased with increasing AIS contents underpinning the results obtained from EPR

spectroscopy. When Pt is deposited on both CN and AIS/CN, the PL emission intensity decreased which is associated with a transfer of excited CB e^- from CN to Pt or from CN via AIS to Pt. Thus, charge carrier recombination is efficiently suppressed, which leads to a concomitant extension of their lifetime enhancing proton reduction to H_2 .

MoS_2 was used as a second metal sulfide and MoS_2/C_3N_4 (MS-CN) composite photocatalysts were synthesized by three different methods such as in situ-photodeposition (PD), sonochemical (SC) and thermal decomposition (TD). Among the synthesized composites, 2H phase MS-CN synthesized by in situ-photodeposition method led to the highest H_2 evolution rate under UV-vis light irradiation. STEM investigations showed, that Pt is deposited on both the CN and MoS_2 in all of the composites, which is in contrast to AIS-CN composites. Moreover, STEM and UV-vis spectroscopy revealed a partial wrapping of the CN phase by larger particles in the case of the less active samples and the formation of a sufficiently thin crystalline layer of 2H MoS_2 only in 2H MS-CN (PD) making an intimate interfacial contact with CN that favors charge separation and enhances the photocatalytic activity. In situ EPR results showed that the EPR CB e^- signal for Pt/MS-CN (PD) is lower compared to all other catalysts indicating a more efficient electron transfer from CN to Pt leading to a higher activity.

A further aspect important in the photocatalytic hydrogen evolution is the choice of the sacrificial reagent. Using the same semiconductor (CN) and the same cocatalyst (Pt) allowed for a certain degree of comparability. Under basic conditions (basic SRs) the oxidation potential of the sacrificial reagent is supposed to have a high influence on hydrogen productivity. However, there are more factors such as different solubility, distinct degradation mechanisms, different pH values of the various sacrificial agents and also different solvent escape probabilities which have to be investigated in much more detail to be able to draw more sophisticated conclusions.

Zusammenfassung

Wasserstoff stellt aufgrund seiner hohen gravimetrischen Energiedichte und sauberen Verbrennung einen für die Umwelt akzeptablen Kraftstoff dar. Die photokatalytische Wasserstofferzeugung mit Sonnenlicht ist eine effiziente Methode zur direkten Umwandlung von Sonnenenergie in eine nutzbare oder speicherbare Energiequelle. In Hinblick auf die künftige praktische Anwendung ist der Einsatz von heterogenen Halbleitern von Vorteil. Eines der Hauptprobleme in der Photokatalyse besteht in der schnellen Rekombination der durch Licht erzeugten Elektronen-Loch-Paare, welche die Gesamteffizienz durch die Abgabe dieser Energie in Form von Hitze oder Licht mindert. Typischerweise liegt die Zeit zur Rekombination bei durch Licht erzeugten Elektronen-Loch-Paaren im Bereich von 10^{-9} s, während die Reaktionszeit der Elektronen und Löcher mit adsorbierten Spezies länger ist (10^{-8} - 10^{-3} s). Jedoch können Ladungstrennung und -rekombination im Fall einer effizienten Verzögerung der Ladungsträgerrekombination als konkurrierende Prozesse betrachtet werden. Die Umwandlungseffizienz von Sonnenlicht in Wasserstoff wird direkt durch die Absorptionsfähigkeit des Materials bestimmt und kann durch Einbringen anderer Elemente oder die Bildung von Heteroübergängen verbessert werden. In diesem Zusammenhang stellt die Entwicklung von Nanokompositen aus C_3N_4 (CN) und anderen Halbleitern eine vielversprechende Strategie dar, die letztendlich aufgrund einer verbesserten Lichtabsorption und Ladungsträgertrennung zu einer höheren photokatalytischen Effizienz führen sollte.

Gegenstand der vorliegenden Arbeit ist die Synthese von Metallsulfid/CN-Kompositen und ihre Anwendung in der photokatalytischen Wasserstofferzeugung. Jedoch ist der Bildungsmechanismus der durch Licht erzeugten Ladungsträger sowie deren Trennung und Transfer während der photokatalytischen Reaktion noch immer nicht klar. Ein umfängliches Verständnis darüber ist aber für die Anpassung und Optimierung der photokatalytischen Eigenschaften unabdingbar, um eine hohe Effizienz in der photokatalytischen Wasserstofferzeugung erreichen zu können. Deshalb wurden verschiedene Strategien zur Synthese von Metallsulfid/CN-Heteroübergangskompositen gewählt. Diese Materialien wurden dann in der photokatalytischen Wasserstofferzeugung untersucht und ihre Kristallinität, optischen Eigenschaften, chemische Zusammensetzung sowie Mikrostruktur mittels XRD, UV-vis-DRS, ATR-IR, XPS und HAADF-STEM analysiert. Darüberhinaus wurden Photolumineszenz (PL) und in situ-Elektronenspinresonanzspektroskopie (in situ-EPR) zur Beobachtung der Ladungstrennung und des Ladungstransfers angewendet.

Zunächst zeigte die Untersuchung von reinem CN in Gegenwart von Platin (Pt/CN) und Triethanolamin (TEOA) als Opferagens eine hohe anfängliche Wasserstoffbildungsrate, die mit dem Fortgang der Reaktion abnahm, weil es zum Einschluss von Pt-Nanopartikeln ins Innere von CN kam, wie mittels STEM, XPS und ICP-OES belegt werden konnte. Dieses Verhalten trat in Gegenwart von Oxalsäure (OA) als Opferagens nicht auf, weil sich die Platin-Nanopartikel in diesem Fall auf der äußersten Oberfläche von CN anreichern. Bei den Pt/AgIn₅S₈-C₃N₄ (Pt/AIS-CN)-Katalysatoren scheiden sich die Pt-Nanopartikel bevorzugt auf der Oberfläche von AIS ab, was deren Migration ins Innere von CN verhindert und sie

zugänglich für die Protonenreduktion erhält. In situ-EPR-Spektren zeigten, dass das EPR-Signal bei Bestrahlung mit UV-vis-Strahlung für reines CN viel höher ist. Mit zunehmendem Gehalt an AIS nimmt dieses Signal jedoch ab, was sehr wahrscheinlich auf einen Elektronentransfer von CN auf AIS zurückzuführen ist. In gleicher Weise nimmt auch die Intensität der Emission der Komposite mit steigendem Anteil an AIS ab, was die Ergebnisse aus der EPR-Spektroskopie untermauert. Wird Platin sowohl auf CN als auch auf AIS-CN abgeschieden, nimmt die Emissionsintensität ebenfalls ab, was einem Transfer von Leitungsbandelektronen aus CN zum Pt oder von CN über AIS zum Pt zugeschrieben wird. Hiermit wird die Ladungsträgerrekombination effizient unterdrückt, was mit einer gleichzeitigen Verlängerung ihrer Lebenszeit und damit einer Erhöhung der Wasserstoffproduktion einhergeht.

Als weiteres Metallsulfid wurde MoS₂ verwendet und die entsprechenden MoS₂/C₃N₄ (MS-CN) Komposite wurden über drei verschiedene Wege hergestellt, nämlich mittels in situ-Photoabscheidung (PD), sonochemisch (SC) und thermischer Zersetzung (TD). Von diesen Photokatalysatoren zeigte das über in situ-Photoabscheidung hergestellte 2H MS-CN die höchste Wasserstoffbildungsrate unter Bestrahlung mit UV-vis-Licht. STEM-Untersuchungen haben ergeben, dass Pt in allen Kompositen sowohl auf CN als auch auf MoS₂ abgeschieden wird, was gegensätzlich zu den Beobachtungen im Fall der AIS-CN-Komposite ist. Außerdem konnte mit STEM und UV-vis-Spektroskopie gezeigt werden, dass CN im Fall der weniger aktiven Proben teilweise von größeren MoS₂-Partikeln bedeckt ist und es nur bei 2H MS-CN(PD) zur Ausbildung hinreichend dünne Schichten an 2H MoS₂ kommt, die einen engen Grenzflächenkontakt mit CN ermöglichen, durch den die Ladungstrennung begünstigt und damit die photokatalytische Aktivität erhöht wird. In situ-EPR-Untersuchungen zeigten, dass das Signal der Leitungsbandelektronen im Fall von Pt/2H MS-CN (PD) niedriger als bei den anderen Katalysatoren ist, was auf einen effektiveren Elektronentransfer von CN zu Pt, der zu einer höheren Aktivität führt, hindeutet.

Ein weiterer wichtiger Gesichtspunkt in der photokatalytischen Wasserstofferzeugung ist die Wahl des Opferagenses. Durch die Verwendung des gleichen Halbleiters (CN) und des gleichen Cokatalysators (Pt) besteht ein gewisses Maß an Vergleichbarkeit. Unter basischen Bedingungen scheint das Oxidationspotential des Opferagenses einen großen Einfluss auf die Wasserstoffproduktion zu haben. Jedoch spielen auch weitere Faktoren, wie zum Beispiel verschiedene Löslichkeiten, unterschiedliche Degradationsmechanismen, ungleiche pH-Werte der diversen Opferagensien und auch unterschiedliche Austrittswahrscheinlichkeiten der Lösungsmittel, eine Rolle, die detaillierter untersucht werden müssen, um zu klareren Schlussfolgerungen zu gelangen.

List of all abbreviations

AIS	AgInS ₈ (Silver indium sulfide)
a. u.	Arbitrary units
at. %	Atomic percentage
ATR-IR	Attenuated total reflectance-infrared spectroscopy
BET	Brunauer-Emmet-Teller
BE	Binding energy
BF	Bright field
BJH	Barrett-Joyner-Halenda
CB	Conduction band
CHNS	Carbon, hydrogen, nitrogen and sulfur elemental analysis
CN	Carbon nitride
CW	Continuous wave
D	Crystallite size
d	Lattice spacing
DFT	Density Functional Theory
e⁻	electron
E_g	Band gap
E_f	Fermi energy
EDXS	Energy-dispersive X-ray spectroscopy
EPR	Electron paramagnetic resonance
eV	Electron volt
F(R_∞)	Kubelka-Munk function
FFT	Fast fourier transform
GC	Gas chromatography
h	hour
h	Planck's constant
h⁺	hole
HAADF	High-angle annular dark field
HOMO	Highest occupied molecular orbital
ICDD	International centre for diffraction data
ICP-OES	Inductively coupled plasma-optical emission spectrometry
KE	Kinetic energy
LUMO	Lowest unoccupied molecular orbital
MS	MoS ₂ (Molybdenum-disulfide)
mL	millilitre
mol	mole
nm	Nanometer
ps	picoseconds
R	Reflectance
N_A	Avogadro number
NHE	Normal hydrogen electrode
NPs	Nanoparticles
p	Pressure
p/p₀	Relative pressure

PD	Photodeposition
PL	Photoluminescence
s	Second
SC	Semiconductor
SC	Sonochemical
SKM	Schuster-Kubelka-Munk
SPR	Surface plasmon resonance
SPS	Surface photovoltage spectroscopy
STEM	Scanning transmission electron microscopy
SRs	Sacrificial reagents
t	time
TCD	Thermal conductivity detector
TD	Thermal decomposition
UV-vis DRS	Ultraviolet-visible diffuse reflectance spectroscopy
UV	Ultraviolet
VB	Valence band
Vis	Visible
wt.%	Weight percentage
XPS	X-ray photoelectron spectroscopy
XRD	X-ray diffraction
ν	light frequency
α	absorption coefficient
λ	wavelength of light
θ	Bragg angle
ΔG	Gibbs free energy change
$^{\circ}\text{C}$	Degree celsius
μmol	Micromole

1 Motivation, objective and state of the art

1.1 Motivation and objective

Increasing concerns about energy demand and environmental pollution have encouraged the scientific community to discover and utilize promising renewable energy resources alternative to fossil fuels, which is one of the primary research topics of the 21st century in view of a more sustainable society.^{1,2} The increased demand for energy production is mainly due to huge population growth and enormous industrial developments. If the growth rate of a population continues at the current levels, the global population is predicted to reach 9.5 billion people by 2050, and consequently, the primary energy consumption is also estimated to increase from 15 TW to 27 TW by 2050.^{2,3} Fossil fuels, such as coal, petroleum, and natural gas are the major energy sources currently available that play an important role to meet our energy requirements, especially for industry, agriculture, transportation and daily life (Fig. 1.1a). Energy Information Administration (EIA) report revealed that more than 85% of primary energy production comes from fossil fuels. On the other hand, fossil fuels are rapidly being depleted. On the other hand, the greenhouse gas such as CO₂ level is increasing due to burning fossil fuels, which is the main cause of climate change i.e. global warming, along with other important environmental problems and health issues.^{4,5} The International Energy Agency (IEA) data shows that atmospheric CO₂ concentration is rapidly increasing since the year 1990 and about 33.1 giga-tonnes of CO₂ was released in 2018 by vast combustion of fossil fuels in order to meet our energy requirements (Fig. 1.1b).

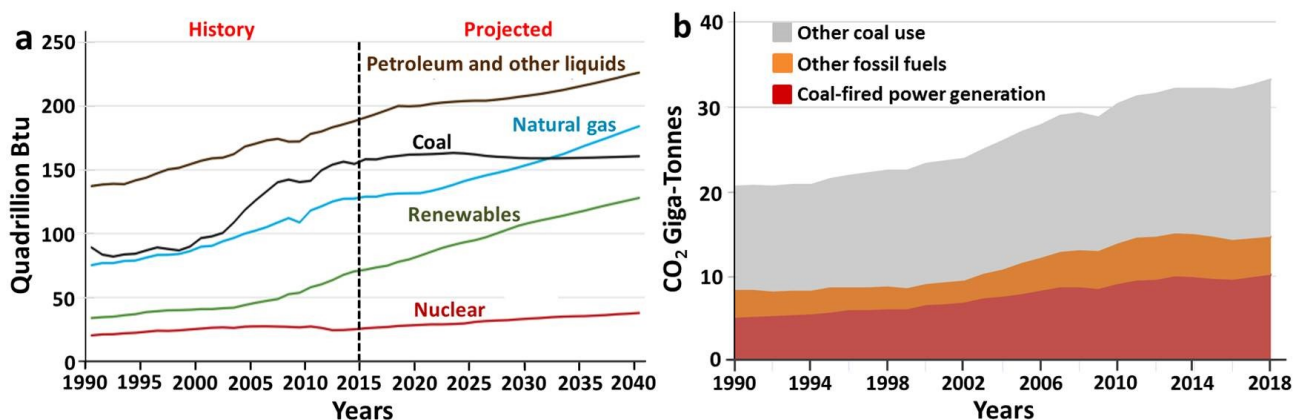


Figure 1.1 (a) World energy consumption by fossil fuels, 1900-2015 (Report from Energy Information Administration, EIA) and (b) global CO₂ emissions by fossil fuels, 1990-2018 (Report from International Energy Agency, IEA).

To effectively address the depletion of fossil fuels and the environmental problems caused by their combustion as well as to meet the increased energy demand, the scientific society has been searching for a new form of energy that should, in principle, be a clean, renewable, cheap, safe, and viable alternative to fossil fuels. Hydrogen is becoming the most environmentally acceptable fuel of the future and it undergoes clean combustion, giving only water as a byproduct ($2\text{H}_2 + \text{O}_2 \rightleftharpoons 2\text{H}_2\text{O}$; $\Delta E = -286 \text{ kJ/mol}$).^{1, 6-8} Therefore, hydrogen is considered a clean fuel, as it does not produce any greenhouse or harmful gases. Moreover,

hydrogen has a high gravimetric energy density of 119.93 MJ/kg compared to gasoline (44.5 MJ/kg). Hydrogen can be produced from both non-renewable sources (coal, petroleum, and natural gas) and renewable energy resources (biomass, geothermal, hydroelectric, tidal, wind, solar and nuclear) (Fig. 1.2).⁶⁻⁸

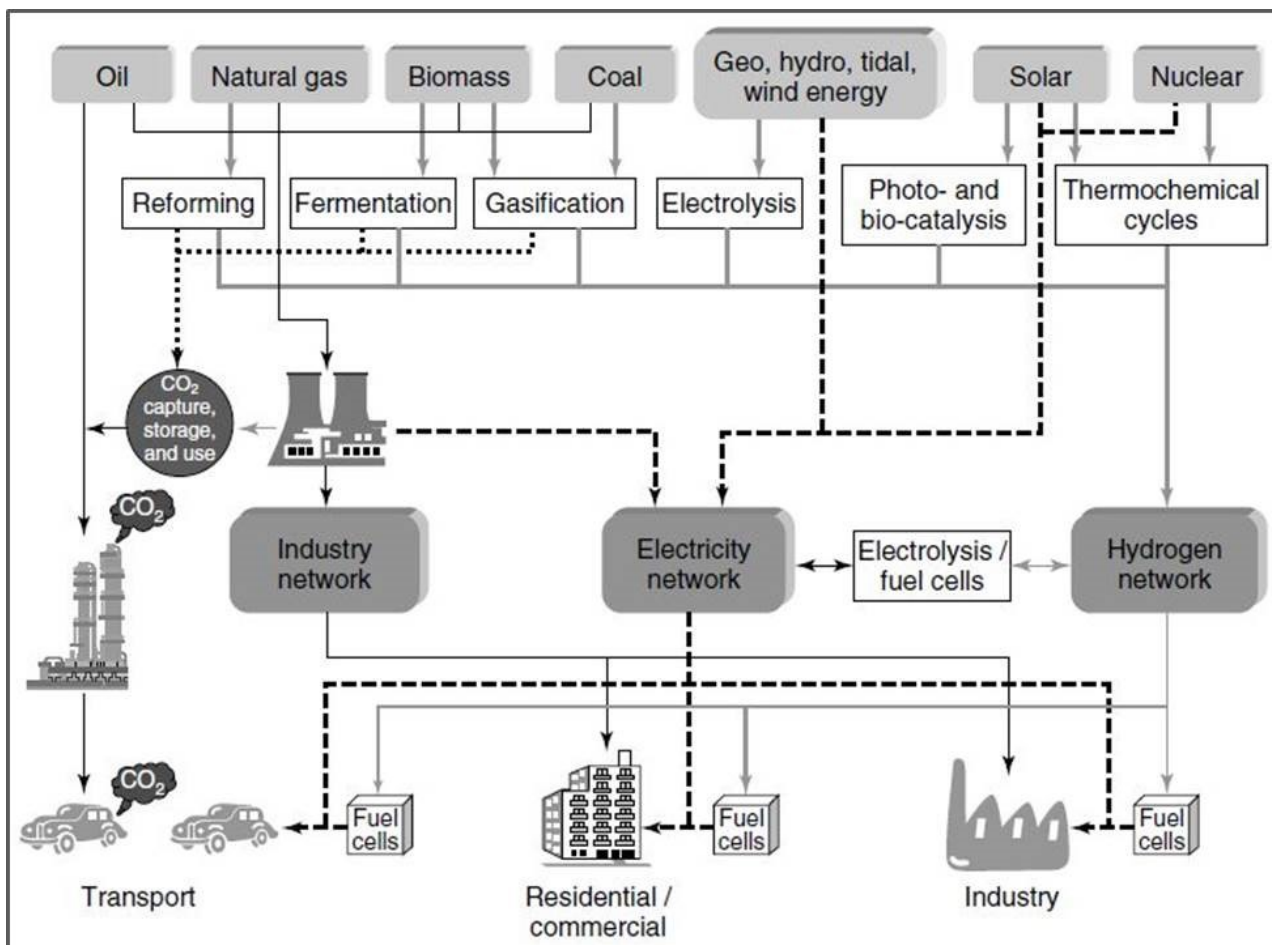


Figure 1.2 A possible model for a hydrogen energy economy. Reproduced with permission from ref.⁴⁰⁷ Copyright 2008 Royal Society of Chemistry.

However, almost 96% of current hydrogen production is derived from fossil fuels via steam reforming of methane and coal gasification technology.^{7, 9} Since both these methods produce huge amounts of CO₂ emissions, therefore, developing environmentally benign and economically feasible methods to produce hydrogen from renewable resources is of paramount research interest in the recent years. Hydrogen is abundant in the form of water, which is cheap, abundant, a renewable resource. On the other hand, the incident solar energy on Earth surface is about 120,000 TW, which is 10⁴ times higher than the current global energy consumption.^{10, 11}

Photocatalytic hydrogen production by using sunlight is an efficient method to convert directly solar energy into a usable or storable energy resource, which is considered to be an alternative energy source to mitigate problems associated with increasing energy demand and environmental pollution.^{1, 12-16} This method utilizes abundantly available solar energy as photon source and water as proton (H⁺) source to produce renewable H₂. In 1972, Fujishima and Honda discovered the photoelectrolysis of water by using TiO₂ photoanode which can split water into hydrogen and oxygen under UV light irradiation.¹⁷ The

pioneering work of Fujishima and Honda inspired many researchers towards developing novel heterogeneous semiconductor-based materials for photocatalytic water splitting. Until now, a wide variety of semiconductors has been explored as photocatalysts for H₂ production, such as metal oxides (e.g. TiO₂, ZnO, SrTiO₃, Sr₂Ti₂O₇, La₂Ti₂O₇, Nb₂O₅, NaNbO₃, Ta₂O₅, NaTaO₃, Sr₂Ta₂O₇, Ba₅Ta₄O₁₅, PbMoO₄, PbWO₄, β-Ga₂O₃, CaIn₂O₄, etc.), metal sulfides and metal (oxy)sulfides (e.g. ZnS, CdS, CuInS₂, CaIn₂S₄, ZnIn₂S₄, AgIn₅S₈, La₂GaOS₂, Sm₂Ti₂O₅S₂, ect.), metal nitrides and metal (oxy)nitrides (e.g. GaN, Ta₃N₅, TaON, LaTiO₂N, ect.), metal halides and metal (oxy)halides (e.g. AgX (X = Cl, Br, I), BiOX, BiTaO₈X, etc.).^{13, 18, 19} Since solar radiation contains visible light as the major fraction besides a small percentage of UV light, catalysts designed for large scale application must work efficiently under irradiation with wavelengths above 400 nm (Fig. 1.3). Unfortunately, metal oxide semiconductor-based photocatalysts, for instance, first and foremost TiO₂ ~3.20, but also titanates, niobates and tantalates, such as SrTiO₃ ~3.20 eV, NaNbO₃ ~3.50 eV and NaTaO₃ ~4.00 eV, respectively, can only be activated by UV light (only 4% present in the solar spectrum) due to their large band gap energy.²⁰ No absorption takes place in the visible light region which constitutes the major part of the solar spectrum over 43%. Alternatively, metal sulfides and metal nitrides have a narrow band gap with suitable band edge positions for photocatalytic water splitting. However, these materials are unstable under light irradiation as they are prone to decompose during the photocatalytic reaction.²⁰ For instance, CdS is itself oxidized by photogenerated holes instead of water and eventually produces Cd²⁺ and S²⁻ in the reaction solution (photocorrosion), which is a demerit of metal sulfide-based photocatalysts.²¹ Although some other metal oxides and sulfides have even narrower band gaps (e.g., WO₃ ~2.60 eV, V₂O₅ ~2.30 eV, Ag₃PO₄ ~2.50 eV, Bi₂WO₆ ~2.80 eV, SnS₂ ~1.76 eV, CuInS₂ ~1.55 eV, AgIn₅S₈ ~1.76 eV, etc.), they possess unsuitable band positions for water splitting and hence, insignificant catalytic performance.²⁰ Moreover, the photocatalytic efficiency of these pristine photocatalysts is still too low to meet practical requirements due to its high recombination rate of photogenerated electron hole pairs. It is therefore essential to develop promising photocatalysts that must absorb light in the visible region, possess suitable band positions and remarkable photocatalytic stability. Fig. 1.3 reveals the necessity of developing visible active photocatalysts for H₂ production.

In 2009, Wang and co-workers observed efficient H₂ production for the first time over graphitic carbon nitride (g-C₃N₄) under visible light irradiation.²² Carbon nitride is a two dimensional (2D) layered polymeric metal free semiconductor with a narrow band gap of 2.70 eV and a proper optical wavelength of 460 nm, allowing the light absorption in the visible region as well as a suitable band position for photocatalytic H₂ production.²² Moreover, it possesses excellent thermal stability (> 600 °C in air atmosphere) as well as chemical stability against acid, alkali, and organic solvents (e.g. lactic acid, triethanolamine and methanol, respectively).²³ Furthermore, it exhibits additional favorable properties like earth abundance, non-toxicity, synthetic accessibility, etc.²⁴

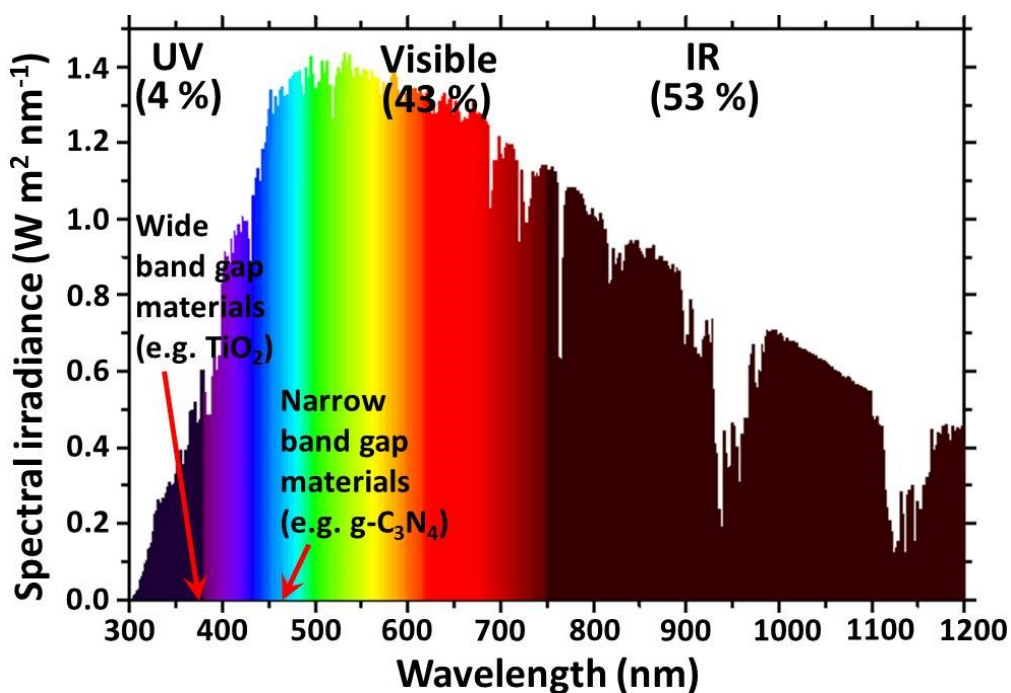


Figure 1.3 Terrestrial solar spectrum (Air Mass 1.5 Global 37° tilted surface). Modified figure adapted from ref.⁴⁰⁸ Brian Tuffy 2016 PhD thesis.

Inspired by the huge advantages of $g\text{-C}_3\text{N}_4$, tremendous efforts have been undertaken towards $g\text{-C}_3\text{N}_4$ catalyzed light driven transformations, such as water splitting, CO_2 reduction and pollutants degradation.^{20, 25-31} However, the bulk C_3N_4 exhibits low photocatalytic activity because of its low surface area, insignificant electrical conductivity, limited light absorption in the visible region (up to 460 nm) and high recombination rate of photogenerated electron-hole pairs. To address these issues, a number of modification techniques has been developed in recent years to improve the photocatalytic activity of C_3N_4 , such as shape control, porous structure formation, composite formation with other semiconductors, doping with metal or non-metal elements, loading noble metals, coupling with carbon dots, carbon nanotubes, graphene, conducting polymers, metal organic frameworks, etc.^{23, 32} Among these modification techniques, developing nanocomposites of C_3N_4 with other semiconductors is a promising strategy that creates synergistic heterojunctions, eventually resulting in an improved charge separation and hence higher photocatalytic efficiency.³³

One of the major problems in photocatalysis is the fast recombination of photogenerated electron-hole pairs, limiting the overall efficiency. Typically, photogenerated electron-hole pairs have a recombination time in the order of 10^{-9} s, whereas the reaction time of electrons and holes with adsorbed species is quite longer (10^{-8} - 10^{-3} s).³⁴ During the photocatalytic reaction, most of the electron-hole pairs can recombine and release the absorbed energy in the form of heat or light, because the charge separation and recombination are the competitive processes. However, a small percentage of these charge carriers can migrate to the photocatalyst surface, where they can interact with the adsorbed molecules and initiates the redox reaction. In this framework, developing nanocomposites of C_3N_4 with other semiconductors is a promising strategy

that creates synergistic heterojunctions, eventually resulting in an improved charge separation and hence higher photocatalytic efficiency.^{33, 35, 36}

Objective of the thesis

Metal sulfides are excellent candidates for photocatalytic hydrogen production due to their narrow band gap with suitable band edge positions.^{13, 20, 37-40} Inspired by the unique properties of metal sulfides, we were aiming at the creation of a heterojunction with C_3N_4 to increase the electron-hole pair separation. Making heterojunction between g- C_3N_4 and metal sulfide, electron hole pair recombination could be significantly reduced, resulting in high photocatalytic efficiency. However, the formation of photogenerated charge carriers as well as their separation and transfer during photocatalytic reaction is still not clear, though its complete understanding is inevitable in order to tune the photocatalytic properties of composite catalysts for achieving high photocatalytic H_2 production efficiency. In this dissertation, different strategies were employed to synthesize metal sulfide/g- C_3N_4 heterojunction composites and then, investigated their applications for photocatalytic H_2 production.

The scope of this dissertation work can be summarized as follows

- Synthesis of $AgIn_5S_8/C_3N_4$ heterojunction composites (Chapter 3)
- Synthesis of MoS_2/C_3N_4 heterojunction composites (Chapter 4)
- Effect of sacrificial agents (Chapter 5)

Among the various spectroscopic techniques, in-situ electron paramagnetic resonance (EPR) spectroscopy has been applied to monitor charge separation and transfer during UV-vis light irradiation. Additionally, photoluminescence (PL) spectroscopy was used to investigate the separation efficiency of photogenerated charge carriers. In combination with EPR and PL, several standard characterization methods were also applied in this work. The crystal structure and phase compositions of the developed catalysts were characterized by powder X-ray diffraction (XRD). The optical properties of as-synthesized catalysts were characterized by ultraviolet-visible diffuse reflectance spectroscopy (UV-vis DRS). The structural properties were characterized by attenuated total reflectance-infrared (ATR-IR) spectroscopy. The morphology and microstructure of the composites were analysed by scanning transmission electron microscopy (STEM). The surface elemental compositions and nature of the species (chemical state of the elements) were analyzed by X-ray photoelectron spectroscopy (XPS). The textural properties, such as specific surface area, pore volume and pore sizes were analyzed by N_2 adsorption-desorption studies (BET analysis). Finally, the bulk elemental composition of as-synthesized catalysts was analysed by inductively coupled plasma-optical emission spectroscopy (ICP-OES) and carbon, hydrogen, nitrogen and sulfur (CHNS analysis). With the help of these techniques, the role of sacrificial agents and co-catalysts, photocatalytic H_2 production activity, catalysts stability, etc. should be investigated in this dissertation.

1.2 State of the art

Fundamental mechanism of photocatalytic water splitting

Fig. 1.4 shows a schematic illustration of the basic principles of photocatalytic water splitting. Thermodynamically, the water splitting reaction is an uphill process, requiring a minimum energy of 1.23 eV because the Gibbs free energy change for the reaction is $\Delta G^\circ = 237 \text{ kJ mol}^{-1}$ per H_2O molecule.^{13, 41} The semiconductor band gap usually determines the wavelength of sunlight needed for the reaction. A semiconductor with a wide band

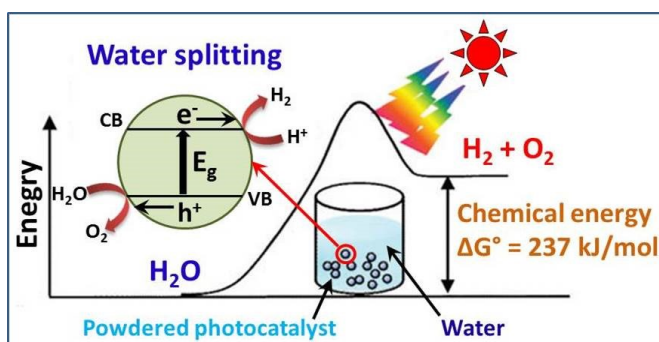
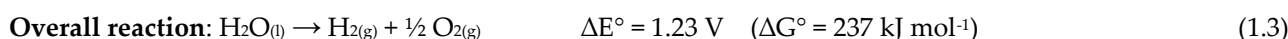
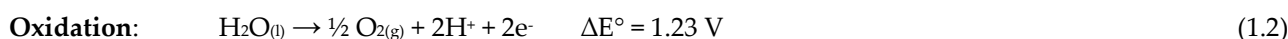
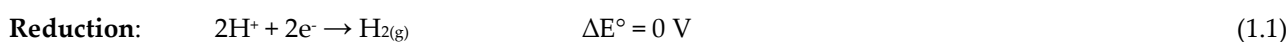


Figure 1.4 Thermodynamics of photocatalytic water splitting. Modified figure adapted from ref.⁴⁰⁹ Copyright 2008 Royal Society of Chemistry.

gap ($E_g > 3 \text{ eV}$) can only absorb UV light, which approximately accounts for 4% of solar energy. In contrast, a narrow band gap semiconductor ($E_g < 3 \text{ eV}$) can be activated by visible light irradiation, which constitutes 43% of solar energy.²⁹



Besides the band gap of the semiconductor, the positions of valence and conduction band play a crucial role in photocatalytic water splitting (Fig. 1.5).^{13, 18} For H_2 evolution, the conduction band edge should be more negative than the reduction potential of H^+ to H_2 ($E_{\text{H}^+/\text{H}_2} = 0 \text{ V vs. NHE at pH} = 0$) (Eq. 1.1). On the other hand, the valence band edge should be more positive than the oxidation potential of water ($E_{\text{O}_2/\text{H}_2\text{O}} = 1.23 \text{ V vs. NHE at pH} = 0$) in order to evolve oxygen (Eq. 1.2). Therefore,

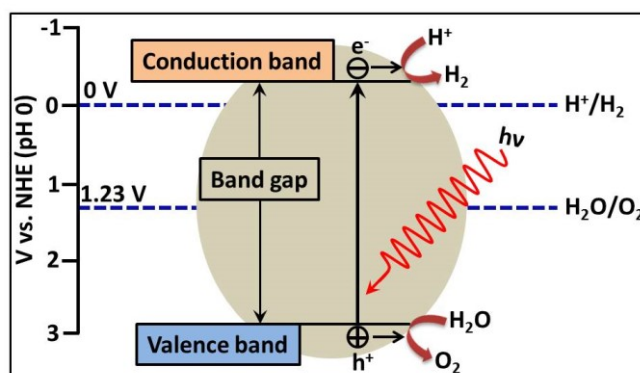


Figure 1.5 Basic principle of photocatalytic water splitting. Modified figure adapted from ref.⁴¹⁰ Copyright 2010 American chemical society.

the band gap of the semiconductor should be at least 1.23 eV in order to split water into H_2 and O_2 (Eq. 1.3). The equivalent light wavelength for this band gap energy is 1100 nm, which is in the near-infrared region of the sunlight spectrum.⁴¹ By considering other factors, such as energy loss during different stages occurred in the photocatalytic process, promising semiconductors must have band gaps greater than 2 eV, which is related to light with wavelength less than 620 nm.⁴²

Main processes involved in photocatalytic water splitting

The electron-hole pairs in photocatalysts are generated upon excitation by the incident light (Fig. 1.6, step 1). Semiconductor photocatalysts have a band structure in which the conduction band (CB) is separated

from the valence band (VB) by a band gap (E_g) with a suitable width. When photocatalyst absorbs light energy equal or greater than its band gap, electrons in the VB can be excited to the CB, as a result a hole formed in the VB and electrons in the CB. This process is known as electron-hole pair generation.

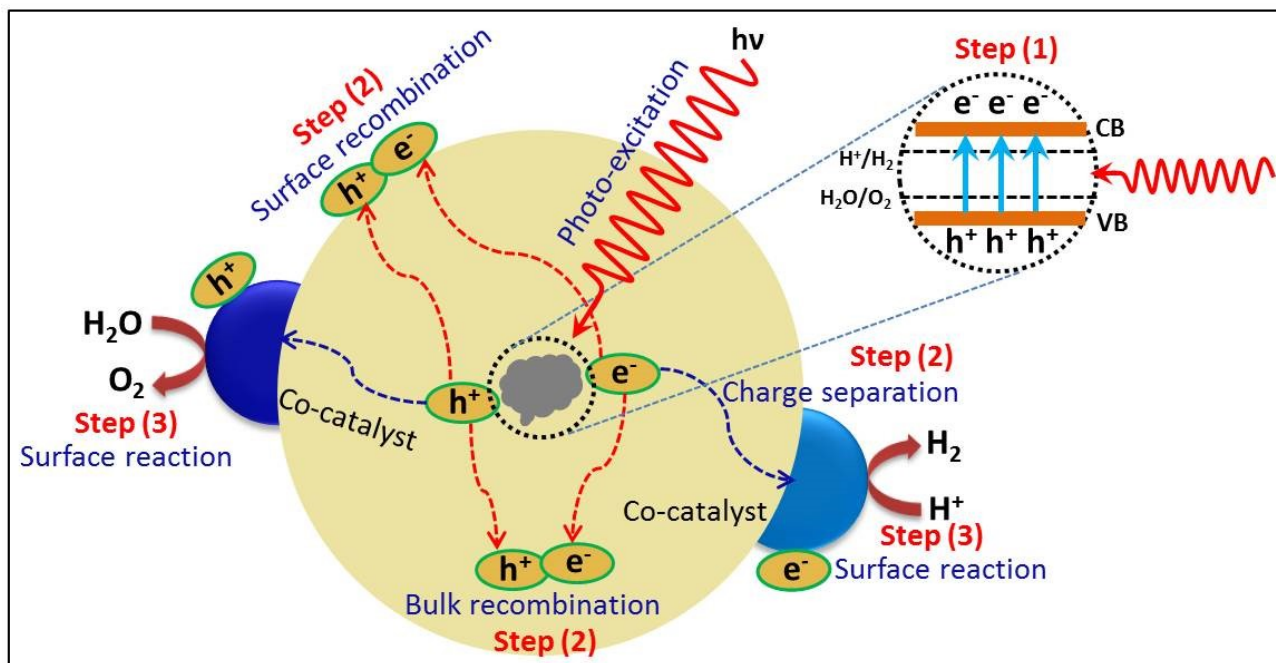


Figure 1.6 Main processes involved in photocatalytic water splitting. Modified figure adapted from ref.⁴¹¹ Copyright 1995 American chemical society.

The excited charges (photogenerated electrons and holes) separate and migrate to the surface of the photocatalyst, which is highly dependent on the crystal structure and particle size of the photocatalyst used for the reaction (Fig. 1.6, step 2). In parallel, charge recombination can also occur, where a fraction of photogenerated electrons and holes radiatively or nonradiatively recombine and release absorbed energy in the form of heat or light (Fig. 1.6, step 2). In order to prevent the recombination of the photoinduced e^-/h^+ pairs, several modification strategies have been suggested such as improving crystallinity, decreasing particle size, and loading a co-catalyst such as Pt, Pd, RuO_2 and NiO_x on the surface of photocatalyst.⁴³ The higher crystallinity of a photocatalyst can result in the presence of less number of defects, which act as the recombination center of photoinduced e^-/h^+ pairs. Defects are usually considered as the trapping and recombination centers between photogenerated electrons and holes, resulting in decreased photocatalytic activity. To achieve higher photocatalytic activity, photocatalysts with smaller sized particles are preferred as they provide higher surface area with more reactive sites, leading shorten the distance to migrate photogenerated excitons to the surface reaction sites and thus, inhibiting the recombination rate of photoinduced e^-/h^+ pairs.⁴⁴

The photogenerated electrons on the surface of a photocatalyst can react with H^+ to produce H_2 whereas holes react with H_2O to produce O_2 , which are governed by surface character (active sites) and quantity (surface area) of the photocatalyst (Fig. 1.6, step 3). Photocatalysis is a surface phenomenon and thus larger surface area provides more number of active sites for the target reaction, enabling the process more efficient.

Even when the potentials of the photogenerated electrons and holes are thermodynamically sufficient for water splitting, they may not be able to split water into H₂ and O₂ if the sufficient active sites for redox reactions are not available on the catalyst surface. Meanwhile, the backward reaction to form water from the evolved H₂ and O₂ proceeds readily because it is a downhill reaction. Therefore, some co-catalysts, such as Pt, Pd, NiO_x and RuO₂ are usually loaded to introduce additional active sites for H₂ evolution because the conduction band levels of many oxide photocatalysts are not high enough to reduce H⁺ into H₂ without co-catalytic assistance.⁴³ In addition to the co-catalysts, sacrificial agents, such as organic/inorganic electron donors also play a significant role in influencing photocatalytic activity. The use of sacrificial agents can greatly minimize the charge carrier recombination by scavenging the photogenerated holes.⁴⁵⁻⁴⁹

All of these processes can greatly affect the overall efficiency of a semiconductor photocatalytic system (Fig. 1.6). Clearly, taking into consideration the basic mechanism and processes of photocatalytic water splitting, there are two key factors that can play a significant role in developing a suitable high-efficiency semiconductor. On the one hand, a photocatalyst should have a sufficiently narrow band gap ($1.23 \text{ eV} < E_g < 3.0 \text{ eV}$) to both harvest visible light and possess the suitable band structure (VB and CB edges). On the other hand, photoinduced electron-hole pairs in the photocatalyst should be separated efficiently in order to avoid their bulk/surface recombination. They must migrate to the respective surface active sites for hydrogen and/or oxygen evolution, thus strictly inhibiting the backward reaction of water formation from H₂ and O₂. Additionally, the stability of the photocatalysts is also vital during photocatalytic reaction.

Band structure of semiconductors and redox potentials of water splitting

Several metal oxide semiconductors, such as TiO₂, ZnO, ZrO₂, Ta₂O₅, SrTiO₃, NaTaO₃, BiPO₄, InNbO₄, SrNb₂O₆, GdT₂O₇, K₄Nb₆O₁₇ and Ba₅Ta₄O₁₅ possess suitable band structures for photocatalytic water splitting (Fig. 1.7).^{13, 20} However, these metal oxide catalysts can only be activated by UV light due to their large band gap energy ($> 3.2 \text{ eV}$). Unfortunately, UV light ($< 400 \text{ nm}$) only accounts for a small portion of solar spectrum (4%). No absorption takes place in the visible region, which constitutes the major part of the solar spectrum (43%). Thus, more efforts have been made to develop promising visible light active photocatalysts over the past few decades (e.g. CdS and SnS₂) (Fig. 1.7).^{13, 20} Non-oxide photocatalyst, such as cadmium sulfide (CdS) can satisfy the two requirements with having sufficient potentials for water splitting and good light absorption properties in the visible region. However, this material is not stable under irradiation because it decomposes during photocatalytic reaction. For instance, CdS is itself oxidized by photogenerated holes instead of water and eventually produces Cd²⁺ and S²⁻ in the reaction solution, which is a demerit of metal sulfide-based photocatalysts (Eq. 1.4). This reaction is called photocorrosion and is often a demerit of a metal sulfide photocatalyst.⁴¹



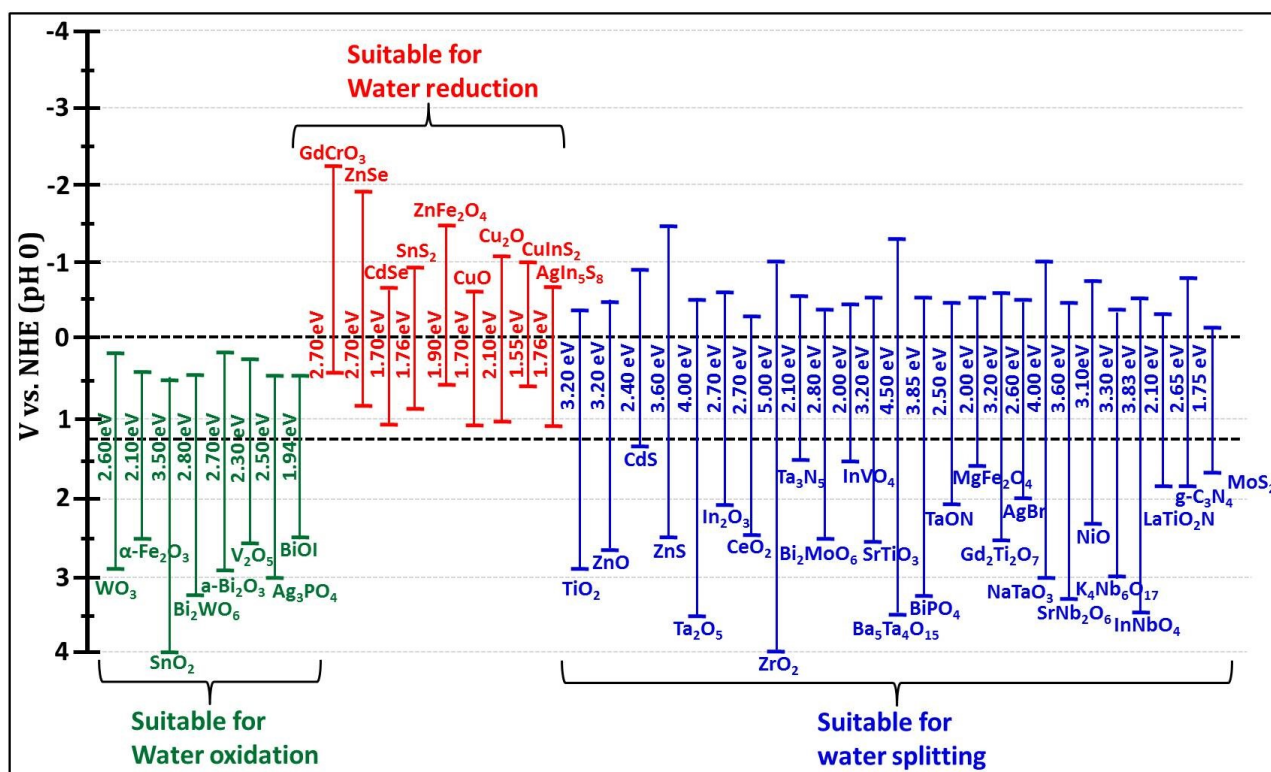


Figure 1.7 Band structure of semiconductors and redox potentials of water.

However, CdS is an excellent photocatalyst for H₂ production under visible light irradiation if a hole scavenger is used (e.g. in the presence of Na₂S/Na₂SO₃).²¹ On the one hand, several metal oxides, for example WO₃, α-Fe₂O₃, Bi₂WO₆, a-Bi₂O₃, V₂O₅, Ag₃PO₄ and BiOI are good photocatalysts for O₂ evolution reaction (OER) under visible light irradiation in the presence of an electron acceptor, such as Ag⁺ and Fe³⁺. However, these catalysts are not active for photocatalytic H₂ evolution reaction (HER) because of their low conduction band level than the H⁺ reduction potential (Fig. 1.7).¹³ On the another hand, several metal oxides and metal sulfides, for example GdCrO₃, ZnFe₂O₄, CuO, Cu₂O, CuInS₂, AgIn₅S₈, SnS₂, CdSe and ZnSe are good photocatalysts for HER under visible light irradiation in the presence of electron donor (e. g. TEOA and lactic acid) but, these are not active for OER because of their high valance band level than water oxidation potential (Fig. 1.7).¹³ Therefore, the band position of the semiconductors is one of the essential requirements for photocatalytic water splitting. Other factors, such as overpotentials, charge separation, mobility and lifetime of photogenerated electrons and holes affects the photocatalytic water splitting as well.^{13, 14, 18}

The essential factors for water splitting reaction are summarized as follows.

- 1) Band gap energy (capable of absorbing light in the visible region, 400-800 nm),
- 2) Suitable band positions (sufficient potential for water splitting),
- 3) High crystallinity (to inhibit the recombination rate of photogenerated electrons and holes),
- 4) Small particle size (to shorten the diffusion length),
- 5) More active sites (for the formation of H₂ and O₂),
- 6) Stability (photostability and insolubility in water),
- 7) Efficient charge carrier separation.

1.2.1 Development of g-C₃N₄ semiconductor for photocatalytic H₂ production

Carbon nitride (C₃N₄) is a two dimensional (2D) layered polymeric metal-free semiconductor, which has been widely investigated in various light driven transformations, such as water splitting, CO₂ reduction and pollutants degradation.^{20, 24, 26-28, 30-33, 50-58} It exhibits a number of favorable properties including earth abundance, non-toxicity, facile synthetic accessibility, suitable electronic band structure and high physicochemical stability.²⁴ Additionally, it has a suitable band structure with a band gap of 2.70 eV, which allows for the absorption of light in the visible region up to 460 nm.²² As shown in Fig. 1.8, both triazine and tri-s-triazine as the building blocks of graphitic carbon nitride (g-C₃N₄) can provide two possible forms with different degrees of stability. One form is based on condensed triazine units as the tectonic units (Fig. 1.8a), while the other form is obtained from tri-s-triazine as the fundamental units interconnected via tertiary amine (Fig. 1.8b).^{24, 27}

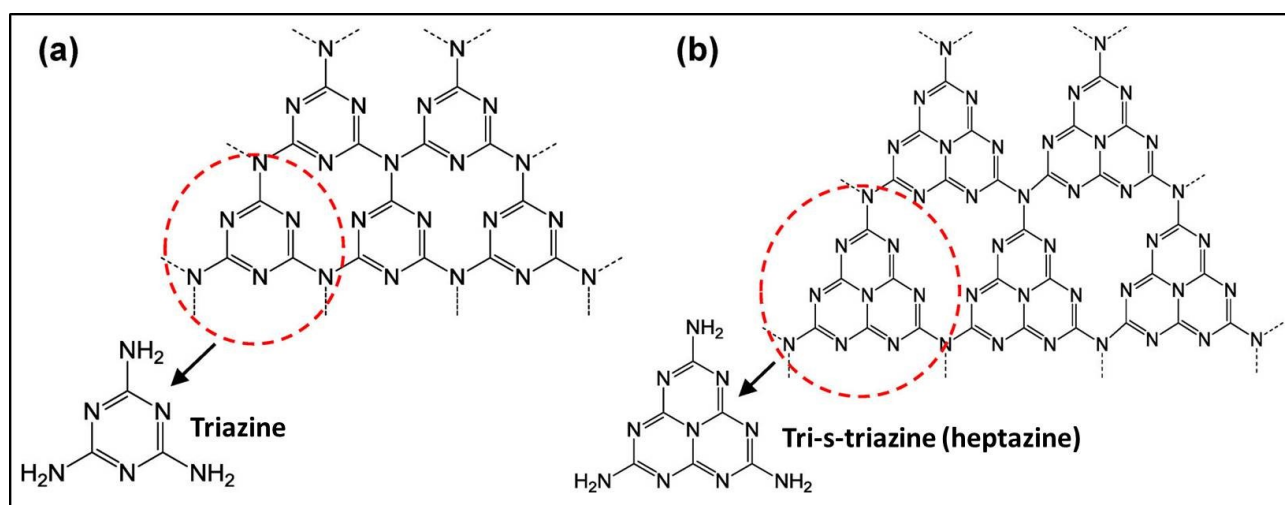


Figure 1.8 Structures of triazine (a) and tri-s-triazine (b) as the primary building blocks of g-C₃N₄. Reproduced with permission from ref.⁴¹² Copyright 2016 American Chemical Society.

This kind of polymeric carbon nitride was first synthesized by Berzelius, and then named as melon by Liebig in 1834, which is regarded as one of the oldest structures of synthetic polymer.⁵⁹ In 1922, Franklin et al. found the empirical composition of 'melon' to be C₃N₄.⁶⁰ Afterwards, Pauling and Sturdivant developed tri-s-triazine derived structure of C₃N₄ in 1937.⁶¹ In 1940, It was demonstrated that this material 'melon' has a graphite structure as reported by Redemann and Lucas in 1940.⁶² In 1972, photocatalysis has received enormous attention after breakthrough work of Fujishima and Honda i.e. photolysis of water on TiO₂.¹⁷ Afterwards, a wide variety of materials, including inorganic semiconductors was evaluated for photocatalytic water splitting. However, until Wang et al. first reported in 2009, there were no studies making use of g-C₃N₄ in photocatalysis. They observed efficient H₂ production for the first time from visible-light photocatalysis on g-C₃N₄ and the quantum efficiency was 0.1% under irradiation at 420-460 nm.²² However, its photocatalytic activity is low owing to

- 1) Its low quantum efficiency, due to fast recombination of the photogenerated electron-hole pairs.

- 2) Limited light absorption in the visible region up to 460, limiting the utilization of broad spectrum of solar light.
- 3) During synthesis, the high degree of condensation of the monomers renders the materials with a low surface area ($\sim 10 \text{ m}^2 \text{ g}^{-1}$) and without forming textured pores.
- 4) The grain boundary effect can disrupt the delocalization of electrons from the surface of a photocatalyst through the interface.

To address these issues, a number of modification strategies have been developed in recent years to improve the photocatalytic activity of g-C₃N₄, such as

- 1) Preparation of mesoporous and ordered mesoporous g-C₃N₄
- 2) Preparing texturally and morphologically controlled g-C₃N₄
- 3) Doping with metals (e.g. Mn, Fe, Co, Ni, Cu, Zn, etc.), non-metals (e.g. O, C, P, S, B, I, F, etc.) and co-doping (e.g. Au/Pt, Au/Pd, Pt/Co, etc.)
- 4) Loading co-catalysts (e.g. Pt, Ru, Rh, Pd, Au, Ag, Co, Ni, Cu, RuO₂, NiO, etc.)
- 5) Constructing synergistic heterojunction with other semiconductors, such as metal oxides (e.g. TiO₂, NaTaO₃, etc.) and sulfides (e.g. CdS, ZnIn₂S₄, etc.)

Among these modification strategies, developing nanocomposites of g-C₃N₄ with other semiconductors was found to be a promising strategy that can create synergistic heterojunctions and hence improved charge separation and higher photocatalytic efficiency. The mesoporous C₃N₄ used in this thesis was prepared by hard template method using tetraethyl orthosilicate (TEOS) and subsequently used to prepare heterojunctions with metal sulfides, such as AgIn₅S₈ and MoS₂ by co-precipitation and in-situ postdeposition method, respectively.

1.2.2 Mesoporous and ordered mesoporous g-C₃N₄

g-C₃N₄ based materials were generally fabricated by direct condensation of abundant nitrogen-rich precursors (Fig. 1.9), such as urea,⁶³⁻⁷¹ melamine,⁷²⁻⁸⁰ cyanamide,^{22, 81-84} dicyandiamide,^{66, 70, 85-94} thiourea,^{66, 70, 71, 85, 95, 96} trithiocyanuric acid,⁹⁷ ammonium thiocyanate,⁹⁸ etc. Both precursors nature and reaction conditions (i.e. temperature, time, and atmosphere) can greatly affect the physicochemical properties of g-C₃N₄, such as C/N ratio, specific surface area, porosity, absorption edge, and nanostructure.^{66, 99-101}

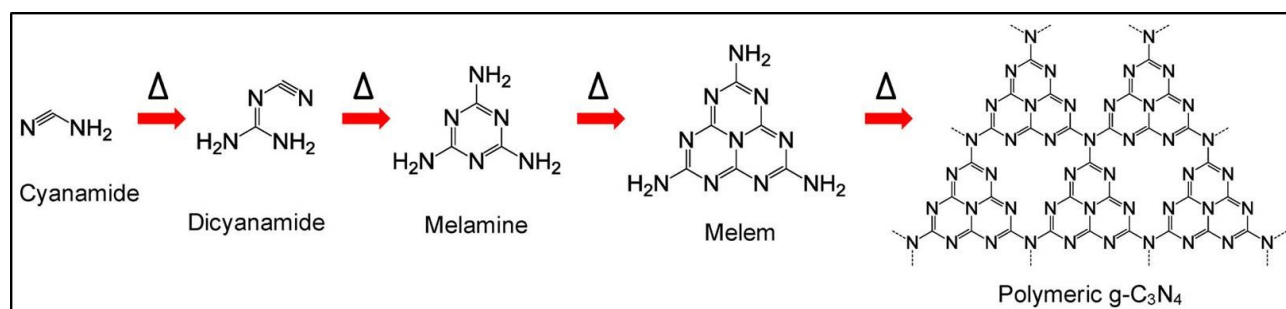


Figure 1.4 Thermal polycondensation pathways for the formation of g-C₃N₄ starting from cyanamide. Reproduced with permission from ref.⁴¹³ Copyright 2016 American Chemical Society.

Porous materials are especially attractive as heterogeneous catalysts photocatalytic H₂ production reactions due to their accessible porosity and large surface area.^{20, 23, 25, 29, 102, 103} One of the main drawbacks of g-C₃N₄ is that the high degree of polycondensation of monomers renders the formation of bulk materials with low surface area (<10 m² g⁻¹), without forming textured pores.²² Low surface area has become one of the main disadvantages hindering the photocatalytic H₂ production activity of g-C₃N₄ because higher surface area catalyst can offer more number of active sites for H₂ production.⁹⁴ Mesoporous g-C₃N₄ is a promising material, because the porous structure can provide a large surface area and numerous channels to facilitate mass diffusion, as well as charge migration and separation.¹⁰⁴⁻¹⁰⁷ As compared to the bulk g-C₃N₄, mesoporous g-C₃N₄ materials exhibits higher specific surface area up to 1116 m² g⁻¹ and larger porosity up to 1.45 cm³ g⁻¹, high concentration of active sites present on the catalyst surface, resulting in enhanced photocatalytic performance.¹⁰⁸

There are two different templating pathways for the preparation of mesoporous g-C₃N₄, such as soft templating (self-assembly along with structure directing agents) and hard templating (nanocasting) (Fig. 1.10).^{20, 23, 25, 29, 58, 102, 103, 109, 110}

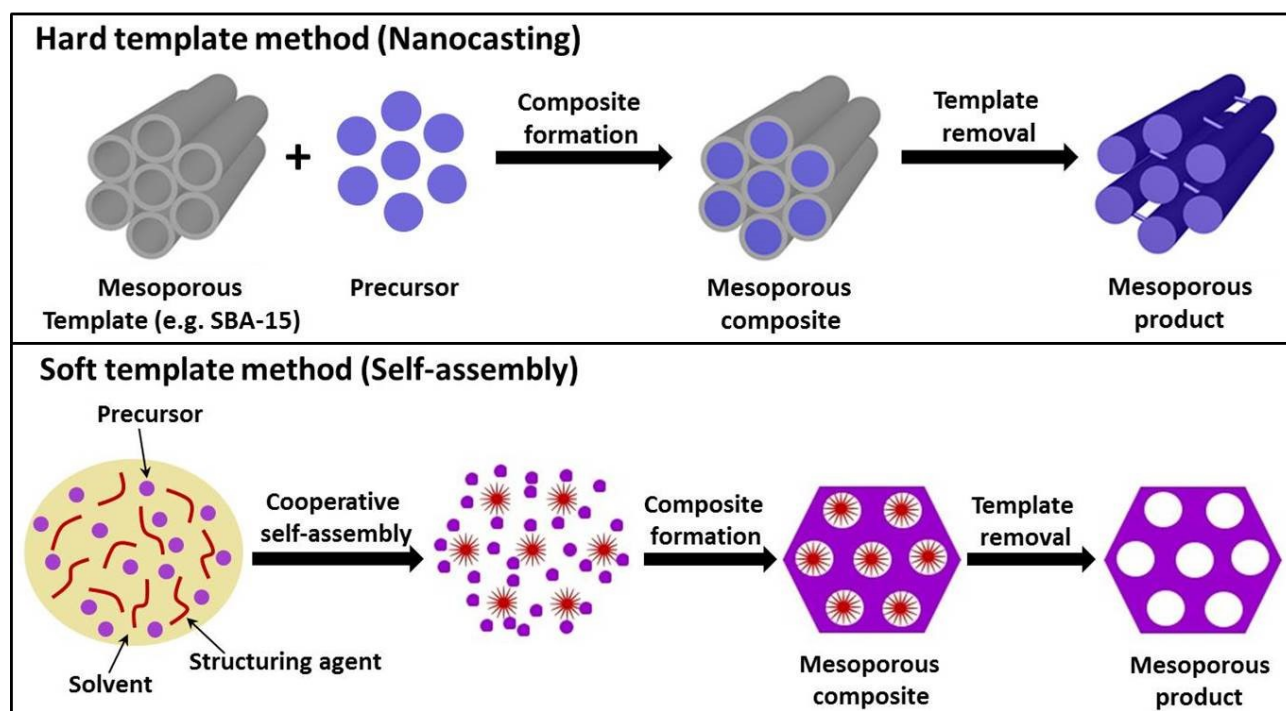


Figure 1.5 Scheme of two major routes for the synthesis of mesoporous g-C₃N₄: hard template method and soft template method. Modified figure adapted from ref.⁴¹⁴ Copyright 2017 Royal Society of Chemistry.

Hard template method is a controllable and precise approach towards the construction of mesoporous nanostructures, and it is highly versatile for the design of different mesoporous nanostructures with well-controlled porosity, size, shape, composition and spatial arrangement.^{111, 112} The most commonly used hard templates are silica nanoparticles (SiO₂ NPs) as well as ordered mesoporous silica templates, such as SBA-15, SBA-16, KCC-1, KIT-6, IBN-4, etc.^{108, 113-118} The porosity, structure, size, morphology and surface area can be easily tuned by using these templates through hard template method. Mesoporous g-C₃N₄ has been synthesized by using various precursors, such as urea, cyanamide, thiourea and ammonium thiocyanate in

the presence of SiO₂ NPs as a hard template, the removal of template can result in a 3D interconnected structure of g-C₃N₄ with a large surface area (Fig. 1.10).^{106, 119} For example, Hong et al. synthesized *in situ* sulfur-doped mesoporous g-C₃N₄ with a large surface area of 128 m² g⁻¹ by hard template method using SiO₂ NPs as hard template and thiourea as precursor. For a better comparison, they prepared bulk g-C₃N₄ with low surface area of 12.1 m² g⁻¹ using melamine as precursor under template-free conditions. Sulfur-doped mesoporous g-C₃N₄ exhibited much higher photocatalytic H₂ evolution rate of 136 μmol h⁻¹ which was 30 times higher than that of bulk material (4.5 μmol h⁻¹). The high catalytic performance of sulfur-doped mesoporous g-C₃N₄ was attributed to the extended light absorption in the visible light region enabled by sulfur doping and efficient mass and charge transfer in the mesoporous structure as well.¹¹⁶

In case of soft templating method, the porosity is introduced by the cooperative self-assembly often being carried out under hydrothermal conditions (Fig. 1.10). Wang et al. prepared mesoporous g-C₃N₄ by polycondensation of dicyandiamide using various soft templates, such as non-ionic surfactants, amphiphilic block polymers (e.g. Triton X-100, P123, F127, Brij30, Brij58 and Brij76) and also using some ionic surfactants (e.g. BmimC1, BmimPF6, BmimBF4 and BmimDCN).¹²⁰⁻¹²⁴ For example, Yan et al. synthesized mesoporous g-C₃N₄ with worm-like porosity by a soft template method using Pluronic P123 surfactant as soft template and melamine as precursor. The synthesized mesoporous g-C₃N₄ has high specific surface area (90 m² g⁻¹) than the bulk g-C₃N₄ (9 m² g⁻¹). The g-C₃N₄ sample synthesized from melamine without P123 showed an obvious visible-light photocatalytic activity and the H₂ production rate reaches 60.5 μmol h⁻¹. The use of 10 wt% P123 as template assisted g-C₃N₄ produced 148.2 μmol h⁻¹ of H₂ production rate, which was attributed to high BET surface area as well as mesoporous g-C₃N₄ with worm-like porosity that promotes light absorption in the visible region up to 800 nm.¹²³

1.2.3 Morphology controlled g-C₃N₄

Besides the ordered mesoporous g-C₃N₄, extensive efforts have been made to develop various types of g-C₃N₄-based nanostructures, namely, nanospheres, hollow nanospheres, nanorods, nanosheets, and nanotubes with the assistance of sacrificial templates.^{108, 125-133} Controlling morphology of the g-C₃N₄ nanostructures is another effective approach to optimize photocatalytic performance of g-C₃N₄ with efficient charge transportation and migration as well as facile mass diffusion during the photocatalytic reaction. For instance, Sun et al. designed hollow carbon nitride nanospheres (HCNS) by hard template method using mesoporous silica shell (SiO₂) as hard template and cyanamide as precursor. The BET surface area was found to be 35 m² g⁻¹ for hollow nanospheres and 11 m² g⁻¹ for bulk g-C₃N₄. g-C₃N₄ hollow nanospheres exhibited high photocatalytic H₂ production rate (224 μmol h⁻¹) than the bulk g-C₃N₄ (9 μmol h⁻¹). The apparent quantum yield is estimated to be 7.5% at 420 nm. The experimental results demonstrated that hollow nanospheres could enhance the effective path length for light absorption due to the existence of multiple reflections and scatterings within the nanostructure.¹²⁹ Moreover, Liu et al. developed uniform sized g-C₃N₄ nanorods (200 nm long and 80 nm wide) with the help of a hard template route using SiO₂

nanorods as the template and cyanamide as the precursor. The one-dimensional hexagonal mesostructured silica nanorods can provide nanoconfinement space for C_3N_4 condensation to produce perfect layered structures. The BET surface area of g- C_3N_4 nanorods was determined to be $52 \text{ m}^2 \text{ g}^{-1}$, which is about twice to that of the bulk g- C_3N_4 ($25 \text{ m}^2 \text{ g}^{-1}$). The g- C_3N_4 nanorods exhibited high photocatalytic H_2 production rate ($25 \mu\text{mol h}^{-1}$) than the bulk g- C_3N_4 ($2.5 \mu\text{mol h}^{-1}$), which is due to the suppressed charge recombination within the C_3N_4 nanorods and blue-shift light absorption compared to bulky g- C_3N_4 .¹²⁸ Table 1.1 showing some examples of mesoporous g- C_3N_4 and their photocatalytic H_2 production activities.

Table 1.1 Synthesis of mesoporous g- C_3N_4 and their photocatalytic H_2 production activities.

No.	Precursor	Template	Morphology of C_3N_4	Pore size (nm)	Pore volume ($\text{cm}^3 \text{ g}^{-1}$)	Surface area ($\text{m}^2 \text{ g}^{-1}$)	H_2 production ($\mu\text{mol g}^{-1} \text{ h}^{-1}$)	Ref.
1	Cyanamide	SiO_2 NPs	Mesoporous	8.3	0.41	126	1420	¹⁰⁶
2	Cyanamide	Mesoporous silica	Hollow nanospheres	-	-	79	3600	¹²⁹
3	Cyanamide	SiO_2 NPs	Hollow nanospheres	-	-	221	11000	¹³²
4	Cyanamide	Chiral mesoporous silica	Helical rod like	3.8/10.7	-	56	3700	¹³³
5	Cyanamide	Chiral silica nanorods	Porous nanorods	-	-	52	8333	¹²⁸
6	Thiourea	SiO_2 NPs	Mesoporous	10-20	-	128	1360	¹¹⁶
7	Cyanamide	Ordered mesoporous SBA-15	Ordered mesoporous	5.3	0.34	239	840	¹¹³
8	Dicyandiamide	SBA-15	Mesoporous	-	0.24	122	2302	¹³⁴
9	Cyanamide	SBA-15	Ordered mesoporous	3.4	0.49	517	12150	¹³⁰
10	Ammonium thiocyanate	SBA-15	Ordered mesoporous	5.3	0.34	239	3040	¹¹⁹
11	Cyanamide	KCC-1 silica spheres	Hierarchical spheres	3.8	0.4	160	14350	¹³¹
12	Cyanamide	Anodic alumini oxide	Nanorods	-	-	25	2700	¹²⁷
13	Melamine	Pluronic P123	Warm-like porous	-	-	90	494	¹²³
14	Melamine	Copolymer-F68	Mesoporous	6.9	0.503	185	1518	¹³⁵
15	Urea	BmimBF ₄	Porous nanosheets	25	0.40	73	2580	¹²⁰

1.2.4 Doped g- C_3N_4

Doping is a process of incorporating external impurities into the g- C_3N_4 framework to tune its optical, electronic and other physical properties (Fig. 1.11).¹³⁶ The bandgap energy of g- C_3N_4 is 2.7 eV, enabling it to utilize only the solar light with wavelength below 460 nm.²² Thus, in order to further enhance the light harvesting ability of g- C_3N_4 , various bandgap engineering strategies, including metal doping, non-metal doping and metal/nonmetal co-doping have been widely exploited and demonstrated to achieve enhanced photocatalytic activity in many cases.^{20, 23, 25, 26, 29, 30, 58, 102, 103, 110, 136}

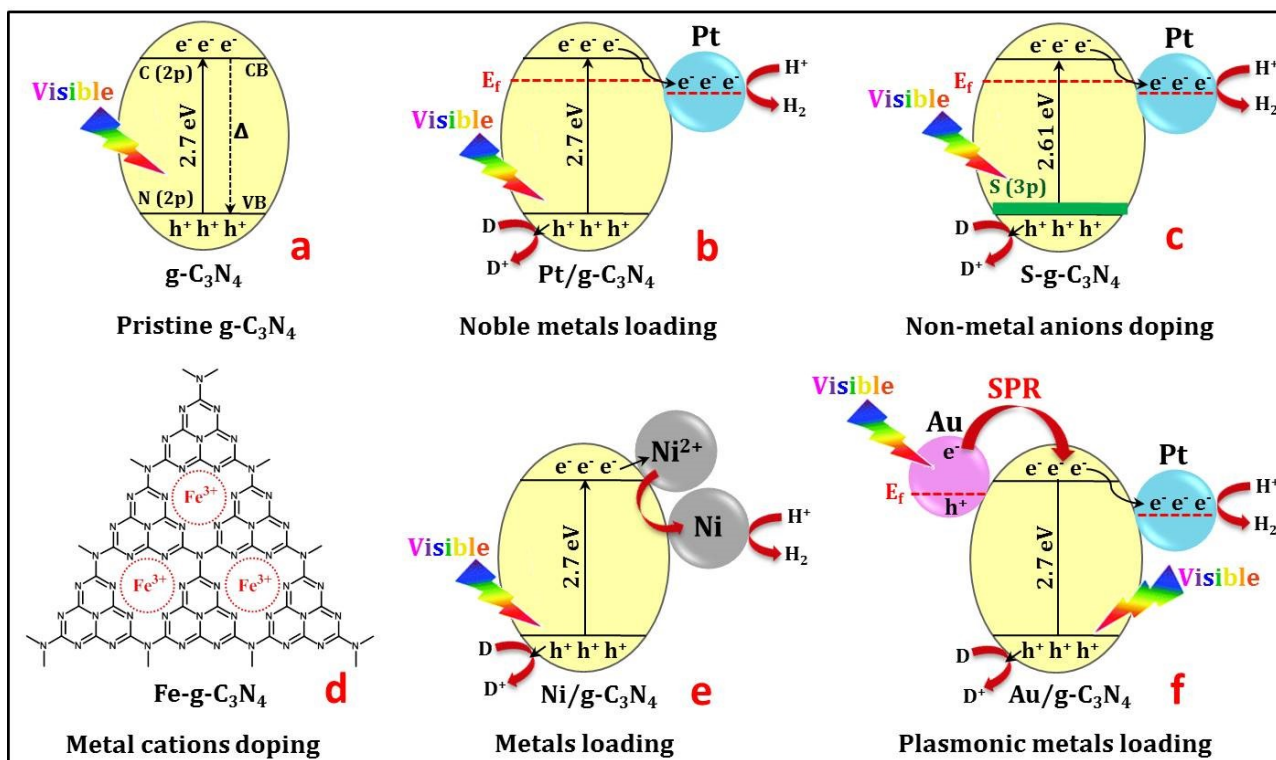


Figure 1.11 Development of g-C₃N₄ semiconductor for photocatalytic H₂ production: (a) pristine g-C₃N₄; (b) noble metal loaded g-C₃N₄; (c) non-metals anions doped g-C₃N₄; (d) metal cations doped g-C₃N₄; (e) metals loaded g-C₃N₄; (f) plasmonic metals loaded g-C₃N₄.

Non-metal ion doped g-C₃N₄

Tremendous efforts have been made to introduce non-metals, such as B,¹³⁷⁻¹⁴⁰ C,¹⁴¹⁻¹⁴⁷ N,^{73, 143, 144} P,^{124, 143, 144, 148-154} O,^{143, 144, 155-158} S,^{95, 97, 116, 143, 144, 159-165} F,¹⁶⁶ Br¹⁶⁷ and I^{92, 168} into g-C₃N₄, as donor states above the valence band for improving light absorption in the visible region (Fig. 1.11c). For example, Wang and co-workers developed a new type of B-doped g-C₃N₄ nanosheets via a simple one-pot pyrolysis strategy. A B-doping amount of 1 at% into g-C₃N₄ exhibited the highest photocatalytic H₂ evolution rate (1880 μmol h⁻¹ g⁻¹) under visible light illumination, which was over 12-fold higher than that of pristine bulk g-C₃N₄. B-Doping reduced the band gap to absorb visible light more easily and developed higher specific surface area (49.47 m² g⁻¹) compared to that of bulk g-C₃N₄ (8.24 m² g⁻¹), which consequently improved the photocatalytic activity dramatically.¹³⁹ In another work, Li et al. prepared oxygen-doped g-C₃N₄ by a hydrothermal route using H₂O₂ as the dopant precursor. XPS studies showed that part of the sp²-hybridized nitrogen atoms in the g-C₃N₄ framework were replaced by oxygen atoms, forming N-C-O bonds, a key reason for the significant changes in the physicochemical properties of g-C₃N₄. The O-doping process effectively enlarges specific surface area, extends visible light response with absorption edge up to 498 nm, and improves charge separation efficiency for H₂ production.¹⁵⁷ Moreover, Liu and co-workers reported that sulfur doping can induce a unique electronic structure, responsible for an increased VB along with an elevated CB minimum and minor declined absorbance. Significant changes in the optical properties and electronic structures would lead to enhanced H₂ evolution rate over the sulfur-doped g-C₃N₄, with 8 times H₂ evolution rate higher than the pristine g-C₃N₄.¹⁶⁴ Furthermore, Zhang et al. prepared iodine-doped g-C₃N₄ by a simple polycondensation

of dicyandiamide with ammonium iodide as dopant. DFT calculations indicated that the sp^2 -bonded N was preferentially substituted by iodine atom. The intimate interaction between g-C₃N₄ and iodine atoms extended the π -conjugated aromatic heterocycle, which assisted to enhance the mobility of free charge carriers evidenced from the EPR analysis. The resulting I-doped g-C₃N₄ showed enhanced optical absorption, enlarged specific surface area as well as accelerated charge separation for excellent H₂ production⁹².

Metal ion doped g-C₃N₄

Apart from non-metal doping, doping of metals, such as Mn,¹⁶⁹⁻¹⁷¹ Fe,^{169, 171-177} Co,^{169, 171, 178} Ni,^{169, 171} Cu^{169, 171, 177, 179, 180}, Zn¹⁸¹, Y¹⁸², Zr,¹⁸³ Mo¹⁸⁴, W¹⁸⁵ has also been broadly employed to modify the optical and electronic properties of g-C₃N₄ by efficiently increasing the light absorption, reducing the band gap, accelerating the charge mobility, and prolonging the lifetime of charge carriers, which are all beneficial for photocatalytic H₂ production (Fig. 1.11d). For example, Gao et al. synthesized Fe doped g-C₃N₄ by a hydrothermal method using formamide and citric acid as precursors for g-C₃N₄ and ferric chloride as the Fe-precursor. The Fe dopant appeared to be in the +3 oxidation state and could significantly influence the electronic and optical properties of g-C₃N₄. The as-prepared Fe doped g-C₃N₄ photocatalyst showed highly efficient visible light-driven H₂ production rate of ~ 16.2 mmol g⁻¹ h⁻¹ and a quantum efficiency of 0.8%. The experimental results demonstrated that Fe doping promotes strong coupling between the metal and the g-C₃N₄, forming unique electronic structures and favoring electron mobilization along with 2D nanomaterial plane. The presence of 2D nanomaterial planes is also responsible for efficient electron transfer process in the photocatalytic system, leading to efficient H₂ evolution.¹⁷³ Jiang and co-workers fabricated a series of mesoporous Cu-doped g-C₃N₄ photocatalysts by using CuCl₂ and melamine as precursors. The embedded Cu²⁺ transformed the optical properties, influenced the energy band structure, and improved the electron-hole separation rate and thus enhanced the photocatalytic properties.¹⁸⁰ Zhang and co-workers synthesized Mn-doped g-C₃N₄ nanoribbons via a two-step calcination approach. In particular, the obtained Mn-doped g-C₃N₄ exhibited excellent photocatalytic properties for HER. The yields of H₂ and O₂ could reach 593.35 and 59.47 μ mol g⁻¹ after 3 h illumination.¹⁷⁰ Ye and co-workers presented a facile soft-chemical approach to prepare Zn-doped g-C₃N₄. Compared with other metal atoms, Zn was easier to incorporate into g-C₃N₄ without destroying its graphite-like structure. The H₂ evolution rate of Zn-doped g-C₃N₄ was as high as 297.5 μ mol h⁻¹ g⁻¹, over 10-fold higher than that of pure g-C₃N₄.¹⁸¹

Besides transition metal ions, the coordination of alkali metal ions, such as Li⁺, K⁺ and Na⁺ and into the nitrogen pots of g-C₃N₄ framework was also studied to enhance its structure-activity performance.¹⁸⁶⁻¹⁹¹ Zhang and co-workers prepared K-doped g-C₃N₄ via a facile thermal polycondensation strategy employing KBr as the K source. The KBr content strongly affected the photocatalytic performance of the K-doped g-C₃N₄, and the photocatalytic H₂ evolution rate of the optimized K-doped g-C₃N₄ nanosheets (10 wt% KBr)

was as high as $1337.2 \mu\text{mol h}^{-1} \text{g}^{-1}$, which was 5.6 fold higher than that of pure $\text{g-C}_3\text{N}_4$ ($239.8 \mu\text{mol h}^{-1} \text{g}^{-1}$). This is due to the narrower band gap and improved light harvesting property of K-doped $\text{g-C}_3\text{N}_4$.¹⁸⁷

Metal and non-metal ions co-doped $\text{g-C}_3\text{N}_4$

Co-doping with metal cation and non-metal anion was also found to be a promising strategy to optimize structural and optical properties of $\text{g-C}_3\text{N}_4$ (Fig. 1.12).¹⁹²⁻¹⁹⁹ Hu et al. developed a metal/nonmetal co-doping method to synthesize Fe and P co-doped $\text{g-C}_3\text{N}_4$ using dicyandiamide, ferric nitrate, and diammonium hydrogen phosphate as precursors. The phosphorus was doped into $\text{g-C}_3\text{N}_4$ to form P-N bonds at the interstitial sites of $\text{g-C}_3\text{N}_4$. On the other hand, the Fe was coordinated with the N at the interstitial

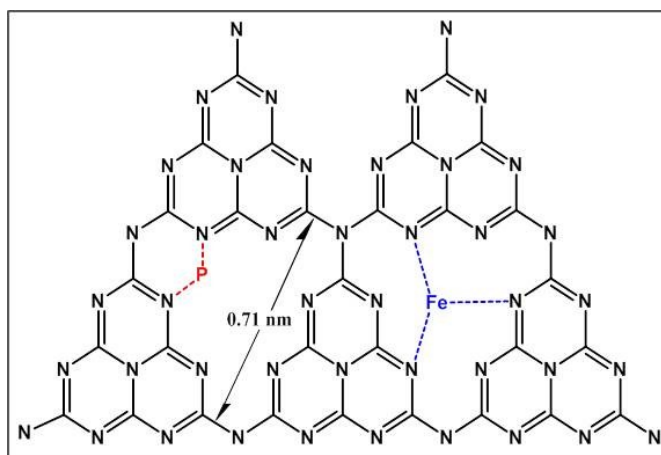


Figure 1.12 Possible doping sites of P and Fe in Fe/P co-doped $\text{g-C}_3\text{N}_4$ photocatalysts. Reproduced with permission from ref.⁴¹⁵ Copyright 2014 Elsevier.

position in the nitrogen pots of $\text{g-C}_3\text{N}_4$. The improved activity of Fe and P co-doped $\text{g-C}_3\text{N}_4$ catalyst compared with pristine $\text{g-C}_3\text{N}_4$ and single-doped $\text{g-C}_3\text{N}_4$ under visible light irradiation was due to the synergistic effect of Fe and P co-doping that assisted to inhibit the crystal growth of $\text{g-C}_3\text{N}_4$, enhance the BET surface area, narrow the band gap energy, and promote the separation efficiency of photogenerated charge carriers.¹⁹⁵

1.2.5 Role of co-catalysts in photocatalytic H_2 and O_2 evolution

The co-catalysts can play an important role in improving the photocatalytic activity of $\text{g-C}_3\text{N}_4$ (Fig. 1.13).^{23, 30, 43} In photocatalytic water splitting, the co-catalysts can be used to enhance either water oxidation or reduction reactions. When the noble metal is loaded on the surface of $\text{g-C}_3\text{N}_4$, the photogenerated electrons could migrate to the surface and entrapped by the noble metal co-catalyst, because the Fermi energy level of noble metal is always lower than the $\text{g-C}_3\text{N}_4$.³⁶ Hence, the presence of such co-catalysts greatly minimizes the possibility of electron-hole recombination, resulting in efficient electron-hole separation and enhanced photocatalytic activity.³⁶

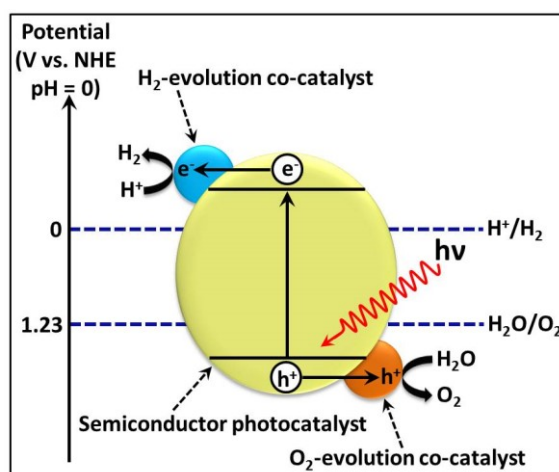


Figure 1.13 Schematic illustration of photocatalytic water splitting over a semiconductor photocatalyst loaded with H_2 and O_2 evolution co-catalysts. Modified figure adapted from ref.⁴¹⁶ Copyright 2014 Royal Society Chemistry.

- (i) Co-catalysts could lower the activation energy or overpotential for H_2 or O_2 evolution reactions.⁴³

- (ii) Co-catalysts are capable of improving electron-hole separation at the co-catalyst/semiconductor interface. As shown in Fig. 1.13, the photogenerated electrons in the conduction band (CB) of a photocatalyst are transferred to the H₂ evolution co-catalyst and reduce protons to H₂ molecules, whereas photogenerated holes in the valence band (VB) migrate to the O₂ evolution co-catalyst and oxidize H₂O to form O₂. The formation of an appropriate heterojunction between the co-catalyst and the semiconductor is the key factor for enhanced charge separation and transfer from the semiconductor to the co-catalyst.³⁴
- (iii) Moreover, co-catalysts could suppress the photocorrosion and increase the stability of semiconductor photocatalysts.^{21, 200}

Many factors can affect the performance of co-catalysts, such as loading amount, particle size and valence states.⁴⁴ Particle size and valence states are strongly dependent on the loading method of the co-catalysts. There are three types of methods to deposit co-catalysts onto the semiconductor surface, i.e. in-situ photodeposition, impregnation and chemical reduction.²⁰¹ In photodeposition method, the semiconductor is mixed with co-catalyst precursor (e.g. g-C₃N₄ with H₂PtCl₆) and then reduced by photoexcited electrons on the semiconductor surface (Pt/g-C₃N₄) under light irradiation in the presence of sacrificial reagents.²⁰¹ The second method is usually followed by a post-calcination step. First, a semiconductor is impregnated with a solution containing co-catalyst precursor, followed by evaporation and drying. Afterwards, the obtained sample is calcined in air or other gases such as hydrogen or argon in order to obtain the desired states of the metal or metal oxide.²⁰¹ The third method is chemical reduction, in which the semiconductor is mixed with co-catalyst precursor and then reduced by using NaBH₄.²⁰¹

Especially, the loading amount of co-catalysts can affect their catalytic performance. Initially, the introduction of a co-catalyst onto a semiconductor surface could gradually enhance the photocatalytic water splitting activity by facilitating efficient charge separation. When the loading amount of a co-catalyst on a semiconductor reaches the optimal value, this co-catalyst/semiconductor system achieves the highest activity. However, further loading of the co-catalyst will drastically decrease the photocatalytic activity. This decreased activity in case of excessive loading of co-catalysts can be explained by the following factors: (i) covering the surface active sites of the semiconductor and hindering its contact with sacrificial reagents or water molecules; (ii) shielding the incident light, and thus preventing the light absorption and generation of photogenerated electrons and holes; and (iii) co-catalysts at high loading amount could act as charge recombination centers, a key factor for decrease of the photocatalytic activity. Another important factor influencing the catalytic activity of co-catalysts is their particle size. Co-catalysts with smaller particle size have a large BET surface area, which provides more number of active sites, and hence, higher photocatalytic activity. In fact, numerous studies showed that the smaller particle size and high dispersion of loaded co-catalysts lead to significantly enhanced photocatalytic activity.⁴³

Various co-catalysts have been used for photocatalytic H₂ and O₂ evolution reactions (Fig. 1.14).⁴³ For example, noble metals, such as Pt, Ru, Rh, Pd, Au and Ag have been extensively investigated as efficient co-

catalysts for photocatalytic H₂ evolution (Fig. 1.14).²⁰²⁻²⁰⁷ Among them, Pt was found to be the most effective co-catalyst because of its high work function and low over potential for H₂ evolution reaction.²⁰⁴ On the other hand, noble metal oxides, such as RuO₂ and IrO₂ are well-known and excellent water oxidation co-catalysts for improving the photocatalytic O₂ evolution rate (Fig. 1.14).^{22, 208} The earth-abundant transition metals, such as Co, Ni and Cu have been applied as co-catalysts for photocatalytic H₂ evolution reaction (Fig. 1.14).²⁰⁹⁻²¹³ In addition, their metal oxides and hydroxides can act as both H₂ and O₂ evolution co-catalysts (Fig. 1.14).^{200, 201, 214-217} Furthermore, metal sulfides,²¹⁸⁻²²² nitrides,^{223, 224} phosphides,²²⁵⁻²²⁷ carbides,²²⁸⁻²³⁰ arsenides²³¹ and borides²³² were found to be good H₂ evolution co-catalysts in recent years.

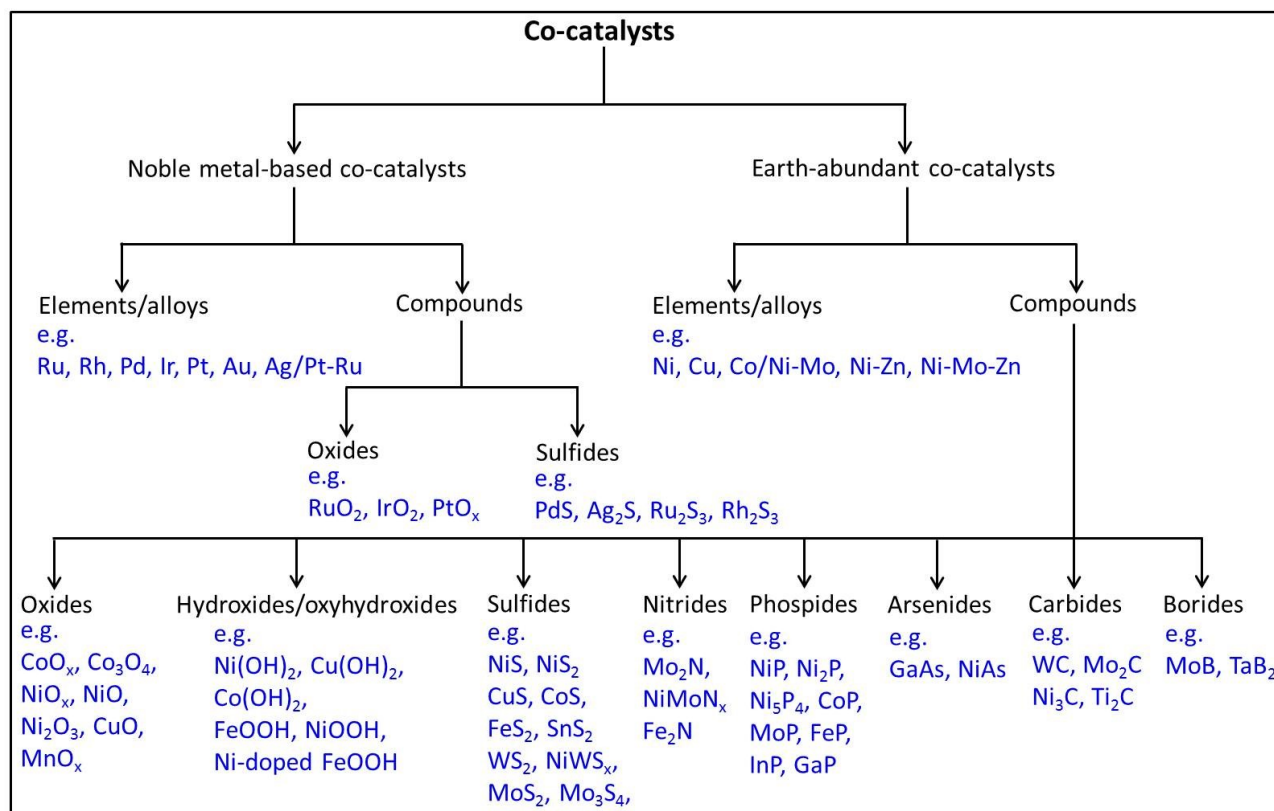


Figure 1.14 Different types of co-catalysts for photocatalytic H₂ and O₂ evolution.

1.2.6 Loading co-catalysts on g-C₃N₄

Besides the elemental doping to tune the light absorption of g-C₃N₄, the loading of co-catalysts was also attempted to enhance its photocatalytic activity for H₂ production (Fig. 1.15).^{23, 26, 33, 43, 233} It was demonstrated that a metal/g-C₃N₄ heterojunction could facilitate the separation and transportation of photogenerated electron-hole pairs.³⁶ In metal/g-C₃N₄ heterojunctions, a Schottky barrier is formed when g-C₃N₄ is in close contact with a metal that results, Fermi level alignment induced by electron flow from higher Fermi level (g-C₃N₄) to lower level (metal) (Fig. 1.15). The loaded metal could effectively act as an electron trap to receive photoelectrons generated from g-C₃N₄ after excitation, improving the charge carrier separation and reducing the recombination rate.^{23, 34, 36, 234, 235} In addition, the loaded metal provides additional active sites for H₂ generation due to its relatively low over-potential for water reduction.⁴³

Noble metal loaded on g-C₃N₄

As mentioned above, the co-catalysts could play an important role in separating photogenerated charge carriers, hosting active sites for H₂ generation, suppressing photocorrosion, and thereby enhancing the photocatalytic activity.^{23, 34, 36, 234, 235} Noble metals, such as Ru,⁸¹ Rh,^{81, 205} Ir,⁸¹ Pd^{81, 126, 203, 236-238} and Pt^{81, 89, 94, 96, 126, 201, 202, 204, 239-248} are commonly used co-catalysts for photocatalytic H₂ production (Fig. 1.11b). Among these noble metals, Pt is the most effective promoter for H₂ evolution due to its large work function for trapping electrons and its lowest activation energy for efficient H₂ evolution.²⁹

For example, Maeda et al. loaded various noble metals, such as Ru, Rh, Pd, Ir, Pt and Au on the surface of g-C₃N₄ by in situ photodeposition method using (NH₄)₂RuCl₆, Na₃RhCl₆·2H₂O, (NH₄)₂PdCl₄, Na₂IrCl₆·6H₂O, H₂PtCl₆·2H₂O and HAuCl₄·4H₂O as precursors, respectively. Among these, Pt/g-C₃N₄ exhibited the highest photocatalytic H₂ production rate (7.3 μmol h⁻¹), whereas lowest H₂ production was obtained with Ir/g-C₃N₄ (0.2 μmol h⁻¹). Platinum possesses an excellent ability to act as a catalytically active site for H₂ evolution due to the smallest overvoltage, while Iridium has the largest values among metals employed in this study.⁸¹ Hence, the presence of such co-catalysts greatly minimizes the possibility of electron-hole recombination, resulting in an efficient electron-hole separation, thus, photocatalytic activity enhanced.⁸¹ Wang et al. also synthesized Pt NPs decorated g-C₃N₄ by simple chemical reduction method using ethylene glycol acting as both solvent and reducing agent. The Pt/g-C₃N₄ catalysts showed a H₂ evolution rate of 45 μmol h⁻¹ from an aqueous solution of triethanolamine under visible light irradiation.²⁴⁹

Cao et al. synthesized different shapes of Pt NPs, such as cubic, octahedral and spherical, and then deposited on g-C₃N₄ surface by adsorption-deposition method for photocatalytic H₂ evolution reaction. These Pt NPs of different shapes have similar sizes of around 10 nm but have different facets exposed on the surface. The experimental results demonstrated that the spherical Pt/g-C₃N₄ exhibits higher photocatalytic H₂ evolution rate than the cubic Pt/g-C₃N₄ and octahedral Pt/g-C₃N₄ under visible light irradiation, indicating the significance of Pt shape in tuning the photocatalytic activity of g-C₃N₄ under visible light irradiation. Such structure-sensitive activity is mainly due to the unique surface atomic structures of different exposed facets of Pt NPs, leading to the disparity of active sites and adsorption energies during photocatalytic reaction. Thus, optimizing the size and shape of co-catalysts is essential for the design of efficient photocatalysts.²⁰²

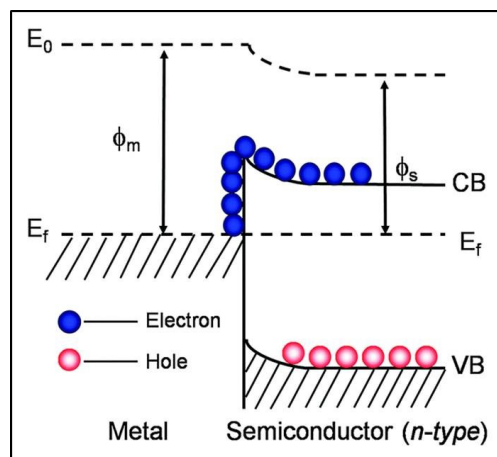


Figure 1.15 Schematic energy band diagram of a typical metal-semiconductor Schottky junction. Reproduced with permission from ref.⁴¹⁷ Copyright 2014 Royal Society of Chemistry.

Besides the noble metals, their oxides and sulfides, such as RuO₂, IrO₂, Ag₂O, PtO_x, PdS, Ag₂S, Ru₂S₃, and Rh₂S₃ were also used as co-catalysts for photocatalytic H₂ and O₂ evolution reactions.^{201, 217}

Decorating with noble metals, such as Ag^{206, 247, 250-268} and Au^{126, 204, 207, 247, 257, 269-277} on the g-C₃N₄ surface can induce the localized surface plasmon resonance (SPR) due to the strong visible light absorption (Fig. 1.11f).^{23, 43, 276, 278, 279} For example, Di et al. deposited Au NPs on the surface of g-C₃N₄ by three different methods, such as deposition-precipitation, in situ photodeposition, and impregnation to construct synergistic metal-semiconductor junctions for photocatalytic H₂ production. The deposition of Au NPs showed enhanced visible light absorption and a characteristic peak at 560 nm belonging to the plasmonic effect of Au NPs. In addition, there was a red shift in the absorbance edge of Au/g-C₃N₄ in comparison with pristine g-C₃N₄. The Au NPs were found to possess an average diameter of 8-20 nm, which were decorated especially on the surface and edges of g-C₃N₄. Among those, the Au/g-C₃N₄ prepared by the deposition-precipitation exhibited much higher photocatalytic H₂ production, owing to (i) higher visible light absorption capacity induced by Au NPs due to the SPR effect and (ii) formation of intimate interfacial contact between g-C₃N₄ and Au NPs that effectively promoted the charge transfer and separation.²⁰⁴

In addition, Samanta et al. also synthesized Au loaded g-C₃N₄ by deposition-precipitation technique, resulting in a localized SPR effect, which could absorb visible light effectively, as evidenced by a characteristic peak centered at 550 nm. The prepared Au/g-C₃N₄ composite showed an improved photocatalytic performance, the H₂ evolution rate was up to 8870 μmol h⁻¹ g⁻¹, which was 23-fold higher than that of neat g-C₃N₄ (383 μmol h⁻¹ g⁻¹), indicating that the size, shape and uniform dispersion of Au NPs on the g-C₃N₄ surface were advantageous to improve the photocatalytic activity.²⁰⁷

In another work, Qin et al. loaded Ag on top of g-C₃N₄ by a chemical reduction method, in which, the visible light absorption was increased due to the localized surface plasmon resonance (LSPR) effect, resulting in reduced recombination of photogenerated electron-hole pairs and enhanced photocatalytic activity. The Ag loaded g-C₃N₄ exhibited excellent photocatalytic H₂ evolution rate (344.51 μmol g⁻¹ h⁻¹), which was about 3.6 times higher than that of pristine g-C₃N₄ (95.15 μmol g⁻¹ h⁻¹). Moreover, the addition of fluorescein, as a photosensitizer, led to increased H₂ evolution rate (2014.20 μmol g⁻¹ h⁻¹) which was about 4.8 times higher than that of the Ag/g-C₃N₄ composite.²⁶²

On the other hand, bimetallic nanocrystals have huge prospects in catalytic activities owing to their extraordinary structural properties and synergistic effect between metals.²⁸⁰⁻²⁸⁷ For example, Han and co-workers developed AuPd bimetallic decorated g-C₃N₄ photocatalysts, via *in situ* chemical deposition method, which could effectively promote the separation efficiency of photogenerated charge carriers, and consequently enhanced H₂ evolution activity. Owing to these advantages, the 0.5 wt% AuPd/g-C₃N₄ catalyst showed the best catalytic performance, with H₂ evolution rate of 326 μmol h⁻¹ g⁻¹, which is about 3.5 and 1.6 times higher than that of pristine Au/g-C₃N₄ and Pd/g-C₃N₄ under visible light irradiation.²⁸²

Non-noble metal loaded on g-C₃N₄

Besides the expensive noble metals, some earth abundant, low-cost transitional metals, such as Bi,^{288, 289} Ni^{209, 212, 213, 290-294} and Cu^{179, 210, 211, 295} have also been applied as co-catalysts in photocatalytic H₂ production (Fig. 1.11e). As an active transition non-noble metal, Ni plays a significant role in photocatalytic systems, which has been widely used in g-C₃N₄-based photocatalysts. The introduction of Ni results in a change in the surface band bending, and thus enhances the separation efficiency.^{209, 290} For example, Bi et al. synthesized Ni loaded g-C₃N₄ by a simple solvothermal method using nickel acetylacetonate as Ni precursor. Ni nanoparticles with size of 30 nm were found to be uniformly distributed on the 2D g-C₃N₄ nanosheet surface with a lattice spacing of 0.209 nm, which corresponded to the (111) plane of metallic Ni. The high distribution of Ni NPs on the g-C₃N₄ could enhance the photocatalytic H₂ evolution activity. The surface photovoltage (SPV) was employed to examine the efficiency of charge separation at the heterojunction interface of Ni/g-C₃N₄. Interestingly, the response intensity of Ni/g-C₃N₄ is markedly larger than the pristine g-C₃N₄, signifying the well separation of charge carriers at the interface to control the recombination process. As noticed by Mott-Schottky plots, Ni loading deepens the surface band bending of g-C₃N₄, resulting in high separation of photogenerated charge carriers, which is contributed to the enhanced photocatalytic H₂ evolution activity.²⁹⁰

In addition, Kong et al. also synthesized Ni loaded g-C₃N₄ by in-situ photodeposition method using NiCl₂·6H₂O as a Ni precursor and NaH₂PO₂ as the hole sacrificial agent. The Ni NPs were obtained by the reduction of Ni(II) via photogenerated electrons and uniformly distributed on the electron outlet points of g-C₃N₄ in 30 minutes. When the loading amount of Ni was 7.40 wt%, a high photocatalytic H₂ production rate (4318 g⁻¹ h⁻¹) was obtained and no noticeable decrease in the photocatalytic H₂ evolution rate after four runs (48 h). Furthermore, the Ni/g-C₃N₄ composite photocatalyst presented a sunlight-driven H₂ production of 4000 μmol g⁻¹ h⁻¹ under natural sunlight outdoors. The photoelectrochemical and steady-state photoluminescence experiments demonstrated that Ni effectively prevented the recombination of the photogenerated electrons and holes of g-C₃N₄ and hence, improved H₂ evolution activity.²¹²

In another related study, Indra and co-workers deposited low-cost and earth-abundant Ni co-catalysts on the porous g-C₃N₄ surface for enhanced H₂ evolution. Upon photoreduction process, Ni metal domains were produced from the Ni²⁺ ions via electron transfer from the CB of g-C₃N₄, as verified by the in-situ EPR spectroscopy. The EPR spectrum of catalyst (Ni deposition in the dark) recorded at 300 K showed no signal, suggesting that all nickel is dispersed as Ni²⁺ species. After visible light irradiation, a broad EPR signal (g = 2.23) was observed, indicating the formation of ferromagnetic Ni⁰ NPs. Importantly, the CB potential of g-C₃N₄ was larger (-1.3 V) than the reduction potential of Ni²⁺ to Ni (-0.26 V), rendering the formation of Ni metal. Thus, the hybrid photocatalytic system comprised both Ni²⁺ and Ni species. In line with that, the as-formed Ni can serve as an efficient co-catalyst for capturing the electrons from g-C₃N₄. Moreover, the charge

separation and transfer during photocatalytic H₂ evolution was investigated by using in-situ EPR spectroscopy.²⁹¹

Furthermore, Fan et al. prepared Cu loaded g-C₃N₄ catalyst by impregnation method using Cu(NO₃)₂ as precursor. The particle size of Cu was found to be 30 nm dispersed on the g-C₃N₄ surface with a lattice spacing of 0.255 nm, corresponding to the (111) plane of metallic Cu phase. The experimental results demonstrated that the Cu NPs could trap the photogenerated electrons and act as a co-catalyst, and hence, it can suppress the charge recombination and enhance the photocatalytic activity.²¹⁰

Besides the transition metals, their oxides (e.g. NiO, CoO_x and MnO_x)^{201, 217}, hydroxides (e.g. Ni(OH)₂, Cu(OH)₂ and Co(OH)₂)^{200, 214-216}, oxyhydroxides (e.g. FeOOH and NiOOH)^{296, 297}, sulfides (e.g. MoS₂, Mo₃S₄, NiS, NiS₂, CuS, CoS, WS₂, NiWS_x, FeS₂ and SnS₂)²¹⁸⁻²²², nitrides (e.g. Mo₂N and NiMoN_x)^{223, 224}, phosphides (e.g. NiP, Ni₂P, CoP, MoP, FeP, InP and GaP)²²⁵⁻²²⁷, arsenides (e.g. GaAs and NiAs)²³¹, carbides (e.g. WC, Mo₂C, Ni₃C and Ti₂C)²²⁸⁻²³⁰ and borides (e.g. MoB and TaB₂)²³², etc., can also be used as co-catalysts for photocatalytic H₂ and O₂ evolution reactions.

1.2.7 Semiconductor/g-C₃N₄ heterojunction

The synthesis of semiconductor heterostructures is an effective approach to promote charge separation for improved photocatalytic activity (Fig. 1.16).^{13, 14, 19, 20, 23, 34, 36, 234, 235, 298-304} One of the major problems in photocatalysis is the fast recombination of photogenerated electron-hole pairs, limiting the overall efficiency. Typically, photogenerated electron-hole pairs have a recombination time in the order of 10⁻⁹ s, whereas the reaction time of electrons and holes with adsorbed species is quite longer (10⁻⁸-10⁻³ s).³⁴ If the recombination

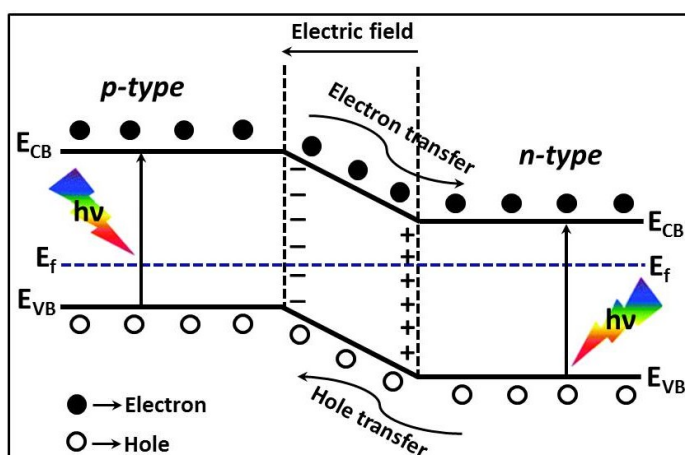


Figure 1.16 Schematic diagram of energy band structure and electron-hole separation in the p-n heterojunction. Modified figure adapted from ref.⁴¹⁸ Copyright 2014 Royal Society of Chemistry.

process can be partly diminished, highly efficient photocatalysts for water splitting reaction will be gained. The photogenerated electron-hole pair recombination could be reduced by making heterojunction between g-C₃N₄ and other semiconductor.^{20, 23} Based on the type of semiconductors, i.e. p-type (holes being the major charge carriers) or n-type (electrons being the major charge carriers), heterojunctions can be categorized into p-p, n-n, and p-n types, which are formed between two p-type SCs, two n-type SCs, and p-type and n-type SCs, respectively.³⁰³

The semiconductor p-n heterojunction is an effective design for achieving efficient charge separation and transportation. In general, when the p-type and n-type semiconductors are in contact, they form a p-n junction with a space-charge region at the interfaces due to the diffusion of electrons and holes, and thus

creating a built-in electrical potential that can direct the electrons and holes to travel in the opposite direction (Fig. 1.16).³⁶ When the p-n heterojunction is irradiated by photons with energy higher or equal than its bandgap, the photogenerated electron-hole pairs can be quickly separated by the built-in electric field within the space charge region. Driven by the electric field, the electrons are transferred to the CB of the n-type semiconductor and the holes to the VB of the p-type semiconductor. This p-n type heterostructure can offer several advantages, i.e. (i) a more effective charge separation, (ii) a rapid charge transfer to the catalyst, (iii) a longer lifetime of the charge carriers, and (iv) a separation of locally incompatible reduction and oxidation reactions.³⁰⁵

Depending on the bandgap and relative energy level of VB and CB, the semiconductor heterojunctions can be divided into three categories: straddling gap (Type-I), staggered gap (Type-II) and broken gap (Type-III), as shown in Fig. 1.17.^{23, 30, 34, 235, 299, 301-304} For the Type-I band alignment, both the VB and CB potentials of smaller band gap semiconductor (SC-2) are confined within the larger band gap semiconductor (SC-1), creating a straddling band alignment. Therefore, upon light irradiation with sufficient energy equivalent to or greater than the band gap of the semiconductors, photogeneration of electron-hole pairs occurred, resulting in the transfer and accumulation of all charge carriers in a single component within a hybrid structure. Since the charge carriers are accumulated in a single semiconductor, there is no evident overall enhancement of charge separation and thus commonly impairing the photoredox efficiency.²³ In Type-II heterojunction, the conduction band of SC-1 is more negative than that of SC-2, while the valence band of SC-1 is less positive than that of SC-2.³⁰³ Importantly, the difference of chemical potential between SC-1 and SC-2 causes band bending at the interface of junction. The band bending induces a built-in-field, which drives the photogenerated electrons and holes in opposite directions, leading to a spatial separation of the electrons and holes on different sides of heterojunction.³⁰³ Thus, the formation of type-II heterostructures is an effective approach to enhance charge separation efficiency for improved photocatalytic activity. Meanwhile, for the Type-III heterojunction, both VB and CB edges of a SC-1 are located above the CB potential of SC-2 without crossing each other.²⁹⁹

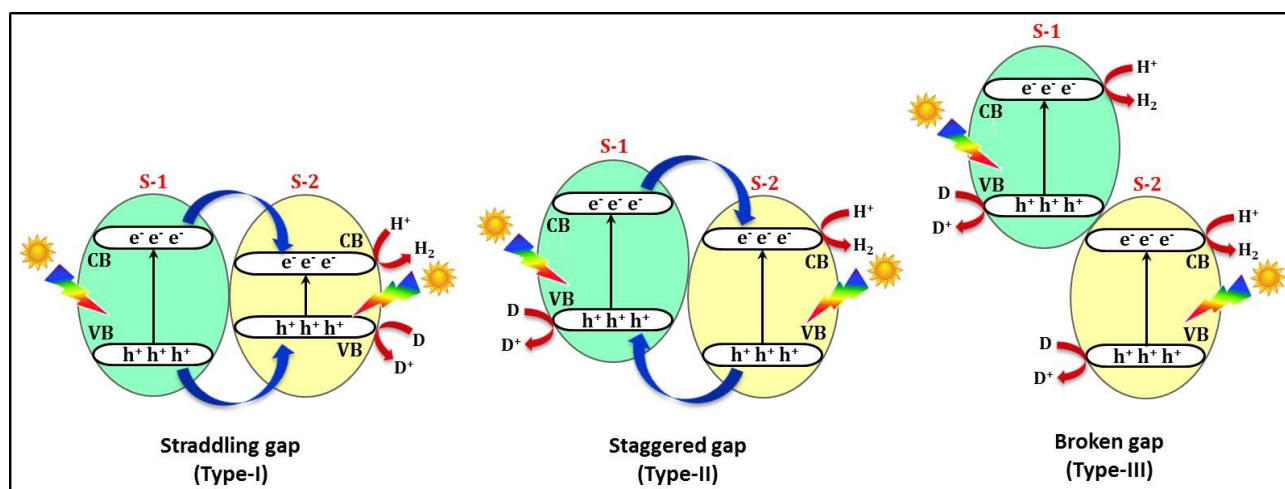


Figure 1.17 Schematic energy band diagram of three types of semiconductor heterojunctions. Modified figure adapted from ref.⁴¹⁹ Copyright 2016 American Chemical Society.

Zhang et al. synthesized sheet-on-sheet ZnIn₂S₄/g-C₃N₄ Type-I heterostructures, by *in situ* growth of ultrathin ZnIn₂S₄ nanosheets onto g-C₃N₄ nanosheets through a hydrothermal method, for photocatalytic H₂ production.³⁰⁶ After introducing ZnIn₂S₄ nanosheets, the specific surface area of g-C₃N₄ nanosheets is considerably improved that led to the availability of more number of active sites for the photoreaction. The optimized hybrid photocatalytic system (15% ZnIn₂S₄/g-C₃N₄) exhibited excellent hydrogen evolution rate of 14.1 μmol h⁻¹, which was about 17.6 times higher than that of pure g-C₃N₄ (0.8 μmol h⁻¹), attributed to efficient interfacial transfer of photoinduced electrons and holes from g-C₃N₄ to ZnIn₂S₄ nanosheets, as a result, decreased charge recombination on g-C₃N₄ nanosheets and the increased amount of photoinduced charge carriers in ZnIn₂S₄ nanosheets. Concurrently, the increased number of surface-active-sites and extended light absorption of g-C₃N₄ nanosheets after the decoration of ZnIn₂S₄ nanosheets may play a certain role for the enhancement of photocatalytic activity. The apparent quantum efficiency of this optimal sample is estimated to be 0.28% at 420 nm. Photovoltage and transient photoluminescence results demonstrated that the ZnIn₂S₄/g-C₃N₄ heterojunction nanosheets considerably boost the charge transfer efficiency, improving the probability of photoinduced charge carriers to reach the photocatalyst surface for efficient H₂ production.

Wu and co-workers fabricated a CdS/g-C₃N₄ visible light driven Type-II heterojunction photocatalysts by chemisorption and self-assembly method.³⁰⁷ The optimized hybrid photocatalysts system (5% Ni₂P-CdS/g-C₃N₄) exhibited the highest hydrogen evolution rate of 44 450 μmol h⁻¹ g⁻¹, which was about 27 times higher than that of pure CdS (1668 μmol h⁻¹ g⁻¹). The apparent quantum yield reaches up to 46.3% at 420 nm. The excellent photocatalytic activity and stability can be ascribed to the synergistic effect of the intimate interfacial contact between CdS and g-C₃N₄ and the surface co-catalyst modification. The outstanding performance of the Ni₂P-CdS/g-C₃N₄ composites can be attributed to the following reasons, i.e. (i) intimate interfacial contact between CdS and g-C₃N₄ can effectively promote the electron-hole pair separation, (ii) The introduction of Ni₂P as co-catalyst further accelerates the separation rate of the photogenerated electron-hole pairs and provides a catalytic active site for H₂ production.

Liu et al. synthesized CdLa₂S₄/mpg-C₃N₄ type-II heterojunction composites by hydrothermal method.³⁰⁸ The CdLa₂S₄/mpg-C₃N₄ composites showed absorption edge to longer wavelengths in comparison with the pure mpg-C₃N₄, attributed to the strong interaction between mpg-C₃N₄ and CdLa₂S₄ in the composites. This interaction can play a favorable role in improving the separation of the photogenerated electron-hole pairs, resulting in higher photocatalytic H₂ evolution rate of 5984.8 μmol h⁻¹ g⁻¹ over CdLa₂S₄/mpg-C₃N₄ composite catalysts, which was 7.7 times higher than the pure CdLa₂S₄ (779.2 μmol h⁻¹ g⁻¹). The apparent quantum yield was estimated to be 7.1% at 420 nm. The results of photoluminescence and photocurrent response demonstrated that the recombination of photogenerated electron-hole pairs was effectively inhibited due to the well-matched band structure and intimate contact interfaces of CdLa₂S₄ and mpg-C₃N₄.

In this thesis work, we synthesized AgIn₅S₈/C₃N₄ (Type-I heterojunction) and MoS₂/C₃N₄ (Type-II heterojunction) has been synthesized for photocatalytic H₂ production. Design of heterojunction between

these metal sulfides and C₃N₄, electron hole pair recombination could be significantly reduced. Table 1.2 showing some examples of heterojunction photocatalysts and their photocatalytic H₂ production activity.

Table 1.2 Photocatalytic H₂ production on metal sulfide/g-C₃N₄ based catalysts.

Catalyst	Synthesis method	Co-catalyst	Sacrificial agent	Light source	Incident light (nm)	Activity ($\mu\text{mol g}^{-1} \text{h}^{-1}$)	Ref.
ZnS/g-C ₃ N ₄	Precipitation	-	Methanol	3 W UV-LED	> 420	194	309
CdS/g-C ₃ N ₄	Sonochemical	Pt	Na ₂ S & Na ₂ SO ₃	350 W Xe	> 420	4152	21
CuInS ₂ /g-C ₃ N ₄	Hydrothermal	Pt	Na ₂ S & Na ₂ SO ₃	300 W Xe	> 420	1290	310
CaIn ₂ S ₄ /g-C ₃ N ₄	Hydrothermal	Pt	Na ₂ S & Na ₂ SO ₃	12 W UV-LED	-	102	35
ZnIn ₂ S ₄ /g-C ₃ N ₄	Hydrothermal	-	TEOA	300 W Xe	> 400	2820	306
CdIn ₂ S ₄ /g-C ₃ N ₄	Hydrothermal	-	Na ₂ S & Na ₂ SO ₃	300 W Xe	> 400	323	311
CdLa ₂ S ₄ /g-C ₃ N ₄	Hydrothermal	-	Na ₂ S & Na ₂ SO ₃	300 W Xe	> 420	5985	308
Cu ₂ MoS ₄ /g-C ₃ N ₄	Hydrothermal	-	TEOA	300 W Xe	> 420	2171	312
MoS ₂ /g-C ₃ N ₄	Sonochemical	Pt	Methanol	300 W Xe	> 420	231	313

1.2.8 Role of sacrificial agents in photocatalytic H₂ and O₂ evolution

In principle, sacrificial agents usually react with one type of charge carrier, while the other charge carrier reacts with water to produce hydrogen or oxygen.^{13, 18, 34, 45-49} The basic principle of photocatalytic reaction using sacrificial reagents is depicted schematically in (Fig. 1.18). When the photocatalytic reaction is conducted in the presence of an electron donor, for example methanol, the photogenerated holes in the valence band can irreversibly oxidize methanol instead of H₂O, thus facilitating water reduction by conduction band electrons. It is possible when the bottom of the conduction band of the photocatalyst is located at a more negative potential than the water reduction potential (0 V vs. NHE, pH 0). On the other hand, in the presence of an electron acceptor, for example, silver cations, the photogenerated electrons in the conduction band irreversibly reduce electron acceptors instead of H⁺, thereby promoting water oxidation by valence band holes. It is possible if the top of the valence band of the photocatalyst is positioned at a more positive level than the water oxidation potential (1.23 V vs. NHE, pH 0). The most commonly used electron donors are methanol,^{45, 47, 48} ethanol,^{45, 48} trimethylamine,^{46, 287} triethanolamine,^{45, 46, 48, 49, 287, 314-316} Na₂S/Na₂SO₃,^{45, 47, 49, 317} lactic acid,^{45, 48, 314} oxalic acid,^{46, 48, 314, 318-320} ascorbic acid,^{46, 49, 314, 316, 317} etc., whereas metal cations such as Ag⁺ and Fe³⁺ are typically used as electron acceptors.^{13, 18, 47}

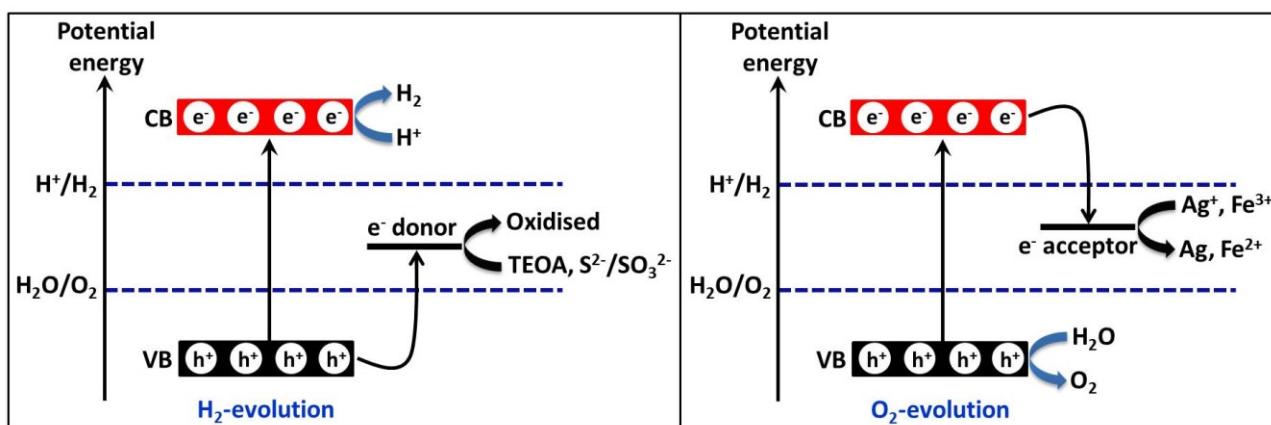


Figure 1.18 Schematic illustration of H₂ and O₂ evolution in the presence of sacrificial reagents. Modified figure adapted from ref.⁴²⁰ Copyright 2015 Royal Society of Chemistry.

2 Experimental

2.1 Catalyst synthesis

2.1.1 Synthesis of mesoporous C₃N₄, AgIn₅S₈ and AgIn₅S₈/C₃N₄ composite

Synthesis of mesoporous C₃N₄ by hard template method (CN)

Mesoporous C₃N₄ (CN) was received from Prof. Arne Thomas group (Technical University Berlin, Germany). Mesoporous C₃N₄ has been synthesized by a hard template method described in detail ref.³²¹ Briefly, cyanamide (CA) was dissolved in a mixed solution of ethanol and HCl at pH =2. After adding tetraethylorthosilicate (TEOS) the mixture was stirred for 30 min, followed by evaporation of the solvent and drying at 80 °C. Afterwards, the dry solid was subjected to a stepwise thermal treatment at 550 °C in argon and at 650 °C in ambient atmosphere. Finally, the formed silica was removed from the composite by treatment with a 4 M NH₄HF₂ solution to create mesopores.

Synthesis of AgIn₅S₈ by co-precipitation method (AIS)

AgIn₅S₈ (AIS) nanoparticles were synthesized by a co-precipitation method.³²² Typically, 0.0680 g (0.4 mmol) of AgNO₃ and 0.7818 g (2.0 mmol) of In(NO₃)₃·5H₂O were dispersed in 120 mL double distilled water under vigorous stirring for 30 minutes. Then, 0.6010 g (8.0 mmol) of thioacetamide (C₂H₅NS) was added to the above reaction mixture. Subsequently, the reaction mixture was kept on an oil bath at 60 °C for 12 hours under magnetic stirring (300 rpm) with a condenser. The resulting grey coloured precipitate was filtered, washed with distilled water and ethanol for several times and then dried for 12 h at 80 °C in ambient atmosphere.

Synthesis of AgIn₅S₈/C₃N₄ by co-precipitation method (AIS-CN)

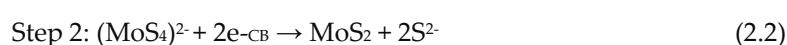
AIS-CN composites with different AIS content (labelled as xAIS-CN, where x denotes the weight percentage of AIS) were synthesized by performing the above described co-precipitation in the presence of CN.³²² In a typical synthesis procedure, 0.1800 g of CN was dispersed in 20 mL double distilled water by vigorous stirring for 30 minutes. To obtain a composite with 10 wt.% AIS, 0.0036 g of AgNO₃ and 0.0417 g of In(NO₃)₃·5H₂O were added to this suspension and vigorously stirred for 30 minutes. After adding 0.0321 g of thioacetamide (C₂H₅NS) the mixture was stirred at 60 °C for 12 hours. The resulting yellow-grey coloured precipitate was filtered, washed and dried in the same way as pure AIS. To obtain composites with 5, 15 and 20 % AIS, the concentrations of the respective precursors have been adjusted accordingly.

2.1.2 Synthesis of 2H and 1T phase MoS₂ and MoS₂/C₃N₄ composites

Synthesis of 2 wt% 2H MoS₂/C₃N₄ composite by in situ photodeposition method (2H MS-CN (PD))

Ammonium tetrathiomolybdate (ATTM), (NH₄)₂MoS₄ was used as precursor for MoS₂ in situ photodeposition.³²³ A typical in situ photodeposition process is given in Section 2.2 as the synthesis was

performed in the same setup like the hydrogen evolution experiments. C_3N_4 (24.5 mg) and ATTM $(NH_4)_2MoS_4$ (0.84 mg, 0.0032 mmol; theoretical loading amount of MoS_2 is 2 wt% or 0.5 mg MoS_2) were dispersed by sonication for 2 minutes in 25 mL of an aqueous solution containing 1.7 mL lactic acid. Before irradiation, the reactor was evacuated several times by applying vacuum and refilling with argon to remove oxygen. A 300 W Xe lamp with an output power of 1.5 W was used to irradiate the sample and temperature was maintained at 25 °C. After 2 hours, the reaction was stopped and the material was recovered by centrifugation. After washing it three times alternately with double distilled water and absolute ethanol the material was dried at room temperature overnight. Ammonium tetrathiomolybdate was dissociated into NH_4^+ and $(MoS_4)^{2-}$. $(MoS_4)^{2-}$ was reduced into MoS_2 by photogenerated CB e^- and then deposited on the surface of CN (Eq. 2.1 & 2.2).



Synthesis of 2 wt% 2H MoS_2/C_3N_4 composite by sonochemical method (2H MS-CN (SC))

For the synthesis of this material, 2H MoS_2 has been prepared separately by a hydrothermal method (2H MS (HT)).³²⁴ In a typical procedure, ammonium heptamolybdate tetrahydrate, $(NH_4)_2Mo_7O_{24} \cdot 4H_2O$ (1.2359 g, 1.0 mmol) was dissolved in 35 mL deionized water by vigorous stirring for 1 h. Thiourea, CH_4N_2S (1.1418 g, 15.0 mmol), was dissolved separately in 35 mL deionized water by vigorous stirring for 1 h. These two reaction solutions were combined and stirred again for 30 minutes. Then, this reaction mixture (transparent solution) was transferred into a 100 mL Teflon-lined stainless steel autoclave and heated at 180 °C for 24 h in the heating oven, and cooled down to room temperature naturally. The black coloured product was collected by centrifugation, washed alternately with distilled water and absolute ethanol until the centrifugate got colourless and odorless (approx. 5-6 times each solvent). Finally, the obtained material was dried at 70 °C for 24 h in the heating oven.

For the synthesis of 2 wt% 2H MoS_2/C_3N_4 composite (2H MS-CN (SC)), C_3N_4 (196 mg) was dispersed in 10 mL of absolute ethanol by stirring for 30 min and then sonicated for 30 min. In a separate flask, 2H MoS_2 (HT) (4 mg) was dispersed in 5 mL of absolute ethanol by stirring for 30 min and then sonicated for 30 min. Then, the exfoliated C_3N_4 and 2H MoS_2 solutions were combined and kept in an oil bath at 70 °C under stirring, until ethanol was evaporated completely. The obtained powder was ground by using mortar and pestle and then heated at 300 °C for 2 h under an Ar atmosphere (ramp rate 5 K/min) in the tubular furnace.^{313, 325}

Synthesis of 2 wt% 1T MoS_2/C_3N_4 composite by sonochemical method (1T MS-CN (SC))

For the synthesis of 1T MS-CN (SC), 1T MoS_2 has been prepared separately by a solvothermal method using N,N-Dimethylformamide (DMF) as a solvent (1T MS (ST)).³²⁶ In a typical synthesis procedure, sodium molybdate dihydrate, $NaMoO_4 \cdot 2H_2O$ (0.3630 g, 1.5 mmol) and L-cysteine, $C_3H_7NO_2S$ (0.608 g, 5.0 mmol) were dissolved in 70 mL of DMF/ H_2O 3/2 (v/v) under stirring for 1 h. The formed yellow coloured

transparent solution was transferred into a 100 ml Teflon-lined stainless steel autoclave and then heated at 180 °C for 12 h in the heating oven and cooled down to room temperature naturally. The resulting black coloured product was centrifuged, washed alternately with distilled water and absolute ethanol for several times and then dried at 70 °C for 24 h in the heating oven.

For the synthesis of 2 wt% 1T MoS₂/C₃N₄ composite (1T MS-CN (SC)), C₃N₄ (196 mg) was dispersed in 10 mL of absolute ethanol by stirring for 30 minutes and then sonicated for 30 minutes. In a separate flask, 1T MoS₂ (ST) (4 mg) was dispersed in 10 mL of absolute ethanol by stirring for 2 h. Then, these two solutions were combined and stirred at room temperature until ethanol was evaporated and allowed to dry at room temperature for another 24 h. Finally, the material was ground by using mortar and pestle.

Synthesis of 2H MoS₂ and 2 wt% 2H MoS₂/C₃N₄ composite by thermal decomposition (impregnation) method (2H MS-CN (TD))

For the synthesis of 2H MoS₂ by a thermal decomposition method (2H MS (TD)),³²⁷ ATTMM (NH₄)₂MoS₄ (200 mg, 0.77 mmol) was dispersed in 20 mL of absolute ethanol by vigorous stirring for 30 minutes and then sonicated for 1 h. This reaction solution was kept in an oil bath at 70 °C under stirring until complete evaporation of ethanol. The obtained black coloured powder was heated at 400 °C for 2 h under an Ar atmosphere (ramp rate 5 K/min.) in the tubular furnace. Finally, the material was ground by using mortar and pestle. In stage 1, ATTMM was decomposed into Mo₂S₅, NH₃, H₂S and S at 160-230 °C (Eq. 2.3). The formation of MoS₂ was occurs at 230-360 °C due to decomposition of Mo₂S₅ (stage 2) (Eq. 2.4).



For the synthesis of 2 wt% 2H MoS₂/C₃N₄ composite (2H MS-CN (TD)), C₃N₄ (196 mg) was dispersed in 10 mL of absolute ethanol by stirring for 30 minutes and then sonicated for 1 h. In a separate flask, ATTMM (NH₄)₂MoS₄ (6.5 mg, 0.025 mmol ; theoretical loading amount of MoS₂ is 2 wt% or 4 mg MoS₂) was dispersed in 5 mL of absolute ethanol by stirring for 30 minutes and then sonicated for 1 h. Then, these two suspensions were combined and kept in an oil bath at 70 °C under stirring until complete evaporation of ethanol. The obtained powder was heated at 400 °C for 2 h under Ar atmosphere (ramp rate 5 K/min.) in the tubular furnace. Finally, the material was ground by using mortar and pestle.

2.2 Catalytic testing

The H₂ evolution measurements were carried out under an argon atmosphere with freshly prepared distilled solvents. Catalytic tests were performed in a double walled and thermostatically controlled reaction vessel connected to an automatic gas burette (Fig. 2.1). Details about the equipment and the experimental set-up are described in ref.³²⁸ Before each experiment, the reactor was several times evacuated and filled with argon to remove air.

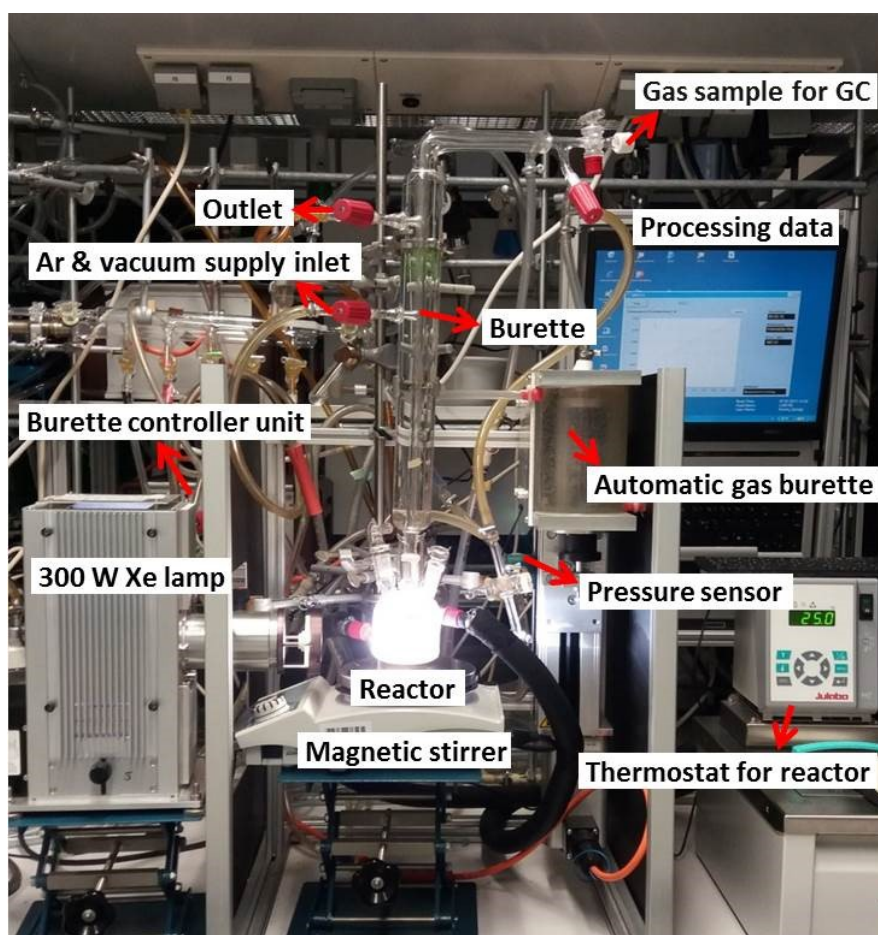


Figure 2.1 Experimental setup for photocatalytic H₂ production.

In a typical experiment, the reactor was charged with 24.5 mg of catalyst and 0.2 mL aqueous H₂PtCl₆, containing 0.5 mg Pt to achieve a nominal Pt loading of 2 wt.% Pt. Then 24.8 mL of a mixture of water and the sacrificial agent (SA) were added to obtain a final ratio of water/SA of 9/1 (v/v), and the temperature was maintained at 25 °C. After stirring for approximately 10 minutes to reach thermal equilibrium the reaction was started by switching the light source on. As light source a 300 W Xe lamp with an output power of 1.5 W was used. For working under visible light irradiation only, a 420 nm cut-off filter was applied. The amounts of evolved gases were continuously determined by the automatic gas burette, equipped with a pressure sensor. After each experiment, a 5 mL gas sample was taken from the burette and quantitatively analyzed by a GC HP 6890N gas chromatograph equipped with a carboxen 1000 column and a thermal conductivity detector (TCD) and Ar as carrier gas. In selected experiments, the reaction was stopped after 3 h or 20 h, respectively, the catalyst was recovered by centrifugation, washed with double distilled water and ethanol and dried overnight at room temperature for further characterization.

The H₂ evolution rate, rH₂ given in μmol g⁻¹ h⁻¹ was calculated according (Eq. 2.5) by assuming ideal gas behavior of H₂ with a molar volume of V_m = 24.48 mol⁻¹.

$$rH_2 = \frac{V_{\text{exp}}}{V_m m t} \quad (2.5)$$

in which, V_{exp} is the gas volume determined experimentally, V_m is the molar volume, t is the reaction time, m is the mass of the sample.

2.3 Catalyst characterization Techniques

2.3.1 X-ray diffraction (XRD)

The crystal structure and crystallinity of semiconductor photocatalysts can highly influence the photocatalytic activity. This technique is used to identify the crystalline phases, crystallite size, chemical composition, strain and defects in the structure. X-ray diffraction is based on the interaction of lattice atoms with a monochromatic beam of incident X-rays causing its diffraction, constructive and destructive interference, into many specific directions. The condition for constructive interference is expressed by Bragg's law (Eq. 2.6).³²⁹ This law relates the wavelength of electromagnetic radiation to the diffraction angle and the lattice spacing in a crystalline sample (Fig. 2.2),

$$n\lambda = 2d \sin \theta \quad (2.6)$$

in which, n is the order of a reflection, λ is the wavelength of X-ray used, d is the distance between parallel lattice planes and θ is the angle between the incident beam and a lattice plane, known as Bragg angle.

Apart from phase identification, XRD pattern can be used to determine mean crystallite size. The mean crystallite size (D) can be estimated from peak broadening by Scherrer's formula (Eq. 2.7),³³⁰

$$D = \frac{K\lambda}{\beta \cos \theta} \quad (2.7)$$

in which, K is the dimensionless shape factor with a value close to unity (0.89), λ is the wavelength of X-ray used (1.5406 Å), β is the full width at half maximum (FWHM) and θ is the diffraction angle. For example, in our studies, the pure AgIn_5S_8 gives several diffraction peaks that can be assigned to the cubic crystal system with face-centered cubic (FCC) lattice (JCPDS card number 26-1477) (Fig. 2.3).

Experimental description:

XRD powder patterns were recorded on a Panalytical X'Pert diffractometer equipped with a Xcelerator detector using automatic divergence slits and $\text{Cu } \alpha_1/\alpha_2$ radiation (40 kV, 40 mA; $\lambda = 0.15406 \text{ nm}, 0.154443 \text{ nm}$). Cu beta-radiation was excluded using a nickel filter foil. The measurements were performed in 0.0167° steps and 25 s of data collecting time per step. The samples were mounted on silicon zero background holders. The obtained intensities were converted

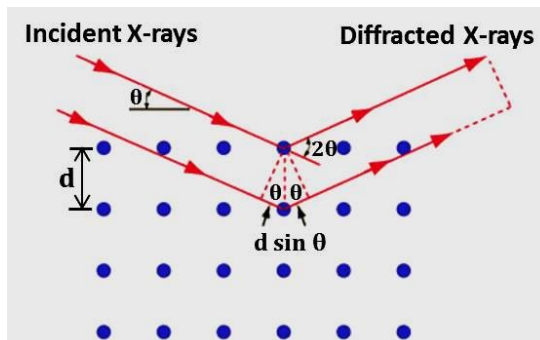


Figure 2.2 Interaction of X-rays with atoms of the crystal.

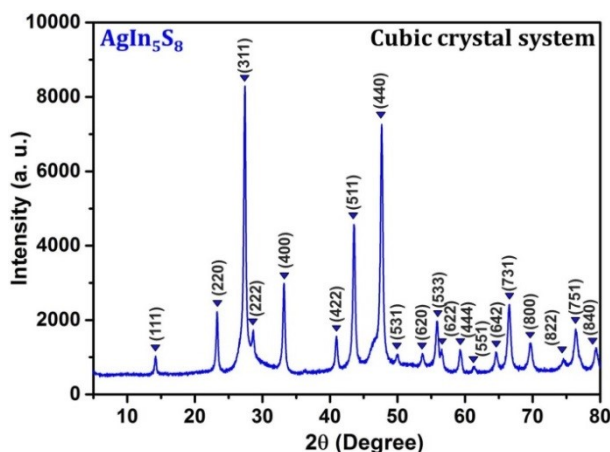


Figure 2.3 XRD powder pattern of pure AgIn_5S_8 .

from automatic to fixed divergence slits (0.25°) for further analysis. Peak positions and profile were fitted with Pseudo-Voigt function using the HighScore Plus software package (Panalytical). Phase identification was done by using the PDF-2 database of the International Center of Diffraction Data (ICDD).

2.3.2 Ultraviolet-visible diffuse reflectance spectroscopy (UV-vis-DRS)

UV-vis diffuse reflectance spectroscopy provides information about band gap of a semiconductor based on the absorptive and light scattering properties of the sample under light excitation from 200-800 nm range. As shown in the Fig. 2.4, incident light reflected symmetrically with respect to the normal line is called specular reflection, while incident light scattered in

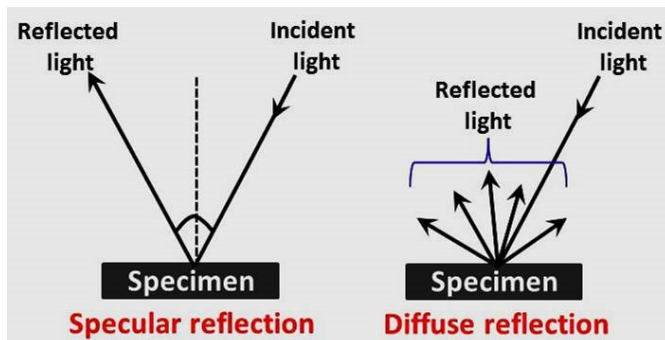


Figure 2.4 The basic forms of reflection.

different directions is called diffuse reflection. The band gap represents the minimum energy difference between the top of the valence band (VB) and bottom of the conduction band (CB). There are two types of electronic transitions in semiconductors, i.e. it can be either direct or indirect, depending on the momentum of electrons in the CB and holes in the VB (Fig. 2.5).³³¹

The minimal-energy state in the conduction band (CB-minimum) and the maximal-energy state in the valence band (VB-maximum) are each characterized by a certain crystal momentum (k -vector) in the Brillouin zone.³³² If the k -vectors are the same, it is called a "direct gap". If they are different, it is called an "indirect gap". The band gap is called "direct" if the momentum of electrons

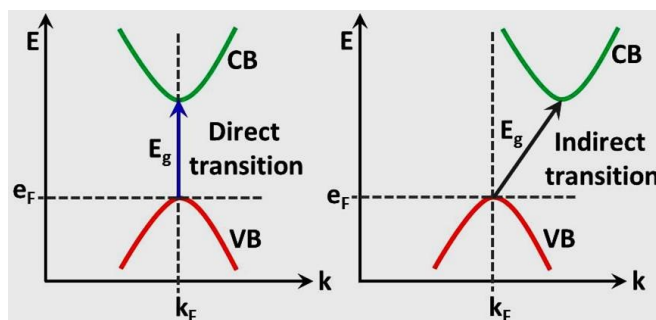


Figure 2.5 Direct and indirect band gap transitions in a semiconductor.

and holes is the same in both the CB and the VB; an electron can directly emit a photon. In an "indirect" gap, a photon cannot be emitted because the electron must pass through an intermediate state and transfer momentum to the crystal lattice. In principle, band gap determination by using UV-vis DRS depends on the excitation of the electrons from the valence band to the conduction band which is observed by an increase in the absorbance at a given wavelength. Since UV-vis spectra of powder catalysts are recorded in diffuse reflectance mode, the diffuse reflectance (R), is directly obtained from the spectrometer. Then the reflectance data were converted to the $F(R)$ function according to the Kubelka-Munk (Eq. 2.8).

$$F(R) = \frac{(1-R)^2}{2R} = \frac{K}{S} \quad (2.8)$$

in which, $F(R)$ function is equivalent to the absorption co-efficient (α), K is the absorption coefficient and S is the scattering coefficient (Schuster-Kubelka-Munk, SKM function). The optical band gap of the semiconductor can be calculated by using Tauc equation (Eq. 2.9).

$$(\alpha h\nu) = A (h\nu - E_g)^n \quad (2.9)$$

in which, α is the absorption co-efficient, h is the Planck constant, ν is the light frequency, A is the proportionality constant, E_g is the band gap of a semiconductor, n depends on the type of optical transition of the semiconductor ($n = 1/2$ for direct transition and $n = 2$ for indirect transition). Thus, the band gap (E_g) of the semiconductor can be estimated from the plot of $(\alpha h\nu)^n$ versus photon energy ($h\nu$). For example, in our studies, C_3N_4 and $AgIn_5S_8$, both are direct band gap semiconductors.^{322, 333} The pure CN shows absorption wavelength from UV to visible

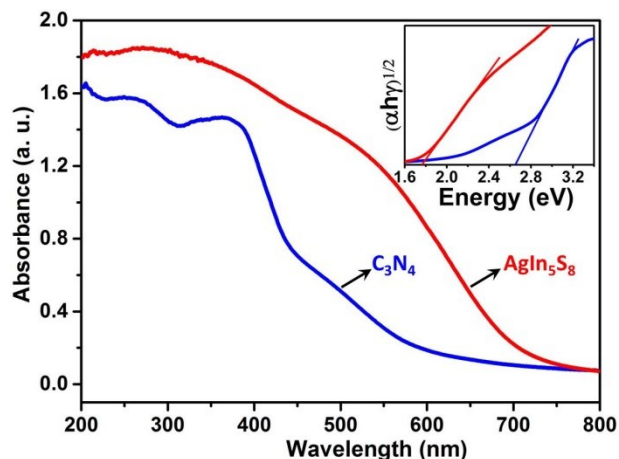


Figure 2.6 UV-vis DRS spectra of C_3N_4 and $AgIn_5S_8$ and band gap estimation from Tauc plot (in-set)

region up to 600 nm and pure $AgIn_5S_8$ shows absorption edge at 720 nm, exhibiting the broad absorption region of visible light (Fig. 2.6). The band gap of C_3N_4 and $AgIn_5S_8$ were estimated to be 2.65eV and 1.75 eV respectively (Fig. 2.6, in-set).

Experimental description:

Diffuse reflectance UV-vis spectra were obtained by a Cary5000 spectrometer (Varian) equipped with a diffuse reflectance accessory (Praying Mantis™, Harrick) by using $BaSO_4$ as white standard reference material. DRS UV-vis spectra were also obtained by using AvaSpec 2048 fiber optical spectrometer (Avantes BV, Apeldoorn, Netherlands) equipped with an AvaLight-DHS light source and a FCR-19UV200-2-ME reflection probe. Each spectrum was acquired taking 24 to 27 accumulations with integration times between 18 and 22 ms.

2.3.3 Attenuated total reflectance-infrared (ATR-IR) spectroscopy

ATR-IR is an effective method for determining the presence of different functional groups in the material. It is a technique based on vibrations of the atoms within a molecule. The selection rule for a vibrational mode of a molecule to be IR active is that there is a change of the electric dipole moment of the molecule upon absorption of light. The absorption of infrared light due to the excitation from the ground vibrational energy level to a higher energy level provides information concerning molecular structure and molecular interactions. It is a powerful tool for identifying types of chemical bonds in a molecule by producing an infrared absorption spectrum that is like a molecular "fingerprint". Due to the existence of the wide absorption spectra database in the mid-infrared region ($4000-400\text{ cm}^{-1}$), infrared spectroscopy is considered as a universal technique since many molecules have strong absorbance in this region. As the resonance frequency of a distinct vibration depends on the reduced mass of the atoms of the vibrating group, μ , and on the strength of the bonds (expressed by the force constant, f) according to eq. 2.10, one observes IR bands at the highest frequencies for light atoms and for groups with high bond energies.

$$\nu = \frac{1}{2\pi} \sqrt{\frac{f}{\mu}} \quad (2.10)$$

The thin-film solid catalyst is in strong contact to the ATR crystal. Passing through the crystal, the incoming IR beam penetrates the catalyst on top of it, so that the attenuated radiation is finally reflected (Fig. 2.7). The intensity of an ATR-IR signal strongly depends on the number of reflections in the crystal as well as on the depth of penetration, which itself increases with higher wavelengths. Measurements were carried out in the spectral range 650-4000 cm⁻¹. Each spectrum was an

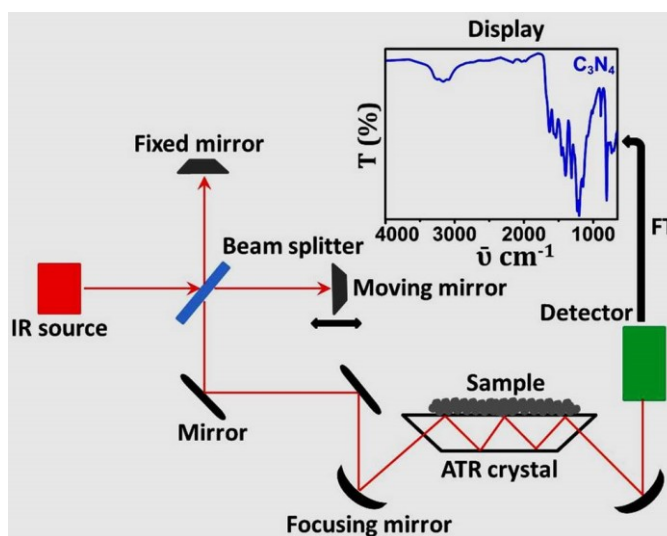


Figure 2.7 Schematic diagram of ATR-IR spectrometer.

average of 64 scans to increase the signal to noise ratio. For example, in our studies, the C₃N₄ shows a wide variety of peaks that correspond to N-H, C-N, and C=N stretching vibrations, present in the triazine unit (Fig. 2.7, in display).⁶⁴

Experimental description:

IR spectra in attenuated total reflectance mode (ATR-IR) were recorded on a Nicolet iS10 instrument.

2.3.4 Scanning transmission electron microscopy (STEM)

STEM provides useful information about morphology, elemental composition, shape and size of the particles. STEM imaging is based on the elastic scattering of electrons in a high energy electron beam (100–300 kV) upon interacting with the atoms of a solid thin sample (< 100 nm), whereby much higher resolutions (atomic scale) are

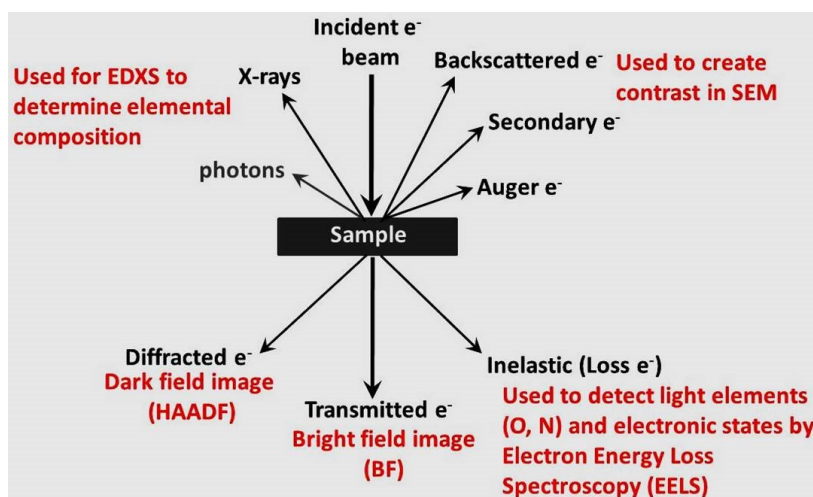


Figure 2.8 Schematic view of electron beam and sample interaction.

obtained due to the small de Broglie wavelength of the electron. There are different modes to detect image e.g. bright field (BF), high angle annular dark field (HAADF), electron energy loss spectroscopy (EELS), energy dispersive X-ray spectroscopy (EDXS).

Fig. 2.8 shows processes initiated by irradiating a sample with an electron beam. A part of electrons passes through the sample directly. A two dimensional image (bright field, BF) is obtained from the transmitted electrons, in which areas of strong scatterers appear dark while those of light scatterers appear

bright since more electrons can pass through. A High Angle Annular Dark Field (HAADF) detector is especially useful to detect electrons scattered from heavy elements. HAADF detects electrons scattered from heavy atoms with a high scattering angle, and shows lattice fringes. Electrons can also be backscattered, especially from heavy elements such as Pt. These can also be used to create contrast, especially in scanning electron microscopy (SEM). Auger electrons and X-rays are emitted as a consequence of relaxation when electrons from higher shells fill core holes which arise when the electron beam ejects core electrons from the sample. This radiation is characteristic for the element and can be used to obtain information on the composition of a sample. For example, in our studies, the Pt NPs are deposited on surface of AgIn_5S_8 and C_3N_4 (Fig. 2.9a). As can be seen in HAADF image, the Pt NPs are clearly visible due electrons scattered with high scattering angle.

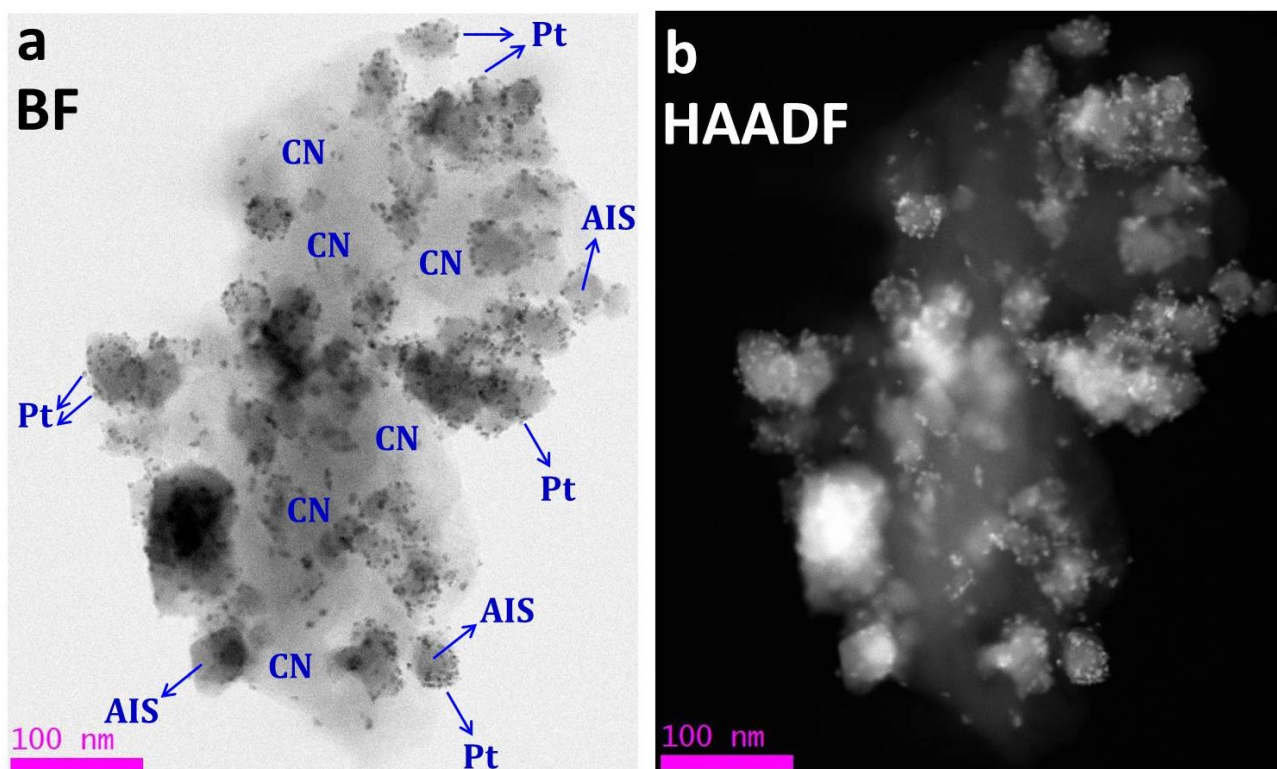


Figure 2.9 (a) Bright field and (b) High angle annular dark field images of image of 2 wt% Pt/10 wt% $\text{AgIn}_5\text{S}_8/\text{C}_3\text{N}_4$ (recovered catalyst after 3 h photocatalytic reaction).

Experimental description:

STEM micrographs were obtained at 200 kV by a probe aberration corrected JEM-ARM200F transmission electron microscope (Jeol Ltd., Akishima, Japan). The microscope is equipped with a JED-2300 (JEOL) energy dispersive X-ray spectrometer (EDXS) for chemical analysis. The catalyst powder was dry deposited on a Cu grid (mesh 300) covered by a holey carbon film and transferred into the microscope.

2.3.5 X-ray photoelectron spectroscopy (XPS)

X-ray photoelectron spectroscopy (XPS) is a surface-sensitive (usually in 1-10 nm depth) quantitative spectroscopic technique that measures the elemental composition as well as chemical state of the elements in a solid catalyst. It is based on the principle of photoelectric effect. XPS spectra are obtained by irradiating a material with a beam of aluminium or magnesium $K\alpha$ X-rays while simultaneously measuring the kinetic energy (E_{kin}) and number of electrons that escape from the top 1 to 10 nm of the material being analyzed (Fig. 2.10). The electrons ejected from the sample are collected by a hemispherical electron energy analyzer which measures the kinetic energy of the ejected electrons. The kinetic energy measured can then be used to determine the binding energy (BE) of the electron from the following Eq. 2.11,

$$E_{BE} = h\nu - E_{kin} - \phi \quad (2.11)$$

in which, h is the Planck's constant, ν is the frequency of incident X-ray and ϕ is the work function of the spectrometer. Each ejected electron from an element has a characteristic binding energy and the position of this binding energy is used to identify the element and core level of the electron that can be found by consulting binding energy tables. The peak intensities can be used to quantitatively determine the elemental composition and the peak positions can be used to determine oxidation states for the elements. In general, binding energies

increases with increasing oxidation state typically shifting by about 0-3 eV. For example, in our studies, the survey spectrum indicates that the presence of C and N elements in C_3N_4 sample (Fig. 2.11). The elemental N 1s spectrum of pure CN could be deconvoluted into three different peaks corresponding to the terminal amino groups (C-N-H), tertiary nitrogen groups (N-(C)₃) and sp^2 -hybridized nitrogen in triazine rings (C-N=C) (Fig. 2.11, inset).²²⁵

Experimental description:

The XPS (X-ray Photoelectron Spectroscopy) measurements were performed on an ESCALAB 220iXL (ThermoFisher Scientific, Waltham, MA, USA) with monochromated Al $K\alpha$ radiation ($E = 1486.6$ eV).

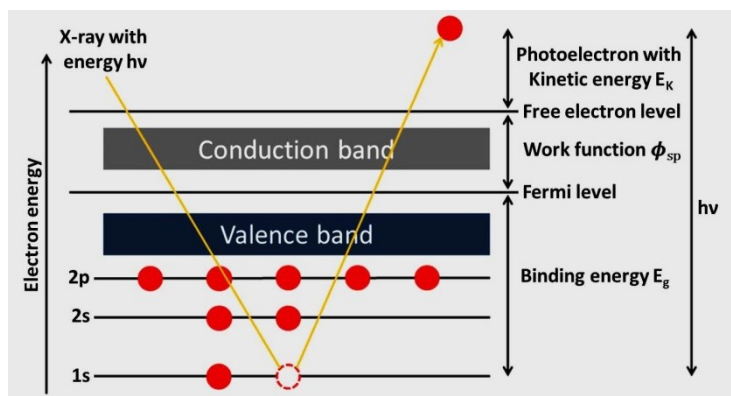


Figure 2.10 Schematic diagram showing the basic principle of XPS.

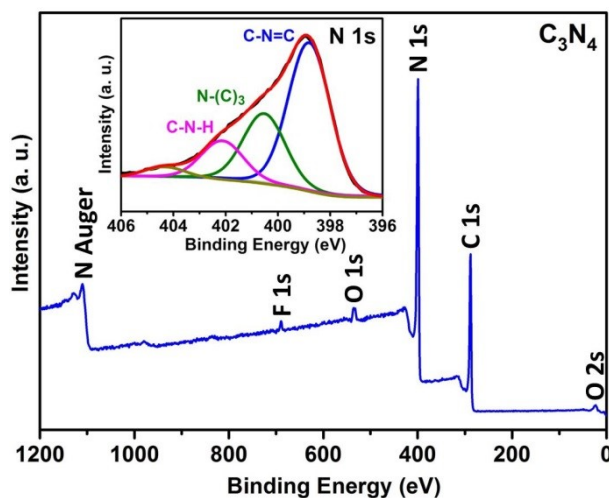


Figure 2.11 XPS survey spectra of C_3N_4 and N 1s elemental spectra (inset).

Samples are prepared on a stainless steel holder with conductive double sided adhesive carbon tape. The electron binding energies were obtained with charge compensation using a flood electron source and referenced to the C1s peak of C-C and C-H bonds at 284.8 eV. For quantitative analysis the peaks were deconvoluted with Gaussian-Lorentzian curves, the peak areas were divided by the transmission function of the spectrometer and a sensitivity factor obtained from the element specific Scofield factor.³³⁴

2.3.6 Brunauer-Emmett-Teller (BET) surface area and pore size distribution analysis

As heterogeneous photocatalytic reactions occur at the catalyst surface, the number of photoactive sites usually depends on the surface area of the catalyst. Its dimension is critically affected by the particle size, morphology, surface texturing and porosity. The specific surface area of a powder catalyst is determined by physical adsorption of a gas on the surface of the solid and by calculating the amount of adsorbate gas corresponding to a monomolecular layer on the surface. Physical adsorption results from

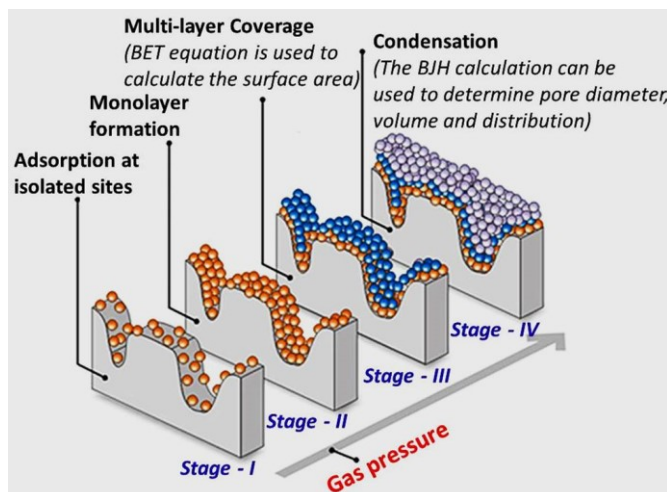


Figure 2.12 The basic principle of gas adsorption on a solid surface

relatively weak forces (van der Waals forces) between the adsorbate gas molecules and the adsorbent surface area of the powder catalyst. Isolated sites on the sample surface begin to adsorb gas molecules at low pressure. As gas pressure increases, coverage of adsorbed molecules increases to form a monolayer (one molecule thick). A further increase in the gas pressure will cause complete coverage of the sample and fill all the pores (Fig. 2.12).³³⁹ The BJH calculation can be used to determine pore diameter, volume and distribution. The determination is usually carried out at the temperature of liquid nitrogen. The amount of gas adsorbed on the surface and pores is monitored with the function of relative pressure to obtain gas adsorption isotherms.

There are generally accepted to be six adsorption isotherms (Fig. 2.13). Each of these types is observed in practice but by far the most common are types I, II and IV. Type I is the characteristic examples of microporous materials while Type IV is an example of the mesoporous material. In addition to BET surface area, N₂-physisorption experiments provide the information about the pore properties as well. Generally, pores are classified in to three categories on the basis of pore width, i.e.

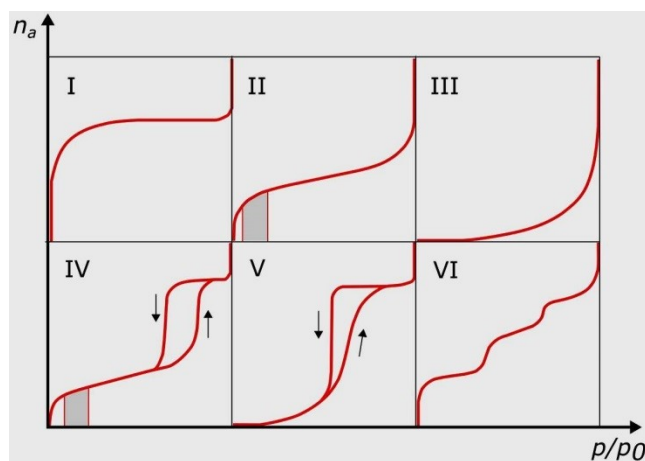


Figure 2.13 IUPAC classifications of adsorption isotherms (Type I - VI)

macropores (> 50 nm), mesopores (2-50 nm) and micropores (< 2 nm).

Based on a simplified model of physisorption and the adsorption isotherm, the Brunauer-Emmett-Teller (BET) method is widely used for evaluating the surface area of catalysts. Assuming that (i) gas molecules can be physically adsorbed on a solid in layers infinitely, (ii) gas molecules only interact with adjacent layers and (iii) Langmuir theory can be applied to each layer, which is a theory for monolayer molecular adsorption. The data can be treated according to the Brunauer-Emmett-Teller (BET) adsorption isotherm equation (Eq. 2.12).

$$\frac{1}{V_a \left(\frac{P_0}{P} - 1 \right)} = \frac{C-1}{V_m C} \times \frac{P}{P_0} + \frac{1}{V_m C} \quad (2.12)$$

in which, P is the partial vapour pressure of adsorbate gas in equilibrium with the surface at 77.4 K (boiling point of liquid nitrogen), P_0 is saturation pressure of adsorbate gas, V_a is volume of gas adsorbed at standard temperature and pressure (STP) (273.15 K and atmospheric pressure (1.013×10^5 Pa)), V_m is volume of gas adsorbed at STP to produce an apparent monolayer on the sample surface, C is dimensionless constant that is related to the enthalpy of adsorption of the adsorbate gas on the powder sample. The specific surface area can be calculated by the following equation (Eq. 2.13).

$$S_{\text{BET}} = \frac{V_m N_A}{22,414 W A_m} \quad (2.13)$$

in which, v_m is volume of gas adsorbed (mL) at STP, N_A is Avogadro number, W is weight of the catalyst (g) and A_m is mean cross sectional area occupied by adsorbate molecule (e.g. for N_2 , it is 16.2 \AA^2). For example, in our studies, the pure CN exhibited type IV isotherm, according to the IUPAC classification, indicating the existence of mesopores (2-50 nm) (Fig. 2.14). The pore size distributions of C_3N_4 were estimated by using the Barrett-Joyner-Halenda (BJH) method from the desorption branches, as shown in Fig. 2.14, inset.

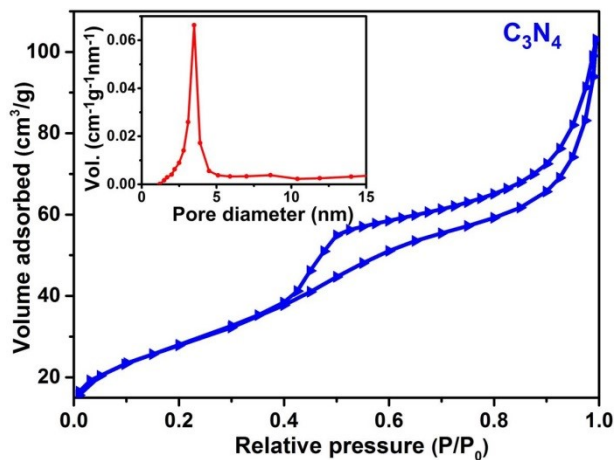


Figure 2.14 N_2 adsorption-desorption isotherms of pure C_3N_4 and pore size distributions estimated by the BJH (inset).

Experimental description:

About 200 mg of the powder sample is taken in a glass tube. Before the measurement, tube was evacuated for 2 h at $150 \text{ }^\circ\text{C}$ to remove physisorbed water. BET surface area, pore volume and pore size distribution of the catalysts were determined by standard nitrogen adsorption at $-196 \text{ }^\circ\text{C}$ (ASAP 2020, Micromeritics GmbH, Aachen, Germany).

2.3.7 Inductively coupled plasma-optical emission spectroscopy (ICP-OES)

ICP-OES is an analytical technique in which the composition of elements in (mostly water-dissolved) samples can be determined using plasma. For example, in our studies, ICP-OES was applied to determine Pt, Ag, In and S in Pt/AgIn₅S₈-C₃N₄ composite catalysts and Pt, Mo and S in Pt/MoS₂-C₃N₄ composite catalysts. Plasma is a gas, in this case argon, which contains a significant number of argon ions. Elements, in the form of atoms, are introduced into the plasma. A proportion of these atoms become ionized within the plasma. When an atom or ion is excited within the plasma, its electrons jump from a lower to higher energy level (Fig. 2.15). Upon relaxation of these electrons to their initial ground state, energy is emitted in the form of photons. The emitted photons possess wavelengths that are characteristic of their respective elements. The intensity of the signal is directly proportional to the concentration of the element present in the sample.

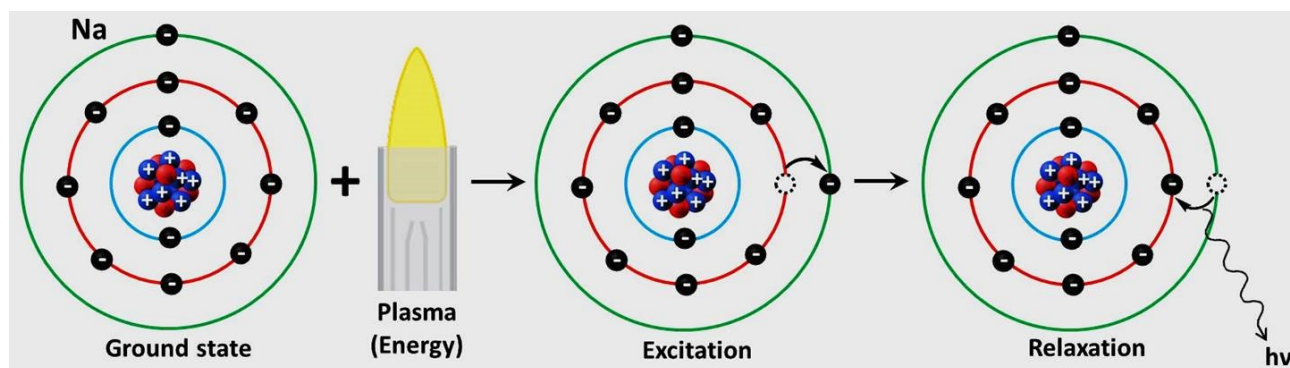


Figure 2.15 Excitation of an atom by plasma.

Experimental description:

A Varian 715-ES ICP-emission spectrometer was used for analysis. In a typical procedure, 10 mg sample was dissolved in 8 mL aqua regia and 2 mL hydrofluoric acid by treatment with the microwave-assisted sample preparation system “MULTI WAVE Pro” (Anton Paar/Perkin-Elmer) at 200 °C and 60 bar. The digested solution was filled up to 100 mL with deionized water and analyzed. The ICP Expert software was used for analysis.

2.3.8 Carbon, hydrogen, nitrogen and sulfur (CHNS) elemental analysis

CHNS elemental analysis used for rapid determination of carbon, hydrogen, nitrogen and sulfur in organic matrices and other types of materials. For example, in our studies, elemental analysis (CHNS) was applied to determine C and N ratio in the C₃N₄ and MoS₂/C₃N₄ photocatalysts. For CHNS analysis, the solid sample (5-10 mg) mixed with an oxidizer such as vanadium

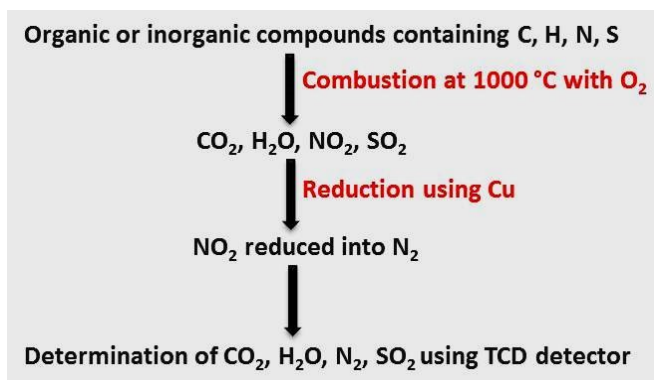


Figure 2.16 CHNS combustion process.

pentoxide (V₂O₅) in a tin (Sn) capsule, which is then combusted in a reactor at 1000 °C. The sample and container melt, and the tin promotes a violent reaction (flash combustion) in an enriched oxygen

atmosphere. The combustion products NO₂, CO₂, H₂O, and SO₂ are carried by a constant flow of carrier gas (helium) that passes through a glass column packed with an oxidation catalyst of tungsten trioxide (WO₃) and a copper reducer, both kept at 1000 °C. At this temperature, Cu removes the excess oxygen and reduces nitrogen oxides into N₂. The N₂, CO₂, and SO₂ are then transported by the helium and separated by a packed column and quantified with a TCD (set at 290 °C) (Fig. 2.16). The chromatographic responses are calibrated against pre-analyzed standards, and the CHNS elemental contents are reported in weight percent (wt. %).

Experimental description:

A CHNS multianalyzer TruSpec (Leco) was used for the quantitative analysis of C, H, N and S. The catalyst (10 mg) was mixed with V₂O₅ as oxidation reagent and packed into a tin container, which is easily oxidizable. The reactor is heated to 1000 °C and the combustion products were quantified by TCD.

2.3.9 In situ electron paramagnetic resonance (EPR) spectroscopy

In situ EPR is a versatile technique to monitor separation and transfer of photogenerated electrons in semiconductors based on oxides³³⁵ or carbon nitrides⁷⁶, since electrons excited to the conduction band can be trapped at oxygen vacancies³³⁵ and carbon defects.³³⁶ In the present thesis, this powerful technique was used to monitor the efficiency of charge separation and transfer during UV-vis light irradiation. An electron has a spin quantum number, $s = 1/2$, which has magnetic components $m_s = 1/2$ and $m_s = -1/2$. In the absence of a magnetic field, the energy of the two m_s states are equivalent. However, a strong external magnetic field generates a difference between the energy levels of the electron spins, $m_s = +1/2$ and $m_s = -1/2$, which results in resonance absorption of an applied microwave energy (Fig. 2.17). The energy difference between the m_s state is dependent on the strength of the magnetic field (Eq. 2.14). This is called the Zeeman effect.

$$\Delta E = h\nu = g_e\mu_B B_0 \tag{2.14}$$

in which, ΔE is the energy difference between the spin levels, g_e is the g-factor (for free electron = 2.0023), μ_B is the Bohr magneton ($9.274 \cdot 10^{-24} \text{ J T}^{-1}$), B_0 is the strength of the external magnetic field (gauss or Testla), h is the Planck's constant ($6.626 \cdot 10^{-34} \text{ J.s}$), ν is the microwave frequency (GHz or MHz). From this relationship, there are two important factors to note, i.e. the two spin states have the same energy when there is no applied magnetic field and the energy difference between the two spin states increases linearly with increasing magnetic field strength.

Usually, all the spectrometers work by changing the magnetic field while holding frequency constant. EPR spectra can be recorded in different frequency regions, the most important being L-band (1-2 GHz), S-band (2-4 GHz), X-band

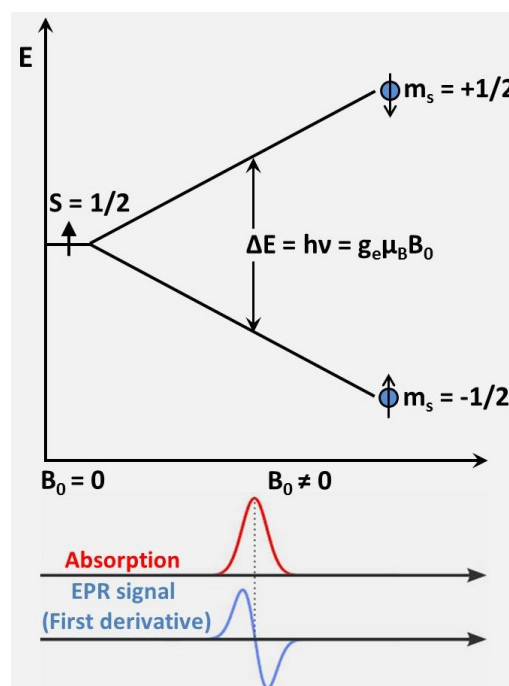


Figure 2.17 Electron Zeeman interaction for a spin $S = 1/2$ system in the presence of an external magnetic field.

(8-10 GHz), Q-band (~35 GHz) and W-band (~90 GHz). In this work, X-band frequency EPR spectrometer was used. There are two methods to record EPR spectra. The first one is called the continuous wave (cw), in which the applied frequency is held constant. In this case, the magnetic field is varied until the resonance condition is fulfilled and the microwave energy matches the energy difference for the allowed spin transitions.

For example, in our studies, pure C_3N_4 , even in the dark (without light irradiation) exhibits a narrow isotropic singlet with Lorentzian line shape at a g -value of 2.0042 which ascribed to the unpaired electrons in the sp^2 -carbon in a typical Tri-s-triazine unit (Fig. 2.18a). This confirms the presence of paramagnetic species in C_3N_4 . Moreover, the observed g -value indicates that this strong signal arises from surface trapped CB e^- that preferentially has carbon character. Moreover, the EPR signal intensity is increased during UV-vis light irradiation due to electron-hole separation and excitation of electrons from VB to CB of C_3N_4 . However, after switched-off light, the EPR signal intensity is decreased due to the recombination of photoexcited electrons with holes (Fig. 2.18b).

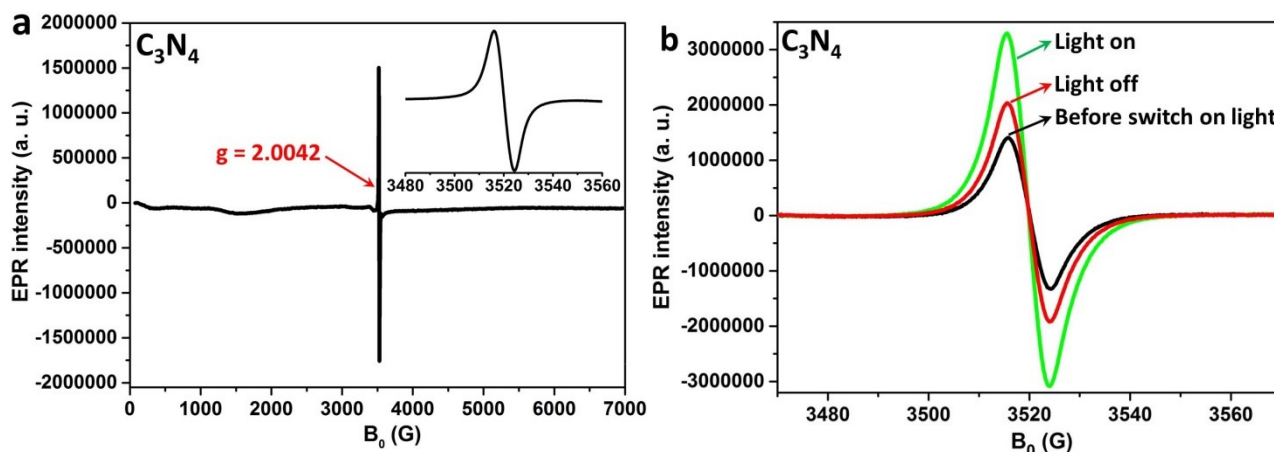


Figure 2.18 (a) EPR signal of pure C_3N_4 at room temperature without light irradiation (inset: magnification from 3480 to 3560 G). (b) EPR $CB-e^-$ signal of pure C_3N_4 during UV-vis light irradiation and after light switched-off.

Experimental description:

In situ-EPR measurements in X-band (microwave frequency ≈ 9.8 GHz) were performed at 300 K by an EMX CW-micro spectrometer (Bruker Biospin GmbH, Rheinstetten, Germany) equipped with an ER 4119HS-WI high-sensitivity optical resonator with a grid in the front side (Bruker Biospin GmbH, Rheinstetten, Germany). The samples were illuminated by a 300 W Xe lamp (LOT-QuantumDesign GmbH, Darmstadt, Germany). All the samples were measured under the same conditions (microwave power: 6.99 mW, receiver gain: 1×10^4 , modulation frequency: 100 kHz, modulation amplitude: 3 G, Sweep time: 122.8 s). g values have been calculated from the resonance field B_0 and the resonance frequency ν using the resonance condition $h\nu = g\beta B_0$. The calibration of the g values was performed using DPPH (2,2-diphenyl-1-picrylhydrazyl) ($g = 2.0036 \pm 0.00004$).

2.3.10 Photoluminescence (PL) spectroscopy

Photoluminescence (PL) analysis is commonly employed to investigate the separation efficiency of photogenerated charge carriers. The PL emission peak is originating from recombination of photogenerated electrons and holes so that the PL intensity can reflect the separation efficiency and lifetime of charge carriers.³³⁷

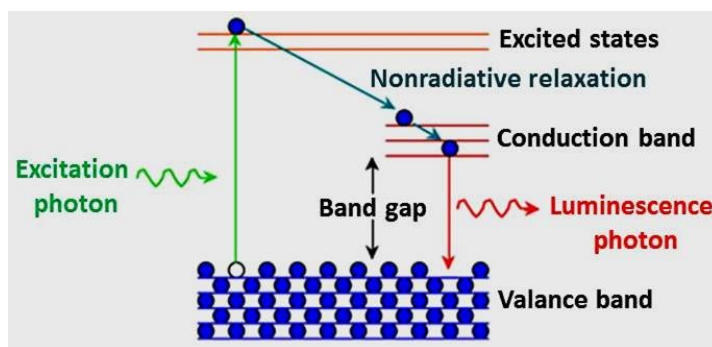


Figure 2.19 schematic diagram showing the basic principle of photoluminescence spectroscopy

For instance, a photocatalyst which exhibited lower PL emission intensity means a higher recombination rate of electron-hole pairs or shorter lifetime.

Photoluminescence is known as the spontaneous radiative emission of a photon due to an electron that is photoexcited to a higher energy state (i.e. conduction band) by absorbing appropriate energy and then makes a transition to the lower energy state (i.e. valence band). The energy that is applied as external light has to be greater than or equal than its bandgap energy of the semiconductor, $h\nu \geq E_g$ (Fig. 2.19). For example, in our studies, pure CN exhibits a strong emission at 460 nm, which corresponds to the band gap charge carrier recombination (Fig. 2.20b). But pure sample doesn't show PL emission, despite the fact that it absorbs UV-vis light able to excite electrons from its valence band to the conduction band. This suggests that electron-hole recombination in the pure AgInS₂ samples might be too fast to emit PL radiation (Fig. 2.20b).

PL spectroscopy is a complimentary technique to UV-vis DRS, it also gives information on the electronic structure from light excitation. PL spectrum is quite different from absorption spectrum in the sense that absorption spectrum measures transitions from the ground state to excited state, while photoluminescence deals with transitions from the excited state to the ground state. The emission of photons from this phenomenon can be measured as fluorescence. This process is relevant to the study of photocatalyst systems since fluorescence occurs when electrons in the conduction band recombine with holes in the valence band. This characterization technique can thus give direct information on electron transfer kinetics during the photocatalytic process. The PL intensity can be used to compare recombination rates for different photocatalyst systems. A laser turned on and passes through monochromator and falls on the sample. An excitation wavelength is selected by monochromator, and luminescence is observed through an emission monochromator, usually positioned at 90° to the incident light to minimize the intensity of scattered light reaching the detector. If the excitation wavelength is fixed and the emitted radiation is scanned, an emission spectrum is produced (Fig. 2.20a).

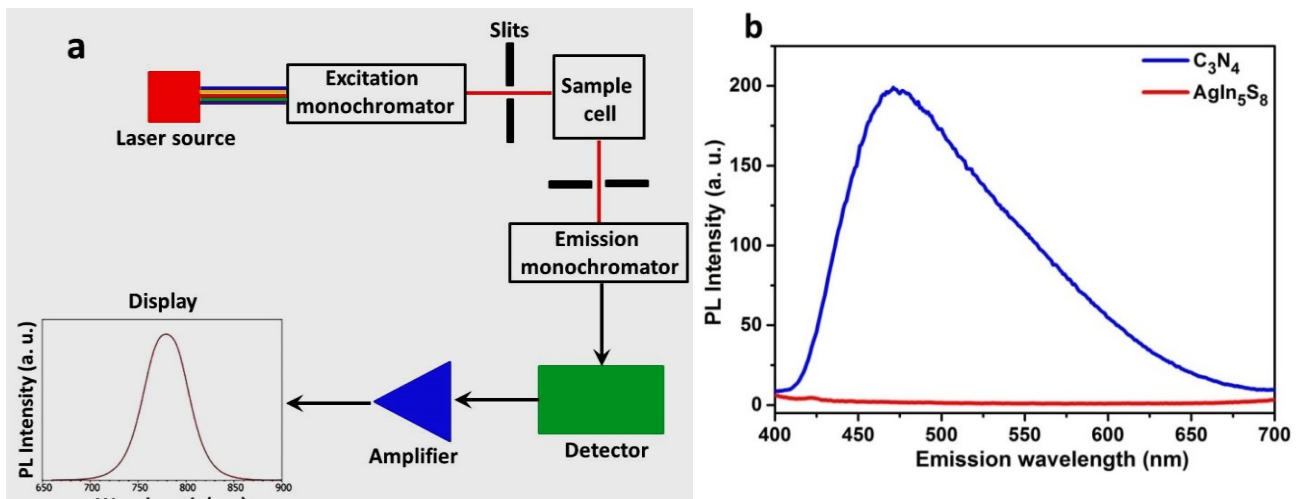


Figure 2.20 (a) Schematic diagram of PL spectrometer. (b) PL spectra of C_3N_4 and $AgIn_5S_8$

Experimental description:

Photoluminescence (PL) spectra were obtained by a Cary Eclipse Fluorescence spectrophotometer (Agilent Technologies Inc., Mulgrave, Australia) with an excitation wavelength of 370 nm.

3 Relations between structure, activity and stability in AgIn₅S₈/C₃N₄ composite photocatalysts used for photocatalytic H₂ production

This work has been published in the journal *Catalysts* (MDPI publishing company). Ramesh P. Sivasankaran, Nils Rockstroh, Dirk Hollmann, Carsten R. Kreyenschulte, Giovanni Agostini, Henrik Lund, Amitava Acharjya, Jabor Rabeah, Ursula Bentrup, Henrik Junge, Arne Thomas and Angelika Brückner*, *Catalysts*, 2018, 8, 52.

Ternary metal sulfides such as I-III-VI (I = Cu, Ag; III = Al, In, Ga; VI = S, Se, Te) with a general formula of I-III-VI₂ or I-III₅-VI₈ have been studied in the field of photocatalysis due to their narrow bandgap energy between 0.8 and 2.0 eV and high absorption co-efficient.^{39, 338, 339} In particular, AgIn₅S₈ is considered to be a promising photocatalyst for visible light driven H₂ production because of its direct bandgap of 1.70–1.80 eV.^{322, 340, 341} Hence, this work has been focused on the photocatalytic behavior of various AgIn₅S₈ (AIS) composites prepared by integrating with mesoporous CN in the presence of a Pt co-catalyst during photocatalytic H₂ evolution from water/SA mixtures by varying the radiation wavelength and the pH of the reaction solution. AIS has been chosen as co-component because it forms a single phase with a direct bandgap of 1.70–1.80 eV and exhibits excellent photocatalytic H₂ production under visible light irradiation. On the other hand, Na₂S/Na₂SO₃ as sacrificial agent^{322,342} is less useful since it produces sulfate as a byproduct via oxidation. A comprehensive catalyst characterization including the *in situ* electron paramagnetic resonance (EPR) spectroscopy was carried out to derive structure-reactivity relationships of the developed composites for photocatalytic H₂ production. Much attention has been paid to understand the role of the SA and AIS with respect to activity, stability and nature of the formed Pt co-catalyst in the photocatalytic H₂ production reaction.

3.1 Catalytic activity

Primarily, the effect of basic (triethanolamine, TEOA) and acidic (oxalic acid, OA) sacrificial reagents in the photocatalytic H₂ production over CN catalyst under both UV-vis and visible light irradiation (Fig. 3.1a and c) was investigated. Fig. 3.1 shows the photocatalytic H₂ production activity versus time of pure CN, pure AIS and AIS/CN composites under both UV-vis and visible light irradiation in the presence of triethanolamine (TEOA) as sacrificial agent. The in-situ photoreduction of H₂PtCl₆ was carried out to deposit Pt nanoparticles (NPs) on the surface of all catalysts.

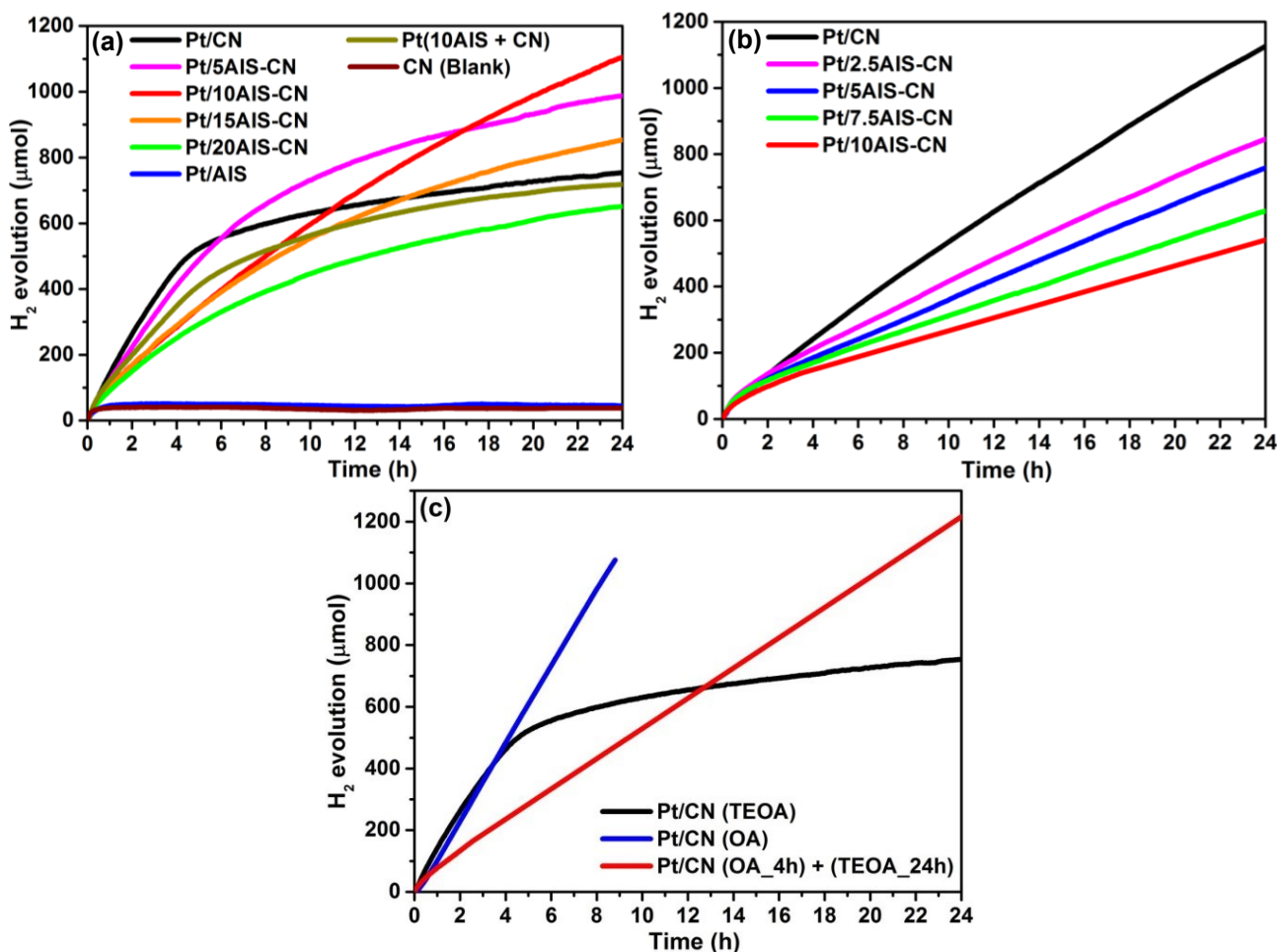


Figure 3.1 H₂ evolution as a function of time for monophasic CN and AIS as well as for xAIS-CN composites with x wt.% of AIS under UV-vis (a) and visible irradiation with $\lambda > 420$ nm (b); (c) Comparison of Pt/CN under UV-vis light with TEOA, with OA and with TEOA again after removal from OA-containing reaction mixture after 4 h. CN: mesoporous C₃N₄; AIS: AgIn₅S₈; TEOA: triethanolamine.

As shown in Fig. 3.1a, the Pt/CN catalyst exhibited a better photocatalytic activity up to 4 hours reaction time and then the H₂ production was drastically decreased. In contrast, the deposition of 5-15 wt.% AIS on CN led to decreased initial H₂ evolution rates, but prevents the catalyst deactivation (Fig. 3.1a). With the addition of 5 wt.% AIS, the deactivation of Pt/CN catalyst is partly inhibited, while the addition of 20 wt.% AIS led to a significant decline in the activity of the Pt/CN catalyst over the whole range of time. Among them, 10 wt.% AIS appeared to be the optimum amount to achieve promising results in terms of H₂ production and catalyst's stability. The activity results obtained with the current catalysts were compared

with that of other types of g-C₃N₄ based catalysts in Table A1 and A2. Though lower initial H₂ evolution rate was found for this sample compared with Pt/CN catalyst, despite a much higher total Pt content (vide infra), the Pt/10AIS-CN catalyst showed a negligible deactivation within 24 h. Interestingly, the Pt/AIS catalyst without CN as well as blank CN without Pt were not active at all for photocatalytic H₂ production (Fig. 3.1a). In case of a physical mixture of AIS (10 wt.%) and CN, a very similar deactivation behavior was noticed as found over the Pt/CN catalyst (Fig. 3.1a). Moreover, the H₂ production rates were lower for all samples, when a 420 nm cut-off filter was used under similar reaction conditions. However, the deactivation of the Pt/xAIS-CN catalysts did not occur within 24 h reaction time (Fig. 3.1b) and was far slower for Pt/CN even though suppression was not complete in the latter case. This clearly indicates that the stability of Pt/CN catalyst is a key concern in case of long-term reaction even under visible light, which has been surprisingly ignored in the past.

Table 3.1 Surface composition derived by XPS.

Sample	Surface Content (at.%)							Total Pt (wt.%) (ICP-OES)
	C	N	O	Ag	In	S	Pt	
CN	44.8	52.3	2.9	-	-	-	-	-
AIS	22.3		9.7	4.7	27.5	35.9	-	-
10AIS-CN	42.8	34.5	7.0	1.2	6.1	8.3	-	-
Pt/CN (3 h)	45.5	50.9	3.5	-	-	-	0.06	0.27
Pt/CN (20 h)	46.6	49.4	3.9	-	-	-	0.05	0.43
Pt/CN_OA (4 h) ¹	46.9	48.5	3.7	-	-	-	0.85	1.69
Pt/CN_OA_TEOA (24 h) ²	44.8	51.3	3.6	-	-	-	0.2	n. d.
Pt/10AIS-CN (3 h)	47.9	35.9	6.6	0.6	2.4	4.1	2.5	1.86
Pt/10AIS-CN (20 h)	45.3	40.6	7.2	0.5	2.6	2.4	1.4	1.87

¹ SA = oxalic acid, ² Pt/CN_OA (4 h) recovered and exposed to UV-vis light for 24 h with TEOA as SA.

In order to estimate the impact of the pH of the reaction solution, which is basic in the presence of TEOA (pH = 10.6), on the stability of the photocatalysts, an analogous experiment was performed with Pt/CN using oxalic acid (OA) as sacrificial agent at pH = 0.67 (Fig. 3.1c, blue line). In this case, total H₂ production is much higher, which was attributed to higher proton concentration. It must also be mentioned that H₂ is not only produced from water, but also from OA providing CO₂ as well. However, the total Pt content as well as the surface Pt concentration of the Pt/CN catalyst is much higher in OA than in TEOA, which could also be the reason for its higher catalytic activity in the presence of OA (Table 3.1). The direct reduction of [PtCl₆]²⁻ to metallic Pt is possible at low pH and the intermediate hydrolysis of the Pt precursor complex, as in basic medium, could be avoided.³⁴³ In the presence of OA, no deactivation of Pt/CN occurs. To further confirm the catalytic deactivation of Pt/CN in basic medium (TEOA), the predeposited Pt/CN catalyst, recovered from the photocatalytic reactor after 4 hours reaction time in the presence of OA under UV-vis irradiation, was again evaluated for photocatalytic H₂ production in TEOA. This Pt/CN (recovered from OA) catalyst exhibited significantly higher photocatalytic performance without any deactivation, yet with TEOA as sacrificial agent, which is due to the predeposited metallic Pt⁰ NPs, providing more active

sites for photocatalytic H₂ production (compare black and red line in Fig. 3.1c). To elucidate reasons for this different behavior, a comprehensive catalyst characterization has been carried out and the results are discussed in the next section. Since the Pt/10AIS-CN catalyst was found to be the best catalyst among the composites tested, it has been selected for comparing it with Pt/CN in all further experiments.

3.2 Catalyst characterization

3.2.1 Crystal structure, optical and structural properties

The crystal structure and phase compositions were characterized by powder XRD. Fig. 3.2 shows XRD powder patterns of AIS, CN and AIS-CN composites with different contents of AIS. The pure CN exhibited two different diffraction peaks, the main peak at 27.5° indexed as (002) diffraction plane, corresponding to the characteristic interlayer stacking reflection of polymeric melon sheets and a minor diffraction peak at 13.2° indexed as (100) plane, corresponds to in-plane structural motif between nitride pores (Fig. 3.2a).³⁴⁴ The pure AIS exhibits various diffraction peaks which are attributed to reflection planes of the cubic face centered lattice with a slight deviation of the unit cell parameters compared to reference (ICDD 01-071-3985: 10.822 Å, found 10.797 Å) (Fig. 3.2a).³²² The XRD powder patterns of the Pt/CN and Pt/10AIS-CN samples removed from the catalytic reactor after 3 h and 20 h exposure to UV-vis light do not show any change of the CN and AIS reflections, suggesting that the bulk structure of these two phases remains stable during catalysis (Fig. 3.2b). This has also been confirmed by ATR-IR spectra being identical for CN, 10AIS-CN as well as for Pt/CN and Pt/10AIS-CN after 3 h and 20 h use (refer to Fig. 3.4). The XRD powder patterns of the latter four catalysts show a small Pt(111) peak at 2θ = 39.9° which confirms the deposition of Pt particles as evidenced by scanning transmission electron microscopy with high angle annular dark field detector (STEM-HAADF), too (Fig. 3.2b and Fig. 3.6).

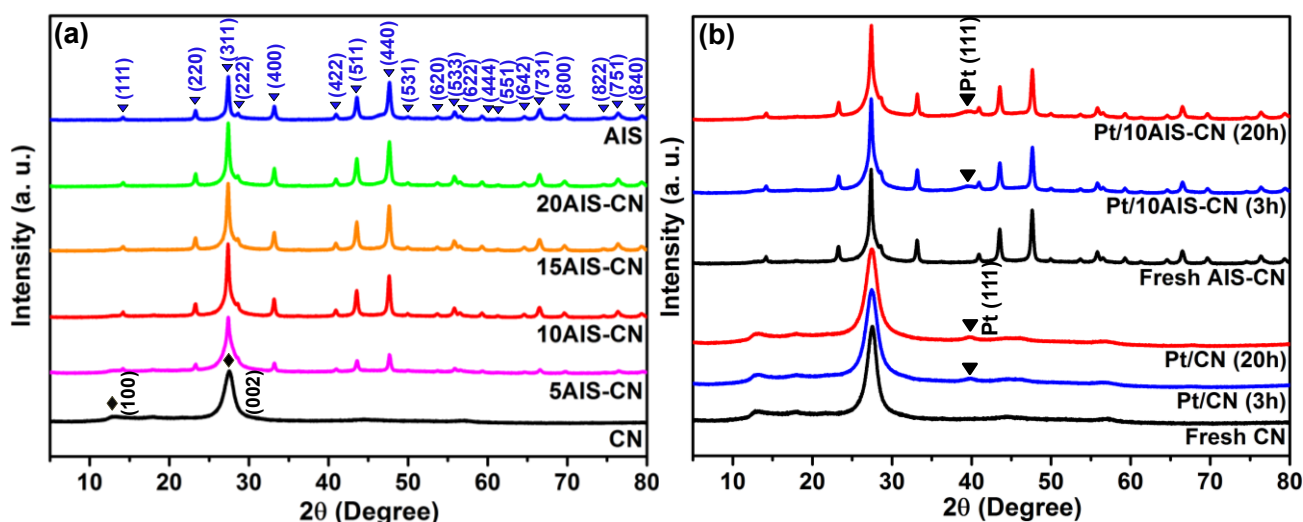


Figure 3.2 XRD powder patterns of (a) as-prepared samples and (b) Pt/CN and Pt/10AIS-CN samples removed from the reactor after 3 h and 20 h irradiation with UV-vis light in the presence of TEOA.

The optical properties of the as synthesized AIS, CN and AIS-CN composites with different contents of AIS were characterized by diffuse reflectance UV-vis spectroscopy. As illustrated in Fig. 3.3a, CN exhibited absorption wavelengths from UV to the visible region up to 600 nm.²²⁵ The AIS absorption edge is about 720

nm, exhibiting the broad absorption region of visible light.^{322, 341} When incorporating AIS into CN, the absorption edges are shifted to longer wavelengths. The band gap of CN decreases upon composite formation with AIS, suggesting that there is an effective interaction between AIS and CN in the composites. The calculated band gaps of the samples are summarized in Table 3.2 the corresponding Tauc plot are depicted in Fig. 3.3b.

Table 3.2 Structural properties of as-prepared (without deposited Pt) and used photocatalysts.

Catalyst	Band Gap (eV) ¹	S _{BET} (m ² /g)	Pore Volume (cm ³ /g)	Mean Pore Size (nm)
CN	2.65	159.1	0.206	3.9
5AIS-CN	2.59	137.4	0.194	4.5
10AIS-CN	2.54	118.4	0.150	3.9
15AIS-CN	2.48	122.7	0.175	4.5
20AIS-CN	2.39	126.7	0.177	4.6
AIS	1.75	90.9	0.272	8.2
Pt/CN (20 h)	-	137.0	0.210	3.9

¹ derived from the absorption edges in the UV-vis-DR spectra (Figure 3.3b) using the Tauc plot (³⁴⁵).

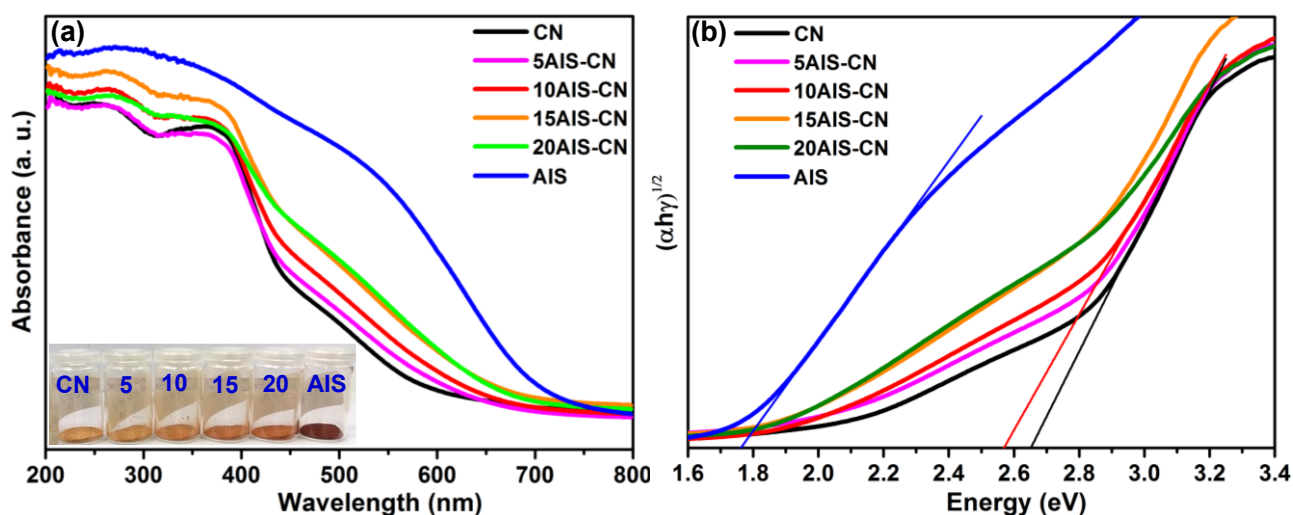


Figure 3.3 (a) UV-vis diffuse reflectance spectra of AIS, CN and AIS-CN composites with different contents of AIS and (b) band gap estimation from Tauc plot.

Fig. 3.4 shows ATR-IR spectra of CN, AIS and AIS-CN composites with different contents of AIS. A wide variety of bands is observed in the pure CN sample: the broad peak at 3152 cm⁻¹ has been assigned to the stretching mode of the N-H bond, while the peaks at 1203, 1315, 1400, 1453 and 1541 cm⁻¹ are attributed to C-N stretching modes. The peak at 1627 cm⁻¹ is associated with C=N stretching vibration modes and the intense band at 806 cm⁻¹ is due to the vibration of the triazine ring (Fig. 3.4a).⁶⁴ For AIS, the peaks at 3152 and 1612 cm⁻¹ are related to adsorption of OH⁻ on the material surface.³⁴⁰ After coupling AIS with CN, the resulting composites show the same IR spectrum as that of CN. Thus, the incorporation of AIS into CN cannot be proven by IR spectroscopy, however, it proves the stability of the carbon nitride support whose chemical structure remains unchanged after photocatalytic reaction (Fig. 3.4b).

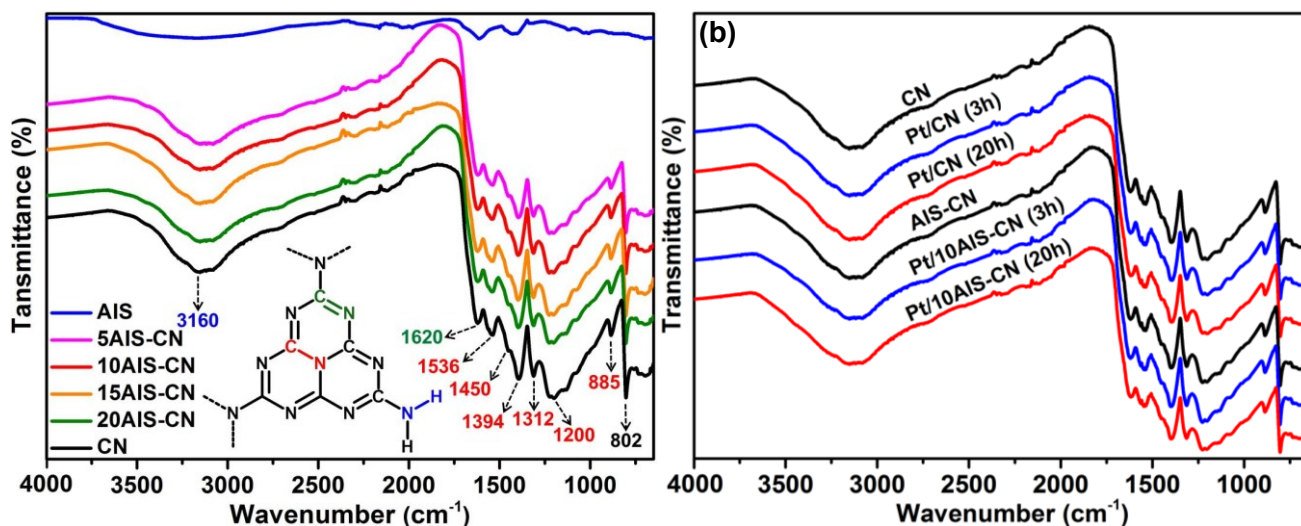


Figure 3.4 ATR-IR spectra of (a) as-prepared samples and (b) Pt/CN and Pt/10AIS-CN samples removed from the reactor after 3 and 20 h of irradiation with UV-vis light in the presence of TEOA.

3.2.2 Surface area analysis: N₂ adsorption-desorption isotherms

Fig. 3.5 shows the N₂ adsorption-desorption isotherms of AIS, CN and 10 wt.% AIS-CN composites and their corresponding pore size distribution plot. As shown in Fig. 3.5a, both the pure CN and 10AIS-CN exhibit type IV isotherms with a H4 hysteresis loop (according to the IUPAC classification) indicating the existence of mesopores (2-50 nm). These H4 hysteresis loops indicate the formation of narrow slit-shaped pores. In contrast, pure AIS displayed type IV isotherm with a H3 hysteresis loop. This H3 hysteresis loop indicates the existence of slit-shaped pores and no limiting N₂ adsorption at high p/p_0 due to the aggregation of particles. The specific surface area, pore volume and average pore size of the samples are summarized in Table 3.2. The pore size distribution of the samples were estimated by Barrett-Joyner-Halenda (BJH) method from the desorption branches, as shown in Fig. 3.5b. The BET surface area of CN (159.1 m² g⁻¹) is higher than the AIS (90.9 m² g⁻¹). Compared with pure CN, the 10 wt% AIS-CN composites showed decreased BET surface area and pore volume. This indicates that the BET surface area is not directly related to the photocatalytic activity. A similar effects was also observed for other g-C₃N₄-based photocatalysts such as g-C₃N₄/Zn₂SnO₄³⁴⁶, g-C₃N₄/CdIn₂S₄³⁴⁷, g-C₃N₄/AgX³⁴⁸, g-C₃N₄/SmVO₄³⁴⁹ and g-C₃N₄/CaIn₂S₄³⁵.

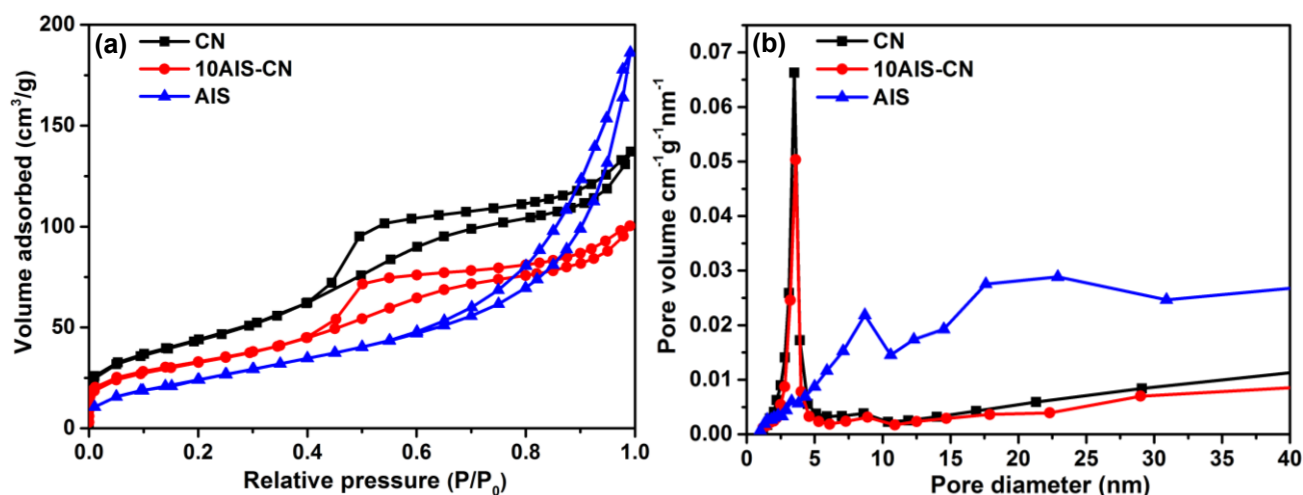


Figure 3.5 (a) N₂ adsorption-desorption isotherms of AIS, CN and 10AIS-CN; (b) Barrett-Joyner-Halenda pore size distribution plot.

3.2.3 Morphology and microstructure analysis by STEM

The aberration corrected STEM-HAADF images of Pt/CN catalyst, removed from the reactor after 3 h (in the active state of the catalyst), show the presence of uniform Pt containing particles with the size of 5-10 nm on the surface of CN (Fig. 3.6a, plots l and m). In addition, single Pt atoms are also distributed on the surface of CN (Fig. 3.6, plot r). Interestingly, the Pt particle size and distribution remain almost unchanged even after 20 h exposure of the Pt/CN catalyst to UV-vis light in the presence of TEOA (Fig. 3.6b). This indicates that the sintering of the Pt co-catalyst particles is not the reason for the observed catalyst deactivation (compare Fig. 3.1a). However, it appeared that the CN phase in the sample used for 20 h is much more sensitive against beam damage than Pt/CN used for 3 h only. This suggests that the prolonged exposure (20 h) of Pt/CN to UV-vis light led to changes in the electronic properties of the CN phase, which facilitate Pt inclusion inside the pores of CN, preventing them from participation in the reaction. This observation is also supported by XPS data (Table 3.1), which confirm the presence of a very low amount of surface Pt species for Pt/CN catalyst used with TEOA.

In case of Pt/10AIS-CN, there was no much change in the particle size of the Pt NPs compared to Pt/CN which are also almost unaltered after 20 h. However, the Pt NPs are preferentially deposited on the AIS phase (Fig. 3.6c and d, plots l and m), which itself formed irregular shaped particles with the size of around 100 nm (Fig. 3.6c and d, plot m). On the CN phase, Pt particles are less abundant on the surface, however, some single Pt atoms are also present (Fig. 3.6, plot r). It is therefore likely that the AIS phase protects the Pt NPs against encapsulation into the CN phase, keeping them accessible to protons and active for photocatalysis. The reason for this interesting observation may be that the polar AIS surface enables efficient adsorption and reduction of the polar [PtCl₆]²⁻ precursor compared with the non-polar CN surface which is also reflected by the higher Pt content in Pt/10AIS-CN after 3 h and 20 h use (Table 3.1).

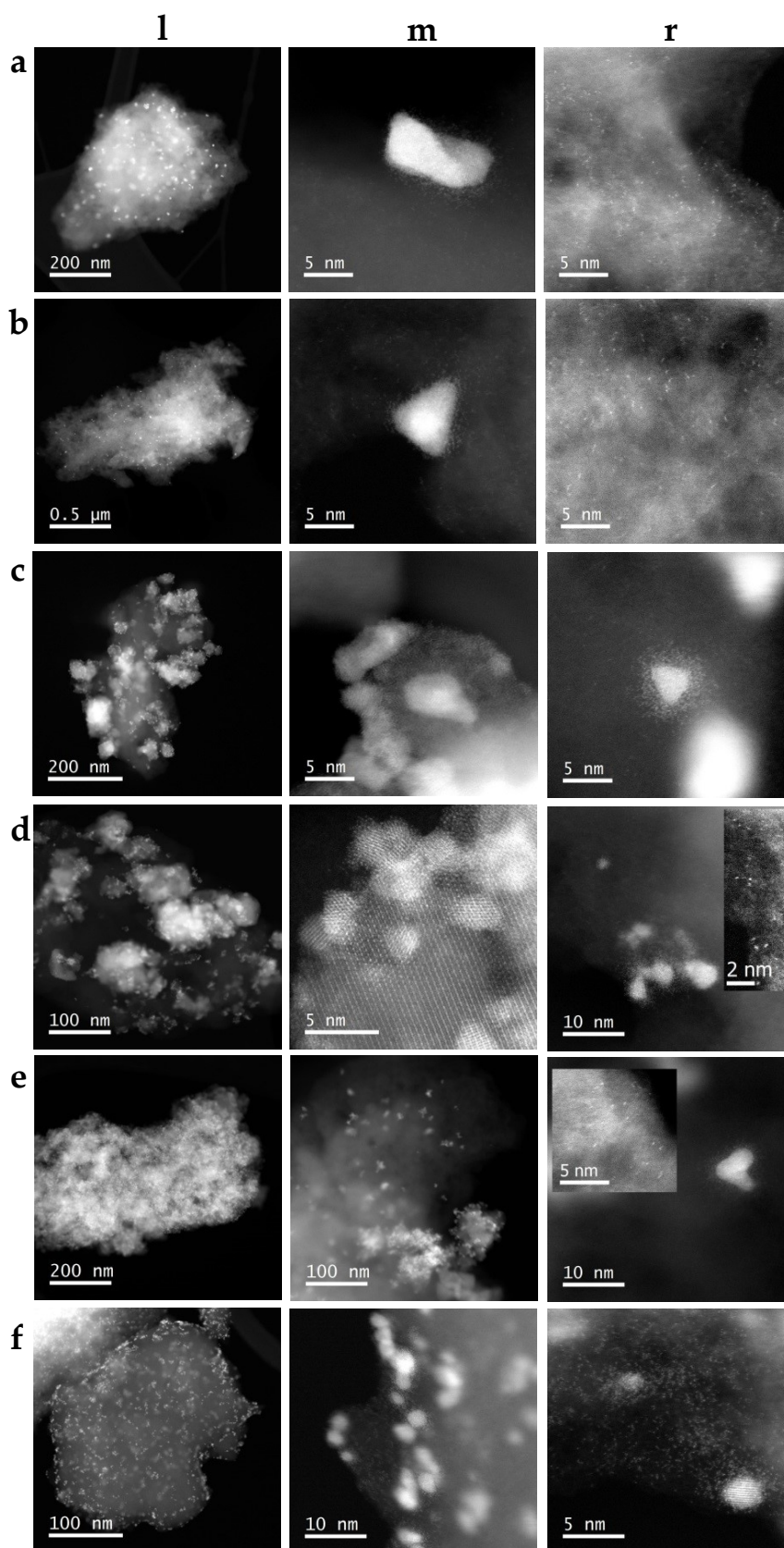


Figure 3.6 STEM-HAADF micrographs of catalysts exposed to UV-vis irradiation with TEOA: (a) Pt/CN for 3 h, (b) Pt/CN for 20 h, (c) Pt/10AIS-CN for 3 h, (d) Pt/10AIS-CN for 20 h, (e) physical mixture Pt/(10 wt.% AIS + CN) for 20 h and (f) Pt/CN after 4 h with oxalic acid (OA) as sacrificial agent. Plots l, m and r show areas of the same sample with different magnification.

The physically mixed Pt/(10 wt.% AIS + CN) (Fig. 3.2e) catalyst contains the similar Pt distribution as in the Pt/10AIS-CN catalyst (Fig. 3.2c and d). Some Pt single atoms are located on the CN phase while the Pt particles are enriched on the AIS surface. However, in the physically mixed catalyst, the CN and AIS phases obviously do not form tight composite, but they are rather separated from each other (Fig. 3.2e, plot m). Since the Pt/AIS catalyst without having strong contact with CN does not produce any H₂ (Fig. 3.1a), it appears that the catalytic activity and the deactivation of the physical mixture Pt/(10 wt.% AIS + CN) is governed by the separately existing Pt/CN phase in this sample, which could be the reason for the observation of a similar activity of physically mixed Pt/(10 wt.% AIS + CN) and Pt/CN (compare Fig. 3.1a).

When the photocatalytic H₂ production reaction was performed on Pt/CN catalyst with oxalic acid instead of TEOA as sacrificial agent, most Pt particles are located on the outermost surface of the CN phase where they remain accessible by protons (Fig 3.2f). This might be the reason for the high stability of the Pt/CN catalyst under these acidic conditions (compare Fig. 1c).

To understand the changes occurred on the catalyst surface during the catalysis, we performed the XPS analysis of the catalysts removed from the reactor after 3 h (Pt/CN is more active than Pt/10AIS-CN) and 20 h (Pt/10AIS-CN is more active than Pt/CN) as well as from samples exposed to OA. The surface Pt content in two Pt/CN samples is almost the same, but about two orders of magnitude lower than that determined by ICP-OES after 3 h and 20 h use (Table 3.1). This indicates that most of the Pt NPs observed by STEM-HAADF (Fig. 3.2a and b) are enclosed in the CN matrix. This observation is different for Pt/10AIS-CN after 3 h and 20 h use in which the surface Pt content is much higher than in AIS-free Pt/CN, in agreement with the STEM-HAADF results, which point out the preferential deposition of Pt on the AIS phase (Fig. 3.2c and d). Moreover, the Ag:In:S atomic ratios in as-prepared 10AIS-CN as well as in two Pt/10AIS-CN samples are close to the theoretical 1:5:8 ratio, suggesting that the deposition-precipitation of the AIS component on the CN phase did not alter the composition and structure of the latter.

It has been shown by simultaneous in situ-SEM/STEM-HAADF analysis that Pt NPs deposited on the surface of carbon tend to migrate into the bulk phase of the support when increasing the temperature up to 200 °C, especially in the presence of air.³⁵⁰ Possibly, a similar process is promoted in the Pt/CN samples treated at high pH conditions. Note that the Pt surface content in Pt/CN_OA (4h) sample irradiated for 4 h in acidic medium is about 10 times higher than in Pt/CN treated for 3 h in TEOA. Thus, the AIS phase keeps Pt enriched and exposed on the catalyst surface. Interestingly, there was no deactivation for Pt/CN (3 h) sample, indicating that, despite diffusion into the mesopores, the Pt NPs remain accessible to reactants during the initial 3 h of reaction. Only after more than 6 h reaction time, the Pt NPs lose their activity (Fig. 3.1a). In basic medium, formation of highly reactive •OH radicals is possible by the reaction of holes with OH⁻ anions. We speculate that these species may attack the CN phase in the vicinity of the Pt NPs, create defects and promote tight wrapping of the Pt NPs by CN. Remarkably, the BET surface area of Pt/CN catalyst after 20 h use is slightly lower than that of the as-prepared CN phase whereas no variation in volume and mean diameter of the pores was observed at all (Table 3.2). This indicates, in agreement with

ATR-IR and XRD results (Fig. 3.2 and 3.4), that it might be a local densification of the CN phase around the Pt NPs, rather than an extended collapse of surface and mesopore structure which reduces accessibility of Pt NPs by reactants. This aspect has been further analyzed by FTIR analysis of adsorbed CO (*vide infra*).

3.2.4 Surface chemical analysis by XPS

From the results discussed thus far it gives the impression that a longer exposure of Pt/CN to strongly basic medium increases the possibility of undesired support changes. Besides the elevated sensitivity of the CN phase against beam damage during STEM-HAADF, this is further substantiated by analyzing the C 1s and N 1s XP spectra which contain contributions from different moieties of the C_3N_4 structure³⁵¹ (Fig. 3.7a and b). Probably, a similar process takes place in Pt/10AIS-CN (20 h) as the CN phase in this sample was prone to beam damage in TEM as well. However, in this sample, high concentration of surface Pt species was found on the AIS phase, which might protect it against inclusion in the CN pores. It can be seen from Fig. 3.7b that the peak belonging to N-(C₃) moieties decreases strongly upon prolonged irradiation in basic medium, while only a tiny peak corresponding to C–N–H moieties was found. In contrast, the as-prepared CN catalyst contains a certain amount of oxygen species, at least a part of which might account for the N=C–O moieties as shown in in Fig. 3.7a, which also disappeared after the reaction. Considering the position of such moieties within the C_3N_4 structure (Fig. 3.7d), defect formation upon their removal seems likely supporting local changes (densification) of the CN structure around the Pt NPs, and hence shielding the latter from the reactants.

There was no much variation in the surface composition of the catalysts treated in TEOA. All the catalysts contain both metallic Pt⁰ and oxidized Pt²⁺, reflected by Pt 4f_{7/2} peaks at 70-72 eV and 74 eV, respectively (Fig. 3.7c).³⁴³ Especially in the AIS-containing samples, these peaks are very broad and hence, a meaningful deconvolution into distinct doublets for 4f_{7/2} and 4f_{5/2} is not possible, which is most likely attributed to the presence of different types of Pt species, i.e. single atoms, small particles and agglomerates of small particles in the vicinity of both CN as well as AIS (evidenced by STEM-HAADF, Fig. 3.6c and d).

When Pt NPs are deposited *in situ* on CN in the presence of OA, the Pt surface concentration is much higher than that obtained in the presence of TEOA (0.85 at.% vs. 0.06 at.%, Table 3.1), since the Pt nanoparticles (Pt⁰ and Pt²⁺ coexist) are located preferentially on the outer surface of CN (Fig. 3.6f and 3.7c, green and blue fitted lines). After the subsequent treatment of Pt/CN_OA (4 h) under UV-vis light in TEOA for 24 h, the Pt²⁺ is even more dominating on the surface than in Pt/CN sample (20 h) treated only in TEOA (compare Fig. 3.7c, bottom plots). This confirms that the enrichment of oxidic Pt is not the reason for catalyst deactivation because the latter catalyst does not deactivate (compare Fig. 3.1c).

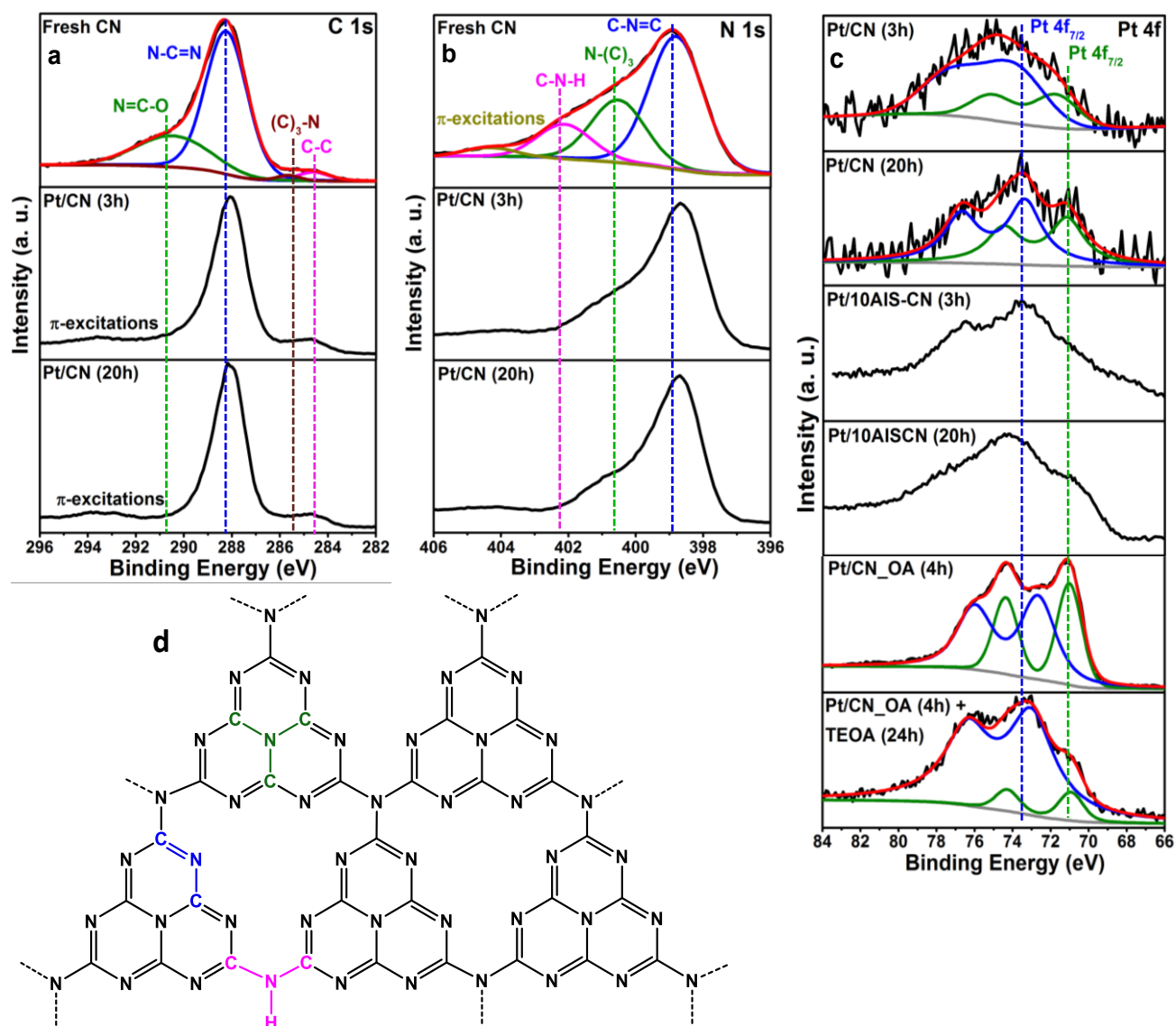


Figure 3.7 XPS spectra of selected samples in the C 1s (a), N 1s (b) and Pt 4f region (c) blue: Pt²⁺, green: Pt⁰ together with a scheme of the C₃N₄ structure (d).

The total Pt content determined by ICP-OES analysis for Pt/CN is much lower than the theoretical value of 2 wt.%, after 3 h and 20 h irradiation with UV-vis light (0.27 and 0.43 wt.%, respectively, Table 3.1) and it is only slightly below 2 wt.% in the respective Pt/10AIS-CN samples (1.86 and 1.87 wt.%). This is probably due to the fact that only a part of the dissolved [PtCl₆]²⁻ precursor is reduced and deposited as Pt NPs in basic TEOA solution. It was shown in literature that a stepwise hydrolysis i.e. [PtCl₆]²⁻ → [Pt(OH)_xCl_{6-x}]²⁻ → [Pt(OH)₆]²⁻ occurs under high pH conditions (TEOA), inhibiting the formation of metallic Pt particles.³⁴³ Moreover, owing to its non-polar nature, the CN is less prone to adsorb the polar Pt complex species compared with the polar AIS surface. Nevertheless, the small percentage of deposited Pt is obviously sufficient for obtaining the best initial H₂ evolution rate of Pt/CN under UV-vis light during the first 4 h.

3.2.5 CO adsorption study by FT-IR

Fig. 3.8 shows the FT-IR spectra of CO adsorbed on the catalysts in order to estimate the accessibility of the active Pt species. Bands of CO adsorbed on oxidized Pt²⁺/Pt⁺ as well as on metallic Pt⁰ were found as

shown in Fig. 3.8,³⁵² supporting the observation of oxidized and zerovalent Pt species with XPS (compare Fig. 3.7c). The band intensities of all species were found to decrease after exposing the Pt/CN catalyst to the photocatalytic reaction for 20 h, indicating decreased accessibility of the Pt surface for reactants, which is a potential explanation for the observed rapid deactivation of Pt/CN after 20 h (Fig. 3.1).

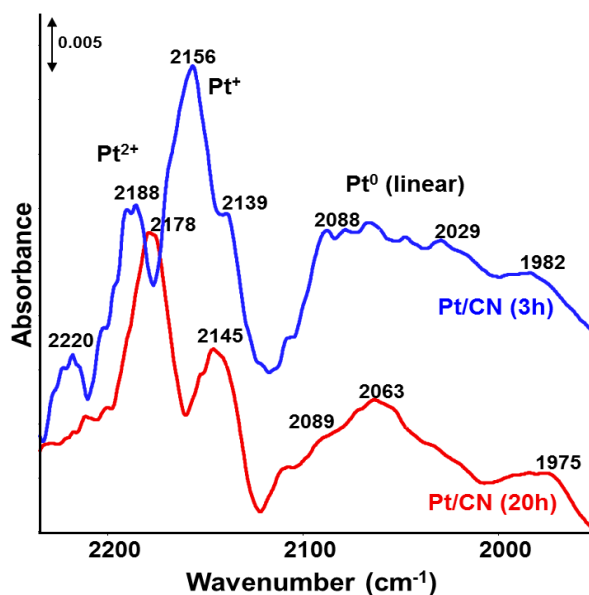


Figure 3.8 FTIR spectra of adsorbed CO for catalyst Pt/CN after 3 h and 20 h use in the reaction with UV-vis light.

3.3 Mechanism: charge separation and transfer

3.3.1 Visualization of charge separation and transfer by in situ-EPR

In situ-EPR is a versatile technique to monitor separation and transfer of photogenerated electrons in semiconductors based on oxides³³⁵ or carbon nitrides,⁷⁶ since electrons excited to the conduction band (CB- e^-) can be trapped at oxygen vacancies³³⁵ and carbon defects.³³⁶ Even under dark conditions, the pure CN and AIS/CN composite catalysts exhibit a single Lorentzian line centered at a g-value of 2.0042 which is ascribed to the unpaired electrons in the sp^2 -carbon in a typical tri-s-triazine (heptazine) unit^{353,354} (Fig. A.1). Moreover, the observed g-value indicates that this strong signal arises from surface trapped CB e^- that preferentially has carbon character. It is important to note that the conduction band (LUMO) of CN is mainly constituted of C 2p orbitals whereas valence band (HOMO) is mainly made up of N 2p orbitals.²²

Fig. 3.9a clearly shows an increase of this EPR CB e^- signal under irradiation with UV-vis light due to electron-hole separation and excitation of electrons into the CN conduction band (solid lines). However, after switching the light off, the EPR CB e^- signal is decreased due to the recombination of photoexcited electrons with holes (dashed lines). This whole process is also called electron-hole pair recombination.

The EPR spectra during UV-vis light irradiation and after light switched-off were integrated twice (background signals in the dark subtracted) to investigate the charge separation efficiency of CN and AIS loaded CN samples (Fig. 3.9b). This integral's intensity is highest upon irradiation of CN, When raising the amount of AIS, the EPR CB e^- signal intensity is decreased most likely due to the transfer of electrons from

the CN conduction band to AIS in the composites. Another indication for such a process is provided by photoluminescence (PL) spectra (vide infra).

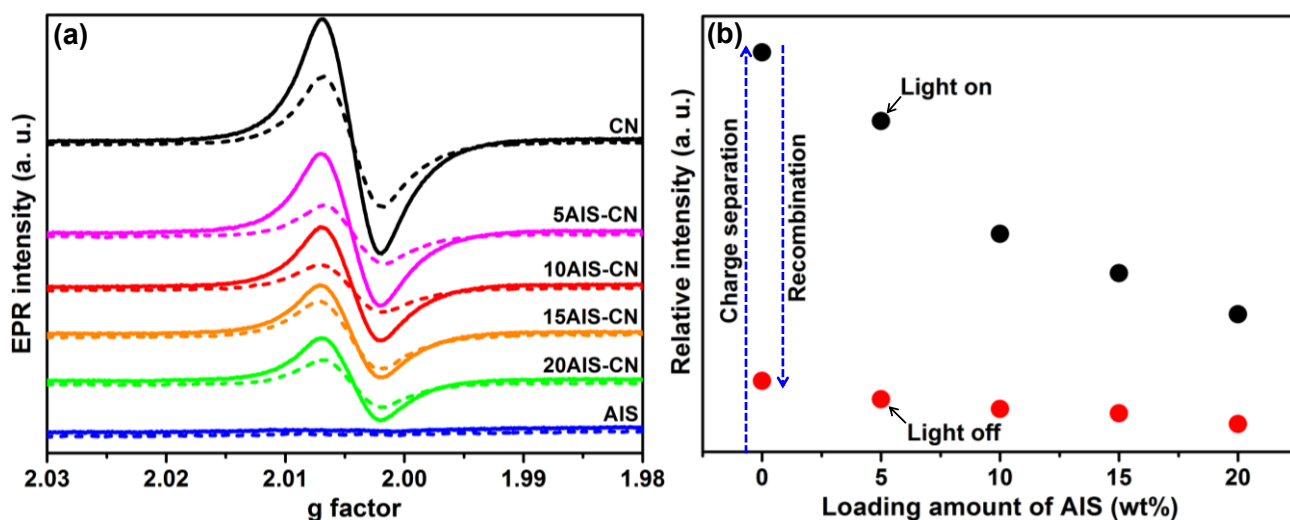


Figure 3.9 (a) Electron paramagnetic resonance (EPR) signal of CB-e⁻ in as-prepared catalysts (without Pt) during UV-vis irradiation (solid lines) and after light switched-off (dashed lines); (b) Double integral of the EPR CB e⁻ signal intensity (initial background signal in the dark subtracted) during UV-vis light irradiation (black dots) and after light switched-off (red dots).

As shown in section 3.1, there is no photocatalytic H₂ production activity when CN alone is used as photocatalyst. This suggests the necessity of a further transfer of the separated CB-e⁻ directly or via AIS to Pt. Thus, 2 wt% Pt co-catalysts were photodeposited on the surface of CN to provide active sites for H₂ production. To prove the impact of those Pt NPs in the electron transfer mechanism during photocatalytic reaction, catalysts Pt/CN and Pt/10% AIS-CN have been removed from the photocatalytic reactor after 3 h and 20 h and comprehensively characterized by *in situ* EPR.

Interestingly, the EPR CB e⁻ signal intensity under UV-vis light irradiation seems to reflect somehow the catalytic behavior. As can be seen in Fig. 3.10, the EPR CB e⁻ signal is higher for fresh CN and drops down after 3 h. It implies that during photocatalytic reaction the photogenerated CB e⁻ of CN is quickly transferred to Pt NPs, where electrons react with H⁺ to produce H₂ molecules. It is higher for Pt/CN after 20 h use, indicating that transfer of CB-e⁻ to Pt and, thus, charge separation is less efficient, which may be a reason for the observed deactivation (Fig. 3.10). In the case of Pt/AIS-CN, the intensity of this CB-e signal under irradiation after 20 h is markedly lower compared to 20 h Pt/CN. This indicates that AIS promotes transfer of separated CB e⁻ from CN to Pt, which may account for the higher H₂ production rate of Pt/AIS-CN after 20 h. This is also supported by TEM results which showed that in Pt/AIS-CN virtually all Pt NPs are deposited on AIS, leaving the CN surface nearly Pt-free. Obviously, in active catalysts fast transfer of CB-e⁻ via CN → (AIS) → Pt → H⁺ → H₂ takes place, keeping the CB-e⁻ electron signal small, while the Pt → H⁺ → H₂ step of this chain might be hindered in less active catalysts, leading to higher EPR intensity.

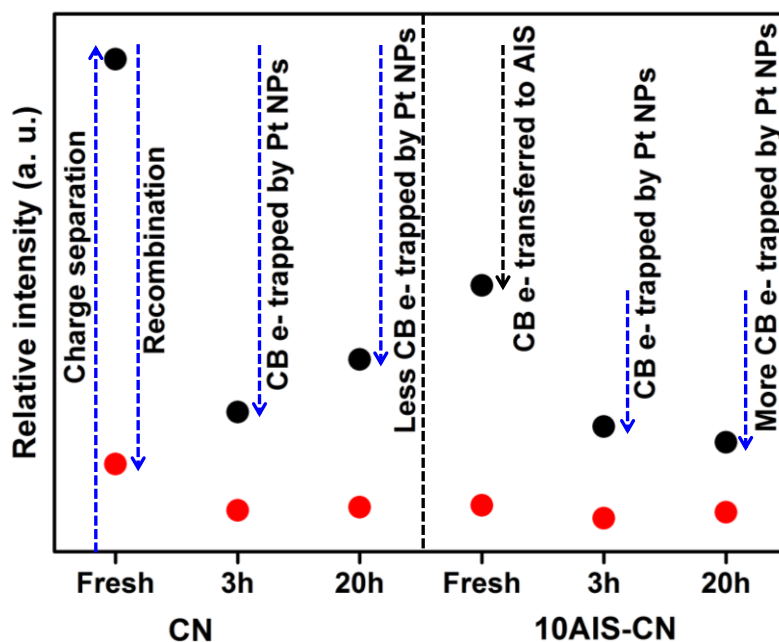


Figure 3.10 Intensity (double integral) of the CB e- EPR signal (initial background signal in the dark subtracted) during UV-vis light irradiation (black dots) and after light switched-off (red dots). Values for as-prepared samples without Pt (fresh) taken from Fig. 3.9b.

3.3.2 Photoluminescence spectroscopy study

Photoluminescence (PL) analysis is commonly employed to investigate the separation efficiency of photogenerated charge carriers. The PL emission peak is originating from recombination of photogenerated electrons and holes so that the PL intensity can reflect the separation efficiency and lifetime of charge carriers. For instance, a photocatalyst which exhibited lower PL emission intensity means a higher recombination rate of electron-hole pairs or shorter lifetime.³³⁷ Fig. 3.11 shows PL spectra of AIS, CN and AIS-CN composites collected after excitation at 370 nm. It can be seen that the pure CN exhibits a strong emission peak exactly at 470 nm, which corresponds to the band gap charge carrier recombination. Pure AIS gives no PL, despite the fact that it absorbs UV-vis light able to excite electrons from the valence to the conduction band. This suggests that electron-hole recombination in the pure AIS phase might be too fast to emit PL radiation. When AIS is introduced into CN, the emission peak intensity was decreased with rising AIS contents, indicative of a transfer of the photogenerated charge carriers from CN to AIS. A similar effect was also observed for other C_3N_4 -based photocatalysts such as $In_2S_3/g-C_3N_4$,³⁵⁵ $ZnFe_2O_4/g-C_3N_4$,³⁵⁶ $Cu_2O/NaTaO_3$,³⁵⁷ $g-C_3N_4/NiFe-LDH$ ³⁵⁸ and $MoS_2/g-C_3N_4$.³⁵⁹ When Pt is deposited on both, pure CN and the 10AIS-CN composite, giving rise to photocatalytic activity, the PL signal decreases (Fig. 3.11b). The reason might be transfer of excited CB e- from CN to Pt or from CN via AIS to Pt, respectively, which efficiently prevents charge carrier recombination and extends their lifetime sufficiently for reduction of protons to H_2 . On the other hand, the reason for the decreasing H_2 evolution rates with rising AIS content in the AIS-CN composites may be AIS mediated quenching of a part of the CB e- before they reach the Pt conduction band.

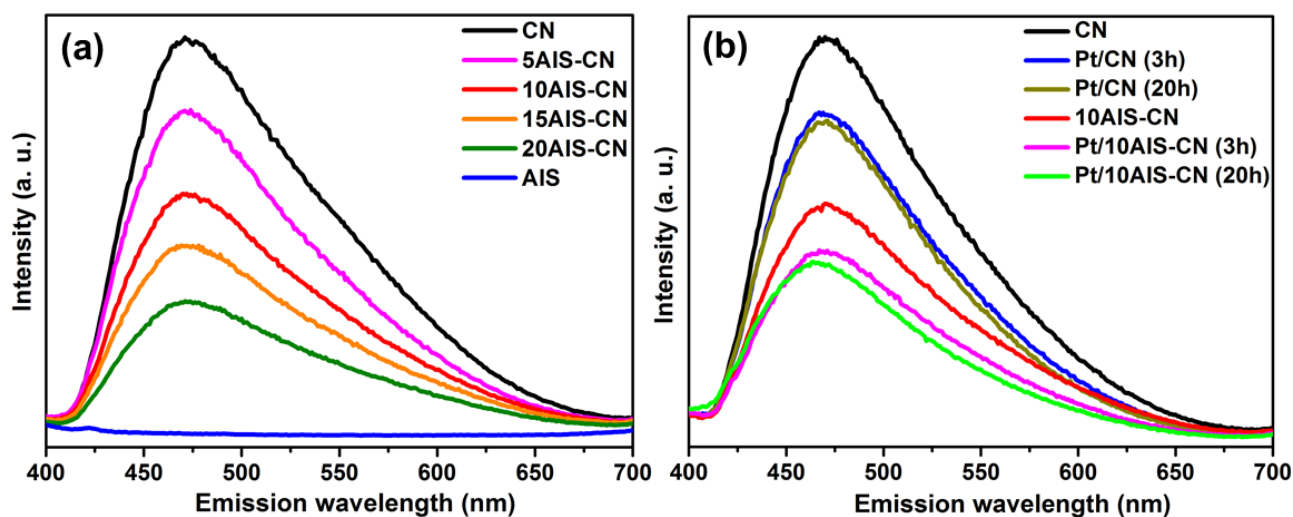


Figure 3.11 Photoluminescence spectra after excitation at 370 nm of as-prepared catalysts without Pt (a) and Pt containing catalysts after 3 h and 20 h use under UV-vis irradiation (b) For comparison the Pt free supports are shown in plot b as well.

3.4 Conclusions

The Pt/CN catalysts without AIS showed the highest initial H₂ production rates in both basic (TEOA) and acidic (OA) aqueous solutions. However, the Pt NPs are encapsulated in the bulk structure of CN in basic medium (pH = 10.6), leading to fast catalytic deactivation within the first 4-6 h of reaction time under UV-vis light conditions, which occurs, though slower, under pure visible light ($\lambda \geq 420$ nm) conditions. The reason for the fast deactivation of Pt/CN catalyst may originate in an attack of the CN structure by highly reactive $\cdot\text{OH}$ radicals, resulting in defect formation and subsequent densification. With the increase of AIS content in the Pt/xAIS-CN ($0 \leq x \leq 20$ wt.%) composites, the initial H₂ evolution rates were found to decrease, while the CN-free Pt/AIS catalyst was completely inactive for photocatalytic H₂ production reaction. This is most likely due to rapid electron-hole recombination in AIS although it absorbs visible light efficiently. This prevents the electron transfer from the AIS conduction band to the Pt particles. In AIS/CN composites, electrons excited from the valence band to the conduction band of CN, travel through the interface to AIS and further to the Pt particles, enriching preferentially on the AIS surface, which is only possible when an effective heterojunction exists. This must be concluded since the course in catalytic activity of a physical mixture of CN and AIS (with no such heterojunction) is similar to Pt/CN without AIS (Fig. 3.1a) and Pt/AIS is not active at all. Apparently, an optimum situation was found for Pt/10AIS-CN sample, in which the CN surface is covered most effectively by AIS particles (indicated by the lowest BET surface area, Table 3.2), which might be still thin enough to enable effective transfer of CB- e^- from CN via AIS to Pt where they reduce protons to hydrogen. The similar process is expected in aqueous oxalic acid solution (pH = 0.67), though the H₂ formation rates are significantly higher, due to the higher proton concentration.

The main difference resulting from the pH of the reaction solution concerns catalyst stability which is related to the nature of the Pt NPs. Both metallic Pt⁰ and oxidic Pt²⁺ are present in all cases, excluding the partial oxidation of metallic Pt as a reason for the fast deactivation of the Pt/CN catalyst. However, the Pt

NPs in Pt/CN catalyst are highly active in acidic medium (pH = 0.67) because most Pt NPs are present on the surface of CN phase and not encapsulated in the CN bulk structure, as observed in basic medium (pH = 10.6).

The following observations were noticed from the catalytic activity studies: (i) the Pt co-catalyst is needed for efficient H₂ production over CN-based photocatalysts as it promotes electron transfer from the conduction band of CN to Pt, while suppressing the recombination of electron-hole pairs. (ii) Although an improvement in the catalyst stability was noticed, composite formation of AIS with CN is detrimental for H₂ formation rates. (iii) Despite the fact that AIS is able to absorb visible light (evidenced by UV-vis diffuse reflectance spectra), the electron-hole separation and/or the electron transfer is insignificant, preventing proton reduction. (iv) The pH of the reaction solution was found to show a considerable effect on the stability of the Pt/CN catalyst for photocatalytic H₂ production.

4 Influence of MoS₂ on Activity and Stability of Carbon Nitride in Photocatalytic Hydrogen Production

This work has been submitted in the journal *Catalysts* (MDPI publishing company). Ramesh P. Sivasankaran, Nils Rockstroh, Carsten R. Kreyenschulte, Stephan Bartling, Henrik Lund, Amitava Acharjya, Henrik Junge, Arne Thomas and Angelika Brückner*.

In this chapter, we synthesized MoS₂/C₃N₄ (MS-CN) composite photocatalysts by three different methods, i. e. in situ-photodeposition (PD), sonochemical (SC) and thermal decomposition (TD). Two dimensional (2D) MoS₂ is a good semiconductor due to its beneficial structural, electronic, optical, chemical and thermal properties which render it very attractive for H₂ production applications.^{360, 361} 2D MoS₂ is composed of hexagonal layers, in which Mo atoms are sandwiched between two layers of S atoms. The layered structure of MoS₂ can form two different polymorphs, a 2H phase (trigonal prismatic coordination of S around Mo) and a 1T phase (octahedral coordination of S around Mo).³²⁴ The 2H phase is semiconducting whereas 1T phase is metallic.³²⁴ The structure of the 2H phase can be described by two S-Mo-S layers composed of edge-shared MoS₆ trigonal prisms, whereas the structure of the 1T phase is described by a single S-Mo-S layer built from edge-sharing MoS₆ octahedra.^{360, 362} In recent work, the 1T MoS₂ phase is considered as more active in electrocatalytic H₂ production than the 2H phase, mainly because it is metallic and exposed more active sites,³²⁴ however, there is still an ongoing debate about this issue. Despite the fact that carbon nitride turned out to be a suitable photocatalyst for visible light driven H₂ production, one major problem is fast recombination of photogenerated electron-hole pairs in pristine C₃N₄ which limits the overall photocatalytic efficiency.³⁴ Inspired by the advantageous properties of MoS₂ nanosheets and by previous investigations (Table A.3), we were aiming at the creation of a heterojunction with C₃N₄ (CN) to improve electron-hole pair separation and stability during photocatalytic hydrogen evolution. In this work, we used MoS₂ since we expected that, due to its 2D structure, it may cover the CN surface with a thin layer rather than forming big particles, which could lead to a more effective heterojunction.

4.1 Catalytic activity

Fig. 4.1a shows the photocatalytic H₂ production activity of MoS₂-free Pt/CN in the presence of lactic acid under UV-vis light (black line), under only visible light ($\lambda > 420$ nm, blue line) and upon irradiation with $\lambda > 420$ nm after 4 h of UV-vis light irradiation (red line).

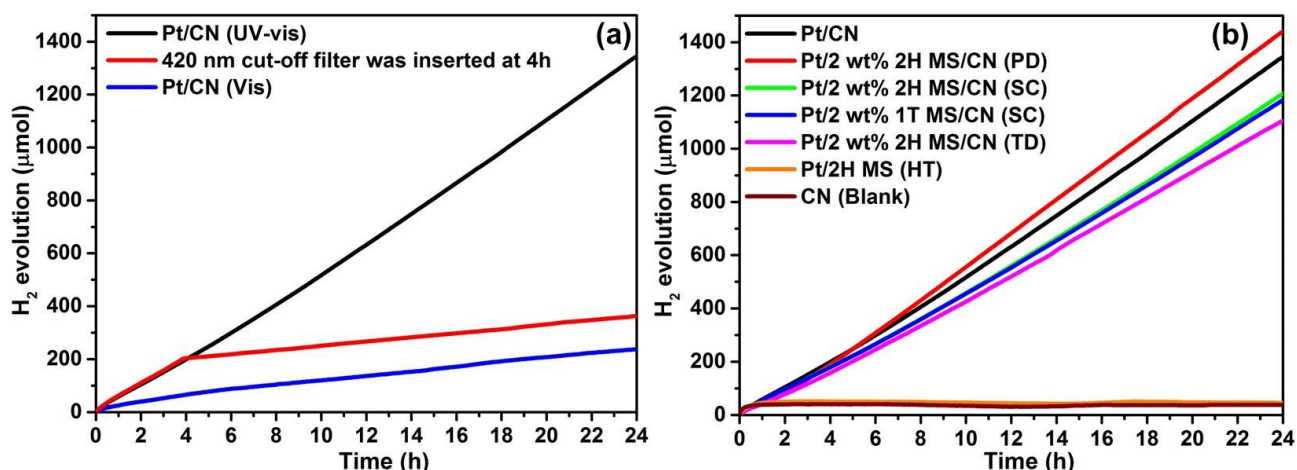


Figure 4.1 Photocatalytic H₂ production of MoS₂-free Pt/CN as a function of time in the presence of lactic acid: (a) under UV-vis light (black), under visible light ($\lambda > 420$ nm, blue) and with a 420 nm cut-off filter inserted after 4 h irradiation under UV-vis light (red); (b) for differently prepared MS-CN composites under UV-vis light irradiation. Reaction conditions: 24.5 mg CN or MS-CN, 0.2 mL of a H₂PtCl₆ stock solution equal to 0.5 mg Pt, 24.8 mL H₂O/lactic acid (final ratio 9/1 (v/v)), 25 °C, 1.5 W light power (Xe lamp) without (UV-vis) or with (vis) a 420 nm cut-off filter.

2.7 wt% Pt nanoparticles (NPs) were deposited as a cocatalyst on the surface of the photocatalysts by in situ photoreduction of H₂PtCl₆, since no photocatalytic activity was observed with pristine CN (Fig. 4.1b). Pt/CN exhibits significantly higher photocatalytic activity under UV-vis light than under pure visible light (2178.7 $\mu\text{mol h}^{-1} \text{g}^{-1}$ compared to 333.7 $\mu\text{mol h}^{-1} \text{g}^{-1}$, Fig. 4.1a). This is due to the higher number of absorbed photons that excite more electrons from the valence to the conduction band.³⁶³ Comparison of the blue and the red line in Fig. 4.1a suggests that formation of Pt particles active for proton reduction under visible light is not a limiting factor since the slope of both curves is the same. Moreover, Pt/CN is stable under the acidic conditions used in this test, in contrast to previous tests performed with TEOA as sacrificial reagent (Chapter 3).³⁶³

As evident from Fig. 4.1b, all composite catalysts showed remarkable H₂ production activity within 24 h while no H₂ evolution was observed with Pt/2H MS, for which the 2H phase MoS₂ was prepared by a hydrothermal method (HT) without CN. While Pt/2H MS-CN (PD) exhibits a higher H₂ production rate (2342 $\mu\text{mol h}^{-1} \text{g}^{-1}$) than Pt/CN (2178.7 $\mu\text{mol h}^{-1} \text{g}^{-1}$), the photocatalytic activity in the composite materials Pt/2H MS-CN (SC), Pt/1T MS-CN (SC) and Pt/2H MS-CN (TD) was lower than that of Pt/CN. This implies a considerable influence of the preparation procedure on the catalyst properties and in turn on the catalytic performance, which has been elucidated by thorough catalyst characterization (vide infra).

4.2 Catalyst characterization

4.2.1 Crystal structure and optical properties

The powder XRD patterns of MoS₂ prepared by solvothermal (ST), hydrothermal (HT) and thermal decomposition (TD) methods and of MS-CN composites are depicted in Fig. 4.2a and b.

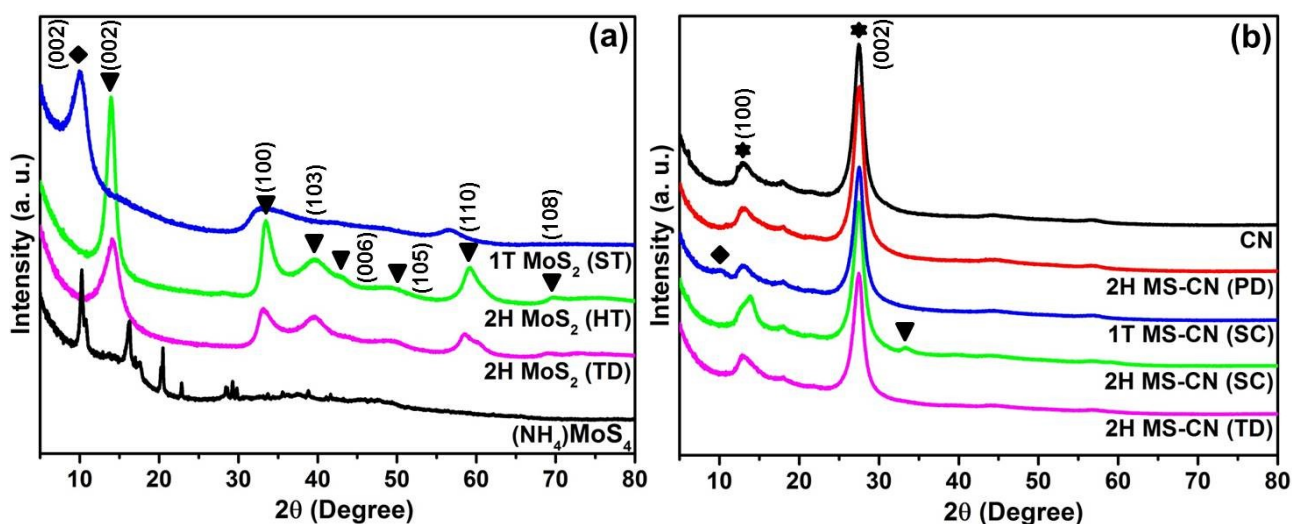


Figure 4.2 XRD powder patterns of (a) 1T MoS₂ (ST), 2H MoS₂ (SC), 2H MoS₂ (TD) and (NH₄)MoS₄; (b) pure CN and differently prepared MS-CN composites.

The 2H phase of MoS₂ exhibits diffraction peaks at 14.1, 32.9, 39.5, 43.3, 49.4, 58.8 and 69.2° which are attributed to the (002), (100), (103), (006), (105), (110) and (108) reflection planes of the hexagonal crystal system (ICDD: 01-075-1539) (Fig. 4.2a).³²⁴ In the 1T MoS₂ phase (ST), the (002) diffraction peak is shifted to a lower value of 2θ (9.9°) (Fig. 4.2a).³²⁶ Pure CN exhibits two diffraction peaks for the interlayer stacking reflection of polymeric melon sheets (27.5°) and an in-plane structural motif between nitride pores (13.2°) (ICDD: 00-066-0813) (Fig. 4.2b).^{344, 363} The XRD patterns of the MS-CN composites show the main peaks of CN (Fig. 4.2b). In the composites 2H MS-CN (SC) and 2H MS-CN (TD), the (002) peak of the 2H phase is superimposed on the (100) peak of CN at 13.2° leading to slight asymmetry. The powder XRD patterns of the used catalysts recovered after 6 hours from the reaction mixture show a small diffraction peak at 2θ = 39.9° for Pt (111) confirming the in situ-photodeposition of Pt NPs (Fig. A.2) which was also evidenced by scanning transmission electron microscopy (STEM, vide infra). The (002) diffraction peak of 1T MS-CN (SC) at 2θ = 14.1° disappeared after 6 h use, possibly due to a phase transition from 1T to 2H MoS₂ during the reaction³²⁴ (compare Fig. 4.2b and A.2).

The light absorption properties of as synthesized pure C₃N₄ and MS-CN composites were analyzed by diffuse reflectance UV-vis spectroscopy (Fig. 4.3). Pure CN exhibits absorption wavelengths from UV to visible region up to 600 nm, indicating its ability to absorb visible light (Fig. 4.3a).³⁶³ Pure MoS₂ is black and absorbs light in the whole wavelength range (Fig. A.3). Hence, the colour becomes darker when CN forms a composite with 2 wt% of MoS₂ (Fig. 4.3a). Surprisingly, a decrease of the absorption bands of CN is observed after loading of MoS₂ on the surface of CN. This may be due to a shielding effect caused by wrapping of the MoS₂ nanosheets around the CN nanosheets (see also STEM results below). Accordingly, absorbance of MS-CN composites in the range of 650-1000 nm increases slightly, which is related to MoS₂ and has been also observed after loading of MoS₂ on BiOI.³⁶⁴ Moreover, the catalytically most active sample Pt/2H MS-CN (PD) (cf. Fig. 4.1) shows the lowest decrease of the CN absorption band around 500 nm. The origin of this band is

most likely due to an increase of the degree of polymerization and π -plane conjugation.¹⁰⁰ As can be seen from Fig. 4.3b, the band gap of CN and 2H MS/CN (PD) estimated to be 2.65 eV.

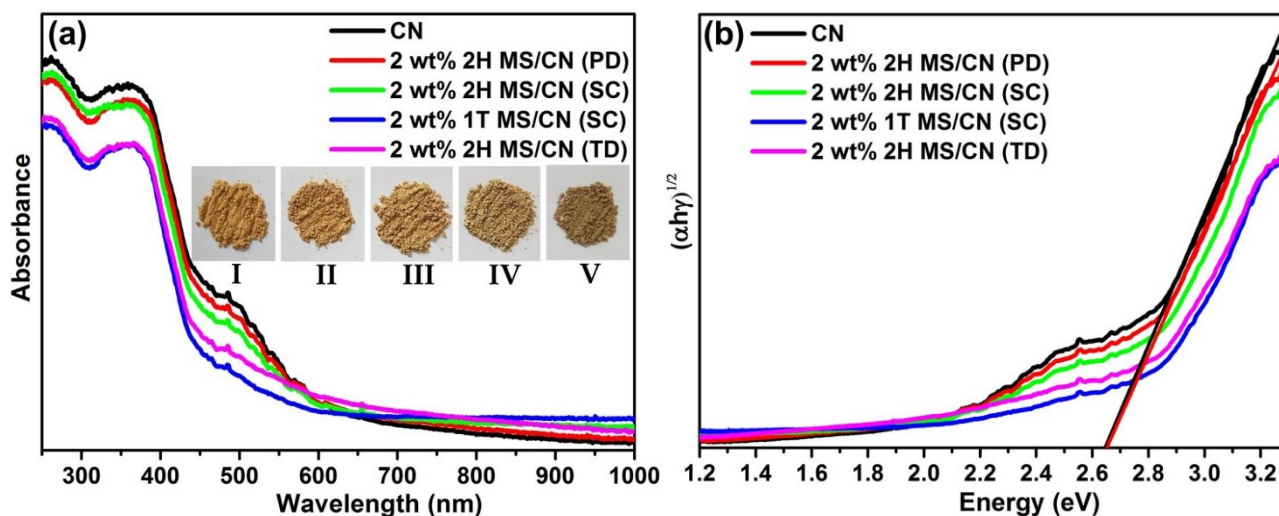


Figure 4.3 a) UV-vis-DR spectra of pure CN and MS-CN composites together with photographs of (I) CN, (II) 2H MS-CN (PD), (III) 2H MS-CN (SC), (IV) 1T MS-CN (SC), (V) 2H MS-CN (TD); (b) Band gap estimation from Tauc plot.

4.2.2 Surface area analysis: N₂ adsorption-desorption isotherms

As shown in Fig. 4.4a, the pure CN and 2H MS-CN (PD) exhibited type IV isotherms with a H4 hysteresis loop, according to the IUPAC classification, indicating the existence of mesopores (2-50 nm). These H4 hysteresis loops indicate the formation of narrow slit-shaped pores. The specific surface area, pore volume and average pore size of the samples are summarized in Table 4.1. The pore size distribution of the samples were estimated by using the Barrett-Joyner-Halenda (BJH) method from the desorption branches, as shown in Fig. 4.4b. The BET surface area of CN is 98.5 m² g⁻¹. Compared with pure CN, the 2H MS/CN (PD) composites showed decreased BET surface (70.6 m² g⁻¹) area and pore volume. This indicates that the surface area is not playing any role in the photocatalytic activity.

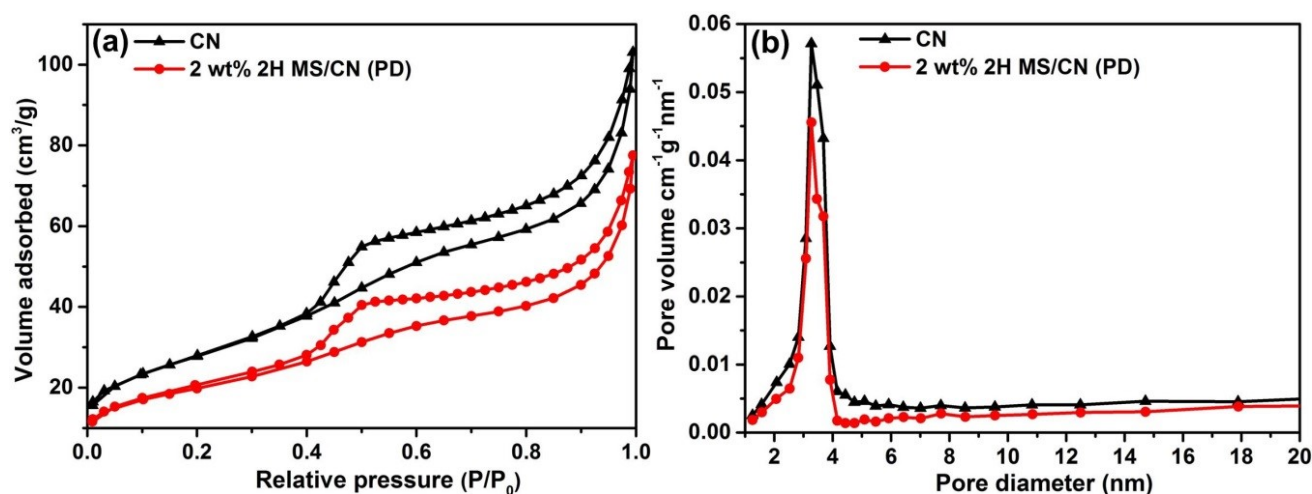


Figure 4.4 (a) N₂ adsorption-desorption isotherms of CN and 2H MS-CN (PD); (b) Barrett-Joyner-Halenda pore size distribution plot.

Table 4.1 Structural properties of as-prepared catalysts.

Catalyst	S _{BET} (m ² /g)	Pore Volume (cm ³ /g)	Mean Pore Size (nm)
C ₃ N ₄	98.5	0.152	4.7
2H MS-CN (PD)	70.6	0.111	4.8
2H MS-CN (SC)	92.9	0.151	4.9
1T MS-CN (SC)	68.8	0.132	4.9
2H MS-CN (TD)	86.4	0.133	4.6

4.2.3 Morphology and microstructure analysis by STEM

STEM-HAADF micrographs of Pt/CN, recovered after 6 h reaction time show a uniform distribution of Pt NPs (single atoms, clusters and particles < 5 nm) on the surface of CN (Fig. 4.5a, Fig. A.4a plots l-r and Fig. A.6) which is similar to that observed for Pt/CN in the presence of TEOA as sacrificial agent.³⁶³

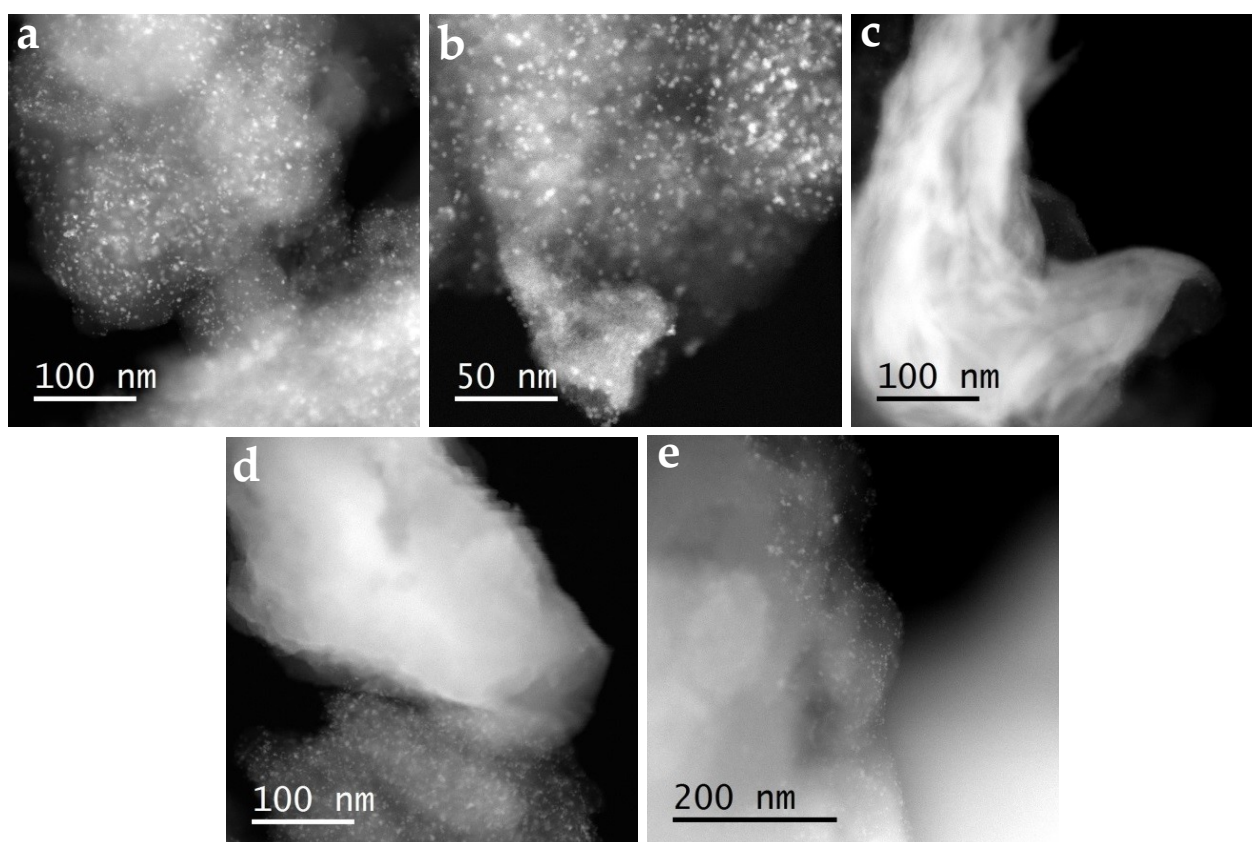


Figure 4.5 STEM-bright field (BF) micrographs of catalysts exposed to UV-vis irradiation for 6 h in the presence of lactic acid. (a) Pt/CN, (b) Pt/2H MS-CN (PD), (c) Pt/2H MS-CN (SC), (d) Pt/1T MS-CN (SC), (e) Pt/2H MS-CN (TD).

In the used composite Pt/2H MS-CN (PD) (Fig. 4.5b and Fig. A.4b plots l-r), bright areas of MoS₂ can be seen in contact with less intense areas of C₃N₄. The MS phase consists of small units with a certain short range order (Fig. A.4b, plots m and r). These units agglomerate in a disordered manner as opposed to the structures achieved by the other preparation method. The Pt NPs are more or less equally distributed on the CN and MS phase with a slight tendency to be more enriched on the CN phase. This is also supported by EDX measurements (Fig. A.8). In the other three samples Pt/2H MS-CN (SC), Pt/1T MS-CN (SC) and Pt/2H MS-CN (TD) markedly larger MS particles are formed (Fig. 4.5c-e and Fig. A.4c-e plots l-r) in which even the

layered crystalline structure of the 2H MoS₂ phase can be seen (Figure 4.5c, A.4c, A.5). This agrees well with the fact that the XRD patterns of sample Pt/2H MS-CN (SC) shows peak of the MS phase while these are not evident in sample Pt/2H MS-CN (PD) (cf. Fig. 4.1b). The formation of smaller and higher dispersed MS particles in sample Pt/2H MS-CN (PD) may have been promoted by the photodeposition procedure of MoS₂ since this is known to create a very high dispersion of the photodeposited species.³⁶⁵ The Pt NPs in samples Pt/2H MS-CN (SC), Pt/1T MS-CN (SC) and Pt/2H MS-CN (TD) are even more enriched on the CN phase while the MS phase contains much less Pt. This is also evident from EDX analysis (Fig. A.5, A.8-A.10). This is different from our previously studied AgIn₅S₈/C₃N₄ composites, in which Pt NPs were deposited preferentially on the sulphide phase (Chapter 3).³⁶³ A possible reason may be too fast charge recombination in big MoS₂ particles that hinders diffusion of photoexcited electrons to the surface of MoS₂ where they would be needed to reduce the Pt⁴⁺ precursor to metallic particles. An indication for such fast charge recombination in MoS₂ is also evident from PL measurements discussed below.

4.2.4 Surface chemical analysis by XPS

As shown in our previous work the surface of the composites is prone to changes under photocatalytic conditions.³⁶³ Therefore, we performed XPS analysis on the most active catalyst 2H MS-CN (PD) and the least active sample 2H MS-CN (TD) before and after use in the catalytic reaction, i. e. without and with deposited Pt particles to elucidate the surface elemental composition and valence states (Fig. 4.6 and Fig. A.11-A.14).

The 3d_{3/2} and 3d_{5/2} peaks of Mo⁴⁺ in the Mo 3d spectra of both samples fall at binding energies characteristic for the 2H phase of MoS₂ (233.4 and 230.3 eV, Fig. 4.6a).³⁶⁶ Besides, a Mo 3d doublet for Mo⁶⁺ is observed at 235.2 and 232.1 eV.³⁶⁶ This arises most probably from partial oxidation of MoS₂ to MoO₃ at the surface¹³. There is no much difference between the Mo 3d spectra of both samples. Comparison of the experimental atomic percentages found by XPS with the theoretical values assuming a homogeneous elemental distribution in the whole sample shows that the relative proportion of Mo on the surface is almost the same as in the bulk phase, suggesting a similar distribution of Mo in the bulk and on the surface of both fresh samples (Table S3). This holds true also for the proportion of sulfur (S:Mo ratio) in the most active sample 2H MS-CN (PD). However, in the least active sample 2H MS-CN (TD) the surface S content is considerably higher. While the S 2p spectra of the former sample show only one peak around 163.5 eV associated with MoS₂,^{360, 367} a second feature at about 169 eV is visible in the S 2p spectrum of sample 2H MS-CN (TD). This is characteristic of surface sulfate species, likely formed during preparation of 2H MS-CN (TD), which included a thermal decomposition step (Fig. 4.6c). Though this was performed in argon, traces of oxygen might have promoted formation of surface sulfate that is also described in the literature.³⁶⁸

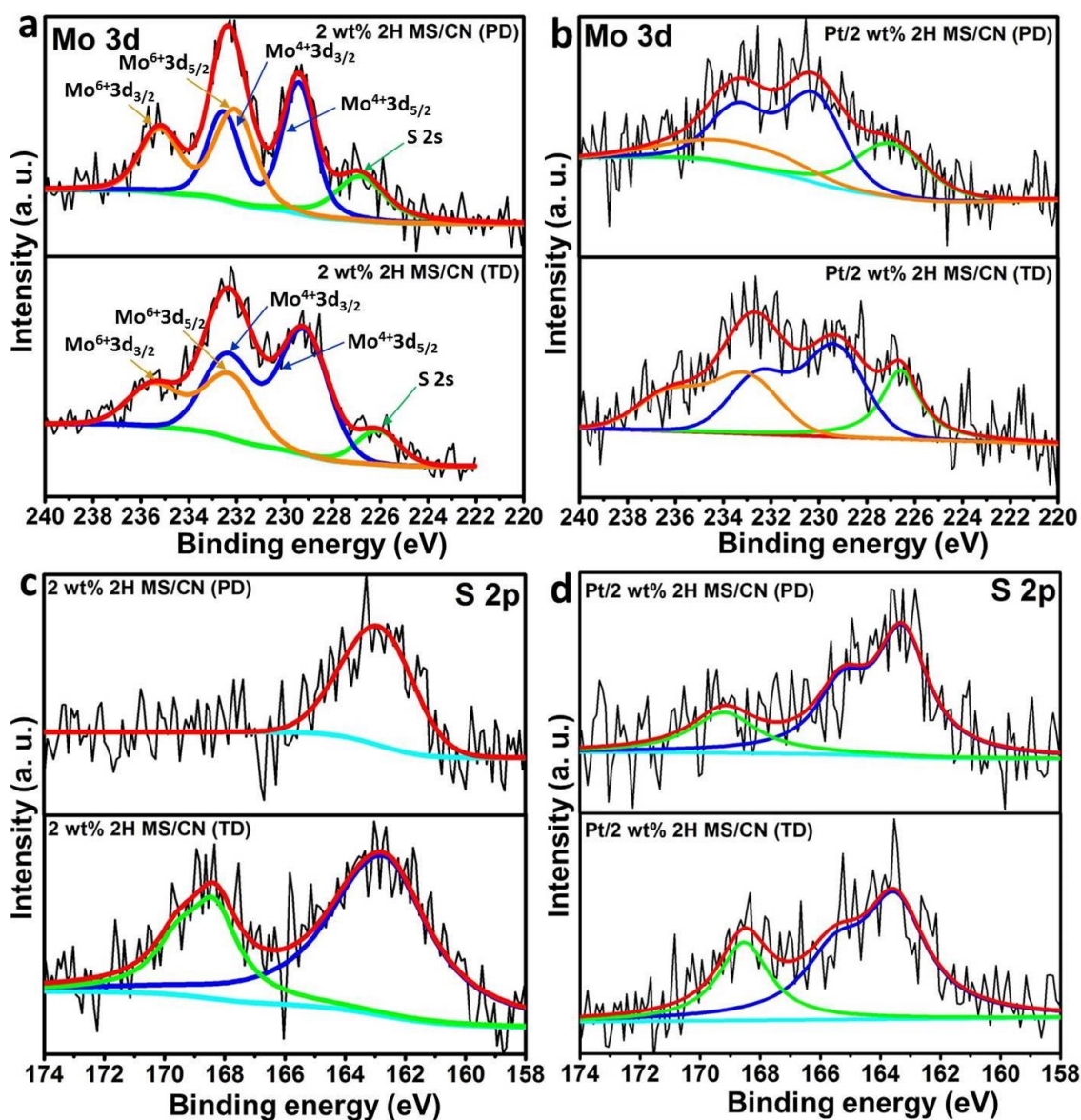


Figure 4.6 XPS spectra of 2H MS-CN (PD) and 2H MS-CN (TD) in the Mo 3d and S 2p region before (a and c) and after 6h of reaction (b and d).

After use in the photocatalytic reaction, the weight percentage of both Mo and S in the whole sample (determined by ICP-OES, Table S2) decreased. This indicates some leaching of Mo and, to a smaller extent, also of S during reaction. The decrease of Mo on the surface is especially pronounced, leading to a strong increase of the S:Mo surface ratio in the used catalysts (Table S3). Moreover, the sulfate XPS peak is more pronounced after use in sample Pt/2H MS-CN (TD) and it is stronger compared to the more active sample Pt/2H MS-CN (PD), in which this peak appears for the first time after use (Fig.4.6d). The oxidation of sulfur species during photocatalysis is not uncommon and also exploited e.g. in the photocatalytic oxidative desulfurization.³⁶⁸ The formed sulfate, however, could interact with the surface Pt species and reduce their activity for proton reduction.

During the photocatalytic reaction, Pt is deposited on the surface of both samples. The Pt4f spectra in Fig. A.14 show signals from Pt⁰ (72.6 and 75.7 eV) and Pt²⁺ (74.9 and 77.7 eV). Interestingly, these values are somewhat higher compared with literature values for surfaces of bulk samples (71.1 and 74.4 eV for Pt⁰; 72.4

and 76.0 eV for Pt²⁺).³⁶⁹ This may be due to the very small particle size (evidenced also by TEM).³⁷⁰⁻³⁷³ Another reason may be strong metal-support interaction which is known to induce shifts in binding energy values.^{374, 375} Such shifts have also been observed by other authors in related substrates.^{132, 201, 376, 377} The total surface Pt content is highest for the least active sample Pt/2H MS-CN (TD) (Table S3), suggesting that not every Pt center is catalytically active or accessible by the reactants. Comparing the TEM investigations, a partial coverage of CN by MoS₂ particles may account for this. Interestingly, in the most active sample Pt/2H MS-CN (PD) the percentage of Pt²⁺ is by far lowest and the amount of surface Pt⁰ is somewhat higher than in Pt/CN. This suggests that it might be the Pt⁰ centers that are active for hydrogen generation. On the other hand, the amount of Pt⁰ is highest in the least active sample Pt/2H MS/CN (TD). This suggests that the surface percentage of Pt⁰ is one but not the only property that governs catalytic activity. It will be demonstrated below, that the amount of reactive photoelectrons is another crucial factor for high photocatalytic performance (vide infra, EPR and photoluminescence spectroscopy).

Table 4.2 Elemental composition of fresh and used catalysts derived from CHNS and ICP-OES.

Sample	C (wt.%)	N (wt.%)	Mo ^{ICP} (wt.%)	S ^{ICP} (wt.%)	Pt ^{ICP} (wt.%)
2H MoS ₂ (HT)			61.55	36.82	-
1T MoS ₂ (ST)			48.64	33.67	-
2H MoS ₂ (TD)			48.44	38.55	-
C ₃ N ₄	31.99	61.75	-	-	-
2H MS-CN (PD)	30.96	56.81	0.85	0.74	-
2H MS-CN (SC)	30.46	57.13	1.04	0.70	-
1T MS-CN (SC)	30.56	57.27	0.88	0.61	-
2H MS-CN (TD)	31.69	58.20	1.0	0.79	-
MS-CN theoretically	38.36	59.64	1.20	0.80	-
Pt/CN			-	-	2.70
Pt/2H MS-CN (PD)			0.62	0.63	2.68
Pt/2H MS-CN (SC)			0.86	0.51	2.70
Pt/1T MS-CN (SC)			0.61	0.54	2.72
Pt/2H MS-CN (TD)			0.67	0.67	2.70

Table 4.3 Surface elemental composition of fresh and used catalysts derived from XPS.

Sample	C (at.%)	N (at.%)	O (at.%)	Mo (at.%)	S (at.%)	S:Mo Ratio	Pt (at.%)	Pt ⁰ (at.%)	Pt ²⁺ (at.%)
C ₃ N ₄	44.67	52.59	2.74	-	-	-	-	-	-
2H MS-CN (PD)	47.80	49.47	2.41	0.11	0.20	1.82	-	-	-
2H MS-CN (TD)	41.42	55.34	2.65	0.15	0.46	3.07	-	-	-
MS-CN theoretically ^a	42.64	56.86	-	0.167	0.334	2	-	-	-
Pt/CN	46.05	48.93	4.12	-	-	-	0.90	0.66	0.24
Pt/CN theoretically ^a	42.80	57.06	-	-	-	-	0.14	-	-
Pt/2H MS-CN (PD)	45.21	49.03	4.43	0.09	0.47	5.22	0.77	0.69	0.08
Pt/2H MS-CN (TD)	47.43	45.75	4.59	0.12	0.75	6.25	1.38	1.16	0.22

^a calculated under the assumption that the elemental composition at the surface is the same as in the bulk.

4.3 Mechanism: charge separation and transfer

4.3.1 Monitoring charge separation and transfer by in situ-EPR

In previous work it was shown that in situ-EPR spectroscopy is a unique method to analyze separation and transfer of photoexcited electrons in semiconductors based on oxides³³⁵ or carbon nitrides.^{76, 363} All C_3N_4 containing samples show a narrow isotropic EPR signal with Lorentzian line shape at a g -value of 2.0047 already in the dark (Fig. A.15). This is attributed to single electrons that are trapped at surface sp^2 carbon atoms of heptazine units.³⁵³ Upon photoexcitation, more electrons are excited from the valence to the conduction band (formed of N 2p and C 2p orbitals, respectively²²) and trapped at carbon defects.³⁴⁹ This causes an intensity increase of this EPR signal, which is reversible upon light switch off due to charge recombination (Fig. 4.7a). Thus, the increase of the EPR signal intensity of bare CN under light irradiation (Fig. 4.7b, open black circle) is a measure for the total number of electrons that can be excited and trapped in pure C_3N_4 while the EPR intensity after light switch-off (red open circle in Fig. 4.7b) reflects electrons that do not immediately recombine.

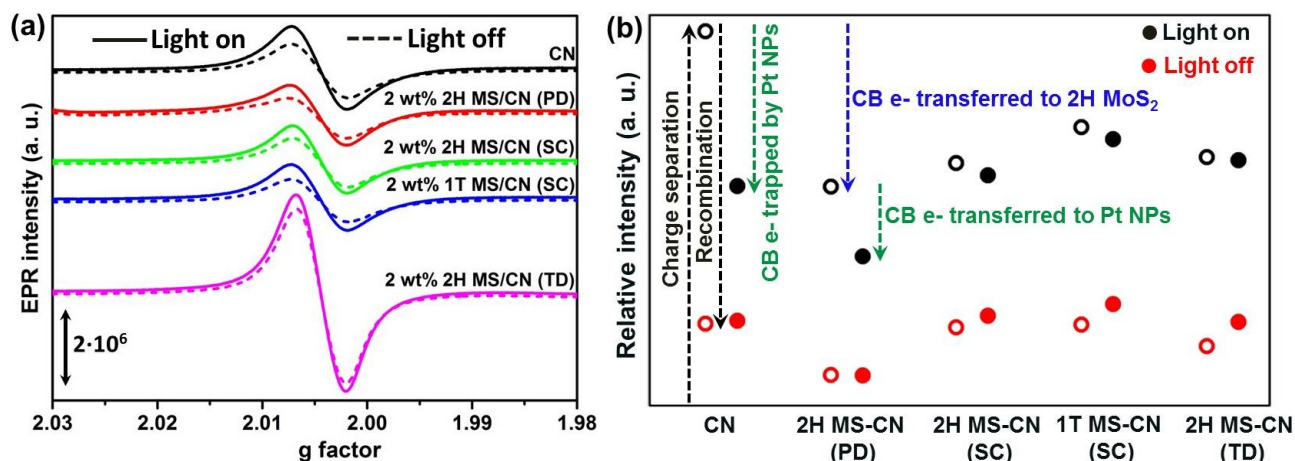


Figure 4.7 (a) EPR spectra of the as-prepared catalysts during UV-vis light irradiation (solid lines) and after light switched-off (dashed lines). (b) Double integral of the EPR CB e⁻ signal intensity (initial background signal in the dark was subtracted) during UV-vis light irradiation (black circles) and after light switched-off (red circles). Hollow circles represent fresh catalysts (without Pt NPs) and solid circles represent used catalysts (with Pt NPs). CN - C_3N_4 ; PD - 2H MS-CN (Photodeposition method); SC (2H) - 2H MS-CN (Sonochemical method); SC (1T) - 1T MS-CN (Sonochemical method); TD - 2H MS-CN (Thermal decomposition method).

As shown in Fig. 4.1b, the photocatalytic H_2 production activity is negligible when bare CN is used as photocatalyst. Therefore, Pt NPs were photodeposited on the surface of CN to provide active sites with sufficient potential for H_2 production. To prove the impact of those Pt NPs on electron transfer during the photocatalytic reaction, Pt/CN has been removed from the photocatalytic reactor after 6 h and characterized by EPR spectroscopy with and without UV-vis irradiation. From Fig. 4.7b it is evident that the EPR signal intensity of Pt/CN under light irradiation is much smaller than that of bare CN (compare the black hollow and solid circles). This is due to fast transfer of CB e⁻ from CN to Pt from which they can react with H^+ to produce H_2 .⁷⁶

When MoS₂ is deposited on the surface of C₃N₄, a similar drop of the CB e⁻ EPR signal intensity is observed already without Pt NPs (hollow black circles in Fig. 4.7b). This suggests that those electrons are quickly transferred via the phase boundary to MoS₂. However, catalytic tests revealed that Pt-free MS-CN materials are not active in photocatalytic H₂ evolution. This implies that excited electrons transferred from the conduction band of C₃N₄ to that of MoS₂ return too quickly to the valence band of the latter so that they cannot be used for proton reduction, which is also supported by photoluminescence results discussed below.

Deposition of Pt NPs onto the MS-CN composites leads to a further drop of intensity, due to electron transfer from the CN and/or MS phase to Pt NPs (black solid circles in Fig. 4.7b). This intensity drop is strongest, indicating the highest number of CB e⁻ transferred to Pt, for the most active sample Pt/2H MS-CN (PD) and decreases as catalytic activity is reduced (compare Fig. 4.1b and 4.7b). A much smaller decrease in intensity is observed for the less active samples Pt/2H MS-CN (SC), Pt/1T MS-CN (SC) and Pt/2H MS-CN (TD). This implies a lower electron transfer from MS-CN to Pt.

4.3.2 Photoluminescence spectroscopy study

Photoluminescence (PL) occurs upon recombination of photogenerated electrons and holes. It is therefore commonly employed to investigate the separation efficiency of photogenerated charge carriers.³³⁷ The PL spectra of MoS₂, CN and MS-CN composites after excitation at 370 nm are shown in Fig. 4.8a.

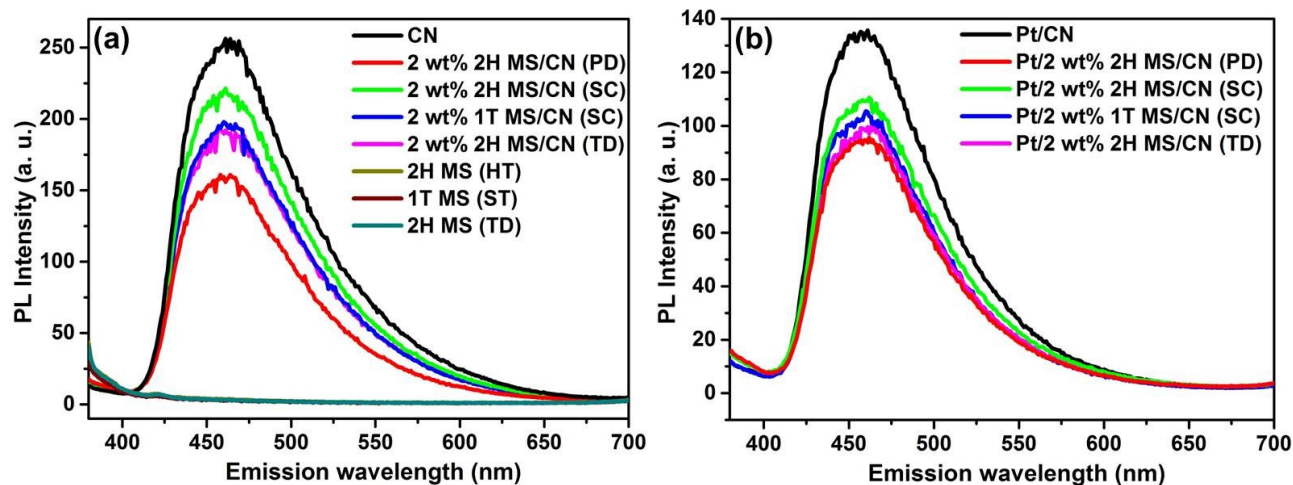


Figure 4.8 Photoluminescence spectra of (a) the as-synthesized catalysts; (b) recovered Pt containing catalysts after 6 h under UV-vis light irradiation.

It can be seen that pure CN exhibits a strong emission at 461 nm, which arises from charge carrier recombination via the band gap, whereas the pure MoS₂ samples show no PL, despite the fact that they absorb UV-vis light able to excite electrons from the valence band to the conduction band (Fig. 4.8a). This suggests that electron-hole recombination in the pure MoS₂ samples might be too fast to emit PL radiation. Upon loading of MoS₂ onto CN, the PL emission peak intensity decreased, which is an indication for electron transfer from the conduction band of CN to that of MoS₂ (Fig. 4.8a). A similar effect was also observed for other CN-based photocatalysts such as AgIn₅S₈/C₃N₄,³⁶³ In₂S₃/g-C₃N₄,³⁵⁵ ZnFe₂O₄/g-C₃N₄,³⁵⁶ Cu₂O/NaTaO₃,³⁵⁷ g-C₃N₄/NiFe-LDH³⁵⁸ and MoS₂/g-C₃N₄.³⁵⁹ When Pt is deposited on the surface of the photocatalysts, the PL

signal intensity decreased even further (Fig. 4.8b). The reason might be a transfer of excited CB electrons from CN to Pt or from CN via MoS₂ to Pt, respectively. As the reduction potential of Pt is sufficient to reduce protons, these electrons are able to form H₂ from H⁺. As can be seen in both plots, the emission intensity decrease is highest in the case of (Pt)/2H MS-CN (PD) which is a further indication for effective electron transfer from the CB of CN directly or via MoS₂ to Pt NPs. In the latter case, the electron transfer efficiency is hampered by fast charge carrier recombination in MoS₂ (see PL spectra of pure MoS₂ samples) only allowing increased charge transfer efficiency in the case of thin MoS₂ layers as present in 2H MS-CN (PD).

4.4 Conclusions

Pt/2H MS-CN (PD) showed the highest photocatalytic hydrogen production activity of all investigated MS-CN composites, and it is the only one in which deposition of MoS₂ improves the performance of Pt/CN. This might be due to the fact that, in Pt/2H MS-CN (PD), MoS₂ forms a very thin overlayer on C₃N₄ which does not hinder light absorption and charge separation in C₃N₄ nor charge transfer from the CB of C₃N₄ through the MoS₂ layer to the Pt NPs. Rather it might be this thin layer that prevents fast charge recombination within C₃N₄. In samples Pt/2H MS-CN (SC), Pt/1T MS-CN (SC) and Pt/2H MS-CN (TD), which all revealed lower activity than sulfide-free Pt/CN, MoS₂ is attached to C₃N₄ in form of big crystalline particles in which even lattice planes were detected by STEM. These particles might partially hinder absorption of visible light by C₃N₄ (evident from a decrease of the UV-vis band between 450 and 550 nm). Moreover, they hinder transfer of electrons from the CB of C₃N₄ to the Pt particles, as evidenced by in situ-EPR and photoluminescence results. Moreover, interaction with surface sulfate, the amount of which is highest in the least active sample Pt/2H MS-CN (TD), may lower the ability of Pt to reduce protons.

In summary, the beneficial performance of Pt/2H MS-CN (PD) is attributed to the formation of an effective heterojunction between the C₃N₄ surface and a thin MoS₂ overlayer that enables an efficient electron transfer from CN via MoS₂ to Pt.

5 Influence of different sacrificial agents on photocatalytic H₂ production over C₃N₄ photocatalysts

In addition to the work described above the C₃N₄ has been subjected to photocatalytic hydrogen evolution in the presence of platinum with various common sacrificial reagents. The results obtained from these experiments are summarized in the following sections.

5.1 Catalytic activity

Sacrificial agents also called sacrificial reductants (SR), electron donors or hole scavengers play an important role in photocatalytic H₂ production. They are essentially providing the electrons for the reduction of the protons to H₂ by reducing the holes in the semiconductor after their photoexcitation. To check the influence of this important class of reactants photocatalytic H₂ production over C₃N₄ photocatalysts by using various acidic and basic sacrificial agents in the presence of Pt as co-catalyst under UV-vis light irradiation was carried out (Fig. 5.1).

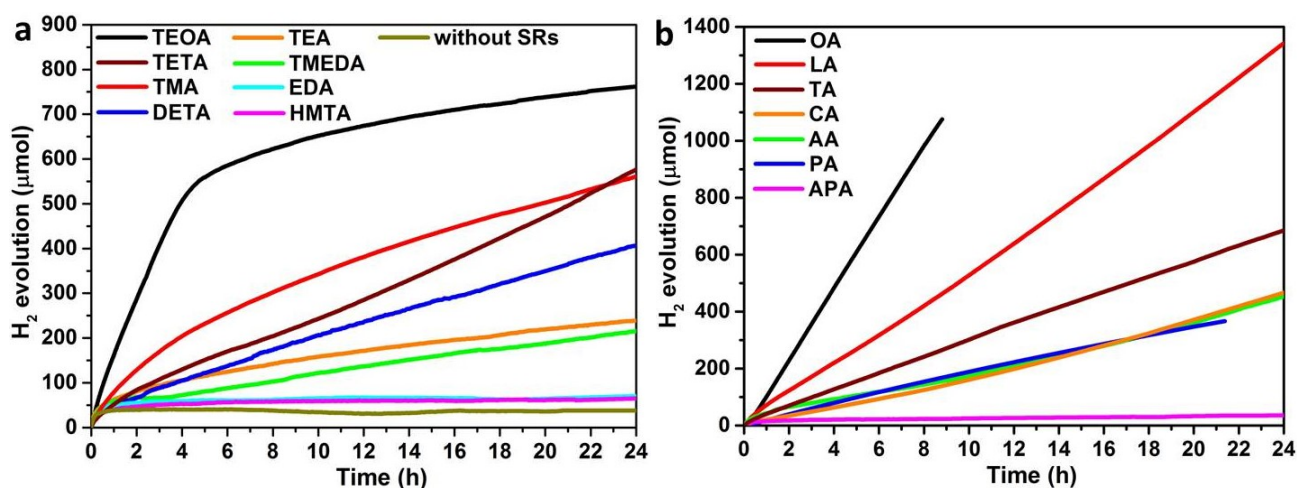


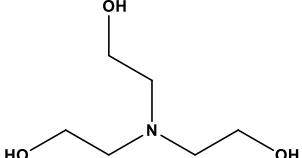
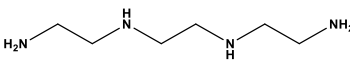
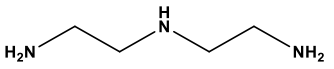
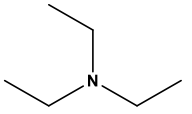
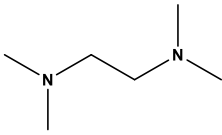
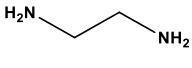
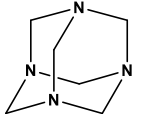
Figure 5.1 Photocatalytic H₂ production activity of Pt/CN by using various sacrificial reagents under UV-vis light irradiation. **(a)** Basic medium; TEOA–Triethylamine, TETA–Triethylenetriamine, TMA–Trimethylamine, DETA–Diethylenetriamine, TEA–Triethylamine, TMEDA–N,N,N',N'-Tetramethylethylenediamine, EDA–Ethylenediamine and HMTA–Hexamethylenetetramine. **(b)** Acidic medium; OA–Oxalic acid, LA–Lactic acid, TA–L-Tartaric acid, CA–Citric acid, AA–L-Ascorbic acid, PA–Pyruvic acid and APA–L-Aspartic acid.

The pH value of the solution is supposed to be an important factor that may influence the reactivity, because protons are the educt in the hydrogen generation reaction. The redox potential is also of great importance because it directly refers to the capability of the SRs to donate electrons to fill the holes in the semiconductor. Furthermore, factors such as collision probability and the conversion mechanism of the sacrificial reagent may also play a role in the reaction.

5.2 Photocatalytic H₂ production with basic sacrificial reagents

As shown in Fig. 5.1a, CN without sacrificial agents shows poor photocatalytic H₂ production activity (even in the presence of a Pt precursor) due to inefficient or missing hole scavenging capability of water. The experiments in the presence of different basic sacrificial reagents indicate that the photocatalytic H₂ production activity of Pt/CN can be enhanced to different degrees (Table 5.1). Among these agents, TEOA aqueous solution gives highest H₂ production compared to the other sacrificial agents. This is most likely associated with its redox potential that is lowest within the class of investigated sacrificial agents in this work (cf. Table 1).

Table 5.1. Compilation of different basic sacrificial agents that were used in the photocatalytic hydrogen production reaction with C₃N₄ and Pt. Conditions: 24.5 mg C₃N₄, 0.2 ml H₂PtCl₆ solution with $c = 0.25 \text{ mg}\cdot\text{mL}^{-1}$ (0.5 mg Pt), $n_{\text{SR}} = 18,94 \text{ mmol}$ (0,757 mM), total volume = 25 mL, Xe lamp without filter, 1.5 W output, 25 °C.

Entry	Sacrificial agents	Structure	pK _b	Oxidation potential (V vs. SCE)	H ₂ (μmol) (24 h)	H ₂ (μmol h ⁻¹ g ⁻¹)
1	Triethanolamine (TEOA)		pK _b = 6.26	0.57 ²⁸⁷	761.7	1259.5
2	Triethylenetetramine (TETA)		pK _{b1} = 3.24	-	576.3	960.5
3	Trimethylamine (TMA)		pK _b = 4.20	0.76 ³⁷⁸	561.0	935.0
4	Diethylenetriamine (DETA)		pK _{b1} = 3.98 pK _{b2} = 4.79 pK _{b3} = 9.58	-	405.2	675.3
5	Triethylamine (TEA)		pK _b = 3.25	0.69 ²⁸⁷	238.8	394.8
6	N,N,N',N'-Tetramethylethylenediamine (TMEDA)		pK _b = 5.85	0.66 ³⁷⁸	215.8	359.7
7	Ethylenediamine (EDA)		pK _{b1} = 4.02 pK _{b2} = 6.44	1.30 ³⁷⁹	70.1	116.8
8	Hexamethylenetetramine (HMTA)		pK _b = 9.5	1.37 ³⁷⁸	64.7	107.8

A lower redox potential means an easier oxidation and more efficient hole scavenging ability. Comparison of these different potentials with the hydrogen evolution activity demonstrated in most cases that the sacrificial agents with lower redox potential allowed for higher photocatalytic H₂ production (Fig. 5.1a). However, there is no strict correlation suggesting also other parameters being involved (Fig. 5.2).

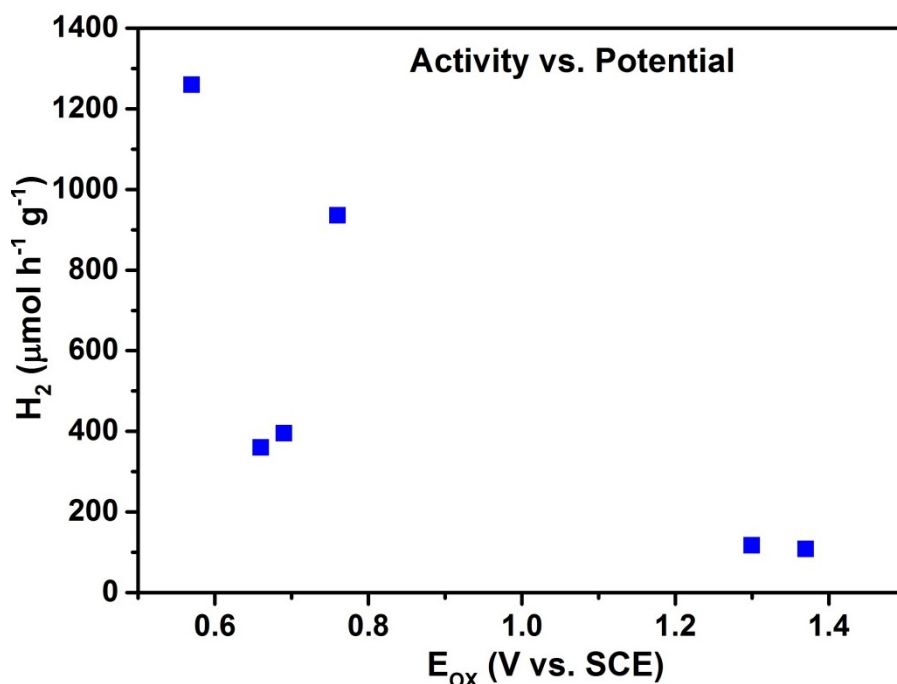


Figure 5.2 Dependency of the observed hydrogen evolution activity from the redox potential of the sacrificial reagent (redox potential values taken from Table 5.1).

One issue is comprised by the irreversibility of the redox processes of the different sacrificial agents. The main other influencing factor may arise from the mechanism. A good example may be given by the comparison of TEOA and TEA. As can be seen in Fig. 5.3 the degradation pathway comprises the same steps and intermediates.²⁸⁷

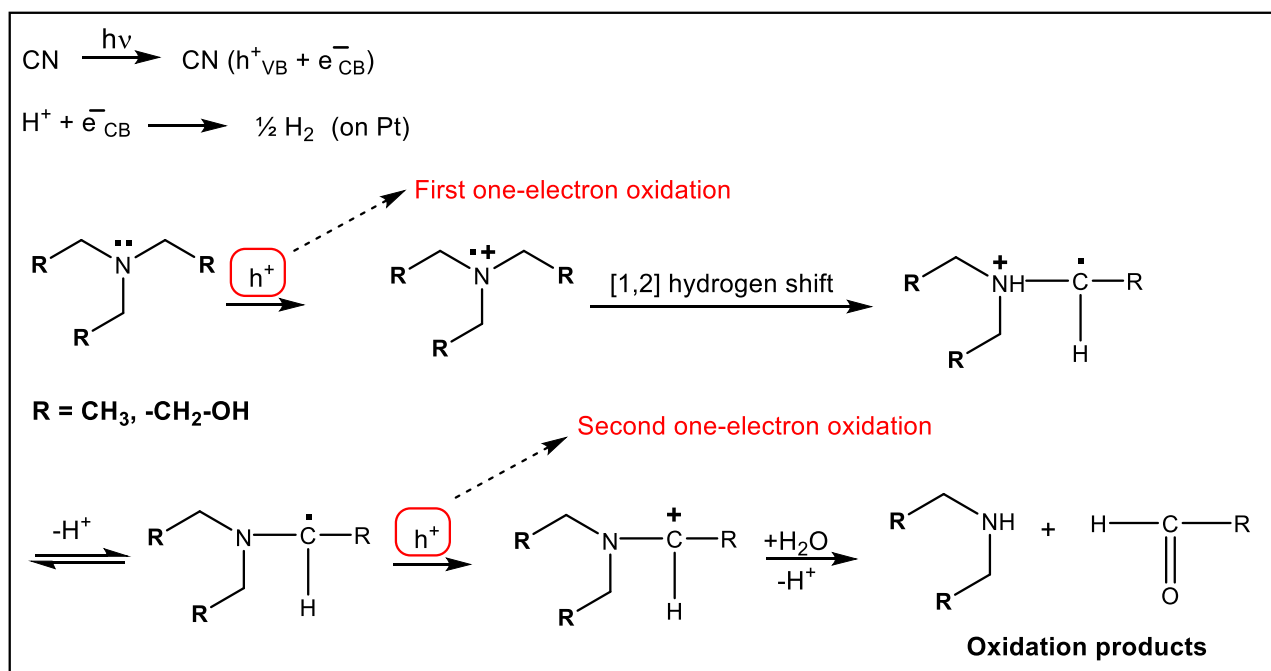


Figure 5.3 Degradation pathway of TEOA (R = CH₂OH) and TEA (R = CH₃) upon two-electron oxidation.

Starting from the formation of a nitrogen centered radical upon initial oxidation, a carbon centered radical is formed and finally, a second oxidation occurs. There are two proton abstraction steps implying a pH dependency. It is reasonable to assume a better proton abstraction capability at higher pH.⁴⁶ However, even though TEA generates the more basic solution, the hydrogen productivity is higher in the case of TEOA. This also points to the influence of more factors and it is also obvious that TEA and TEOA are used in excess so that proton abstraction is not the rate determining step in the investigated system here. Another point in the mechanism is the initial formation of the aminyl radical after oxidation that might either react again with reduced species (intermediate $[C_3N_4]^-$ or H_2) or further to a carbon centered radical.⁴⁶ As the carbon centered radical has reducing power itself it is beneficial for H_2 productivity.^{46, 380-383} Another aspect covers the capability of the reaction products to escape from the solvent cage. The more efficient the reaction products escape the higher the productivity, because there will be no accumulation of reductive species then.^{46, 384} Also, the presence of either a reductive or an oxidative quenching mechanism similar to homogeneous systems may affect the proton reduction.⁴⁶ If first the protons are reduced and hole quenching occurs subsequently, an oxidative quenching mechanism is present, while hole quenching followed by proton reduction comprises the reductive mechanism.⁴⁶ In the case of TEA and TEOA, both mechanisms are possible, that are influenced by the choice of the photosensitizer.⁴⁶ Moreover, also the miscibility of the SR with water may play an important role as this directly affects the "active" concentration of the SR in solution.⁴⁶ In this respect, TEOA with its hydroxyl groups has advantages compared to TEA, which might be a reasonable explanation for the largely decreased activity of TEA compared with TEOA. Also TMA with an even higher redox potential exhibits a higher activity as TEA.

5.3 Photocatalytic H_2 production with acidic sacrificial reagents

Comparison of the results obtained with SRs that are acidic under the chosen reaction conditions shows also huge differences (Fig. 5.1). As the data basis on redox potentials is quite poor here, these cannot be discussed here. Compared to the results obtained under basic conditions higher activities have been observed with the best performing acidic SRs. This implies an influence of the pH. However, as can be derived from the pK_a values given in Table 5. 2, no real trend can be seen suggesting also the influence of other parameters, most likely solubility and redox potential as well as cage escape probability.

Table 5.2. Compilation of different acidic sacrificial reagents that were used in the photocatalytic hydrogen production reaction with C_3N_4 and Pt. Conditions: 24.5 mg C_3N_4 , 0.2 ml H_2PtCl_6 solution with $c = 0.25$ $mg \cdot mL^{-1}$ (0.5 mg Pt), $n_{SR} = 18,94$ mmol (0,757 mM), total volume = 25 mL, Xe lamp without filter, 1.5 W output, 25 °C.

Entry	Sacrificial agents	Structure	pKa	H ₂ (μmol)	H ₂ (μmolh ⁻¹ g ⁻¹)
1	Oxalic acid (OA)		pKa ₁ = 1.23 pKa ₂ = 4.19	1075.5 (9 h)	5371.7
2	Lactic acid (LA)		pKa ₁ = 3.86 pKa ₂ = 15.1	1342.1 (24 h)	2219.5
3	L-tartaric acid (TA)		pKa ₁ = 2.89 pKa ₂ = 4.40	685.1 (24 h)	1141.8
4	Citric acid (CA)		pKa ₁ = 3.13 pKa ₂ = 4.76 pKa ₃ = 6.40	466.2 (24 h)	777.0
5	L-ascorbic acid (AA)		pKa ₁ = 4.10 pKa ₂ = 11.80	452.9 (24 h)	754.8
6	Pyruvic acid (PA)		pKa = 2.50	366.3 (21 h)	697.7
7	L-aspartic acid (APA)		pKa (A) = 2.09 pKa (B) = 9.82 pKa (C) = 3.86	35.2 (24 h)	58.7

Another point might arise from the mechanism. While the acids with carboxy groups form thermodynamically stable CO_2 , ascorbic acid is transformed to the trioxo product dehydroascorbic acid (see Fig. 5.4 and 5.5).^{46, 314, 318-320, 385-387 16} It shall be noted here that in the carboxylic acids CO_2 abstraction occurs always and in oxalic acid, the formation of a second CO_2 molecule may enhance H_2 production. A comparison between the acids with carboxy function is difficult as there are no potentials available. However, considering group effects, one can see that lactic acid with its electron donating $CH_3-CH(OH)$ -group is much more active than pyruvic acid with an acyl group adjacent to the carboxy functionality.^{386, 387} A more electron withdrawing adjacent group will potentially decelerate carbon dioxide formation that is the final step in the conversion mechanism of carboxylic acids.^{314, 318-320, 385-387}

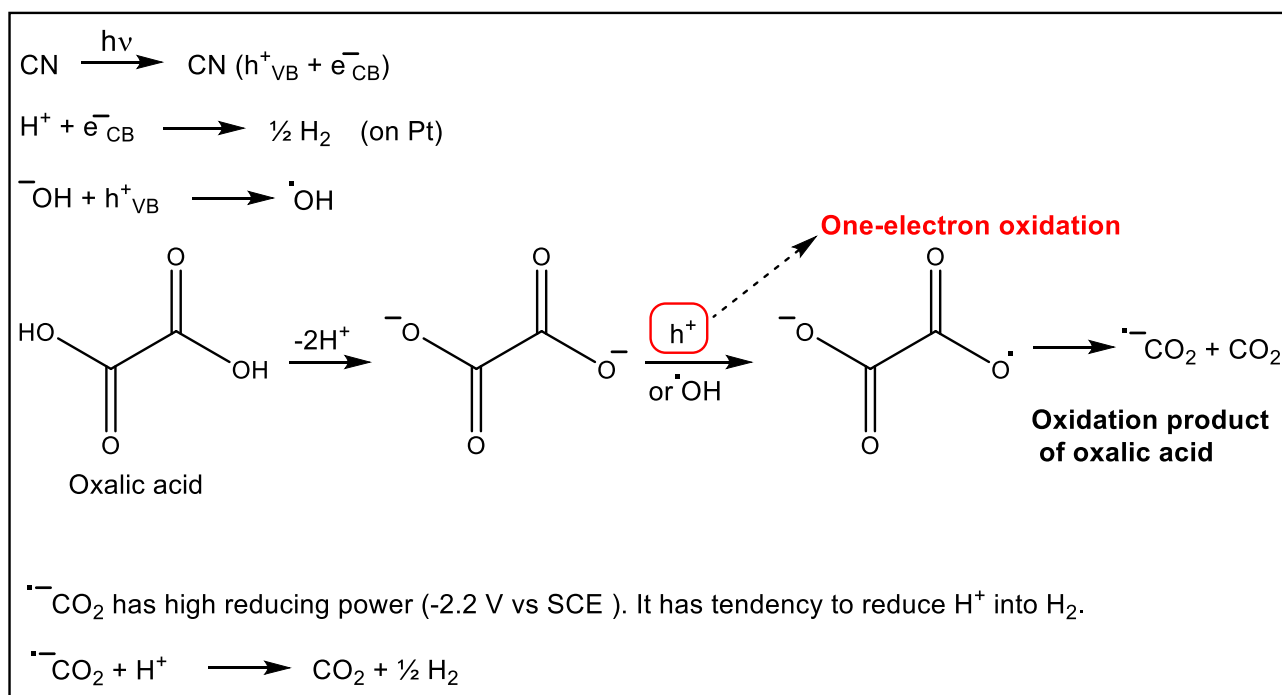


Figure 5.4 Degradation pathway of oxalic acid upon one-electron oxidation.

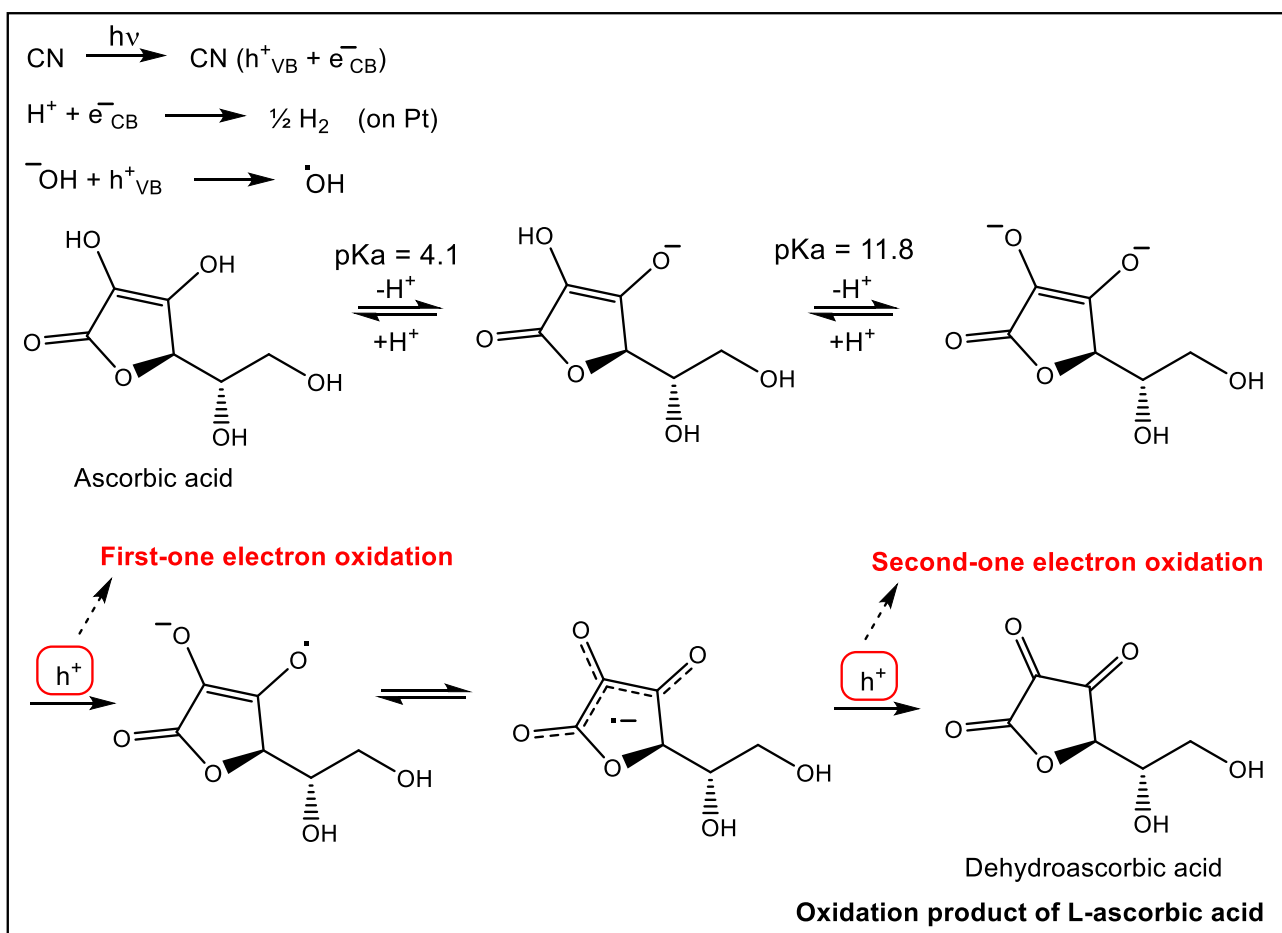


Figure 5.5 Degradation pathway of L-ascorbic acid upon two-electron oxidation.

Ascorbic acid undergoes a two-electron oxidation pathway (Fig. 5.5)^{388, 46}. (Fig. 5.5). It dissociates into ascorbate anions and H^+ in water. Holes in the VB can react with ascorbate anions to produce ascorbate anion radical. Besides, hydroxyl radicals ($\cdot\text{OH}$) can also react with ascorbate

anion radicals. Subsequently, this ascorbate anion radical can react with another hole to produce dehydroascorbic acid ³⁸⁸. By this way, ascorbic acid reacts irreversibly with the photogenerated holes to suppress the rate of electron-hole pair recombination and increases the rate of hydrogen evolution on Pt.

5.4 Conclusion

Based on the aforementioned results, a huge influence of the sacrificial reagent was observed in the present work. The application of the same semiconductor and the same co-catalyst in each experiment provides a certain degree of comparability of the results. However, the overall conclusion that can be drawn from these experiments is limited by issues such as different solubility, distinct degradation mechanisms and changing pH as well as different solvent cage escape probabilities. More detailed investigations by EPR, NMR and IR spectroscopy in combination with kinetic analyses would be necessary for a deeper understanding of the underlying processes.

References

1. N. Armaroli and V. Balzani, *Angew. Chem.*, 2007, **46**, 52-66.
2. N. S. Lewis and D. G. Nocera, *Proc. Natl. Acad. Sci.*, 2006, **103**, 15729-15735.
3. UNO - World Population Prospects-The 2012 Revision.
4. T. Abbasi and S. A. Abbasi, *Renew. Sust. Energ. Rev.*, 2011, **15**, 1828-1834.
5. C. McGlade and P. Ekins, *Nature.*, 2015, **517**, 187-190.
6. G. Marbán and T. Valdés-Solís, *Int. J. Hydrog. Energy.*, 2007, **32**, 1625-1637.
7. A. Sartbaeva, V. L. Kuznetsov, S. A. Wells and P. P. Edwards, *Energy Environ. Sci.*, 2008, **1**, 79-85.
8. S. A. Wells, A. Sartbaeva, V. L. Kuznetsov and P. P. Edwards, *Encyclopedia of Inorganic Chemistry.*, 2011, 1- 24.
9. S. Badoga and A. K. Dalai, *Sustainable Utilization of Natural Resources*, 2017, 121-143.
10. M. Grätzel, *Nature.*, 2001, **414**, 338-344.
11. P. D. Tran, L. H. Wong, J. Barber and J. S. C. Loo, *Energy Environ. Sci.*, 2012, **5**, 5902-5918.
12. G. Colón, *Appl. Catal. A.*, 2016, **518**, 48-59.
13. A. Kudo and Y. Miseki, *Chem. Soc. Rev.*, 2009, **38**, 253-278.
14. X. Li, J. Yu, J. Low, Y. Fang, J. Xiao and X. Chen, *J. Mater. Chem. A.*, 2015, **3**, 2485-2534.
15. K. Takanabe and K. Domen, *ChemCatChem.*, 2012, **4**, 1485-1497.
16. J. A. Turner, *Science.*, 2004, **305**, 972-974.
17. A. Fujishima and K. Honda, *Nature.*, 1972, **238**, 37-38.
18. X. Chen, S. Shen, L. Guo and S. S. Mao, *Chem. Rev.*, 2010, **110**, 6503-6570.
19. S. Y. Tee, K. Y. Win, W. S. Teo, L. D. Koh, S. Liu, C. P. Teng and M. Y. Han, *Adv. Sci.*, 2017, **4**, 1600337.
20. G. Liao, Y. Gong, L. Zhang, H. Gao, G.-J. Yang and B. Fang, *Energy Environ. Sci.*, 2019.
21. J. Zhang, Y. Wang, J. Jin, J. Zhang, Z. Lin, F. Huang and J. Yu, *ACS Appl. Mater. Interfaces.*, 2013, **5**, 10317-10324.
22. X. Wang, K. Maeda, A. Thomas, K. Takanabe, G. Xin, J. M. Carlsson, K. Domen and M. Antonietti, *Nat. Mater.*, 2009, **8**, 76-80.
23. W. J. Ong, L. L. Tan, Y. H. Ng, S. T. Yong and S. P. Chai, *Chem. Rev.*, 2016, **116**, 7159-7329.
24. X. Wang, S. Blechert and M. Antonietti, *ACS Catal.*, 2012, **2**, 1596-1606.
25. S. Cao, J. Low, J. Yu and M. Jaroniec, *Adv. Mater.*, 2015, **27**, 2150-2176.
26. A. Naseri, M. Samadi, A. Pourjavadi, A. Z. Moshfegh and S. Ramakrishna, *J. Mater. Chem. A.*, 2017, **5**, 23406-23433.
27. W.-J. Ong, L.-L. Tan, Y. H. Ng, S.-T. Yong and S.-P. Chai, *Chem. Rev.*, 2016, **116**, 7159-7329.
28. S. Patnaik, S. Martha and K. M. Parida, *RSC Adv.*, 2016, **6**, 46929-46951.
29. S. Sun and S. Liang, *Nanoscale.*, 2017, **9**, 10544-10578.
30. J. Wen, J. Xie, X. Chen and X. Li, *Appl. Surf. Sci.*, 2017, **391**, 72-123.
31. Y. Zheng, L. Lin, B. Wang and X. Wang, *Angew. Chem. Int. Ed.*, 2015, **54**, 12868-12884.
32. S. Yin, J. Han, T. Zhou and R. Xu, *Catal. Sci. Technol.*, 2015, **5**, 5048-5061.
33. Z. Zhao, Y. Sun and F. Dong, *Nanoscale.*, 2015, **7**, 15-37.
34. M. Reza Gholipour, C. T. Dinh, F. Beland and T. O. Do, *Nanoscale.*, 2015, **7**, 8187-8208.
35. D. Jiang, J. Li, C. Xing, Z. Zhang, S. Meng and M. Chen, *ACS Appl. Mater. Interfaces.*, 2015, **7**, 19234-19242.
36. H. Wang, L. Zhang, Z. Chen, J. Hu, S. Li, Z. Wang, J. Liu and X. Wang, *Chem. Soc. Rev.*, 2014, **43**, 5234-5244.
37. C.-H. Lai, M.-Y. Lu and L.-J. Chen, *J. Mater. Chem.*, 2012, **22**, 19-30.

38. Y. Liu, Y. Li, H. Kang, T. Jin and L. Jiao, *Mater. Horiz.*, 2016, **3**, 402-421.
39. Q. Lu, Y. Yu, Q. Ma, B. Chen and H. Zhang, *Adv. Mater.*, 2016, **28**, 1917-1933.
40. K. Zhang and L. Guo, *Catal. Sci. Technol.*, 2013, **3**, 1672-1690.
41. J. L. White, M. F. Baruch, J. E. Pander Iii, Y. Hu, I. C. Fortmeyer, J. E. Park, T. Zhang, K. Liao, J. Gu, Y. Yan, T. W. Shaw, E. Abelev and A. B. Bocarsly, *Chem. Rev.*, 2015, **115**, 12888-12935.
42. Y. Qu and X. Duan, *Chem. Soc. Rev.*, 2013, **42**, 2568-2580.
43. I. F. Teixeira, E. C. M. Barbosa, S. C. E. Tsang and P. H. C. Camargo, *Chem. Soc. Rev.*, 2018, **47**, 7783-7817.
44. K. Maeda, *J. Photoch. Photobio. C.*, 2011, **12**, 237-268.
45. V. Kumaravel, M. Imam, A. Badreldin, R. Chava, J. Do, M. Kang and A. Abdel-Wahab, *Catalysts.*, 2019, **9**, 276-311.
46. Y. Pellegrin and F. Odobel, *C. R. Chim.*, 2017, **20**, 283-295.
47. J. Schneider and D. W. Bahnemann, *J. Phys. Chem. Lett.*, 2013, **4**, 3479-3483.
48. M. Wang, S. Shen, L. Li, Z. Tang and J. Yang, *J. Mater. Sci.*, 2017, **52**, 5155-5164.
49. X. Zhang, B. Peng, S. Zhang and T. Peng, *ACS Sustain. Chem. Eng.*, 2015, **3**, 1501-1509.
50. S. Cao, J. Low, J. Yu and M. Jaroniec, *Adv. Mater.*, 2015, **27**, 2150-2176.
51. D. Masih, Y. Ma and S. Rohani, *Appl. Catal. B.*, 2017, **206**, 556-588.
52. Y. Wang, X. Wang and M. Antonietti, *Angew. Chem. Int. Ed.*, 2012, **51**, 68-89.
53. S. Ye, R. Wang, M.-Z. Wu and Y.-P. Yuan, *Appl. Surf. Sci.*, 2015, **358**, 15-27.
54. S. Yin, J. Han, T. Zhou and R. Xu, *Catal. Sci. Technol.*, 2015, **5**, 5048-5061.
55. J. Low, B. Cheng, J. Yu and M. Jaroniec, *Energy Storage Mater.*, 2016, **3**, 24-35.
56. G. Mamba and A. K. Mishra, *Appl. Catal. B.*, 2016, **198**, 347-377.
57. Y. Xu, M. Kraft and R. Xu, *Chem. Soc. Rev.*, 2016, **45**, 3039-3052.
58. Y. Zheng, J. Liu, J. Liang, M. Jaroniec and S. Z. Qiao, *Energy Environ. Sci.*, 2012, **5**, 6717-6731.
59. J. Liebig, *Annalen der Pharmacie.*, 1834, **10**, 1-47.
60. E. C. Franklin, *J. Am. Chem. Soc.*, 1922, **44**, 486-509.
61. L. Pauling and J. H. Sturdivant, *Proc. Natl. Acad. Sci.*, 1937, **23**, 615-620.
62. C. E. Redemann and H. J. Lucas, *J. Am. Chem. Soc.*, 1940, **62**, 842-846.
63. F. Dong, Z. Wang, Y. Sun, W.-K. Ho and H. Zhang, *J. Colloid Interface Sci.*, 2013, **401**, 70-79.
64. F. Dong, L. Wu, Y. Sun, M. Fu, Z. Wu and S. C. Lee, *J. Mater. Chem.*, 2011, **21**, 15171-15174.
65. J. Liu, T. Zhang, Z. Wang, G. Dawson and W. Chen, *J. Mater. Chem.*, 2011, **21**, 14398-14401
66. D. J. Martin, K. Qiu, S. A. Shevlin, A. D. Handoko, X. Chen, Z. Guo and J. Tang, *Angew. Chem. Int. Ed.*, 2014, **53**, 9240-9245.
67. G. Wu, S. S. Thind, J. Wen, K. Yan and A. Chen, *Appl. Catal. B.*, 2013, **142-143**, 590-597.
68. P. Yang, J. Zhao, W. Qiao, L. Li and Z. Zhu, *Nanoscale.*, 2015, **7**, 18887-18890.
69. Y.-P. Yuan, W.-T. Xu, L.-S. Yin, S.-W. Cao, Y.-S. Liao, Y.-Q. Tng and C. Xue, *Int. J. Hydrog. Energy.*, 2013, **38**, 13159-13163.
70. G. Zhang, J. Zhang, M. Zhang and X. Wang, *J. Mater. Chem.*, 2012, **22**, 8083-8091.
71. Y. Zhang, J. Liu, G. Wu and W. Chen, *Nanoscale.*, 2012, **4**, 5300-5303.
72. Y. Chen, B. Wang, S. Lin, Y. Zhang and X. Wang, *J. Phys. Chem. C.*, 2014, **118**, 29981-29989.
73. J. Fang, H. Fan, M. Li and C. Long, *J. Mater. Chem. A.*, 2015, **3**, 13819-13826.
74. H. Gao, S. Yan, J. Wang, Y. A. Huang, P. Wang, Z. Li and Z. Zou, *Phys. Chem. Chem. Phys.*, 2013, **15**, 18077-18084.
75. Q. Gu, Z. Gao, H. Zhao, Z. Lou, Y. Liao and C. Xue, *RSC Adv.*, 2015, **5**, 49317-49325.

76. D. Hollmann, M. Karnahl, S. Tschierlei, K. Kailasam, M. Schneider, J. Radnik, K. Grabow, U. Bentrup, H. Junge, M. Beller, S. Lochbrunner, A. Thomas and A. Brückner, *Chem. Mater.*, 2014, **26**, 1727-1733.
77. A. B. Jorge, D. J. Martin, M. T. S. Dhanoa, A. S. Rahman, N. Makwana, J. Tang, A. Sella, F. Corà, S. Firth, J. A. Darr and P. F. McMillan, *J. Phys. Chem. C.*, 2013, **117**, 7178-7185.
78. Q. Liang, Z.-H. Huang, F. Kang and Q.-H. Yang, *ChemCatChem.*, 2015, **7**, 2897-2902.
79. H. Yan, Y. Chen and S. Xu, *Int. J. Hydrog. Energy.*, 2012, **37**, 125-133.
80. J. Xiao, J. Rabeah, J. Yang, Y. Xie, H. Cao and A. Brückner, *ACS Catal.*, 2017, 6198-6206.
81. K. Maeda, X. Wang, Y. Nishihara, D. Lu, M. Antonietti and K. Domen, *J. Phys. Chem. C.*, 2009, **113**, 4940-4947.
82. Y. Shiraishi, S. Kanazawa, Y. Sugano, D. Tsukamoto, H. Sakamoto, S. Ichikawa and T. Hirai, *ACS Catal.*, 2014, **4**, 774-780.
83. Y. Shiraishi, Y. Kofuji, H. Sakamoto, S. Tanaka, S. Ichikawa and T. Hirai, *ACS Catal.*, 2015, **5**, 3058-3066.
84. J. Zhu, Y. Wei, W. Chen, Z. Zhao and A. Thomas, *Chem. Commun.*, 2010, **46**, 6965-6967.
85. F. Dong, Y. Sun, L. Wu, M. Fu and Z. Wu, *Catal. Sci. Technol.*, 2012, **2**, 1332-1335.
86. Y. Kang, Y. Yang, L.-C. Yin, X. Kang, G. Liu and H.-M. Cheng, *Adv. Mater.*, 2015, **27**, 4572-4577.
87. X. Li, G. Hartley, A. J. Ward, P. A. Young, A. F. Masters and T. Maschmeyer, *J. Phys. Chem. C.*, 2015, **119**, 14938-14946.
88. Q. Liang, Z. Li, Z.-H. Huang, F. Kang and Q.-H. Yang, *Adv. Funct. Mater.*, 2015, **25**, 6885-6892.
89. G. Liu, T. Wang, H. Zhang, X. Meng, D. Hao, K. Chang, P. Li, T. Kako and J. Ye, *Angew. Chem. In. Ed.*, 2015, **54**, 13561-13565.
90. K. Schwinghammer, B. Tuffy, M. B. Mesch, E. Wirnhier, C. Martineau, F. Taulelle, W. Schnick, J. Senker and B. V. Lotsch, *Angew. Chem. In. Ed.*, 2013, **52**, 2435-2439.
91. Q. Tay, P. Kanhere, C. F. Ng, S. Chen, S. Chakraborty, A. C. H. Huan, T. C. Sum, R. Ahuja and Z. Chen, *Chem. Mater.*, 2015, **27**, 4930-4933.
92. G. Zhang, M. Zhang, X. Ye, X. Qiu, S. Lin and X. Wang, *Adv. Mater.*, 2014, **26**, 805-809.
93. Y. Zhang, J. Liu, G. Wu and W. Chen, *Nanoscale.*, 2012, **4**, 5300-5303.
94. P. Niu, L. Zhang, G. Liu and H.-M. Cheng, *Adv. Funct. Mater.*, 2012, **22**, 4763-4770.
95. K. Wang, Q. Li, B. Liu, B. Cheng, W. Ho and J. Yu, *Appl. Catal. B.*, 2015, **176-177**, 44-52.
96. J. Yu, K. Wang, W. Xiao and B. Cheng, *Phys. Chem. Chem. Phys.*, 2014, **16**, 11492-11501.
97. J. Zhang, J. Sun, K. Maeda, K. Domen, P. Liu, M. Antonietti, X. Fu and X. Wang, *Energy Environ. Sci.*, 2011, **4**, 675-678.
98. Y. Cui, G. Zhang, Z. Lin and X. Wang, *Appl. Catal. B.*, 2016, **181**, 413-419.
99. H. Xiao, W. Wang, G. Liu, Z. Chen, K. Lv and J. Zhu, *Appl. Surf. Sci.*, 2015, **358**, 313-318.
100. Z. Mo, X. She, Y. Li, L. Liu, L. Huang, Z. Chen, Q. Zhang, H. Xu and H. Li, *RSC Adv.*, 2015, **5**, 101552-101562.
101. S. C. Yan, Z. S. Li and Z. G. Zou, *Langmuir.*, 2009, **25**, 10397-10401.
102. S. Patnaik, S. Martha and K. M. Parida, *RSC Adv.*, 2016, **6**, 46929-46951.
103. Y. Zheng, L. Lin, B. Wang and X. Wang, *Angew. Chem. In. Ed.*, 2015, **54**, 12868-12884.
104. M. Groenewolt and M. Antonietti, *Adv. Mater.*, 2005, **17**, 1789-1792.
105. J. Wang, C. Zhang, Y. Shen, Z. Zhou, J. Yu, Y. Li, W. Wei, S. Liu and Y. Zhang, *J. Mater. Chem. A.*, 2015, **3**, 5126-5131.
106. X. Wang, K. Maeda, X. Chen, K. Takanae, K. Domen, Y. Hou, X. Fu and M. Antonietti, *J. Am. Chem. Soc.*, 2009, **131**, 1680-1681.
107. Z. Yang, Y. Zhang and Z. Schnepf, *J. Mater. Chem. A.*, 2015, **3**, 14081-14092.

108. Z. Zhao, Y. Dai, J. Lin and G. Wang, *Chem. Mater.*, 2014, **26**, 3151-3161.
109. W. Iqbal, B. Yang, X. Zhao, M. Rauf, M. Waqas, Y. Gong, J. Zhang and Y. Mao, *Catal. Sci. Technol.*, 2018, **8**, 4576-4599.
110. L. Zhou, H. Zhang, H. Sun, S. Liu, M. O. Tade, S. Wang and W. Jin, *Catal. Sci. Technol.*, 2016, **6**, 7002-7023.
111. Y. Liu, J. Goebel and Y. Yin, *Chem. Soc. Rev.*, 2013, **42**, 2610-2653.
112. Y. Shi, Y. Wan and D. Zhao, *Chem. Soc. Rev.*, 2011, **40**, 3854-3878.
113. X. Chen, Y.-S. Jun, K. Takanebe, K. Maeda, K. Domen, X. Fu, M. Antonietti and X. Wang, *Chem. Mater.*, 2009, **21**, 4093-4095.
114. A. Fihri, M. Bouhrara, U. Patil, D. Cha, Y. Saih and V. Polshettiwar, *ACS Catal.*, 2012, **2**, 1425-1431.
115. F. Goettmann, A. Fischer, M. Antonietti and A. Thomas, *Angew. Chem. In. Ed.*, 2006, **45**, 4467-4471.
116. J. Hong, X. Xia, Y. Wang and R. Xu, *J. Mater. Chem.*, 2012, **22**, 15006-15012.
117. Z. Huang, F. Li, B. Chen, T. Lu, Y. Yuan and G. Yuan, *Appl. Catal. B.*, 2013, **136-137**, 269-277.
118. Y.-S. Jun, W. H. Hong, M. Antonietti and A. Thomas, *Adv. Mater.*, 2009, **21**, 4270-4274.
119. Y. Cui, J. Zhang, G. Zhang, J. Huang, P. Liu, M. Antonietti and X. Wang, *J. Mater. Chem.*, 2011, **21**, 13032-13039.
120. Z. Lin and X. Wang, *ChemSusChem.*, 2014, **7**, 1547-1550.
121. W. Shen, L. Ren, H. Zhou, S. Zhang and W. Fan, *J. Mater. Chem.*, 2011, **21**, 3890-3894.
122. Y. Wang, J. Zhang, X. Wang, M. Antonietti and H. Li, *Angew. Chem. In. Ed.*, 2010, **49**, 3356-3359.
123. H. Yan, *Chem. Commun.*, 2012, **48**, 3430-3432.
124. Y. Zhang, T. Mori, J. Ye and M. Antonietti, *J. Am. Chem. Soc.*, 2010, **132**, 6294-6295.
125. Y.-S. Jun, J. Park, S. U. Lee, A. Thomas, W. H. Hong and G. D. Stucky, *Angew. Chem. In. Ed.*, 2013, **52**, 11083-11087.
126. X.-H. Li, X. Wang and M. Antonietti, *Chem. Sci.*, 2012, **3**, 2170-2174.
127. X.-H. Li, J. Zhang, X. Chen, A. Fischer, A. Thomas, M. Antonietti and X. Wang, *Chem. Mater.*, 2011, **23**, 4344-4348.
128. J. Liu, J. Huang, H. Zhou and M. Antonietti, *ACS Appl. Mater. Interfaces.*, 2014, **6**, 8434-8440.
129. J. Sun, J. Zhang, M. Zhang, M. Antonietti, X. Fu and X. Wang, *Nat. Commun.*, 2012, **3**, 1-7.
130. J. Zhang, F. Guo and X. Wang, *Adv. Funct. Mater.*, 2013, **23**, 3008-3014.
131. J. Zhang, M. Zhang, C. Yang and X. Wang, *Adv. Mater.*, 2014, **26**, 4121-4126.
132. D. Zheng, C. Huang and X. Wang, *Nanoscale.*, 2015, **7**, 465-470.
133. Y. Zheng, L. Lin, X. Ye, F. Guo and X. Wang, *Angew. Chem.*, 2014, **53**, 11926-11930.
134. X. Li, A. F. Masters and T. Maschmeyer, *ChemCatChem.*, 2015, **7**, 121-126.
135. Y. Wang, M. F. Ibad, H. Kosslick, J. Harloff, T. Beweries, J. Radnik, A. Schulz, S. Tschierlei, S. Lochbrunner and X. Guo, *Micropor. Mesopor. Mat.*, 2015, **211**, 182-191.
136. L. Jiang, X. Yuan, Y. Pan, J. Liang, G. Zeng, Z. Wu and H. Wang, *Appl. Catal. B.*, 2017, **217**, 388-406.
137. C. Lu, R. Chen, X. Wu, M. Fan, Y. Liu, Z. Le, S. Jiang and S. Song, *Appl. Surf. Sci.*, 2016, **360**, 1016-1022.
138. N. Sagara, S. Kamimura, T. Tsubota and T. Ohno, *Appl. Catal. B.*, 2016, **192**, 193-198.
139. S. Thaweesak, S. Wang, M. Lyu, M. Xiao, P. Peerakiatkhajohn and L. Wang, *Dalton Trans.*, 2017, **46**, 10714-10720.
140. S. C. Yan, Z. S. Li and Z. G. Zou, *Langmuir.*, 2010, **26**, 3894-3901.
141. P.-K. Chuang, K.-H. Wu, T.-F. Yeh and H. Teng, *ACS Sustain. Chem. Eng.*, 2016, **4**, 5989-5997.
142. G. Dong, K. Zhao and L. Zhang, *Chem. Commun.*, 2012, **48**, 6178-6180.
143. Z. Lin and X. Wang, *Angew. Chem. In. Ed.*, 2013, **52**, 1735-1738.
144. X. She, L. Liu, H. Ji, Z. Mo, Y. Li, L. Huang, D. Du, H. Xu and H. Li, *Appl. Catal. B.*, 2016, **187**, 144-153.

145. P. Zhang, X. Li, C. Shao and Y. Liu, *J. Mater. Chem. A.*, 2015, **3**, 3281-3284.
146. Z. Zhao, Y. Sun, F. Dong, Y. Zhang and H. Zhao, *RSC Adv.*, 2015, **5**, 39549-39556.
147. Y. Zhou, L. Zhang, W. Huang, Q. Kong, X. Fan, M. Wang and J. Shi, *Carbon*, 2016, **99**, 111-117.
148. B. Chai, J. Yan, C. Wang, Z. Ren and Y. Zhu, *Appl. Surf. Sci.*, 2017, **391**, 376-383.
149. S. Guo, Z. Deng, M. Li, B. Jiang, C. Tian, Q. Pan and H. Fu, *Angew. Chem. Int. Ed.*, 2016, **55**, 1830-1834.
150. S. Hu, L. Ma, J. You, F. Li, Z. Fan, F. Wang, D. Liu and J. Gui, *RSC Adv.*, 2014, **4**, 21657-21663.
151. J. Ran, T. Y. Ma, G. Gao, X.-W. Du and S. Z. Qiao, *Energy Environ. Sci.*, 2015, **8**, 3708-3717.
152. L. Zhang, X. Chen, J. Guan, Y. Jiang, T. Hou and X. Mu, *Mater. Res. Bull.*, 2013, **48**, 3485-3491.
153. Y. Zhou, L. Zhang, J. Liu, X. Fan, B. Wang, M. Wang, W. Ren, J. Wang, M. Li and J. Shi, *J. Mater. Chem. A.*, 2015, **3**, 3862-3867.
154. Y.-P. Zhu, T.-Z. Ren and Z.-Y. Yuan, *ACS Appl. Mater. Interfaces.*, 2015, **7**, 16850-16856.
155. S. Guo, Y. Zhu, Y. Yan, Y. Min, J. Fan and Q. Xu, *Appl. Catal. B.*, 2016, **185**, 315-321.
156. Z.-F. Huang, J. Song, L. Pan, Z. Wang, X. Zhang, J.-J. Zou, W. Mi, X. Zhang and L. Wang, *Nano Energy*, 2015, **12**, 646-656.
157. J. Li, B. Shen, Z. Hong, B. Lin, B. Gao and Y. Chen, *Chem. Commun.*, 2012, **48**, 12017-12019.
158. S. Liu, D. Li, H. Sun, H. M. Ang, M. O. Tadé and S. Wang, *J. Colloid Interface Sci.*, 2016, **468**, 176-182.
159. J. Chen, Z. Hong, Y. Chen, B. Lin and B. Gao, *Mater. Lett.*, 2015, **145**, 129-132.
160. Q. Fan, J. Liu, Y. Yu, S. Zuo and B. Li, *Appl. Surf. Sci.*, 2017, **391**, 360-368.
161. L.-L. Feng, Y. Zou, C. Li, S. Gao, L.-J. Zhou, Q. Sun, M. Fan, H. Wang, D. Wang, G.-D. Li and X. Zou, *Int. J. Hydrog. Energy.*, 2014, **39**, 15373-15379.
162. L. Ge, C. Han, X. Xiao, L. Guo and Y. Li, *Mater. Res. Bull.*, 2013, **48**, 3919-3925.
163. F. He, G. Chen, Y. Yu, Y. Zhou, Y. Zheng and S. Hao, *Chem. Commun.*, 2015, **51**, 425-427.
164. G. Liu, P. Niu, C. Sun, S. C. Smith, Z. Chen, G. Q. Lu and H.-M. Cheng, *J. Am. Chem. Soc.*, 2010, **132**, 11642-11648.
165. C. Lu, P. Zhang, S. Jiang, X. Wu, S. Song, M. Zhu, Z. Lou, Z. Li, F. Liu, Y. Liu, Y. Wang and Z. Le, *Appl. Catal. B.*, 2017, **200**, 378-385.
166. Y. Wang, Y. Di, M. Antonietti, H. Li, X. Chen and X. Wang, *Chem. Mater.*, 2010, **22**, 5119-5121.
167. Z.-A. Lan, G. Zhang and X. Wang, *Appl. Catal. B.*, 2016, **192**, 116-125.
168. Q. Han, C. Hu, F. Zhao, Z. Zhang, N. Chen and L. Qu, *J. Mater. Chem. A.*, 2015, **3**, 4612-4619.
169. Z. Ding, X. Chen, M. Antonietti and X. Wang, *ChemSusChem.*, 2011, **4**, 274-281.
170. J.-C. Wang, C.-X. Cui, Q.-Q. Kong, C.-Y. Ren, Z. Li, L. Qu, Y. Zhang and K. Jiang, *ACS Sustain. Chem. Eng.*, 2018, **6**, 8754-8761.
171. X. Wang, X. Chen, A. Thomas, X. Fu and M. Antonietti, *Adv. Mater.*, 2009, **21**, 1609-1612.
172. J. Gao, Y. Wang, S. Zhou, W. Lin and Y. Kong, *ChemCatChem.*, 2017, **9**, 1708-1715.
173. L.-F. Gao, T. Wen, J.-Y. Xu, X.-P. Zhai, M. Zhao, G.-W. Hu, P. Chen, Q. Wang and H.-L. Zhang, *ACS Appl. Mater. Interfaces.*, 2016, **8**, 617-624.
174. S. Hu, R. Jin, G. Lu, D. Liu and J. Gui, *RSC Adv.*, 2014, **4**, 24863-24869.
175. X. Song, H. Tao, L. Chen and Y. Sun, *Mater. Lett.*, 2014, **116**, 265-267.
176. S. Tonda, S. Kumar, S. Kandula and V. Shanker, *J. Mater. Chem. A.*, 2014, **2**, 6772-6780.
177. Z. Li, C. Kong and G. Lu, *J. Phys. Chem. C.*, 2015, **120**, 56-63.
178. P.-W. Chen, K. Li, Y.-X. Yu and W.-D. Zhang, *Appl. Surf. Sci.*, 2017, **392**, 608-615.
179. J. Gao, J. Wang, X. Qian, Y. Dong, H. Xu, R. Song, C. Yan, H. Zhu, Q. Zhong, G. Qian and J. Yao, *J. Solid State Chem.*, 2015, **228**, 60-64.
180. S. Le, T. Jiang, Q. Zhao, X. Liu, Y. Li, B. Fang and M. Gong, *RSC Adv.*, 2016, **6**, 38811-38819.
181. B. Yue, Q. Li, H. Iwai, T. Kako and J. Ye, *Sci. Technol. Adv. Mater.*, 2011, **12**, 034401-034408.
182. Y. Wang, Y. Li, X. Bai, Q. Cai, C. Liu, Y. Zuo, S. Kang and L. Cui, *Catal. Commun.*, 2016, **84**, 179-182.

183. Y. Wang, Y. Wang, Y. Li, H. Shi, Y. Xu, H. Qin, X. Li, Y. Zuo, S. Kang and L. Cui, *Catal. Commun.*, 2015, **72**, 24-28.
184. Y. Wang, Y. Xu, Y. Wang, H. Qin, X. Li, Y. Zuo, S. Kang and L. Cui, *Catal. Commun.*, 2016, **74**, 75-79.
185. X. Rong, F. Qiu, J. Rong, X. Zhu, J. Yan and D. Yang, *Mater. Lett.*, 2016, **164**, 127-131.
186. S. Hu, F. Li, Z. Fan, F. Wang, Y. Zhao and Z. Lv, *Dalton Trans.*, 2015, **44**, 1084-1092.
187. Y. Wang, S. Zhao, Y. Zhang, J. Fang, Y. Zhou, S. Yuan, C. Zhang and W. Chen, *Appl. Surf. Sci.*, 2018, **440**, 258-265.
188. M. Wu, J.-M. Yan, X.-n. Tang, M. Zhao and Q. Jiang, *ChemSusChem.*, 2014, **7**, 2654-2658.
189. T. Xiong, W. Cen, Y. Zhang and F. Dong, *ACS Catal.*, 2016, **6**, 2462-2472.
190. J. Zhang, S. Hu and Y. Wang, *RSC Adv.*, 2014, **4**, 62912-62919.
191. M. Zhang, X. Bai, D. Liu, J. Wang and Y. Zhu, *Appl. Catal. B.*, 2015, **164**, 77-81.
192. H. Dou, S. Zheng and Y. Zhang, *Catal. Lett.*, 2017, **148**, 601-611.
193. H. Dou, S. Zheng and Y. Zhang, *RSC Adv.*, 2018, **8**, 7558-7568.
194. C. Hu, W.-Z. Hung, M.-S. Wang and P.-J. Lu, *Carbon*, 2018, **127**, 374-383.
195. S. Hu, L. Ma, J. You, F. Li, Z. Fan, G. Lu, D. Liu and J. Gui, *Appl. Surf. Sci.*, 2014, **311**, 164-171.
196. L. Jiang, X. Yuan, G. Zeng, X. Chen, Z. Wu, J. Liang, J. Zhang, H. Wang and H. Wang, *ACS Sustain. Chem. Eng.*, 2017, **5**, 5831-5841.
197. Q. Liu, T. Chen, Y. Guo, Z. Zhang and X. Fang, *Appl. Catal. B.*, 2017, **205**, 173-181.
198. S. Zhang, J. Li, M. Zeng, J. Li, J. Xu and X. Wang, *Chem. Eur. J.*, 2014, **20**, 9805-9812.
199. J. Zhao, L. Ma, H. Wang, Y. Zhao, J. Zhang and S. Hu, *Appl. Surf. Sci.*, 2015, **332**, 625-630.
200. J. Ran, J. Yu and M. Jaroniec, *Green. Chem.*, 2011, **13**, 2708-2713.
201. G. Zhang, Z.-A. Lan, L. Lin, S. Lin and X. Wang, *Chem. Sci.*, 2016, **7**, 3062-3066.
202. S. Cao, J. Jiang, B. Zhu and J. Yu, *Phys. Chem. Chem. Phys.*, 2016, **18**, 19457-19463.
203. C. Chang, Y. Fu, M. Hu, C. Wang, G. Shan and L. Zhu, *Appl. Catal. B.*, 2013, **142-143**, 553-560.
204. Y. Di, X. Wang, A. Thomas and M. Antonietti, *ChemCatChem.*, 2010, **2**, 834-838.
205. Y. Zhang, D. A. J. M. Ligthart, X.-Y. Quek, L. Gao and E. J. M. Hensen, *Int. J. Hydrog. Energy.*, 2014, **39**, 11537-11546.
206. J. Chen, C.-L. Dong, Y. Du, D. Zhao and S. Shen, *Adv. Mater. Interfaces*, 2015, **2**, 1500280.
207. S. Samanta, S. Martha and K. Parida, *ChemCatChem.*, 2014, **6**, 1453-1462.
208. N. Wang and X. Li, *Inorg. Chem. Front.*, 2018, **5**, 2268-2275.
209. L. Bi, D. Meng, Q. Bu, Y. Lin, D. Wang and T. Xie, *Phys. Chem. Chem. Phys.*, 2016, **18**, 31534-31541.
210. M. Fan, C. Song, T. Chen, X. Yan, D. Xu, W. Gu, W. Shi and L. Xiao, *RSC Adv.*, 2016, **6**, 34633-34640.
211. M. Jourshabani, Z. Shariatnia and A. Badiie, *J. Phys. Chem. C.*, 2017, **121**, 19239-19253.
212. L. Kong, Y. Dong, P. Jiang, G. Wang, H. Zhang and N. Zhao, *J. Mater. Chem. A.*, 2016, **4**, 9998-10007.
213. M.-H. Vu, M. Sakar, C.-C. Nguyen and T.-O. Do, *ACS Sustainable Chem. Eng.*, 2018, **6**, 4194-4203.
214. J. Yu, S. Wang, B. Cheng, Z. Lin and F. Huang, *Catal. Sci. Technol.*, 2013, **3**, 1782-1789.
215. G. Zhang, S. Zang and X. Wang, *ACS Catal.*, 2015, **5**, 941-947.
216. X. Zhou, Z. Luo, P. Tao, B. Jin, Z. Wu and Y. Huang, *Mater. Chem. Phys.*, 2014, **143**, 1462-1468.
217. F. Raziq, L. Sun, Y. Wang, X. Zhang, M. Humayun, S. Ali, L. Bai, Y. Qu, H. Yu and L. Jing, *Adv. Energy Mater.*, 2018, **8**, 1701580-1701590.
218. J. Hong, Y. Wang, Y. Wang, W. Zhang and R. Xu, *ChemSusChem.*, 2013, **6**, 2263-2268.
219. Y. Hou, Y. Zhu, Y. Xu and X. Wang, *Appl. Catal. B.*, 2014, **156-157**, 122-127.
220. F. Xue, M. Liu, C. Cheng, J. Deng and J. Shi, *ChemCatChem.*, 2018, **10**, 5441-5448.
221. H. Zhao, Y. Dong, P. Jiang, H. Miao, G. Wang and J. Zhang, *J. Mater. Chem. A.*, 2015, **3**, 7375-7381.
222. Y. Zhu, Y. Xu, Y. Hou, Z. Ding and X. Wang, *Int. J. Hydrog. Energy.*, 2014, **39**, 11873-11879.
223. S. Gong, Z. Jiang, P. Shi, J. Fan, Q. Xu and Y. Min, *Appl. Catal. B.*, 2018, **238**, 318-327.

224. W. Qi, S. Liu, F. Li, H. Jiang, Z. Cheng, S. Zhao and M. Yang, *Catal. Sci. Technol.*, 2019, **9**, 2571-2577.
225. A. Indra, A. Acharjya, P. W. Menezes, C. Merschjann, D. Hollmann, M. Schwarze, M. Aktas, A. Friedrich, S. Lochbrunner, A. Thomas and M. Driess, *Angew. Chem. In. Ed.*, 2017, **56**, 1653-1657.
226. Z. Sun, M. Zhu, M. Fujitsuka, A. Wang, C. Shi and T. Majima, *ACS Appl. Mater. Interfaces.*, 2017, **9**, 30583-30590.
227. D. Zeng, W.-J. Ong, Y. Chen, S. Y. Tee, C. S. Chua, D.-L. Peng and M.-Y. Han, *Part. Part. Syst. Char.*, 2018, **35**, 1700251-1700258.
228. K. He, J. Xie, Z.-Q. Liu, N. Li, X. Chen, J. Hu and X. Li, *J. Mater. Chem. A.*, 2018, **6**, 13110-13122.
229. J. Zhang, M. Wu, B. He, R. Wang, H. Wang and Y. Gong, *Appl. Surf. Sci.*, 2019, **470**, 565-572.
230. M. Shao, Y. Shao, J. Chai, Y. Qu, M. Yang, Z. Wang, M. Yang, W. F. Ip, C. T. Kwok, X. Shi, Z. Lu, S. Wang, X. Wang and H. Pan, *J. Mater. Chem. A.*, 2017, **5**, 16748-16756.
231. L. E. Garner, K. X. Steirer, J. L. Young, N. C. Anderson, E. M. Miller, J. S. Tinkham, T. G. Deutsch, A. Sellinger, J. A. Turner and N. R. Neale, *ChemSusChem.*, 2017, **10**, 767-773.
232. Z. Zhuang, Y. Li, Z. Li, F. Lv, Z. Lang, K. Zhao, L. Zhou, L. Moskaleva, S. Guo and L. Mai, *Angew. Chem. In. Ed.*, 2018, **57**, 496-500.
233. G. Zhang, Z.-A. Lan and X. Wang, *Chem. Sci.*, 2017, **8**, 5261-5274.
234. S. Liu, C. Han, Z.-R. Tang and Y.-J. Xu, *Mater. Horizons.*, 2016, **3**, 270-282.
235. S. J. A. Moniz, S. A. Shevlin, D. J. Martin, Z.-X. Guo and J. Tang, *Energy Environ. Sci.*, 2015, **8**, 731-759.
236. S. Bai, X. Wang, C. Hu, M. Xie, J. Jiang and Y. Xiong, *Chem. Commun.*, 2014, **50**, 6094-6097.
237. J. Ding, G. Long, Y. Luo, R. Sun, M. Chen, Y. Li, Y. Zhou, X. Xu and W. Zhao, *J. Hazard. Mater.*, 2018, **355**, 74-81.
238. W. Yin, L. Bai, Y. Zhu, S. Zhong, L. Zhao, Z. Li and S. Bai, *ACS Appl. Mater. Interfaces.*, 2016, **8**, 23133-23142.
239. M. Caux, F. Fina, J. T. S. Irvine, H. Idriss and R. Howe, *Catal. Today.*, 2017, **287**, 182-188.
240. F. Fina, H. Ménard and J. T. S. Irvine, *Phys. Chem. Chem. Phys.*, 2015, **17**, 13929-13936.
241. K. Li, Z. Zeng, L. Yan, S. Luo, X. Luo, M. Huo and Y. Guo, *Appl. Catal. B.*, 2015, **165**, 428-437.
242. X. Li, W. Bi, L. Zhang, S. Tao, W. Chu, Q. Zhang, Y. Luo, C. Wu and Y. Xie, *Adv. Mater.*, 2016, **28**, 2427-2431.
243. J. Liu, Y. Zhang, L. Lu, G. Wu and W. Chen, *Chem. Commun.*, 2012, **48**, 8826-8828.
244. W.-J. Ong, L.-L. Tan, S.-P. Chai and S.-T. Yong, *Dalton Trans.*, 2015, **44**, 1249-1257.
245. M. Schröder, K. Kailasam, S. Rudi, K. Fündling, J. Rieß, M. Lublow, A. Thomas, R. Schomäcker and M. Schwarze, *RSC Adv.*, 2014, **4**, 50017-50026.
246. Y. Shiraishi, Y. Kofuji, S. Kanazawa, H. Sakamoto, S. Ichikawa, S. Tanaka and T. Hirai, *Chem. Commun.*, 2014, **50**, 15255-15258.
247. J. Xue, S. Ma, Y. Zhou, Z. Zhang and M. He, *ACS Appl. Mater. Interfaces.*, 2015, **7**, 9630-9637.
248. J. Zhang, M. Zhang, C. Yang and X. Wang, *Adv. Mater.*, 2014, **26**, 4121-4126.
249. Y. Wang, J. Hong, W. Zhang and R. Xu, *Catal. Sci. Technol.*, 2013, **3**, 1703-1711.
250. X. Bai, R. Zong, C. Li, D. Liu, Y. Liu and Y. Zhu, *Appl. Catal. B.*, 2014, **147**, 82-91.
251. Y. Bu, Z. Chen and W. Li, *Appl. Catal. B.*, 2014, **144**, 622-630.
252. T. Chen, W. Quan, L. Yu, Y. Hong, C. Song, M. Fan, L. Xiao, W. Gu and W. Shi, *J. Alloys Compd.*, 2016, **686**, 628-634.
253. X. Chen, Z. Zheng, X. Ke, E. Jaatinen, T. Xie, D. Wang, C. Guo, J. Zhao and H. Zhu, *Green. Chem.*, 2010, **12**, 414-419.
254. O. Fontelles-Carceller, M. J. Muñoz-Batista, M. Fernández-García and A. Kubacka, *ACS Appl. Mater. Interfaces.*, 2016, **8**, 2617-2627.
255. Y. Fu, T. Huang, L. Zhang, J. Zhu and X. Wang, *Nanoscale.*, 2015, **7**, 13723-13733.

256. L. Ge, C. Han, J. Liu and Y. Li, *Appl. Catal. A.*, 2011, **409-410**, 215-222.
257. M. A. Gondal, A. A. Adeseda, S. G. Rashid, A. Hameed, M. Aslam, I. M. I. Ismail, U. Baig, M. A. Dastageer, A. R. Al-Arfaj and A. U. Rehman, *J. Mol. Catal. A-Chem.*, 2016, **423**, 114-125.
258. D. Jiang, L. Chen, J. Xie and M. Chen, *Dalton Trans.*, 2014, **43**, 4878-4885.
259. M. E. Khan, T. H. Han, M. M. Khan, M. R. Karim and M. H. Cho, *ACS Appl. Nano Mater.*, 2018, **1**, 2912-2922.
260. S. Ma, S. Zhan, Y. Jia, Q. Shi and Q. Zhou, *Appl. Catal. B.*, 2016, **186**, 77-87.
261. M. J. Muñoz-Batista, O. Fontelles-Carceller, M. Ferrer, M. Fernández-García and A. Kubacka, *Appl. Catal. B.*, 2016, **183**, 86-95.
262. J. Qin, J. Huo, P. Zhang, J. Zeng, T. Wang and H. Zeng, *Nanoscale.*, 2016, **8**, 2249-2259.
263. K. Sridharan, E. Jang, J. H. Park, J.-H. Kim, J.-H. Lee and T. J. Park, *Chem. Eur. J.*, 2015, **21**, 9126-9132.
264. Y. Sun, T. Xiong, Z. Ni, J. Liu, F. Dong, W. Zhang and W.-K. Ho, *Appl. Surf. Sci.*, 2015, **358**, 356-362.
265. J. Wang, J. Cong, H. Xu, J. Wang, H. Liu, M. Liang, J. Gao, Q. Ni and J. Yao, *ACS Sustain. Chem. Eng.*, 2017, **5**, 10633-10639.
266. Y. Yang, W. Guo, Y. Guo, Y. Zhao, X. Yuan and Y. Guo, *J. Hazard. Mater.*, 2014, **271**, 150-159.
267. Y. Yang, Y. Guo, F. Liu, X. Yuan, Y. Guo, S. Zhang, W. Guo and M. Huo, *Appl. Catal. B.*, 2013, **142-143**, 828-837.
268. W. Zhang, L. Zhou and H. Deng, *J. Mol. Catal. A-Chem.*, 2016, **423**, 270-276.
269. T. Bhowmik, M. K. Kundu and S. Barman, *RSC Adv.*, 2015, **5**, 38760-38773.
270. N. Cheng, J. Tian, Q. Liu, C. Ge, A. H. Qusti, A. M. Asiri, A. O. Al-Youbi and X. Sun, *ACS Appl. Mater. Interfaces.*, 2013, **5**, 6815-6819.
271. Y. Guo, H. Jia, J. Yang, H. Yin, Z. Yang, J. Wang and B. Yang, *Phys. Chem. Chem. Phys.*, 2018, **20**, 22296-22307.
272. J. Jiang, J. Yu and S. Cao, *J. Colloid Interface Sci.*, 2016, **461**, 56-63.
273. K. Leng, W. Mai, X. Zhang, R. Liu, X. Lin, J. Huang, H. Lou, Y. Xie, R. Fu and D. Wu, *Chem. Commun.*, 2018, **54**, 7159-7162.
274. J. Liu, Y. Yang, N. Liu, Y. Liu, H. Huang and Z. Kang, *Green. Chem.*, 2014, **16**, 4559-4565.
275. S. Patnaik, S. Martha, G. Madras and K. Parida, *Phys. Chem. Chem. Phys.*, 2016, **18**, 28502-28514.
276. A. Tanaka, K. Teramura, S. Hosokawa, H. Kominami and T. Tanaka, *Chem. Sci.*, 2017, **8**, 2574-2580.
277. S. Tonda, S. Kumar and V. Shanker, *Mater. Res. Bull.*, 2016, **75**, 51-58.
278. X. Zhang, Y. L. Chen, R. S. Liu and D. P. Tsai, *Rep. Prog. Phys.*, 2013, **76**, 046401-046442.
279. Z. Zheng, W. Xie, B. Huang and Y. Dai, *Chem. Eur. J.*, 2018, **24**, 18322-18333.
280. K. Bhunia, M. Chandra, S. Khilari and D. Pradhan, *ACS Appl. Mater. Interfaces.*, 2019, **11**, 478-488.
281. G. Darabdhara and M. R. Das, *Chemosphere*, 2018, **197**, 817-829.
282. C. Han, Y. Gao, S. Liu, L. Ge, N. Xiao, D. Dai, B. Xu and C. Chen, *Int. J. Hydrog. Energy.*, 2017, **42**, 22765-22775.
283. C. Han, Y. Lu, J. Zhang, L. Ge, Y. Li, C. Chen, Y. Xin, L. Wu and S. Fang, *J. Mater. Chem. A.*, 2015, **3**, 23274-23282.
284. C. Han, L. Wu, L. Ge, Y. Li and Z. Zhao, *Carbon*, 2015, **92**, 31-40.
285. S. Liang, Y. Xia, S. Zhu, S. Zheng, Y. He, J. Bi, M. Liu and L. Wu, *Appl. Surf. Sci.*, 2015, **358**, 304-312.
286. I. Majeed, U. Manzoor, F. K. Kanodarwala, M. A. Nadeem, E. Hussain, H. Ali, A. Badshah, J. A. Stride and M. A. Nadeem, *Catal. Sci. Technol.*, 2018, **8**, 1183-1193.
287. Y. Zhu, A. Marianov, H. Xu, C. Lang and Y. Jiang, *ACS Appl. Mater. Interfaces.*, 2018, **10**, 9468-9477.
288. F. Dong, Z. Zhao, Y. Sun, Y. Zhang, S. Yan and Z. Wu, *Environ. Sci. Technol.*, 2015, **49**, 12432-12440.
289. J. Wang, L. Tang, G. Zeng, Y. Liu, Y. Zhou, Y. Deng, J. Wang and B. Peng, *ACS Sustain. Chem. Eng.*, 2017, **5**, 1062-1072.

290. L. Bi, D. Xu, L. Zhang, Y. Lin, D. Wang and T. Xie, *Phys. Chem. Chem. Phys.*, 2015, **17**, 29899-29905.
291. A. Indra, P. W. Menezes, K. Kailasam, D. Hollmann, M. Schröder, A. Thomas, A. Brückner and M. Driess, *Chem. Commun.*, 2016, **52**, 104-107.
292. C. Sun, H. Zhang, H. Liu, X. Zheng, W. Zou, L. Dong and L. Qi, *Appl. Catal. B.*, 2018, **235**, 66-74.
293. J. Wen, J. Xie, H. Zhang, A. Zhang, Y. Liu, X. Chen and X. Li, *ACS Appl. Mater. Interfaces.*, 2017, **9**, 14031-14042.
294. G. Zhang, G. Li and X. Wang, *ChemCatChem.*, 2015, **7**, 2864-2870.
295. Y. Bao and K. Chen, *Mol. Catal.*, 2017, **432**, 187-195.
296. D. He, Y. Chen, Y. Situ, L. Zhong and H. Huang, *Appl. Surf. Sci.*, 2017, **425**, 862-872.
297. X. Qian, Y. Wu, M. Kan, M. Fang, D. Yue, J. Zeng and Y. Zhao, *Appl. Catal. B.*, 2018, **237**, 513-520.
298. X. Chen, S. Shen, L. Guo and S. S. Mao, *Chem. Rev.*, 2010, **110**, 6503-6570.
299. R. Marschall, *Adv. Funct. Mater.*, 2014, **24**, 2421-2440.
300. J. Ran, J. Zhang, J. Yu, M. Jaroniec and S. Z. Qiao, *Chem. Soc. Rev.*, 2014, **43**, 7787-7812.
301. Y. Wang, Q. Wang, X. Zhan, F. Wang, M. Safdar and J. He, *Nanoscale.*, 2013, **5**, 8326-8339.
302. Y.-P. Yuan, L.-W. Ruan, J. Barber, S. C. Joachim Loo and C. Xue, *Energy Environ. Sci.*, 2014, **7**, 3934-3951.
303. L. Zhang and M. Jaroniec, *Appl. Surf. Sci.*, 2018, **430**, 2-17.
304. H. Zhou, Y. Qu, T. Zeid and X. Duan, *Energy Environ. Sci.*, 2012, **5**, 6732.
305. Y. Liu, H. He, J. Li, W. Li, Y. Yang, Y. Li and Q. Chen, *RSC Adv.*, 2015, **5**, 99378-99384.
306. Z. Zhang, K. Liu, Z. Feng, Y. Bao and B. Dong, *Sci. Rep.*, 2016, **6**, 19221.
307. T. Wu, P. Wang, J. Qian, Y. Ao, C. Wang and J. Hou, *Dalton Trans.*, 2017, **46**, 13793-13801.
308. H. Liu, Z. Xu, Z. Zhang and D. Ao, *Appl. Catal. B.*, 2016, **192**, 234-241.
309. F. Shi, L. Chen, C. Xing, D. Jiang, D. Li and M. Chen, *RSC Adv.*, 2014, **4**, 62223-62229.
310. X. Li, K. Xie, L. Song, M. Zhao and Z. Zhang, *ACS Appl. Mater. Interfaces.*, 2017, **9**, 24577-24583.
311. W. Chen, T. Huang, Y.-X. Hua, T.-Y. Liu, X.-H. Liu and S.-M. Chen, *J. Hazard. Mater.*, 2016, **320**, 529-538.
312. Y. Zou, J.-W. Shi, D. Ma, Z. Fan, C. He, L. Cheng, D. Sun, J. Li, Z. Wang and C. Niu, *Catal. Sci. Technol.*, 2018, **8**, 3883-3893.
313. L. Ge, C. Han, X. Xiao and L. Guo, *Int. J. Hydrog. Energy.*, 2013, **38**, 6960-6969.
314. J. Hong, Y. Wang, Y. Wang, W. Zhang and R. Xu, *ChemSusChem.*, 2013, **6**, 2263-2268.
315. Y. Li, K. Zhang, S. Peng, G. Lu and S. Li, *J. Mol. Catal. A-Chem.*, 2012, **363-364**, 354-361.
316. X. Zhang, L. Yu, C. Zhuang, T. Peng, R. Li and X. Li, *ACS Catal.*, 2013, **4**, 162-170.
317. J. Song, H. Zhao, R. Sun, X. Li and D. Sun, *Energy Environ. Sci.*, 2017, **10**, 225-235.
318. Y. Li, G. Lu and S. Li, *Appl. Catal. A.*, 2001, **214**, 179-185.
319. Y. Li, G. Lu and S. Li, *Chemosphere*, 2003, **52**, 843-850.
320. M.-h. Yao, Y.-g. Tang, L. Zhang, H.-h. Yang and J.-h. Yan, *T. Nonferr. Metal. Soc.*, 2010, **20**, 1944-1949.
321. K. Kailasam, J. D. Epping, A. Thomas, S. Losse and H. Junge, *Energy Environ. Sci.*, 2011, **4**, 4668-4674.
322. K. Li, J. Xu, X. Zhang, T. Peng and X. Li, *Int. J. Hydrogen Energy*, 2013, **38**, 15965-15975.
323. M. Nguyen, P. D. Tran, S. S. Pramana, R. L. Lee, S. K. Batabyal, N. Mathews, L. H. Wong and M. Graetzel, *Nanoscale.*, 2013, **5**, 1479-1482.
324. Q. Liu, X. Li, Q. He, A. Khalil, D. Liu, T. Xiang, X. Wu and L. Song, *Small*, 2015, **11**, 5556-5564.
325. J. Li, E. Liu, Y. Ma, X. Hu, J. Wan, L. Sun and J. Fan, *Appl. Surf. Sci.*, 2016, **364**, 694-702.
326. M. Wu, J. Zhan, K. Wu, Z. Li, L. Wang, B. Geng, L. Wang and D. Pan, *J. Mater. Chem. A.*, 2017, **5**, 14061-14069.
327. W. Dai, J. Yu, Y. Deng, X. Hu, T. Wang and X. Luo, *Appl. Surf. Sci.*, 2017, **403**, 230-239.

328. F. Gärtner, S. Losse, A. Boddien, M.-M. Pohl, S. Denurra, H. Junge and M. Beller, *ChemSusChem.*, 2012, **5**, 530-533.
329. H. Bragg William and L. Bragg William, *Proceedings of the Royal Society of London. Series A, Containing Papers of a Mathematical and Physical Character*, 1913, **88**, 428-438.
330. P. Scherrer, *Goett. Nachr.*, 1918, **2**, 98-100.
331. R. López and R. Gómez, *J. Sol-Gel Sci. Technol.*, 2012, **61**, 1-7.
332. P. Xiao, J. Lou, H. Zhang, W. Song, X.-L. Wu, H. Lin, J. Chen, S. Liu and X. Wang, *Catal. Sci. Technol.*, 2018, **8**, 201-209.
333. J. Wang, D. Hao, J. Ye and N. Umezawa, *Chem. Mater.*, 2017, **29**, 2694-2707.
334. J. H. Scofield, *J. Electron Spectrosc. Relat. Phenom.*, 1976, **8**, 129-137.
335. J. B. Priebe, J. Radnik, A. J. J. Lennox, M.-M. Pohl, M. Karnahl, D. Hollmann, K. Grabow, U. Bentrup, H. Junge, M. Beller and A. Brückner, *ACS Catal.*, 2015, **5**, 2137-2148.
336. R. C. Barklie, *Diam. Relat. Mater.*, 2003, **12**, 1427-1434.
337. K. Miyashita, S.-i. Kuroda, S. Tajima, K. Takehira, S. Tobita and H. Kubota, *Chem. Phys. Lett.*, 2003, **369**, 225-231.
338. D. Aldakov, A. Lefrançois and P. Reiss, *J. Mater. Chem. C*, 2013, **1**, 3756-3776.
339. K. Zhang and L. Guo, *Catal. Sci. Technol.*, 2013, **3**, 1672-1690.
340. W. Che, Y. Luo, F. Deng, A. Zhang, L. Zhao, X. Luo and Q. Ruan, *Appl. Catal. A.*, 2018, **565**, 170-180.
341. K. Li, B. Chai, T. Peng, J. Mao and L. Zan, *ACS Catal.*, 2013, **3**, 170-177.
342. D. Chen and J. Ye, *J. Phys. Chem. Solids*, 2007, **68**, 2317-2320.
343. F. Zhang, J. Chen, X. Zhang, W. Gao, R. Jin, N. Guan and Y. Li, *Langmuir.*, 2004, **20**, 9329-9334.
344. T. Tyborski, C. Merschjann, S. Orthmann, F. Yang, M. C. Lux-Steiner and T. Schedel-Niedrig, *J. Phys. Condens. Matter.*, 2013, **25**, 395402-395409.
345. A. Nashim, S. Martha and K. M. Parida, *RSC Adv.*, 2014, **4**, 14633-14643.
346. L. Zhang, X. Wang, Q. Nong, H. Lin, B. Teng, Y. Zhang, L. Zhao, T. Wu and Y. He, *Appl. Surf. Sci.*, 2015, **329**, 143-149.
347. W. Chen, T. Huang, Y.-X. Hua, T.-Y. Liu, X.-H. Liu and S.-M. Chen, *J. Hazard. Mater.*, 2016, **320**, 529-538.
348. H. Xu, J. Yan, Y. Xu, Y. Song, H. Li, J. Xia, C. Huang and H. Wan, *Appl. Catal. B.*, 2013, **129**, 182-193.
349. T. Li, L. Zhao, Y. He, J. Cai, M. Luo and J. Lin, *Appl. Catal. B.*, 2013, **129**, 255-263.
350. S. Isakozawa, I. Nagaoki, A. Watabe, Y. Nagakubo, N. Saito, H. Matsumoto, X. F. Zhang, Y. Taniguchi and N. Baba, *Microsc.*, 2016, **65**, 353-362.
351. A. Indra, A. Acharjya, P. W. Menezes, C. Merschjann, D. Hollmann, M. Schwarze, M. Aktas, A. Friedrich, S. Lochbrunner, A. Thomas and M. Driess, *Angew. Chem.*, 2017, **129**, 1675-1679.
352. A. Davydov, *Molecular Spectroscopy of Oxide Catalyst Surfaces*, John Wiley & Sons Ltd., Chichester, 2003.
353. J. Zhang, G. Zhang, X. Chen, S. Lin, L. Mohlmann, G. Dolega, G. Lipner, M. Antonietti, S. Blechert and X. Wang, *Angew. Chem.*, 2012, **51**, 3183-3187.
354. J. B. Priebe, M. Karnahl, H. Junge, M. Beller, D. Hollmann and A. Bruckner, *Angew. Chem.*, 2013, **52**, 11420-11424.
355. C. Xing, Z. Wu, D. Jiang and M. Chen, *J. Colloid Interface Sci.*, 2014, **433**, 9-15.
356. J. Chen, S. Shen, P. Guo, P. Wu and L. Guo, *J. Mater. Chem. A.*, 2014, **2**, 4605-4612.
357. M. Fan, B. Hu, X. Yan, C. Song, T. Chen, Y. Feng and W. Shi, *New J. Chem.*, 2015, **39**, 6171-6177.
358. S. Nayak, L. Mohapatra and K. Parida, *J. Mater. Chem. A.*, 2015, **3**, 18622-18635.
359. X. Jin, X. Fan, J. Tian, R. Cheng, M. Li and L. Zhang, *RSC Adv.*, 2016, **6**, 52611-52619.
360. Z. Lei, J. Zhan, L. Tang, Y. Zhang and Y. Wang, *Adv. Energy Mater.*, 2018, 1703482-1703511.

361. C. Wu, Q. Fang, Q. Liu, D. Liu, C. Wang, T. Xiang, A. Khalil, S. Chen and L. Song, *Inorg. Chem. Front.*, 2017, **4**, 663-667.
362. M. Zeng and Y. Li, *J. Mater. Chem. A.*, 2015, **3**, 14942-14962.
363. R. Sivasankaran, N. Rockstroh, D. Hollmann, C. Kreyenschulte, G. Agostini, H. Lund, A. Acharjya, J. Rabeah, U. Bentrup, H. Junge, A. Thomas and A. Brückner, *Catalysts.*, 2018, **8**, 52-68.
364. X. Li, J. Xia, W. Zhu, J. Di, B. Wang, S. Yin, Z. Chen and H. Li, *Colloids Surf. A*, 2016, **511**, 1-7.
365. K. Wenderich and G. Mul, *Chem. Rev.*, 2016, **116**, 14587-14619.
366. T. Xiang, Q. Fang, H. Xie, C. Wu, C. Wang, Y. Zhou, D. Liu, S. Chen, A. Khalil, S. Tao, Q. Liu and L. Song, *Nanoscale.*, 2017, **9**, 6975-6983.
367. Q. Liu, Q. Fang, W. Chu, Y. Wan, X. Li, W. Xu, M. Habib, S. Tao, Y. Zhou, D. Liu, T. Xiang, A. Khalil, X. Wu, M. Chhowalla, P. M. Ajayan and L. Song, *Chem. Mater.*, 2017, **29**, 4738-4744.
368. P. Afanasiev and C. Lorentz, *J. Phys. Chem. C.*, 2019, **123**, 7486-7494.
369. X. Chen, L. Zhang, B. Zhang, X. Guo and X. Mu, *Sci. Rep.*, 2016, **6**, 28558-28571.
370. S. Garbarino, A. Pereira, C. Hamel, É. Irissou, M. Chaker and D. Guay, *J. Phys. Chem. C.*, 2010, **114**, 2980-2988.
371. R. J. Isaifan, S. Ntais and E. A. Baranova, *Appl. Catal. A.*, 2013, **464-465**, 87-94.
372. P. Marcus and C. Hinnen, *Surf. Sci.*, 1997, **392**, 134-142.
373. M. G. Mason, *Phys. Rev. B*, 1983, **27**, 748-762.
374. J. P. Espinós, J. Morales, A. Barranco, A. Caballero, J. P. Holgado and A. R. González-Elipe, *J. Phys. Chem. B*, 2002, **106**, 6921-6929.
375. J. Morales, J. P. Espinos, A. Caballero, A. R. Gonzalez-Elipe and J. A. Mejias, *J. Phys. Chem. B*, 2005, **109**, 7758-7765.
376. J. S. Jang, S. H. Choi, H. G. Kim and J. S. Lee, *J. Phys. Chem. C.*, 2008, **112**, 17200-17205.
377. J. Xue, S. Ma, Y. Zhou, Z. Zhang and M. He, *ACS Appl. Mater. Interfaces.*, 2015, **7**, 9630-9637.
378. Y. L. Chow, W. C. Danen, S. F. Nelsen and D. H. Rosenblatt, *Chem. Rev.*, 1978, **78**, 243-274.
379. J. P. Blandine Barbier, Georges Desarmot and Manuel Sanchez, *J. Electrochem. Soc.*, 1990, **137**, 1757-1764.
380. P. J. DeLaive, T. K. Foreman, C. Giannotti and D. G. Whitten, *J. Am. Chem. Soc.*, 1980, **102**, 5627-5631.
381. K. Kalyanasundaram, J. Kiwi and M. Grätzel, *Helvetica Chimica Acta*, 1978, **61**, 2720-2730.
382. Y.-J. Yuan, Z.-T. Yu, X.-Y. Chen, J.-Y. Zhang and Z.-G. Zou, *Chem. Eur. J.*, 2011, **17**, 12891-12895.
383. Y.-J. Yuan, J.-Y. Zhang, Z.-T. Yu, J.-Y. Feng, W.-J. Luo, J.-H. Ye and Z.-G. Zou, *Inorg. Chem.*, 2012, **51**, 4123-4133.
384. G. Neshvad and M. Z. Hoffman, *J. Phys. Chem.*, 1989, **93**, 2445-2452.
385. J. Yan, L. Zhang, H. Yang, Y. Tang, Z. Lu, S. Guo, Y. Dai, Y. Han and M. Yao, *Sol. Energy.*, 2009, **83**, 1534-1539.
386. J. Xu and X. Cao, *Chem. Eng. J.*, 2015, **260**, 642-648.
387. W. Zhang, Y. Wang, Z. Wang, Z. Zhong and R. Xu, *Chem. Commun.*, 2010, **46**, 7631-7633.
388. V. R. Chelli and A. K. Golder, *Chemosphere*, 2018, **208**, 149-158.
389. D. Jiang, L. Chen, J. Xie and M. Chen, *Dalton Trans*, 2014, **43**, 4878-4885.
390. J. Zhang, Y. Wang, J. Jin, J. Zhang, Z. Lin, F. Huang and J. Yu, *ACS Appl. Mater. Interfaces.*, 2013, **5**, 10317-10324.
391. D. Jiang, J. Li, C. Xing, Z. Zhang, S. Meng and M. Chen, *ACS Appl. Mater. Interfaces.*, 2015, **7**, 19234-19242.
392. Z. Mao, J. Chen, Y. Yang, D. Wang, L. Bie and B. D. Fahlman, *ACS Appl. Mater. Interfaces.*, 2017, **9**, 12427-12435.

393. J. Chen, S. Shen, P. Guo, M. Wang, P. Wu, X. Wang and L. Guo, *Appl. Catal. B.*, 2014, **152-153**, 335-341.
394. S.-W. Cao, X.-F. Liu, Y.-P. Yuan, Z.-Y. Zhang, Y.-S. Liao, J. Fang, S. C. J. Loo, T. C. Sum and C. Xue, *Appl. Catal. B.*, 2014, **147**, 940-946.
395. J. Xu, Y. Li and S. Peng, *Int. J. Hydrog. Energy.*, 2015, **40**, 353-362.
396. H. Zhao, Y. Dong, P. Jiang, H. Miao, G. Wang and J. Zhang, *J. Mater. Chem. A*, 2015, **3**, 7375-7381.
397. Y. Hou, A. B. Laursen, J. Zhang, G. Zhang, Y. Zhu, X. Wang, S. Dahl and I. Chorkendorff, *Angew. Chem.*, 2013, **52**, 3621-3625.
398. D. Zheng, G. Zhang, Y. Hou and X. Wang, *Appl. Catal., A*, 2016, **521**, 2-8.
399. Q. Gu, H. Sun, Z. Xie, Z. Gao and C. Xue, *Appl. Surf. Sci.*, 2017, **396**, 1808-1815.
400. H. Yu, P. Xiao, P. Wang and J. Yu, *Appl. Catal., B*, 2016, **193**, 217-225.
401. C. Wu, Q. Fang, Q. Liu, D. Liu, C. Wang, T. Xiang, A. Khalil, S. Chen and L. Song, *Inorg. Chem. Front.*, 2017, **4**, 663-667.
402. M. Li, L. Zhang, X. Fan, M. Wu, Y. Du, M. Wang, Q. Kong, L. Zhang and J. Shi, *Appl. Catal. B.*, 2016, **190**, 36-43.
403. D. Lu, H. Wang, X. Zhao, K. K. Kondamareddy, J. Ding, C. Li and P. Fang, *ACS Sustain. Chem. Eng.*, 2017, **5**, 1436-1445.
404. W. J. Ong, L. L. Tan, S. P. Chai, S. T. Yong and A. R. Mohamed, *Nanoscale.*, 2014, **6**, 1946-2008.
405. A. Thomas, A. Fischer, F. Goettmann, M. Antonietti, J.-O. Müller, R. Schlögl and J. M. Carlsson, *J. Mater. Chem.*, 2008, **18**, 4893-4908.
406. K. Li, X. An, K. H. Park, M. Khraisheh and J. Tang, *Catal. Today.*, 2014, **224**, 3-12.
407. A. Sartbaeva, V. L. Kuznetsov, S. A. Wells and P. P. Edwards, *Energy Environ. Sci.*, 2008, **1**, 79-85.
408. Brian Tuffy, Ludwig Maximilian University of Munich, 2016 PhD thesis.
409. A. Kudo and Y. Miseki, *Chem. Soc. Rev.*, 2009, **38**, 253-278.
410. X. Chen, S. Shen, L. Guo and S. S. Mao, *Chem. Rev.*, 2010, **110**, 6503-6570.
411. A. L. Linsebigler, G. Lu and J. T. Yates, *Chem. Rev.*, 1995, **95**, 735-758.
412. W.-J. Ong, L.-L. Tan, Y. H. Ng, S.-T. Yong and S.-P. Chai, *Chem. Rev.*, 2016, **116**, 7159-7329.
413. W.-J. Ong, L.-L. Tan, Y. H. Ng, S.-T. Yong and S.-P. Chai, *Chem. Rev.*, 2016, **116**, 7159-7329.
414. S. Sun and S. Liang, *Nanoscale.*, 2017, **9**, 10544-10578.
415. S. Hu, L. Ma, J. You, F. Li, Z. Fan, G. Lu, D. Liu and J. Gui, *Appl. Sur. Sci.*, 2014, **311**, 164-171.
416. J. Ran, J. Zhang, J. Yu, M. Jaroniec and S. Z. Qiao, *Chem. Soc. Rev.*, 2014, **43**, 7787-7812.
417. H. Wang, L. Zhang, Z. Chen, J. Hu, S. Li, Z. Wang, J. Liu and X. Wang, *Chem. Soc. Rev.*, 2014, **43**, 5234-5244.
418. H. Wang, L. Zhang, Z. Chen, J. Hu, S. Li, Z. Wang, J. Liu and X. Wang, *Chem. Soc. Rev.*, 2014, **43**, 5234-5244.
419. W.-J. Ong, L.-L. Tan, Y. H. Ng, S.-T. Yong and S.-P. Chai, *Chem. Rev.*, 2016, **116**, 7159-7329.
420. M. Reza Gholipour, C. T. Dinh, F. Beland and T. O. Do, *Nanoscale.*, 2015, **7**, 8187-8208.

Appendix

Chapter-3

Table A.1 Surface area, reaction conditions and H₂ evolution rates of selected C₃N₄-based photocatalysts.

No.	Catalyst	S _{BET} (m ² /g)	Co- catalyst/wt.%	Sacrificial agent	Light source	Incident light (nm)	Activity (μmol g ⁻¹ h ⁻¹)	Time (h)	Ref.
1	SG-C ₃ N ₄	1	Pt/0.8	TEOA	300 W Xe	> 395	143	24	321
2	SG-C ₃ N ₄	131	Pt/0.8	TEOA	300 W Xe	> 395	1379	24	321
3	g-C ₃ N ₄	142	Ni/0.73	TEOA	300 W Xe	> 420	103	48	291
4	g-C ₃ N ₄	-	Cu/3.0	Methanol	300 W Xe	> 400	20	6	210
5	Ag ₂ S/g-C ₃ N ₄	13	-	Methanol	3 W UV-LED	> 420	200	4	389
6	MoS ₂ /g-C ₃ N ₄	-	Pt/1.0	Methanol	300 W Xe	> 420	231	6	313
7	WS ₂ /g-C ₃ N ₄	-	-	Lactic acid	300 W Xe	> 420	240	-	219
8	CdS/g-C ₃ N ₄	23	Pt/0.6	Na ₂ S/Na ₂ SO ₃	350 W Xe	> 420	4152	-	390
9	CuInS ₂ /g-C ₃ N ₄	96	Pt/1.0	Na ₂ S/Na ₂ SO ₃	300 W Xe	> 420	1290	5	310
10	ZnIn ₂ S ₄ /g-C ₃ N ₄	66	-	TEOA	300 W Xe	> 400	2820	2	306
11	CaIn ₂ S ₄ /g-C ₃ N ₄	54	Pt/1.0	Na ₂ S/Na ₂ SO ₃	12 W UV-LED	-	102	-	391
12	CoO/g-C ₃ N ₄	111	Pt/1.0	TEOA	300 W Xe	> 400	651.3	1	392
13	Cu ₂ O/g-C ₃ N ₄	-	Pt/1.0	TEOA	300 W Xe	> 420	241	11	393
14	In ₂ O ₃ /g-C ₃ N ₄	-	Pt/0.5	Ascorbic acid	300 W Xe	> 420	198.0	4	394
15	AgIn ₅ S ₈ /C ₃ N ₄	118	Pt/≤ 2.0	TEOA	300 W Xe	> 420	≤ 1395	24	

Table A.2 Reaction conditions and H₂ evolution rates of AgIn₅S₈ photocatalysts.

No.	Catalyst	S _{BET} (m ² /g)	Co- catalyst/wt.%	Sacrificial agent	Light source	Incident light (nm)	Activity (μmol g ⁻¹ h ⁻¹)	Time (h)	Ref.
1	AgIn ₅ S ₈	-	Pt/2.0	Na ₂ S/Na ₂ SO ₃	300 W Xe	> 420	1001	3	322
2	AgIn ₅ S ₈	-	Pt/2.0	Na ₂ S/Na ₂ SO ₃	300 W Xe	> 420	110	-	341
3	AgIn ₅ S ₈	-	Pt/0.5	Na ₂ S/K ₂ SO ₃	300 W Xe	> 420	1150	7	342

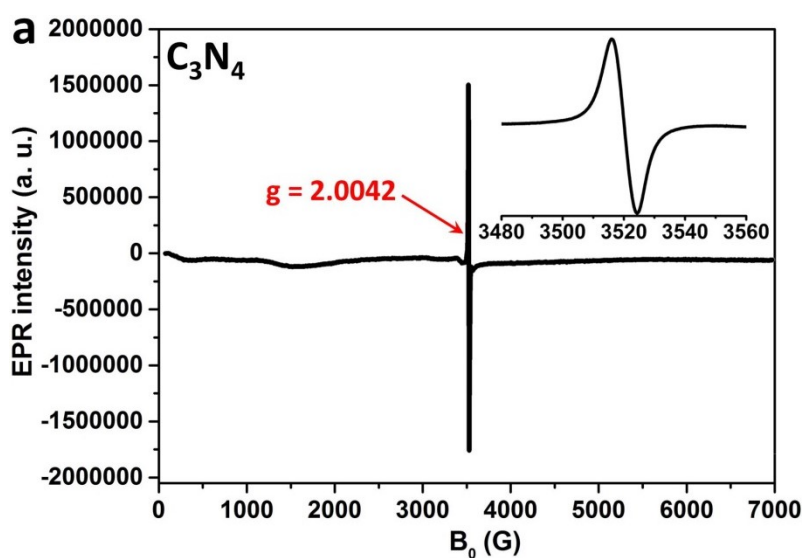


Figure A.1 EPR signal of pure C_3N_4 at room temperature without light irradiation (inset: magnification from 3480 to 3560 G).

Chapter-4

Table A.3 Synthesis method, reaction conditions and H_2 production rates of selected metal sulfide/ C_3N_4 based photocatalysts.

No.	Catalyst	Synthesis method	Optimum amount of MoS ₂ /wt.%	Sacrificial agent	Light source	Incident light (nm)	Activity ($\mu\text{mol h}^{-1} \text{g}^{-1}$)	Ref.
1	EB/MoS _x /g-C ₃ N ₄	In-situ photodeposition	0.5	TEOA	400 W Hg	> 420	180	395
2	MoS ₂ /g-C ₃ N ₄	In-situ photodeposition	2.89	TEOA	300 W Xe	> 400	252	396
3	Pt/MoS ₂ /g-C ₃ N ₄	Sonochemical	0.5	Methanol	300 W Xe	> 400	231	313
4	MoS ₂ /mpg-C ₃ N ₄	Impregnation & Sulfidation	0.2	Lactic acid	300 W Xe	420	1125	397
5	MoS ₂ /g-C ₃ N ₄	Impregnation-sulfidation	0.5	Lactic acid	300 W Xe	> 420	1340	398
6	MoS ₂ /C ₃ N ₄	Hydrothermal	4	TEOA	300 W Xe	> 420	90	399
7	MoS _x /g-C ₃ N ₄	-	3	Lactic acid	3 W LED	420	273.1	400
8	1T MoS ₂ /g-C ₃ N ₄	Solvothermal	0.2	Lactic acid	300 W Xe	-	949	401
9	1T MoS ₂ /O-g-C ₃ N ₄	Solvothermal	0.2	TEOA	300 W Xe	> 400	1842	394
10	MoS ₂ /py-C ₃ N ₄	Hydrothermal	3	TEOA	300 W Xe	> 420	500	402
11	g-C ₃ N ₄ /Ag/MoS ₂	Hydrothermal	-	TEOA	300 W Xe	> 420	104	403
12	Pt/MoS ₂ /C ₃ N ₄	In-situ photodeposition	2	Lactic acid	300 W Xe		2342	

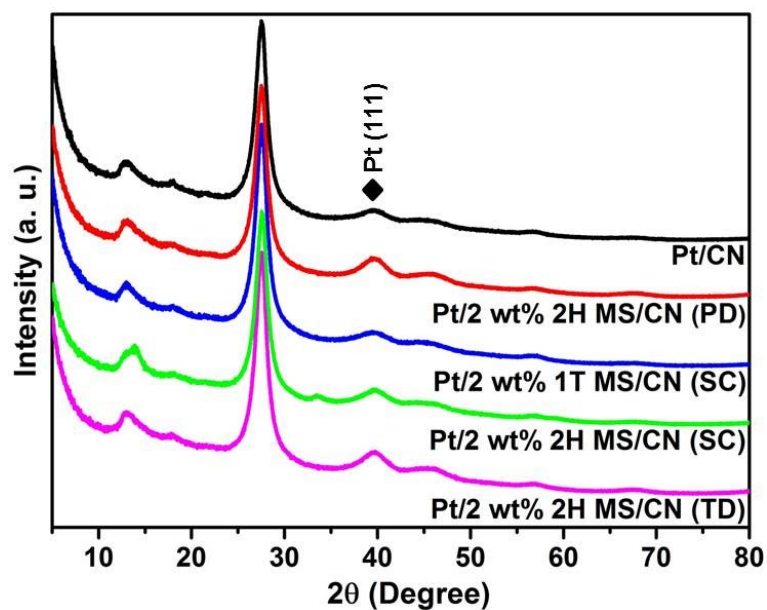


Figure A.2 XRD powder patterns of Pt/CN and Pt/MS-CN composite catalysts removed from the reactor after 6 h irradiation under UV-vis light in the presence of lactic acid.

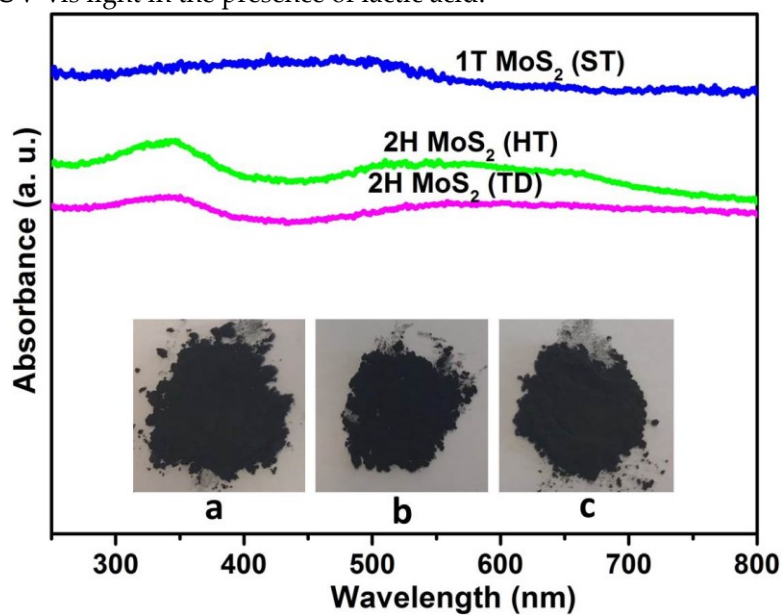


Figure A.3 DRS UV-vis spectra of 2H MoS₂ (HT), 1T MoS₂ (ST) and 2H MoS₂ (TD). Photos: (a) 2H MoS₂ (HT), (b) 1T MoS₂ (ST) and (c) 2H MoS₂ (TD).

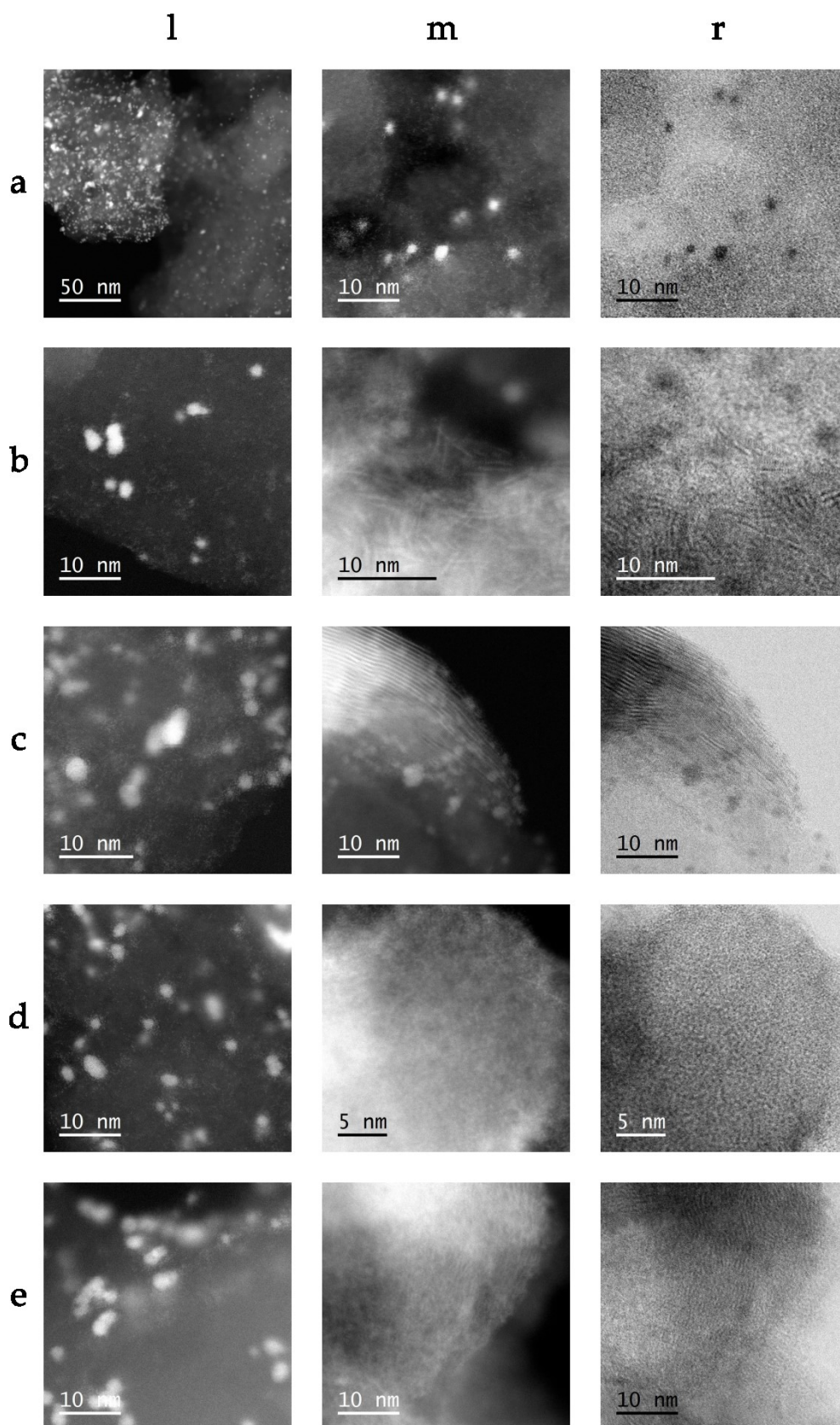


Figure A.4 STEM high angle annular dark field (HAADF) micrographs of CN phase decorated with Pt (column l), high resolution HAADF (column m) and bright field (BF) micrographs (column r) of MoS₂ phase (when present) in catalysts exposed to UV-vis irradiation for 6 h in the presence of lactic acid; (line a) Pt/CN, (b) Pt/2H MS-CN (PD), (c) Pt/2H MS-CN (SC), (d) Pt/1T MS-CN (SC), (e) Pt/2H MS-CN (TD).

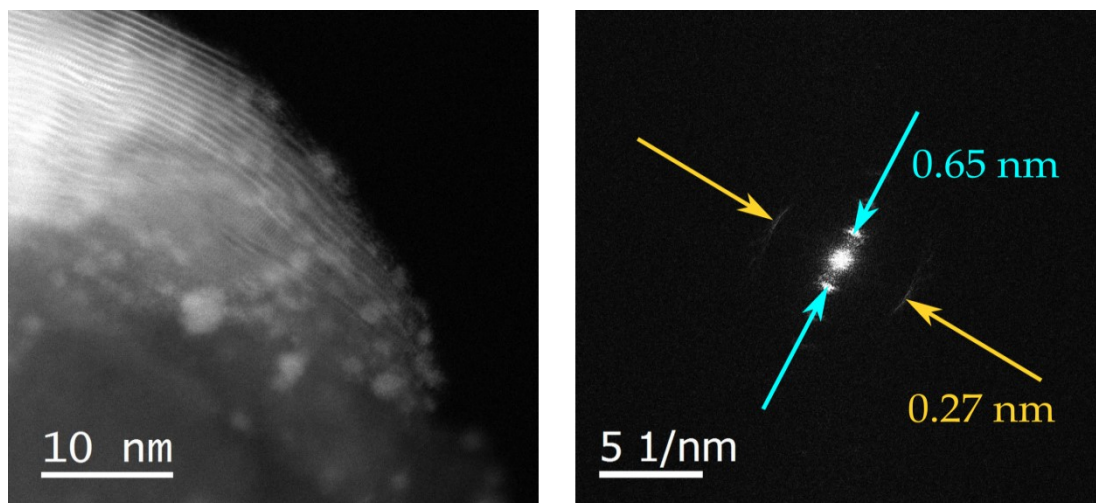


Figure A.5 High resolution STEM-HAADF image with corresponding FFT of Pt/2H MS-CN (SC).

In Fig. A.5, the high resolution STEM-HAADF image of Pt/2H MS-CN (SC) illustrates that 2H MoS₂ has a typical layered structure. Analysis of the Fast Fourier Transformation (FFT) of that image revealed an interlayer spacing of 0.27 and 0.65 nm, which corresponds to the (100) and (002) planes of hexagonal 2H MoS₂ (ICDD: 01-075-1539) which also confirms the existence of 2H MoS₂ species in the composite catalysts.

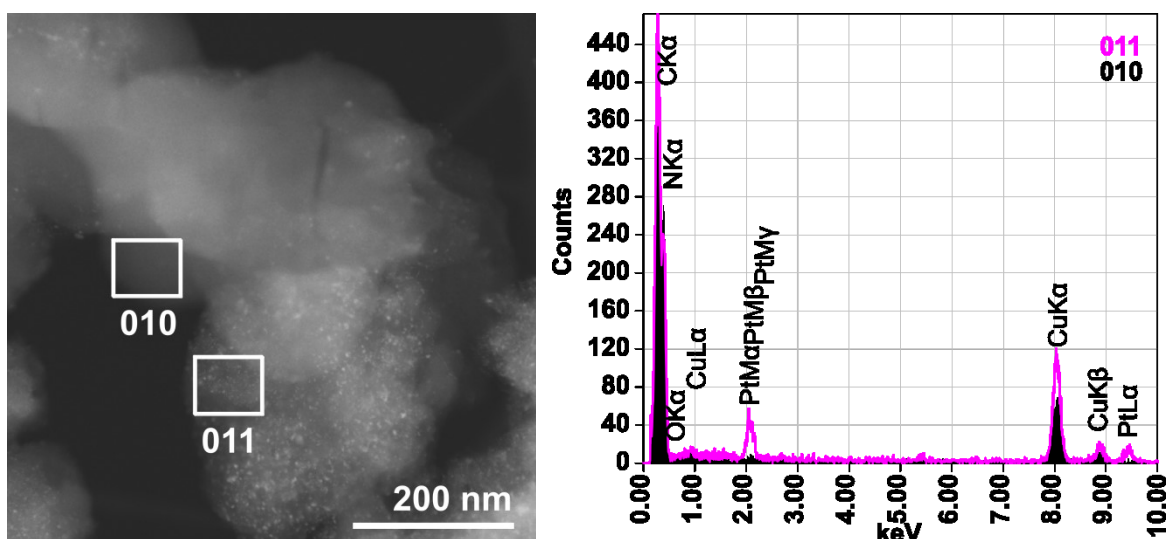


Figure A.6 STEM-HAADF micrograph with corresponding EDX spectra of Pt/CN.

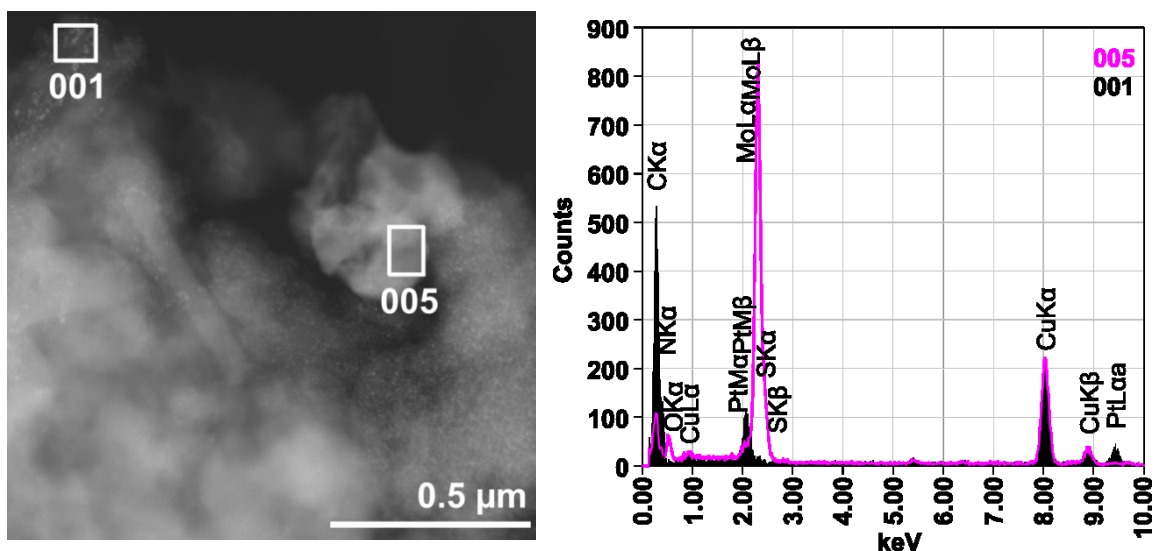


Figure A.7 STEM-HAADF micrograph with corresponding EDX spectra of Pt/2H MS-CN (PD).

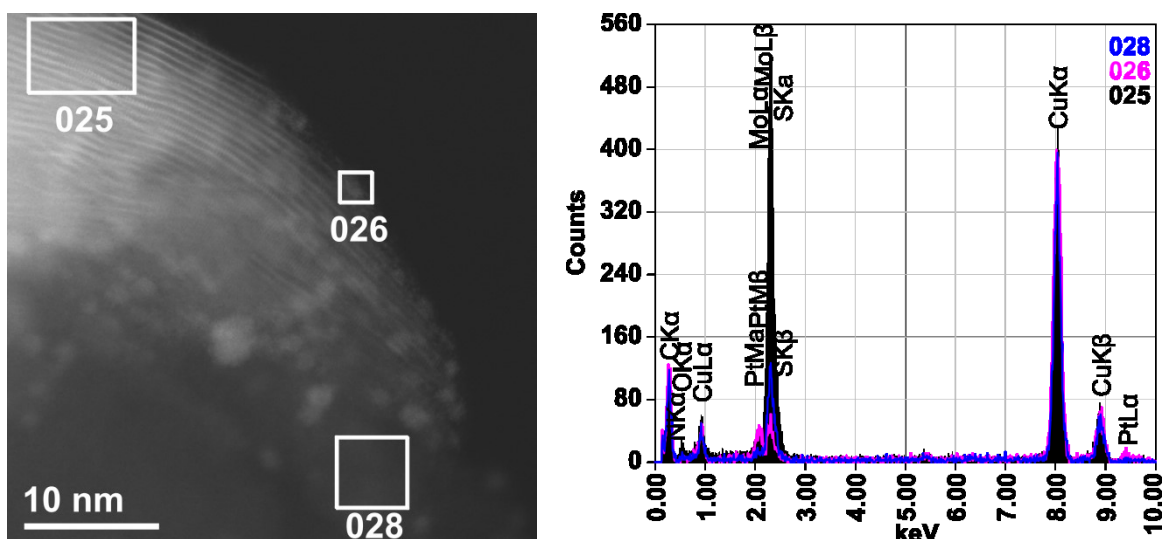


Figure A.8 STEM-HAADF micrograph with corresponding EDX spectra of Pt/2H MS-CN (SC).

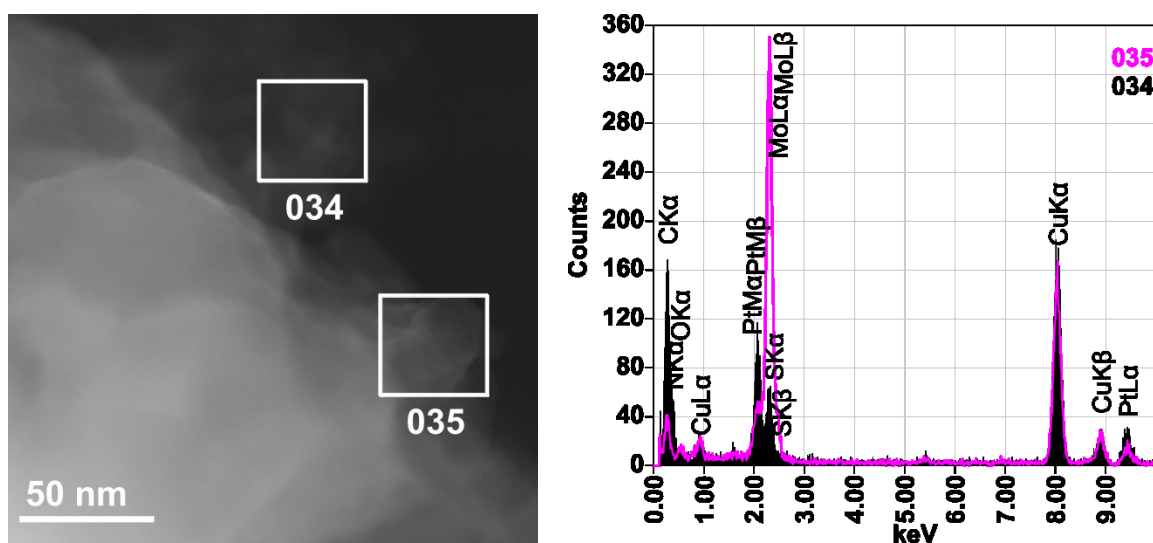


Figure A.9 STEM-HAADF micrograph with corresponding EDX spectra of Pt/1T MS-CN (SC).

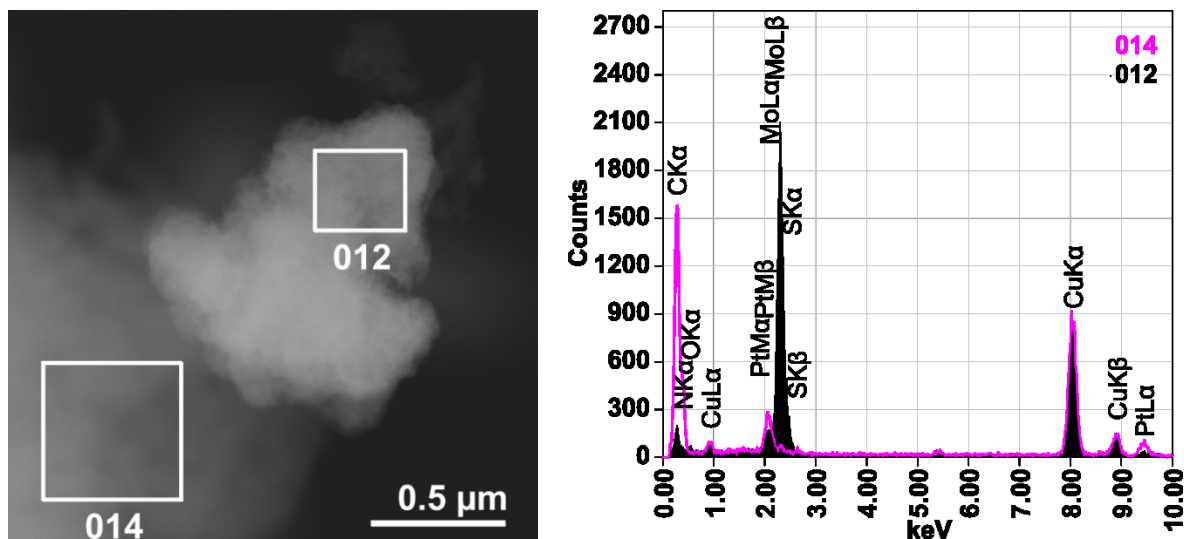


Figure A.10 STEM-HAADF micrograph with corresponding EDX spectra of Pt/2H MS-CN (TD).

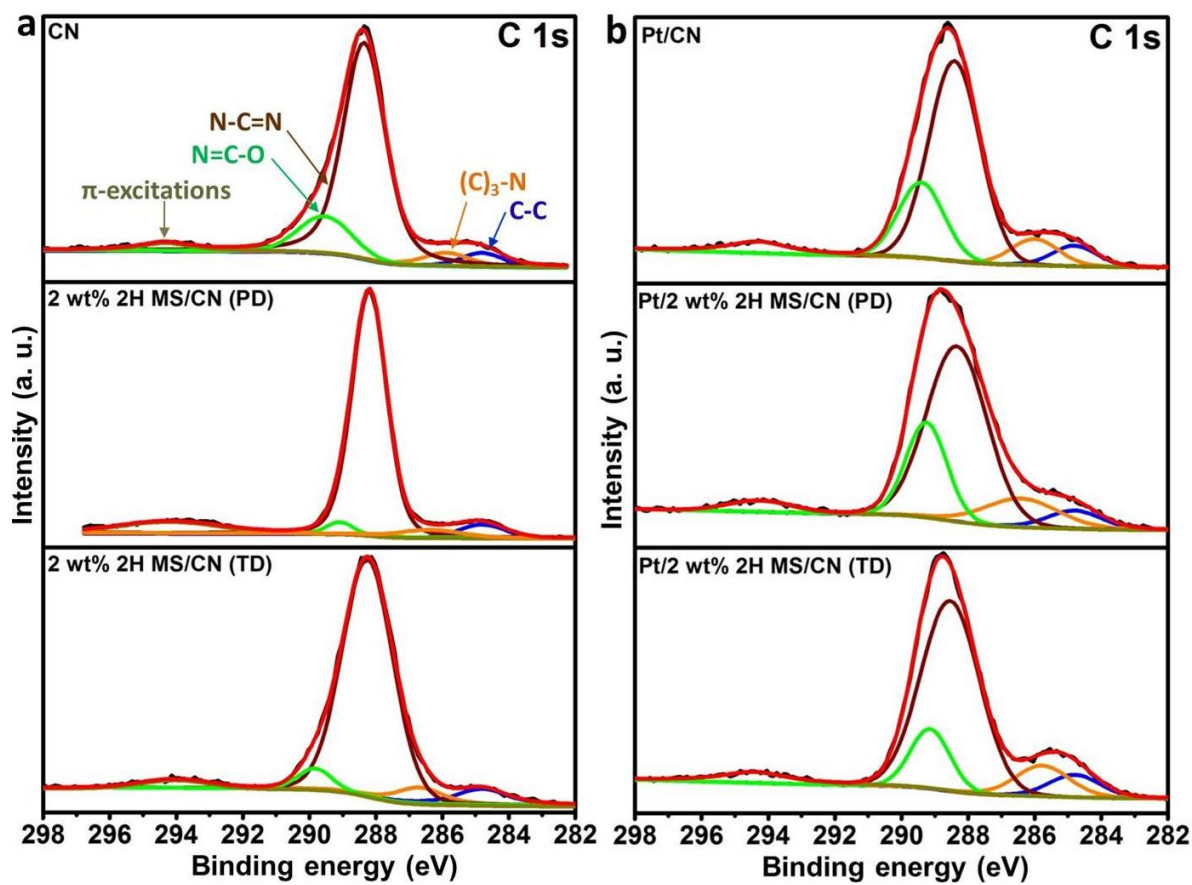


Figure A.11 XPS spectra of C 1s: (a) Fresh catalysts; (b) Recovered catalysts after 6 h reaction.

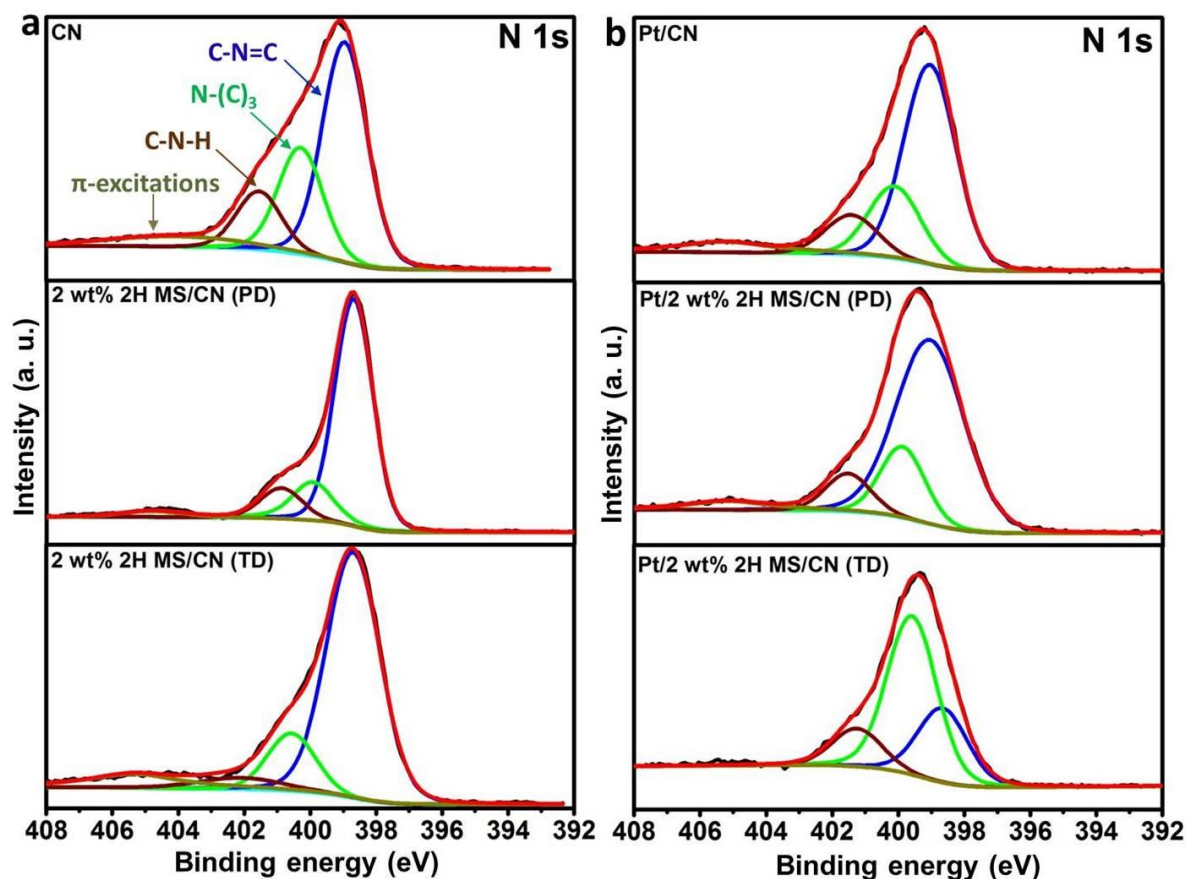


Figure A.12 XP spectra of N 1s: (a) Fresh catalysts; (b) Recovered catalysts after 6 h reaction.

The elemental C 1s spectrum of pure CN (Fig. A11a, top) can be deconvoluted into four different peaks with binding energies centered at 289.5, 288.3, 285.9 and 284.8 eV. The peak located at 289.5 eV can be attributed to (N=C-O) groups, while the peak centered at 288.3 eV is associated with the sp^2 -bonded carbon in an N-containing aromatic structure (N-C=N) which is the major carbon environment in the CN matrix. The peak at 285.9 eV is ascribed to carbon attached with tertiary nitrogen ((C)₃-N) and the peak at 284.8 eV corresponds to adventitious carbon species (C-C).⁴⁰⁴ The respective elemental N 1s spectrum of pure CN (Fig. A.12a, top) could be deconvoluted into three different peaks at binding energies of 401.5, 400.3 and 398.9 eV which can be assigned to the terminal amino groups (C-N-H), tertiary nitrogen groups (N-(C)₃) and sp^2 -hybridized nitrogen involved in triazine rings (C-N=C), respectively.³⁵¹ Moreover, there is a weak peak present at 404.35 eV that is attributed to charging effects in CN.^{405, 406}

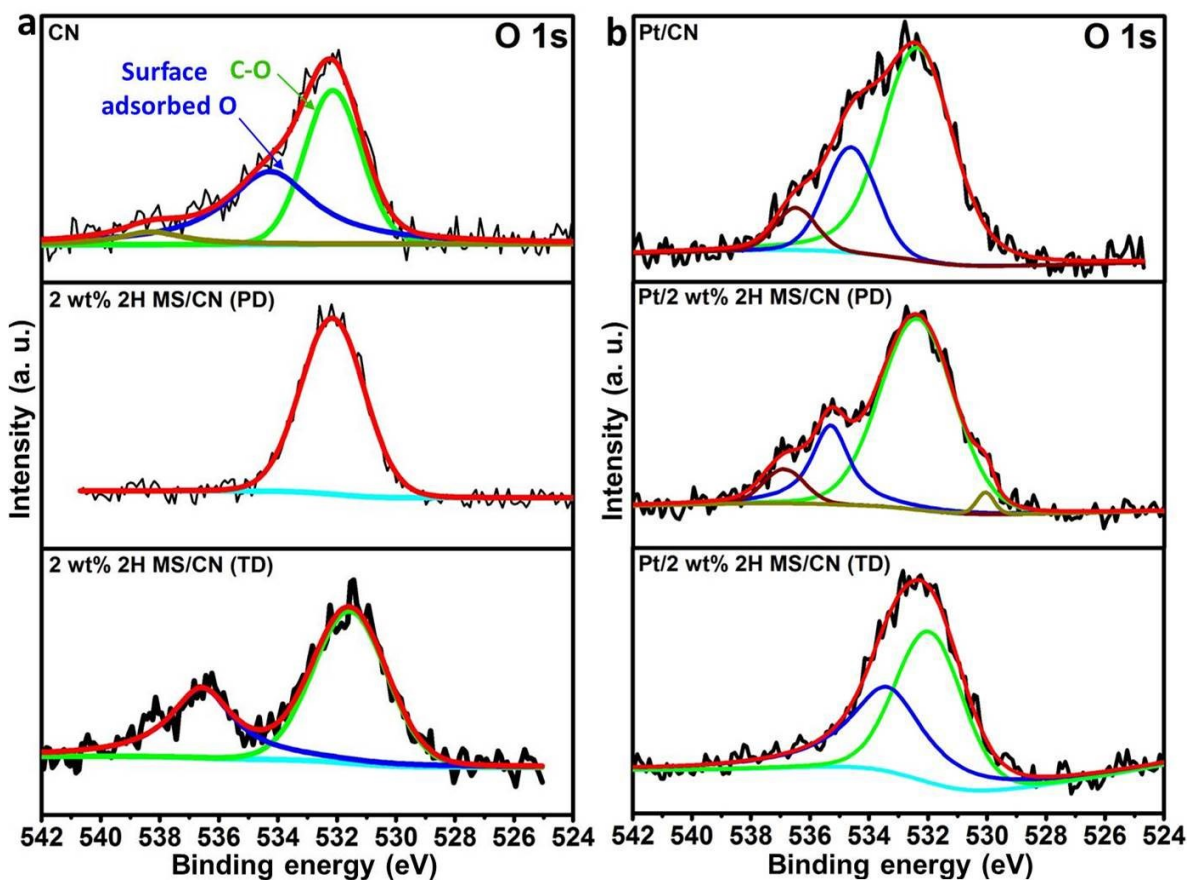


Figure A.13 XP spectra of O 1s: (a) Fresh catalysts; (b) Recovered catalysts after 6 h reaction.

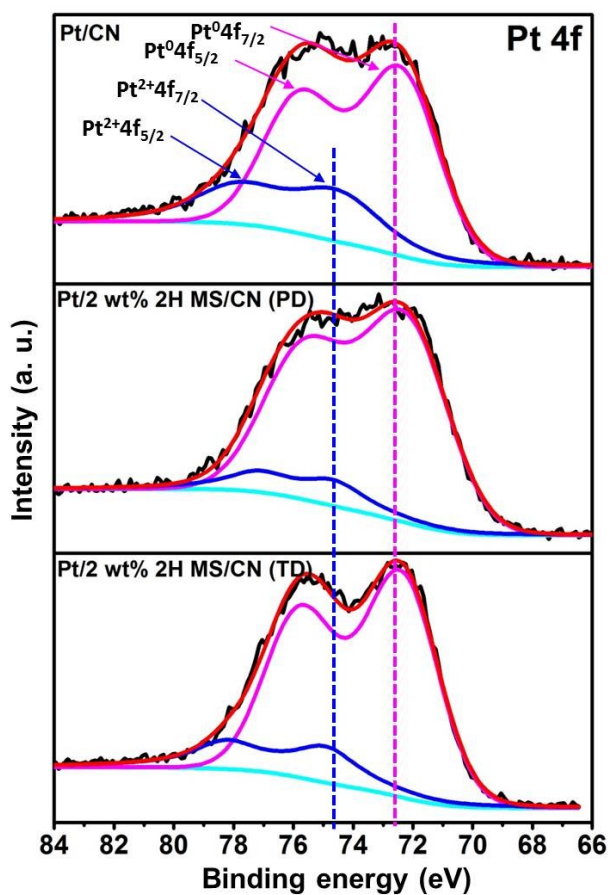


Figure A.14 XP spectra of Pt 4f: Pt/CN, Pt/2H MS-CN (PD) and Pt/2H MS-CN (TD).

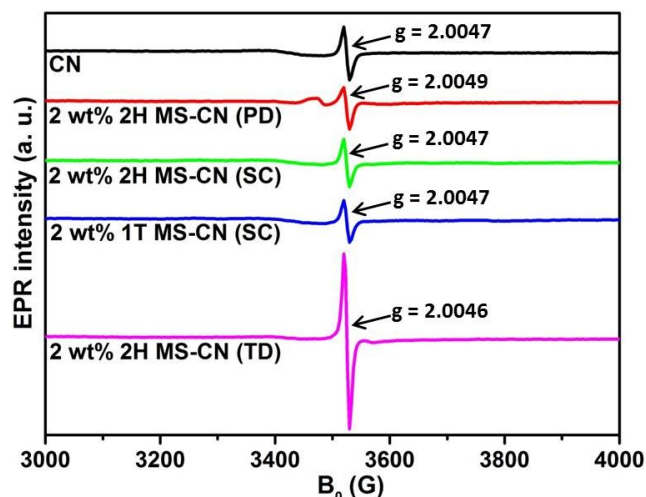


Figure A.15 EPR signal of as synthesized catalysts at 300 K (without light irradiation).

List of scientific publications and conferences

List of scientific publications

- 1) **R. P. Sivasankaran**, N. Rockstroh, D. Hollmann, C. R. Kreyenschulte, G. Agostini, H. Lund, A. Acharjya, J. Rabeah, U. Bentrup, H. Junge, A. Thomas and A. Brückner*. Relations between structure, activity and stability in C_3N_4 based photocatalysts used for solar hydrogen production. *Catalysts*, 2018, 8, 52.
- 2) **R. P. Sivasankaran**, N. Rockstroh, C. R. Kreyenschulte, S. Bartling, H. Lund, A. Acharjya, H. Junge, A. Thomas and A. Brückner*. Influence of MoS_2 on activity and stability of carbon nitride in photocatalytic hydrogen production (Submitted to in the journal *Catalysts*, MDPI publishing company).

Additional scientific publications

- 1) P. Pachfule, A. Acharjya, J. Roeser, **R. P. Sivasankaran**, M. Ye, I. Ilić, A. Brückner, J. Schmidt and A. Thomas. Donor-acceptor covalent organic frameworks for visible light induced free radical polymerization (Accepted in *Chemical Science*).
- 2) A. Indra, R. Beltrán-Suito, **R. P. Sivasankaran**, M. Müller, M. Schwarze, A. Acharjya, A. Brückner, P. W. Menezes and M. Driess. Promoting photocatalytic hydrogen evolution activity of graphitic carbon nitride with hole transfer agents (Under preparation).
- 3) **R. P. Sivasankaran**, D. N. Srivastava*. Distinguishing Polymorphs of Copper-Tetracyanoquinodimethane charge-Transfer Salts. *Science and Technology Journal*. **2015**, 3, 125-133.
- 4) **R. P. Sivasankaran**, N. S. Sangeetha, A. Kalaivani, S. Sriman Narayanan*. Synthesis of exclusive star shaped PbS nanocrystals and determination of Cd(II) ions using Hg(II)-PbS modified graphite electrode by differential pulse anodic stripping voltammetry. *Asian J. Chem.* **2013**, 25, 30-34.

List of contribution in conferences

- 1) **R. P. Sivasankaran**, N. Rockstroh, D. Hollmann, C. R. Kreyenschulte, G. Agostini, H. Lund, A. Acharjya, J. Rabeah, U. Bentrup, H. Junge, A. Thomas and A. Brückner*. Relations between structure, activity and stability in C_3N_4 photocatalysts used for solar hydrogen production. 51st Jahrestreffen Deutscher Katalytiker in Weimar, Germany, March 14-16, 2018 (Poster presentation).
- 2) **R. P. Sivasankaran**, N. Rockstroh, D. Hollmann, C. R. Kreyenschulte, G. Agostini, H. Lund, J. Rabeah, U. Bentrup, H. Junge, A. Thomas and A. Brückner*. Relations between structure, activity and stability in $AgIn_5S_8/C_3N_4$ photocatalysts used for solar hydrogen production. 21st Norddeutsches Doktorandenkolloquium at Technische Universität Braunschweig, Germany, September 03-04, 2018 (Oral presentation).

- 3) **N. Rockstroh**, R. P. Sivasankaran, D. Hollmann, A. E. Surkus, M. Polyakov, U. Bentrup, A. Brückner*. Assessing key features of active catalysts in photo- and electrocatalytic water splitting by in situ spectroscopy. 7th EuCheMS Chemistry Congress in Liverpool, United Kingdom, August 26-30, 2018 (Oral presentation).
- 4) **N. Rockstroh**, R. P. Sivasankaran, D. Hollmann, J. Rabeah, U. Bentrup, A. Brückner*. Influence of Sulfide Cocatalysts on Stability and Activity of Carbon Nitrides in Photocatalytic Hydrogen Evolution. VIIIth International Symposium on Molecular Aspects of Catalysis by Sulfides (MACS VIII), Cabourg, France, May 19-23, 2019 (Oral presentation).

Selbständigkeitserklärung

Ich erkläre, dass ich die hier vorgelegte Arbeit selbständig und ohne fremde Hilfe verfasst, andere als die von mir angegebenen Quellen und Hilfsmittel nicht benutzt und die den benutzten Werken wörtlich oder inhaltlich entnommenen Stellen als solche kenntlich gemacht habe.

Rostock: 26-07-2019